Multi-Wavelength Properties of Submillimeter-Selected Galaxies

Thesis by

Laura Jeannine Hainline

In Partial Fulfillment of the Requirements

for the Degree of

Doctor of Philosophy

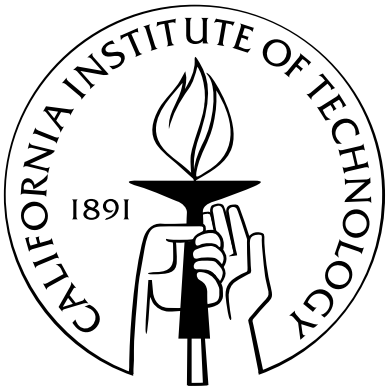

California Institute of Technology

Pasadena, California

2008

(Defended November 2, 2007)

Acknowledgements

Many people have made this thesis possible. I would just like to take a moment to thank a few who have played important roles in its creation. First off, I have to thank my fellow classmates, Milan, Elina, Stuartt, Melissa, Margaret, and Cathy, who have been great sources of humor, advice, inspiration, and friendship. And I must single out Stuartt, who has patiently put up with me as an office mate for six years. Karin Ménendez has also been great to share an office with, and I have greatly enjoyed talking about science with her since she moved in to Super-D this past year. Of course, I have to thank my parents and siblings: my parents for their support, and my siblings for not *too* often reminding me what a dork I am for wanting to study astronomy, when I could be going to medical school! I would also like to thank Catherine Stevens and Mary T. Moran, who would be very unhappy if I didn't mention them!

I must also acknowledge the contribution to my scientific development of my undergraduate research advisor, Constantine Deliyannis, who took a chance on a random student who wanted to try some astronomy research, and later didn't give me a hard time when I decided to try extragalactic astronomy. I would like to thank my advisor, Andrew Blain, for steering me towards projects which encompass a wide range of wavelengths; it was my intention to become a multi-wavelength astronomer when I came to Caltech, and I have gotten off to a good start. I must also thank Nick Scoville, who first steered me into the high redshift realm with observing high-z QSOs at OVRO. I would like to take a moment to thank my thesis committee in advance for the taking the time to read my thesis and give me helpful comments (please!): the committee consists of the previously mentioned Andrew and Nick, plus Richard Ellis, Wal Sargent, and Marc Kamionkowski.

Saving the best for last, I must also thank my husband Sean, for everything. Mine?

Abstract

The resolution of the cosmic far-infrared background at long wavelengths has uncovered a population of high-redshift, highly infrared-luminous galaxies that indicate that a significant amount of highly obscured star formation occurred in the early history of the Universe, which has not been taken into account in studies of the cosmic star formation and mass assembly histories. Since such studies are important tests of hierarchical galaxy formation models in a cold dark matter- dominated universe, it is vital that the contribution of these luminous submillimeter-selected galaxies to the buildup of stellar mass in the Universe be understood and included when testing galaxy formation models. Progress in understanding the nature of submillimeter-selected galaxies has been slow, however, due to the faintness of the population outside of the submillimeter bands and the coarse resolution of the single-dish submillimeter surveys in which the galaxies were discovered. The slow progress has at least two important consequences: (1) there is still much that is unknown about submillimeter-selected galaxies at all wavelengths, so the properties of and evolutionary predictions for the population are often inferred by making analogies to local galaxies of similar luminosity and assuming the high-redshift galaxies represent a uniform population of galaxies; and (2) the relationships of the submillimeter-selected galaxies to other high-redshift galaxy populations selected at other wavelengths remain poorly understood.

In this work we capitalize on recently-available observing resources of the *Spitzer Space Telescope*, at near- and mid-infrared wavelengths, and the Green Bank Telescope, at 1 cm, to improve the characterization of the largest representative sample of submillimeter-selected galaxies with spectroscopic redshifts. We combine our new data with data from the literature at a variety of wavelengths to place new constraints on the fundamental properties of gas mass, stellar mass, infrared luminosity, and spectral energy distribution, and use our new constraints to test a variety of assumptions which have been used in the past to predict and infer characteristics of submillimeter-selected galaxies. We also use our new data to

compare different populations of high-redshift galaxies selected at different wavelengths in an effort to understand the relationships between the different types of galaxies.

First, we use observations of CO rotational line emission with the Green Bank Telescope to constrain the cold gas mass and gas conditions in several submillimeter-selected galaxies. We obtain the first detection of CO(1→0) emission from a submillimeter-selected galaxy, finding that the CO(4→3)/CO(1→0) brightness temperature ratio of ~ 0.26 suggests $n(\mathrm{H_2}) > 3 - 10 \times 10^2\,\mathrm{cm^{-3}}$ and the presence of sub-thermally excited gas. The integrated line flux implies a cold molecular gas mass 4 times larger than the mass predicted from the CO(4→3) line, assuming a brightness temperature ratio of 1.0, suggesting that extrapolating molecular gas masses from $J_{upper} \geq 3$ transitions of CO, which is the primary method of estimating molecular gas masses of high-z galaxies in the literature, leads to considerable uncertainties.

Next, we use deep imaging with the Multiband Imaging Photometer for *Spitzer* (MIPS) on the *Spitzer Space Telescope* of the spectroscopic sample of radio-detected submillimeter-selected galaxies of Chapman et al. (2005) to derive new estimates of the infrared luminosity for these objects. Our *Spitzer* data constrain the Wien side of the infrared spectral energy distribution peak of high-redshift submillimeter-selected galaxies, and thus are extremely important to determine the contribution of hot dust emission to the total infrared luminosity. We find that most submillimeter-selected galaxies do not have dominant contributions from hot dust at rest-frame mid-infrared wavelengths. We also find that the spectral energy distribution of the nearest ultraluminous infrared galaxy, Arp 220, is significantly different on average from most high-z submillimeter-selected galaxies and is thus a poor template with which to predict properties of submillimeter-selected galaxies even though it has been often used in the past. Using our new infrared luminosity estimates constrained by multiple infrared and submillimeter data points, we show that submillimeter-selected galaxies display a relatively tight, almost linear correlation between total infrared luminosity and radio luminosity, which is not largely different from the far-infrared–radio correlation of local galaxies selected by the *Infrared Astronomical Satellite* (*IRAS*).

We examine the rest-frame ultraviolet through near-infrared spectral energy distributions of the same sample of radio-detected submillimeter-selected galaxies with spectroscopic redshifts, obtained using measurements from imaging with the Infrared Array Camera (IRAC) on *Spitzer* in combination with observed-frame optical and near-infrared data

from the literature. We find from these spectral energy distributions, which trace the stellar light from a galaxy in the absence of an active nucleus, that submillimeter-selected galaxies suffer significant extinction at rest-frame optical wavelengths, and that both stars and dust emission contribute to the near-infrared luminosity in many $z > 2$ submillimeter-selected galaxies. We estimate stellar masses for the individual galaxies in the sample using rest-frame H-band luminosities interpolated from the observed spectral energy distributions, obtaining a median stellar mass for the sample of $6 - 7 \times 10^{10}\,M_{\odot}$. By comparing our stellar mass estimates to molecular gas and dynamical mass estimates for 13 individual submillimeter-selected galaxies in our sample observed in CO emission lines, we determine that the molecular gas fraction in submillimeter-selected galaxies declines with increasing stellar mass, which is suggestive of an evolutionary trend. If the molecular gas masses for the 13 galaxies for which gas mass estimates are available are typical of the entire radio-detected submillimeter-selected galaxy population, then a typical lower limit to the total baryonic mass of submillimeter-selected galaxies is $\sim 10^{11}\,M_{\odot}$, and these galaxies are unlikely to significantly increase their stellar mass in the current epoch of activity which is the source of their enormous infrared luminosity.

Lastly, we compare the IRAC and MIPS properties of submillimeter-selected galaxies and their stellar masses to those of high-redshift ultraviolet- and optically-selected galaxies, $24\,\mu$m-selected galaxies, and powerful radio galaxies. In the IRAC bands, submillimeter-selected galaxies are brighter and redder than ultraviolet-selected galaxies, suggesting they have higher dust content, higher stellar mass, a higher contribution from an active nucleus, or some combination of these factors. The near-infrared colors of submillimeter-selected galaxies are most similar to those of high-z radio galaxies, objects which are known to contain powerful, obscured active nuclei. However, submillimeter-selected galaxies are fainter in the MIPS $24\,\mu$m band than high-z radio galaxies, suggesting that the dust in the submillimeter-selected galaxies is not heated to such high temperatures as in the radio sources. We find that the typical stellar mass of submillimeter-selected galaxies is larger by a factor of 3–4 than that of high-redshift ultraviolet-selected galaxies, roughly similar to the typical stellar mass of optically-selected high-z galaxies, and lower than the typical stellar mass of powerful high-z radio galaxies. These comparisons suggest that submillimeter-selected galaxies are among the more massive galaxies of their epoch, but not necessarily the most massive, as has been suggested in the literature. However, systematic errors in

the stellar masses of any of the high-redshift galaxy samples of a factor of a few, which are certainly possible, can alter this conclusion.

Contents

List of Figures

List of Tables

Chapter 1

Introduction

In the local universe, most galaxies are observed to fall into several distinct classes: old spheroidal and elliptical galaxies with little gas or ongoing star formation; spiral galaxies which are rich in gas and have a mix of old stars and ongoing star formation; and gas-rich dwarf irregular galaxies, forming stars at modest rates. A long-standing astrophysical problem is how to explain the formation of such different systems. In the currently favored scenario of galaxy formation (e.g., White & Rees 1978), galaxies form through hierarchical clustering of dark matter halos which grow out of density perturbations in the early universe, as baryons within the dark matter halos collapse into stars and galaxies. Progressively larger structures are formed gradually over the history of the Universe, as dark matter halos continue merging. Theoretical galaxy formation models employing hierarchical clustering in a Λ-dominated cold dark matter universe predict that the most massive galaxies and structures form late in the history of the Universe ($z \lesssim 1$; e.g., Kauffmann & Charlot 1998; Baugh et al. 1998), and in principle we should observe in the current epoch the most massive structures forming.

However, it is quite clear in observing local galaxies that most massive galaxies are not only *not* still forming (star-wise), but seem to have stopped forming long ago. Galaxies with $M_\star > 10^{11}\,M_\odot$ are generally all early type (elliptical or spheroidal) out to $z \sim 1$ (e.g., Brinchmann & Ellis 2000; Bundy et al. 2005), and no significant evolution in the stellar mass function nor the near-infrared luminosity function of galaxies has occurred since $z \sim 1$ (Fontana et al. 2004; Pozzetti et al. 2003). We also observe that the most massive galaxies, with $M_\star > 10^{11.5}\,M_\odot$, are all early-types, with seemingly uniformly old stellar populations and little to no cold gas for future star formation. In fact, much of the stellar mass in the local universe is contained within massive early-type galaxies (Kauffmann et al. 2003),

which have not formed more than a few percent of their stars in the last 2 Gyr. On the other hand, the integrated stellar properties of a stellar population become degenerate after a few Gyr of evolution (see, e.g., Bruzual & Charlot 2003), so exactly how old the stars are in early-type galaxies is not something one can easily distinguish. Thus, one of the great unsolved questions in cosmology arises: do the old stars of massive galaxies in the current epoch necessarily require that cold dark matter (CDM) hierarchical models of galaxy formation be revised?

In order to answer the question, the predictions of CDM models must be thoroughly tested by determining observationally the star formation history and mass assembly history of massive systems in the Universe. The general concern of this thesis is to improve the current understanding of star formation and mass assembly in massive galaxies at high redshift. Much effort has been made to catalog high-redshift galaxies at optical wavelengths to trace the cosmic star formation history, as we describe below; however, it is also important to consider the contribution of obscured star formation to the star formation history of the Universe. The main focus in this thesis will thus be the examination of the fundamental properties of a particularly mysterious group of obscured high-redshift galaxies apparently in the process of formation, the submillimeter-selected galaxies, and relating them to the populations of high-redshift galaxies identified at optical and near-infrared wavelengths, which have been most frequently used in studies of high-redshift star formation and galaxy assembly.

1.1 Testing CDM Models: Finding Massive Galaxies at High Redshift at Optical Wavelengths

Tremendous effort within the last decade has been expended in identifying and studying massive galaxies at high redshift, towards the goal of determining the cosmic mass assembly and star formation histories. Before then, most of the high-redshift galaxies known were quasars or lobe-dominated radio galaxies due to their extreme luminosities; however, these types of objects are relatively rare in the Universe and do not represent "typical" high-redshift galaxies. Numerous deep optical surveys have been carried out to study high-redshift galaxies: the Hubble Deep Field (HDF) Survey (Williams et al. 1996), the Canada-France Redshift Survey (CFRS; Lilly et al. 1995), the Great Observatories Origins Deep

Survey (GOODS; Giavalisco et al. 2004), the K20 Survey (Cimatti et al. 2002), COSMOS (Scoville et al. 2007), etc., just to name a few. From the enormous quantities of survey data, the high-redshift galaxies must be identified and then studied in detail to determine their masses, star formation rates, and integrated stellar properties. In order to efficiently select high-redshift galaxies for follow-up studies, numerous selection techniques have been developed by various authors. Here, we present a brief discussion of the most successful and frequently used optical and near-IR selection techniques for finding high-redshift galaxies for analyses of the cosmic star formation rate history and mass assembly history as well as the characteristics of the galaxies they select.

1.1.1 Lyman Break Galaxies

The Lyman break technique for selecting high-redshift galaxies, summarized in Steidel et al. (2003), assumes high-z galaxies have a flat rest-frame far-UV spectrum and a prominent spectral break at the Lyman limit (912 Å). Then, using a custom set of filters ($U_n, G, \mathcal{R}$), which are designed to fall shortward and longward of the Lyman limit for objects in the range $3.0 < z < 3.5$, Lyman break galaxies (LBGs) are selected from field samples if they meet the color criteria $G - \mathcal{R} \leq 1.2$ and $U_n - G \geq G - \mathcal{R} + 1.0$.

Spectroscopic follow up (e.g., Steidel et al. 1996) confirms that most LBGs fall within the redshift range $2.5 < z < 3.5$, with low ($< 5\%$) percentages of $z < 2$ galaxies contaminating the sample. The population of LBGs consists of generally faint ($\mathcal{R} \sim 23 - 25.5$), blue, strongly star forming galaxies (star formation rate [SFR] $\sim 10 - 100\,M_{\odot}\,\mathrm{yr}^{-1}$) with low extinction [$E(B-V) \lesssim 0.35$] and a low frequency of active galactic nuclei (AGN) (3%; Steidel et al. 2003). These galaxies have a surface density on the sky of $1.7\,\mathrm{arcmin}^{-2}$ (Steidel et al. 2003).

1.1.2 BX and BM Galaxies

The BX/BM technique resulted from a tailoring of the Lyman break technique to select galaxies with similar intrinsic properties to LBGs (reddening, UV luminosity, SFR) which lay at $z \sim 2$ instead of $z \sim 3$. The BX galaxies are selected to be at $z \sim 2.0 - 2.6$, while the BM galaxies are selected to lie at $z \sim 1.5 - 2.0$ (Steidel et al. 2004). The spectroscopically confirmed BX/BM sample indeed has similar rest-frame UV spectra, average SFR, reddening, and AGN fraction as the LBG sample, though they are more red in observed-frame

near-infrared colors than LBGs and seem to have higher velocity dispersion as well (Steidel et al. 2004). BX galaxies have a surface density on the sky of $3.6\,\mathrm{arcmin}^{-2}$, while for BM galaxies the density is $5.3\,\mathrm{arcmin}^{-2}$ (Steidel et al. 2004).

1.1.3 Balmer/4000 Å-Break Galaxies, a.k.a. Distant Red Galaxies

The Balmer break/4000 Å break technique, introduced by Franx et al. (2003), is designed to select "normal" galaxies at $z \sim 2-3.5$ whose optical light is dominated by evolved stars, not by an unobscured starburst. The technique selects galaxies to be relatively bright in the observed K-band ($K \lesssim 22$) and exploits the Balmer break and 4000 Å break shifting into the J band at $z > 2$. Galaxies selected by this technique, also referred to as distant red galaxies (DRGs), must satisfy the color criterion $J - K_s > 2.3$.

The $J - K_s > 2.3$ criterion selects both passively evolving galaxies and dusty, reddened star-forming galaxies. Analyses by van Dokkum et al. (2003, 2006) and Förster Schreiber et al. (2004) indicate that the typically faint population of DRGs ($R_{AB} \sim 26$) are luminous ($M_V \sim -24$), massive galaxies at $z \sim 1.5-3.5$ with rest-frame optical colors similar to local spiral galaxies and typical reddening $E(B-V) \sim 0.3$ (Papovich et al. 2006). Star formation rates for these objects from *Spitzer Space Telescope* (*Spitzer* hereafter) data typically range from 100–1000 $M_\odot\,\mathrm{yr}^{-1}$ (Papovich et al. 2006), and an estimated 5–30% of DRGs contain AGN (van Dokkum et al. 2003; Rubin et al. 2004; Papovich et al. 2006). DRGs have estimated surface densities of $\sim 1-3\,\mathrm{arcmin}^{-2}$ (Franx et al. 2003; Förster Schreiber et al. 2004; Papovich et al. 2006).

1.1.4 BzK Galaxies

Daddi et al. (2004) introduced the BzK color criteria to identify high-redshift star forming galaxies and passively-evolving galaxies. All of the BzK galaxies are selected by their observed K-band magnitude, and the star-forming BzK galaxies satisfy $(z-K)-(B-z) \geq -0.2$, while the passively evolving BzK galaxies must satisfy both $(z-K)-(B-z) < -0.2$ and $z-K > 2.5$. Pérez-González et al. (2007) find that the BzK and DRG-selected galaxies overlap significantly: 95% of the DRGs at $1.0 < z < 3.0$ in their sample satisfy the BzK criteria as well.

The star-forming BzK galaxies span a range in redshift of $z \sim 1-3$, from the results of both spectroscopic and photometric redshifts (Daddi et al. 2004; Reddy et al. 2005), while

the passively-evolving galaxies lie at $z \sim 1.5 - 2$. The star-forming BzK galaxies have typical reddening $E(B-V) \sim 0.3$, and from *Spitzer* data appear to have star formation rates of typically 10–100 $M_\odot\,\mathrm{yr}^{-1}$ and infrared luminosities of $\sim 10^{12}\,L_\odot$ (Daddi et al. 2007). 20–30% of these same galaxies are estimated to host obscured AGN. The star-forming BzKs have a surface density on the sky of $\sim 1\,\mathrm{arcmin}^{-2}$ (Daddi et al. 2004), while the surface density for passively-evolving BzKs is $0.2\,\mathrm{arcmin}^{-2}$ (Pérez-González et al. 2007). BzK galaxies appear to be strongly clustered as well (Kong et al. 2006).

1.1.5 Extremely Red Objects

Extremely red objects (EROs) are galaxies which are selected by their extremely red $R-K$ colors, requiring $R-K \geq 5.5$. While initially found one-by-one (e.g, Hu & Ridgeway 1994), the large-area deep extragalactic surveys mentioned in § 1.1 have uncovered large numbers of EROs. Spectroscopic redshifts for these objects have typically been difficult to obtain, though the bulk of this somewhat mysterious population of objects likely lies at $z \sim 1 - 2$ (McCarthy 2004).

EROs appear to be a mix of dusty, star forming galaxies (e.g., HR 10; Dey et al. 1999) and passively-evolving elliptical galaxies. It has been estimated that perhaps 50% are dominated by old stellar populations (McCarthy 2004), but without spectroscopy for many objects this fraction is highly uncertain. EROs also overlap with DRG and BzK samples: Lane et al. (2007) find that the majority of $K_{\mathrm{AB}} < 22.5$ DRGs are also EROs. Similar to BzK galaxies, bright EROS are strongly clustered (e.g., Daddi et al. 2000; Brown et al. 2005; Georgakakis et al. 2005), which suggests that they reside in the most massive dark matter halos. The AGN fraction of this population is not well constrained, but estimated to be $\sim 10\%$, and the surface density of objects with $K < 20$ is $\sim 1\,\mathrm{arcmin}^{-2}$ (McCarthy 2004).

1.1.6 Cosmic Star Formation History from Optically-Selected Galaxies

These various types of galaxies selected at optical wavelengths present a relatively consistent picture of the star formation history of the Universe in which the star formation rate density in the Universe rises steeply, by more than an order of magnitude, from $z = 0$ to a peak near $z \sim 2 - 2.5$, then levels off or falls slightly to $z \sim 6$ (see compilation of Hopkins 2004, and references therein). The assembly history of massive galaxies resulting from studies of

optically-selected galaxies are also consistent, indicating that 50% of the stellar mass in the Universe has formed by $z \sim 1$ (e.g., Rudnick et al. 2003; Drory et al. 2005; Pérez-González et al. 2007). These studies show that the most massive galaxies ($M_\star > 10^{11.5}\,M_\odot$) were already assembled and had formed most of their stars by $z \sim 2-3$ (e.g., Glazebrook et al. 2004; Pérez-González et al. 2007), and half of the stellar mass in $M_\star \sim 10^{11}\,M_\odot$ galaxies formed sometime between $z \sim 2.5$ and $z \sim 1$ (Pérez-González et al. 2007). Such rapid formation of massive galaxies is rather at odds with the predictions of galaxy formation models (e.g., Baugh et al. 1998; Cole et al. 2000; Somerville et al. 2001, 2004), though some models predict that the formation is even more rapid than the observations imply (Nagamine et al. 2004, 2006). To account for the numbers of massive galaxies and ages of stellar populations observed, CDM models of galaxy formation, both semi-analytic and numerical, must invoke large amount of dust (e.g., Somerville et al. 2001, 2004; Nagamine et al. 2005), top-heavy stellar initial mass functions (IMFs) (e.g., Baugh et al. 2005), and AGN feedback (e.g., Granato et al. 2004).

However, we know from observations of star formation within the Milky Way and in the $z \lesssim 0.2$ population of ultraluminous infrared galaxies (ULIRGs) that star formation can be highly obscured, and thus by determining the star formation history from galaxies selected only at rest-frame UV and optical wavelengths we may be missing star formation which is strongly obscured. The star formation histories derived observationally will be incomplete until obscured star formation is taken into account, and comparison to models of galaxy formation without including obscured star formation may be misleading.

1.2 The Cosmic Far-Infrared Background and Obscured Star Formation at High Redshift

The far-infrared (far-IR) emission from galaxies is dominated by thermal dust emission. Early infrared (IR) observations of nearby star-forming regions in the Milky Way indicated that dusty regions of star formation produce thermal dust emission in addition to starlight, and observations of nearby star-forming galaxies with the *Infrared Astronomical Satellite* (*IRAS*) showed that star-forming regions can be traced through their far-IR emission even if they are invisible at optical wavelengths. In star forming regions, much of the luminosity generated by the stars is from massive, short-lived stars and emitted in the UV and short-

wavelength optical bands; however, dust grains absorb these high-energy photons and re-emit the energy in the IR wavebands, giving rise to the observed far-IR emission. The population of ULIRGs discovered by *IRAS*, which are highly IR-luminous ($L_{\rm IR} \sim 10^{12}\,L_{\odot}$) galaxies at $z < 0.2$ undergoing strong interactions or mergers (see Sanders & Mirabel 1996, and references therein) indicates that enormous amounts of IR luminosity can be generated in such a way by highly obscured starbursts. Yet, it can also be generated by dust obscuring a central, supermassive black hole, in which a hard-UV radiation field from the accretion disk heats the obscuring material, which then re-emits the energy in the IR bands. In cases in which the dust heating is dominated by young, massive stars, the far-IR emission will reflect the star formation rate of the starburst event; thus, the far-IR emission of a galaxy can be used as a tracer of its star formation history.

Franceschini et al. (1991), Blain & Longair (1993a,b), and Pearson & Rowan-Robinson (1996) showed by modeling dust emission from star formation that star formation events at high redshift, aided by strongly negative K-corrections in the far-IR for galaxies with steeply increasing flux, could produce a measurable far-IR/submillimeter background. Blain & Longair (1993b) predicted the spectrum of this submillimeter (submm) background using models in which mergers of dark matter halos at high redshift produce massive, luminous, heavily obscured star formation events, similar to those observed in ULIRGs. With the Cosmic Background Explorer (*COBE*) satellite, Puget et al. (1996) found that indeed, a significant far-IR/submm background above the level of zodiacal emission did exist, with a similar spectrum as that predicted by Blain & Longair (1993b), suggesting that a great deal of obscured star formation did occur at earlier epochs. However, the far-IR background itself does not indicate when or how precisely the star formation took place, especially considering that dust heated by obscured AGN can also significantly contribute to the observed background. It is necessary to resolve the cosmic far-IR/submm background into individual galaxies to determine this information.

The advent of the Submillimeter Common-User Bolometer Array (SCUBA; Holland et al. 1999) instrument on the 15-meter James Clerk Maxwell Submillimeter Telescope (JCMT) and the Max-Planck Millimeter Bolometer Array (MAMBO) (Kreysa et al. 1998) camera on the Institut de Radio Astronomie Millimétrique (IRAM) 30-m telescope opened a new era in the study of obscured star formation at high redshift, being the first submm instruments with sufficient sensitivity and field of view to survey the sky for faint submm sources. The

resolution of the far-IR/submm background through ground-based submm- and millimeter-wave surveys with SCUBA and MAMBO (e.g., Smail, Ivison, & Blain 1997; Hughes et al. 1998; Barger et al. 1998; Eales et al. 1999; Bertoldi et al. 2000) revealed a population of IR-luminous, but optically faint, high-redshift galaxies, whose submillimeter flux densities suggest large bolometric luminosities ($\sim 10^{13}\,L_{\odot}$) mostly emitted in IR wavebands, when SEDs of local ULIRGs were used as templates. High rates of star formation (thousands of solar masses per year) and/or efficient accretion of material onto an AGN are required to produce such luminosities. With a surface density on the sky of $\sim 0.2\,\mathrm{arcmin}^{-2}$ for sources brighter than 4 mJy (Coppin et al. 2006), these galaxies are thought to contribute significantly to the fraction of the luminosity density from high-redshift galaxies (Blain et al. 1999c). Understanding the nature of these luminous submm sources is important for determining the assembly of massive galaxies: if they are powered by star formation, then the huge star formation rates implied by their IR luminosities indicate a higher star formation rate density at high redshift than optically selected galaxies, which is difficult to reconcile with CDM models of galaxy formation (Baugh et al. 2005), and suggest that massive galaxies formed the bulk of their stellar populations very quickly. On the other hand, if much of the luminosity of the submm sources is produced by accretion onto a central, supermassive black hole, then they represent important phases in supermassive black hole formation and the evolution of active galaxies. Even in the case that submm sources are AGN-dominated, they are still likely to be massive galaxies by extrapolating the local relation between the mass of central black holes and the bulge masses of their host galaxies to high redshifts.

1.3 Characterizing Submillimeter-Selected Galaxies

Discerning the nature of submm-selected sources has proved to be difficult, and prior to 2003, only a small percentage of submm sources had measured redshifts. One of the primary problems is the identification of counterparts to the submm sources at other wavelengths. The size of the SCUBA beam at 850 μm is $15''$ with a typical position uncertainty of $3'' - 4''$, much more coarse than typical of deep ground-based optical observations ($\sim 1''$). The faint source density on the sky is much higher at optical and near-IR wavelengths than in the submm, which can result in multiple faint optical sources falling within the

SCUBA error circle. The SCUBA sources in the HDF-N provide an illustrative example of the difficulty in matching submm sources to faint optical counterparts: Borys et al. (2004) point out that they detect 34 submm sources above 3.5σ significance in their SCUBA map of the HDF, while the optical catalog of the HDF from Capak et al. (2004) contains $\sim 49,000$ sources within the 0.2-square degree area. Thus, connecting submm sources with optical counterparts without additional information can be difficult, if not impossible; even with additional information, authors still disagree on the counterparts to submm sources. Another large problem in making follow-up observations of submillimeter sources is that the sources are typically very faint in not only optical-band images, but at near-IR, radio, and X-ray wavelengths as well; thus, significant quantities of observing time are required to detect them.

Substantial progress was made in the study of submm sources when deep ($1\sigma < 10\,\mu$Jy), high-resolution ($\sim 1''$) interferometric maps at 1.4 GHz were used to identify counterparts to the submm sources with higher accuracy. The far-IR–radio correlation observed for local star forming galaxies (see Condon 1992, and references therein), if observed by submm sources, says that the far-IR emission and radio emission arise from the same regions, so a faint radio source within the error circle of the submm source position is likely to be associated with the submm source. The much lower faint source density on the sky at 1.4 GHz compared to that at optical wavebands also facilitates submm source counterpart identification. Ivison et al. (2002) presented the first identifications of a large number of submm sources from radio imaging, but found that approximately 30–40% of the submm sources had no detected radio counterpart, which was subsequently confirmed in later studies (e.g., Chapman et al. 2003a; Wang et al. 2004; Borys et al. 2004). Since most of the population can be detected in the radio, radio source identifications are still important to studies of this class of galaxies, Chapman et al. (e.g., 2003c, 2005) used deep radio images to identify counterparts to submm sources and obtain positions of sufficient accuracy to carry out optical spectroscopy. They then proceeded to obtain redshifts for a representative sample of 73 submm-selected galaxies and verified that the submm sources were indeed typically high-redshift (median $z = 2.2$), very luminous galaxies (median $L_{\rm IR} = 8.5 \times 10^{12}\,L_\odot$).

The precise radio positions and accurate spectroscopic redshifts for a representative sample have permitted extensive follow-up observations of submm-selected galaxies (SMGs).

Observations of CO emission in SMGs provided the first evidence that SMGs were massive and gas rich (Frayer et al. 1998; Greve et al. 2005). Deep X-ray observations from the *Chandra* X-ray Observatory suggest that the bulk of the IR emission is not powered by obscured, Compton-thick AGNs (Alexander et al. 2003, 2005). Thus, high rates of star formation ($\sim 10^3\,M_\odot\,\mathrm{yr}^{-1}$) are likely to be responsible for the majority of the enormous luminosities of SMGs; the analysis of Chapman et al. (2005) of the IR luminosities of SMGs suggests that these galaxies even dominate star formation in the Universe at $z \sim 2-3$. Theses analyses would not have been possible without spectroscopic redshifts, illustrating the importance of obtaining redshifts for a representative sample.

Yet, despite the significant progress in the last 5 years in characterizing SMGs, much is still unknown. For example, we still do not know redshifts nor detailed characteristics for the SMGs lacking radio detections. Nor do we have a good understanding of the far-IR colors and overall IR spectral energy distribution for SMGs both with and without radio detections; thus, it is still not clear if SMGs represent a uniform population. The conditions of the interstellar medium (ISM), which can indicate how the proposed prodigious star formation is occurring, are almost unknown, as are the gas and stellar dynamics of most SMGs. Mass information (stellar, gas, and dynamical) is limited to small subsets of the SMG sample. Perhaps the most important pieces of missing information are the relationship between SMGs and other high-redshift galaxy populations and how SMGs fit into the scenario of hierarchical galaxy formation, since determining masses of SMGs (both stellar and dynamical), their lifetime, and their end state has proved a major challenge. In this work, we will address some of these unknowns for SMGs, focusing on the radio-detected sub-sample of the SMG population with measured spectroscopic redshifts, and attempt to build a more complete picture of the niche in the cosmic mass assembly history which SMGs occupy. We will pay particular attention to fundamental properties of SMGs, including mass, luminosity, and IR spectral energy distribution, using new data from the Green Bank Telescope and the *Spitzer Space Telescope* to place better constraints on these quantities than previously available. We will then use the new constraints on fundamental properties to test some of the frequently-used assumptions in studies of SMGs and compare SMGs to other populations of high-redshift galaxies.

1.4 Plan for Thesis

1.4.1 Cold Gas and Excitation Conditions in SMGs

We begin our study of the fundamental properties of SMGs in Chapter 2, in which we look at molecular gas and excitation in the ISM of several SMGs. CO rotational line emission is used as a tracer of cold molecular hydrogen for the Milky Way, nearby galaxies, and high-redshift sources, since for cold clouds the temperatures are not nearly high enough to excite emission from individual H_2 molecules. The CO surveys of Greve et al. (2005) and Tacconi et al. (2006) have recently greatly expanded our knowledge of the gas and dynamical mass of SMGs. Yet, these studies mostly produced detections of a single CO line in $J \rightarrow J-1$ transitions where $J \geq 3$; information on density, temperature, and excitation in molecular gas requires detections in multiple CO lines. Detection of the CO(1→0) line, in combination with higher-J transitions, allows us to place strong constraints on the average gas density within a galaxy. Also, in cold gas, we expect much of it to have low excitation, so a single high-J transition may not represent all of the cold gas mass present in a galaxy; thus, CO(1→0) emission should be a more representative tracer of the mass of cold gas. In Chapter 2 we present a study of CO(1→0) emission in a small sample of SMGs using the Green Bank Telescope in an attempt to constrain the excitation and cold molecular gas mass in SMGs.

1.4.2 The IR SEDs and Luminosities of SMGs

In Chapters 3 and 4 we move to a new wavelength range, exploring the IR spectral energy distributions (SEDs) and determining total IR luminosities for a large sample of SMGs with spectroscopic redshifts. The IR SEDs and far-IR colors of SMGs have been rather poorly determined, with most objects having only one data point (the 850 μm observation). Estimates of the IR luminosity of SMGs have had to be made without knowing the SEDs of the individual galaxies, and often in the past templates based on local star-forming galaxies or ULIRGs (e.g., Chary & Elbaz 2001; Dale & Helou 2002) were used to estimate luminosity without knowing if the templates represent SMGs at all. Alternatively, the locally-observed far-IR–radio correlation has also been used to estimate SMG luminosities without knowing if SMGs follow the correlation. The lack of knowledge of the range of possible SEDs of SMGs hinders other studies as well, such as determining photometric redshifts from the

submm-radio index, predicting the colors and fluxes of SMGs to help plan observations or identify counterparts, and building galaxy evolution models. Often in such cases, SMGs are assumed to be a uniform population, all having the same SED shape, and the SED of Arp 220, the nearest ULIRG, is used as a template. Furthermore, without SEDs for a large sample of SMGs, it is difficult to estimate the reliability of predictions made assuming a single template SED.

Kovács et al. (2006) and Laurent et al. (2006) significantly improved our knowledge of the SEDs of SMGs by presenting photometry at 350 μm for 20 SMGs; however, even with their data we lack information on the Wien side of the IR SED peak, which can indicate the contribution of warm or hot dust to the total IR luminosity of SMGs and possibly help identify the contribution of obscured AGN. In Chapter 4 we use near, mid, and far-IR data from the *Spitzer Space Telescope*, presented in Chapter 3, in combination with existing submm and radio data to constrain the full IR SED of SMGs. In doing so, we will be able to make new estimates of the total IR luminosity and dust temperature of SMGs, which are constrained at the shorter IR wavelengths and independent of any templates. We will use the new temperatures and luminosities to look at the effects of SED variation in predicting photometric redshifts for SMGs from submm and radio data. We will also examine the far-IR–radio correlation for SMGs using our new IR luminosities, and compare the relation found for high-z galaxies to that for local galaxies.

1.4.3 The Stellar SEDs and Stellar Masses of SMGs

In Chapters 5 and 6, we examine the stellar properties and stellar masses of SMGs. Given the high obscuration of SMGs in observed-frame optical and near-IR images (Smail et al. 2004), constraints on the stellar populations of SMGs have been loose at best, unlike those of optically-selected galaxies. However, in the rest-frame near-IR, which *Spitzer* data samples for $z \sim 2$ galaxies, the effects of dust extinction are much lower, and low-mass and evolved stars dominate the stellar emission. Borys et al. (2005) have estimated stellar masses for SMGs with X-ray detected AGN in the GOODS-N field; the typical stellar mass they obtain for their sample of 13 SMGs, $M_\star = 10^{11.4}\,M_\odot$, is the best estimate so far of the stellar masses of SMGs. Our *Spitzer* data set presented in Chapter 3 greatly expands the sample size of SMGs with rest-frame near-IR measurements, with which we can characterize the rest-frame near-IR properties of SMGs and determine masses. We first examine the fluxes and near-IR

colors of SMGs in Chapter 5, then analyze the rest-frame UV–near-IR SEDs to estimate stellar masses for the SMGs in Chapter 6.

1.4.4 Comparing to High-z Galaxy Populations

As mentioned earlier, the role of SMGs in scenarios of hierarchical galaxy formation and evolution is not yet understood. We also do not understand how the various populations of high-z galaxies selected at other wavelengths are related to SMGs or how collectively the different types of galaxies fit into hierarchical scenarios. There are hints that SMGs are an important population of galaxies to the buildup of stellar mass in the Universe: for example, SMGs have a surface density on the sky a factor of 10 smaller than LBGs (Steidel et al. 2003; Coppin et al. 2006), but are 10 times as luminous, suggesting that they contribute just as much to the buildup of stellar mass as optically-selected galaxies. Also, SMGs seem to be strongly clustered (Blain et al. 2004b), which suggests that they represent the formation epoch of some of the most massive galaxies or trace out unusually active regions. Yet, comparing different high-z populations has proved very difficult, since current submm instrumentation cannot detect less IR-luminous galaxies than SMGs (as optically-selected galaxies are expected to be). However, the *Spitzer* bands present a region of overlap for all of the high-z populations, as a variety of studies (e.g., Reddy et al. 2006b; Papovich et al. 2006; Pope et al. 2006; Daddi et al. 2007) indicate that a large fraction of the different high-z populations are well-detected in the *Spitzer* bands. In Chapters 5 and 6 we will compare the properties we observe for the SMGs to those of some of the high-z galaxy populations described in §1.1 using our rest-frame near and mid-IR observations from *Spitzer*.

Finally, in Chapter 7, we present conclusions from our studies of SMGs and from the results of our comparisons of different high-z galaxy types. We then describe future studies, which can shed more light on the nature of SMGs and the relationships between different high-z galaxy populations.

Throughout this work, we assume a "concordance" cosmology of $\Omega_{\rm M} = 0.3$, $\Omega_\Lambda = 0.7$, and $H_0 = 71$ km s^{-1} Mpc^{-1} (Spergel et al. 2003).

Chapter 2

Cold Molecular Gas and Gas Excitation in Submillimeter-Selected Galaxies

Studies[1] of molecular gas emission provide the crucial mass and dynamical information needed to evaluate the evolution and mass of submillimeter-selected galaxies (SMGs) in the context of hierarchical galaxy formation and evolution scenarios. The total intensity of molecular emission indicates the mass of gas that is available to fuel future star formation, and the brightness temperature ratios from rotational transitions of different quantum number J constrain the temperature and density of the gas, suggesting how the gas is being consumed. Although millimeter-wave CO emission from SMGs is near currently achievable detection limits, a series of interferometric surveys (e.g., Frayer et al. 1998, 1999; Neri et al. 2003; Greve et al. 2005; Tacconi et al. 2006) have successfully detected $J \geq 3$ CO($J \rightarrow J-1$) transitions in SMGs, finding that SMGs are massive (median $M_{dyn} > 7 \times 10^{10}\,M_{\odot}$; Tacconi et al. 2006), gas-rich (median $M(\mathrm{H_2}) = 3.0 \times 10^{10}\,M_{\odot}$; Greve et al. 2005), and compact (median $D < 4\,\mathrm{kpc}$; Tacconi et al. 2006), consistent with the hypotheses that SMGs are high-z counterparts of ULIRGs and progenitors of massive spheroids or ellipticals. All of this information derives from warm molecular gas, but we have limited knowledge of the less excited, cold molecular gas that makes up a substantial fraction by mass of the gas content of present-day galaxies (e.g., the observations of M82 of Weiß, Walter, & Scoville 2005b). With a low threshold for excitation, requiring $n(\mathrm{H_2}) \sim 10^2\,\mathrm{cm^{-3}}$ and $\Delta E/k \sim 5\,\mathrm{K}$, CO(1→0) emission ($\nu_{rest} = 115.271\,\mathrm{GHz}$) is the most representative tracer of the metal-enriched molecular gas mass in galaxies because it is sensitive to the cold, diffuse gas that

[1]This chapter has been published in similar form as Hainline et al. (2006).

may dominate. Papadopoulos & Ivison (2002) and Greve, Ivison, & Papadopoulos (2003) present evidence for large amounts of cold, low-excitation gas at high redshift, as first suggested by Papadopoulos et al. (2001), in the galaxy HR 10. In this submillimeter-bright extremely red object (ERO) that lacks obvious active galactic nucleus (AGN) signatures, at $z_{CO} = 1.439$, the CO(5→4) line luminosity underestimates the cold molecular gas mass by nearly an order of magnitude. Observations of CO($1 \rightarrow 0$) in SMGs are thus complementary to studies of $J \geq 3$ gas and necessary to determine the total mass of molecular gas they contain.

Previous studies of CO(1→0) emission from high-z galaxies have been carried out with the Very Large Array (VLA) (e.g., Papadopoulos et al. 2001; Carilli et al. 2002b; Greve et al. 2003; Greve, Ivison, & Papadopoulos 2004). The Robert C. Byrd Green Bank Telescope (GBT) far exceeds the current capabilities of the VLA in instantaneous spectral bandwidth (800 MHz maximum per spectrometer bank, compared with 50 MHz at the VLA) with a comparable effective collecting area. Since high-z CO lines can be wider than the VLA bandwidth (Greve et al. 2004a), the GBT is better suited to search for and measure accurately the spectral shape of CO emission from SMGs at the expense of limited spatial resolution.

In this chapter, we present the results of a search for CO(1→0) emission from SMGs, undertaken with the GBT and the facility's K-band receiver (18–26 GHz). The tuning range of the GBT's K-band receiver restricts our potential SMG targets to those with redshifts greater than $z \simeq 3.35$, of which there are only four with measured redshifts (Chapman et al. 2005; Ledlow et al. 2002). Of these four SMGs, we chose to target for GBT observations the two that also have previous high-J CO detections [both from CO(4→3) observations at the Institut de Radio Astronomie Millimétrique (IRAM) Plateau de Bure interferometer] so we could compare the line strengths and widths of any detections: SMM J09431+4700 (hereafter SMM 09431) at $z_{CO} = 3.346$ (Neri et al. 2003) and SMM J13120+4242 (hereafter SMM 13120) at $z_{CO} = 3.408$ (Greve et al. 2005).

2.1 Observations

We searched for CO(1→0) emission from SMM 09431 and SMM 13120 with the 18–26 GHz dual-feed, dual-polarization receiver (K-band) at the GBT on UT 2004 December 1. We

used the position-switching "Nod" observing pattern, in which the two feeds alternate between the target position and a blank-sky position $3'$ away in azimuth such that one feed (beam) is always on the target source. A 2-minute integration (scan) was completed before the receiver moved in azimuth to the alternate position; thus, a full Nod sequence, consisting of a pair of scans, lasted 4 minutes. Every 90 minutes, the pointing and focus of the telescope were checked on a nearby bright radio source. Observing conditions were excellent through both night and day, with low atmospheric opacity ($\simeq 0.02$ nepers) and system temperatures in the range 30–50 K. Total on-source integration times were 6.0 hr for SMM 09431 and 6.2 hr for SMM 13120. The size of the main beam at the GBT at 26 GHz is $28''$, so our observations are not spatially resolved. However, since $1''$ corresponds to ~ 7.4 kpc at $z \simeq 3.4$, it is very likely the entire extent of our target galaxies and any companions will be within the main beam (~ 210 kpc at $z \simeq 3.4$), and our observations should be representative of the average cold gas properties over the observed galaxy.

We used the GBT's Autocorrelation Spectrometer (ACS) in three-level sampling mode. For each of the two target sources, we observed an 800 MHz bandpass centered on the frequency at which the CO(1→0) line should fall based on the CO system redshift obtained from the previous CO(4→3) detection. The spectrometer banks were configured in low-resolution mode, providing 2048 channels of width 391 kHz each ($\sim 4.4\,\mathrm{km\,s^{-1}}$ at 26 GHz) for the two circular polarizations of each feed. The noise diode for the K-band receiver was fired every 1.0 s for calibration; we average the data taken with the calibration noise diode on with that taken with the noise diode off to improve our signal-to-noise ratio (S/N). The noise diode temperature (T_{cal}) values for the K-band receiver provided by the observatory were verified using spectral observations of the radio-loud quasars 3C 147 (for SMM 09431) and 3C 295 (for SMM 13120) taken with the same spectrometer setup as the science targets.

2.2 Calibration

In single-dish radio observations, the spectral baseline is the limiting factor in detecting very faint, broad lines like those expected to be produced by CO(1→0) emission from a high-z galaxy. Vanden Bout, Solomon, & Maddalena (2004) discuss the significant baseline curvature seen in wide-bandwidth GBT spectral data obtained over a range of elevations and timescales despite the off-axis feed arm design of the telescope, which was intended to

reduce reflections of signal along the optical path. The spectral baselines at the GBT are caused by a combination of small differences in the telescope system power between on- and off-source scans and reflections between components in the optical system, and cannot be simply modeled with a low-order ($n < 10$) polynomial. Our GBT data are certainly affected by complex baseline shapes, since we average over ~ 6 hr of integration and 60° of elevation. The calibration of our spectral data is thus nontrivial; we must take special care to minimize the systematic errors in our spectra associated with baseline ripples or curvature and strive to not introduce any line-scale structure into our spectrum while attempting to remove the baseline.

vanden Bout et al. (2004) outline a method for calibrating GBT spectral data of faint sources, in which the baseline shape is determined directly from the data and subtracted. They first produce a difference spectrum for both polarizations of each beam for every pair of scans that comprise a full Nod sequence according to the formula

$$T_{diff}(\nu) = \frac{ON - OFF}{OFF}\, T_{sys}, \tag{2.1}$$

where ON and OFF represent an on-source scan and a blank-sky reference scan, respectively, observed with the same receiver feed. The resulting spectra are averaged over time and feed, weighted by $(T_{sys})^{-2}$, to produce a master average science spectrum $T(\nu)$ for each polarization. The template containing the baseline shape of each master spectrum is constructed next by first taking the scans in pairs of Nod sequences (four scans) and subtracting successive ON scans and OFF scans in the following manner:

$$\frac{(ON_a - ON_b)_{\,beam1}}{(ON_b)_{\,beam1}}\, T_{sys,\,b}, \tag{2.2}$$

$$\frac{(OFF_a - OFF_b)_{\,beam1}}{(OFF_b)_{\,beam1}}\, T_{sys,\,b}, \tag{2.3}$$

$$\frac{(ON_a - ON_b)_{\,beam2}}{(ON_b)_{\,beam2}}\, T_{sys,\,b}, \tag{2.4}$$

$$\frac{(OFF_a - OFF_b)_{\,beam2}}{(OFF_b)_{\,beam2}}\, T_{sys,\,b}, \tag{2.5}$$

where ON_a and ON_b are the ON scans from the first and second Nod sequences, respectively, and similarly for OFF_a and OFF_b. Then, the sequence of ON-ON and OFF-OFF spectra is averaged to form the master baseline template $B(\nu)$ for each polarization. vanden Bout et

al. (2004) point out that $B(\nu)$ contains the same baseline structure as the science spectrum $T(\nu)$ (although with higher amplitude due to the longer time delay between differenced quantities), but without signal from the emission line being observed. Hence, to remove the baseline described by the template so that the only spectral shape remaining is due to the observed source, $B(\nu)$ is smoothed and fit to the master science spectrum for each polarization by finding the best-fit coefficients (a, b, c) such that

$$T(\nu) = aB(\nu) + b\,\nu + c. \tag{2.6}$$

The best-fit template is then subtracted from $T(\nu)$. In Figure 2.1(a) we show the final averaged spectrum after applying this method of baseline reconstruction and subtraction to our Feed 1 data on SMM 09431 and averaging the two polarizations of the feed together. The majority of the baseline shape has clearly been removed in Figure 2.1(a), but a slight residual baseline remains. While this residual is less complex than the original baseline shape, its origin is unclear; this causes it to be difficult to fit and subtract, which may interfere with identification of faint lines from the target source.

We preferred not to fit and subtract a baseline template from our final averaged spectrum at all, hoping to avoid the uncertainties associated with the process. As a result, we chose to use a different method of calibration, a variation of the traditional method of single-dish radio spectrum calibration described in Equation 2.1, which we refer to as the $\alpha\mathrm{OFF}_1$ + $\beta\mathrm{OFF}_2$ method. In effect, we use the two OFF scans surrounding each ON scan to construct an improved, interpolated OFF, separately for each polarization in each feed. However, instead of assuming that the preceding and subsequent OFFs contribute equally to the spectral shape of each ON scan, which might be expected if the spectral baseline was purely a linear function of time, we use least-squares fitting to find values α and β for each scan such that

$$\frac{ON - (\alpha\, OFF_1 + \beta\, OFF_2)}{\alpha\, OFF_1 + \beta\, OFF_2} = 0, \tag{2.7}$$

where OFF_1 refers to the scan prior to the ON scan, and OFF_2 refers to the scan following the ON scan (all taken through the same feed). Allowing α and β to vary by scan helps remove systematic shapes caused by sporadic phenomena of varying amplitude; we found such coefficient variation necessary because even though for $\sim$ 70% of scans the (α, β) values were (0.5 ± 0.05,0.5 ± 0.05), it was not unusual (the remaining $\sim$ 30% of scans) for

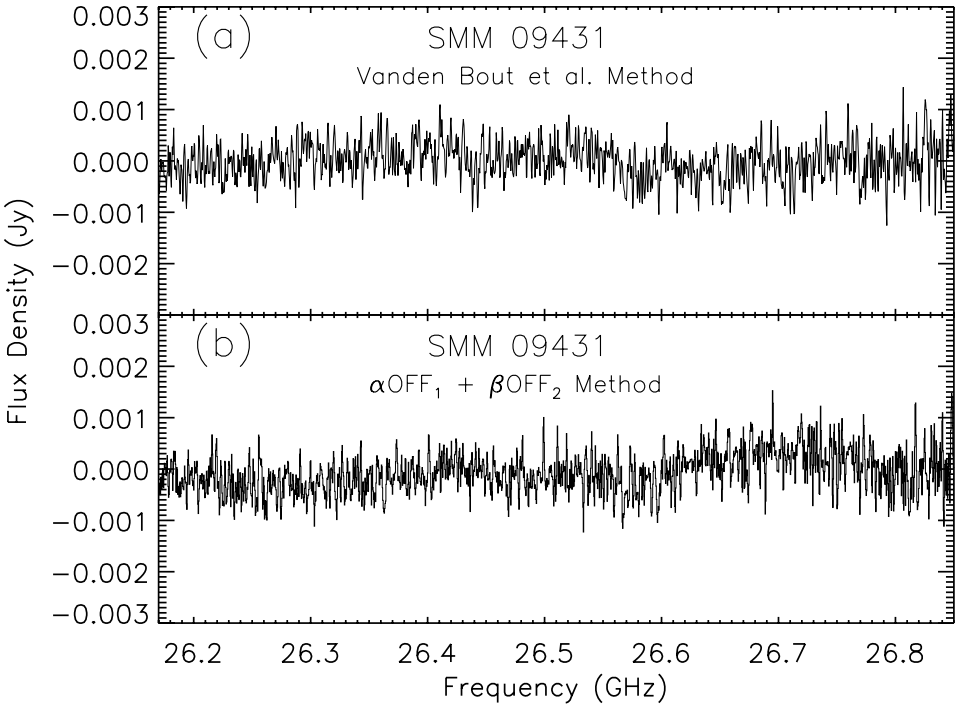

Figure 2.1 (a) Final averaged spectrum of Feed 1 for SMM 09431 data, produced by the GBT spectral calibration method of vanden Bout et al. (2004). The RMS per spectral channel is 0.37 mJy. (b) Final averaged spectrum resulting from the application of the $\alpha\mathrm{OFF}_1 + \beta\mathrm{OFF}_2$ calibration method on the same data. The RMS per spectral channel is 0.41 mJy. Based on the CO(4→3) redshift of $z = 3.346$ from Neri et al. (2003), we expect to see the CO(1→0) line at $\nu_{obs} = 26.523$ GHz.

α and β to lie in the range 0.25–0.45 or 0.55–0.75, where $\beta = 1 - \alpha$. After the spectral fits, we apply the derived values of α and β to obtain the normalized difference spectrum, for each scan, in units of antenna temperature:

$$T_{diff}(\nu) = \frac{ON - (\alpha\, OFF_1 + \beta\, OFF_2)}{\alpha\, OFF_1 + \beta\, OFF_2}(\alpha\, T_{sys1} + \beta\, T_{sys2}), \tag{2.8}$$

where T_{sys1} is the system temperature derived for the first OFF scan, and T_{sys2} is the system temperature derived for the second OFF scan. The difference spectra from all scans are then averaged together, weighted by the root-mean-square (RMS) deviation of each scan. In Figure 2.1(b) we show the result of the $\alpha\mathrm{OFF}_1 + \beta\mathrm{OFF}_2$ method on the same spectral data used in Figure 2.1(a). The final averaged spectrum in Figure 2.1(b) lacks obvious residual ripples on the scale of a galaxy emission line ($\sim 100 - 1000\,\mathrm{km\,s^{-1}}$, or $\sim 9 - 90\,\mathrm{MHz}$ at $\nu_{obs} = 26.5\,\mathrm{GHz}$), although a long- period ($\sim$ few hundred MHz), low-amplitude ripple may be present which is not likely to hinder faint line detection. Note that this reasonably flat spectrum was produced without subtracting a curved or rippled baseline template. In the case of SMM 13120, a clearly linear baseline appeared in the final averaged spectrum produced by this method, which was easily fit and removed. In general, we find that the $\alpha\mathrm{OFF}_1 + \beta\mathrm{OFF}_2$ method produces qualitatively similar results to that used by vanden Bout et al. (2004): sources detected with one calibration method are also detected by the other method, and the resulting spectra have comparable single-channel RMS values (the RMS values of the final average spectra, in the sense vanden Bout et al. method versus $\alpha\mathrm{OFF}_1 + \beta\mathrm{OFF}_2$ method, are 0.37 mJy versus 0.41 mJy for SMM 09431 and 0.44 mJy versus 0.42 mJy for SMM 13120). In addition, neither method can completely remove all baseline shape from our GBT data. Consequently, we cannot say that one method produces better results than the other. Even so, we prefer the $\alpha\mathrm{OFF}_1 + \beta\mathrm{OFF}_2$ method because no curved baseline subtraction is required. However, it is important to note that the method is suitable only for sources with very weak or undetectable continuum emission at $\lambda_{rest} = 2.6\,\mathrm{mm}$. SEDs of SMGs (e.g., Chapman et al. 2005) predict that continuum emission from SMGs at 30 GHz is undetectable in 6 hr of integration time with the GBT.

Before averaging the spectral data from the different polarizations and feeds, we examined the periodograms (Fourier power spectra) of the calibrated spectra from both polarizations and feeds of the individual scans, looking for any peaks that might indicate systematic

spectral features not removed in the calibration process. Such ripples could influence the appearance of the spectrum, and we were especially concerned about any ripples of width similar to the expected width of a CO emission line from a high-z source ($\sim 300\,\mathrm{km\,s^{-1}}$, or $\sim 30\,\mathrm{MHz}$). We found that the right polarization of feed 2 nearly always showed an irregularly changing pattern of power between 0 and $0.03\,\mathrm{MHz^{-1}}$ (periods $\gtrsim 30\,\mathrm{MHz}$). This feature was not found in feed 1 data, and was found in approximately half of the left polarization data from feed 2. Thus, in an effort to ensure that what appears as noise on the scale of an emission line is due to random processes, we have not included any feed 2 data in the averaged calibrated spectra. While this exclusion cuts our effective integration time in half and increases the spectral rms, it helps ensure that the quoted noise is uncorrelated in frequency and increases our confidence in the reality of any possible emission line detection by removing ripples and structure that could obscure the line.

To convert our object spectra to units of Janskys, we corrected for atmospheric attenuation and then applied the parametrization of the GBT gain versus elevation curve found by Condon (2003), re-scaled for K-band by assuming an aperture efficiency at 26 GHz of 0.55 from an interpolation of GBT aperture efficiency measurements at nearby frequencies. We estimate that our flux calibration is accurate to within 15%, due to uncertainties in the temperatures of the calibrator diodes, the GBT gain curve, and the calibration noise diode variations across the observed bandwidth, as well as the opacity estimate.

All of the calibration of our spectral data was accomplished with the new library of routines written by the GBT staff in IDL, GBTIDL.[2]

2.3 Results

2.3.1 SMM 13120

SMM 13120, also known as SSA 13-332, was identified as a source in the Hawaii Deep Field SSA 13, with $S_{850\mu\mathrm{m}} = 6.2\,\mathrm{mJy}$. The galaxy, with an optical redshift of $z = 3.405$, is not known to be lensed, and its optical spectrum reveals active nucleus signatures (C IV, Si IV, and O III; Chapman et al. 2005). Chapman et al. (2005) estimate from the radio-submillimeter SED a bolometric luminosity for SMM 13120 $L_{bol} = 2.02 \times 10^{13}\,L_{\odot}$ and a characteristic dust temperature of $T_d = 47\,\mathrm{K}$, although Kovács et al. (2006) find from their

[2]Information on GBTIDL is available at http://gbtidl.sourceforge.net./.

350μm SHARC-II observations of SMGs from the Chapman et al. (2005) sample that the luminosities presented in Chapman et al. (2005) are typically overestimated by a factor of 2 and that the dust temperatures are overestimated by 13%, which would bring down the values for SMM 13120 to $L_{bol} = 1.01 \times 10^{13}\,L_{\odot}$ and $T_d = 42\,\mathrm{K}$. High-J CO observations have confirmed the redshift and shown SMM 13120 to be very massive in molecular gas. Greve et al. (2005) detect CO(4→3) emission from SMM 13120 with the IRAM Plateau de Bure interferometer at $z = 3.408$, with velocity width $\Delta V_{\mathrm{FWHM}} = 530 \pm 50\,\mathrm{km\,s^{-1}}$ and integrated line flux $S_{CO}\,\Delta V = 1.7 \pm 0.3\,\mathrm{Jy\,km\,s^{-1}}$. Assuming a CO luminosity-to-H_2 conversion factor $\alpha = 0.8\,M_{\odot}\,(\mathrm{K\,km\,s^{-1}\,pc^2})^{-1}$, this yields a molecular gas mass of $M(\mathrm{H_2}) = (4.2 \pm 0.7) \times 10^{10}\,M_{\odot}$. Greve et al. (2005) also estimate a lower limit on the dynamical mass of SMM 13120 of $M_{dyn} \gtrsim 1.2 \times 10^{11}\,M_{\odot}$. SMM 13120 is unresolved in the $6\farcs9 \times 4\farcs8$ beam at IRAM, so no information on the spatial structure of the molecular gas is available.

We detect CO(1→0) emission from SMM 13120 centered at $\nu_{obs} = 26.1481\,\mathrm{GHz}$, with an intensity-weighted line centroid in redshift space of $z = 3.408 \pm 0.004$. This detection represents the first detection of CO(1→0) from a bona fide SMG and the first SMG CO(1→0) detection with spectral information. In Figure 2.2 we show our calibrated and averaged spectrum of SMM 13120, produced by the $\alpha\mathrm{OFF}_1 + \beta\mathrm{OFF}_2$ method described in §2.2. We have subtracted a linear baseline from the spectrum, fit to all the channels away from the line, and smoothed it from its original velocity resolution of $4.47\,\mathrm{km\,s^{-1}}$ and RMS per spectral channel $\sigma = 0.42\,\mathrm{mJy}$ to $94\,\mathrm{km\,s^{-1}}$ and $\sigma = 0.16\,\mathrm{mJy}$. The detected line is still visible if the data from feed 2 are included in the final average spectrum.

The Gaussian fit overplotted in Figure 2.2 shows a wide CO(1→0) line, $\Delta V_{\mathrm{FWHM}} = 1040 \pm 190\,\mathrm{km\,s^{-1}}$. However, the Gaussian fit to the line profile shown in Figure 2.2 appears poor, possibly because of the triple-peaked appearance of the line, although the χ^2-value of the Gaussian fit, $\chi^2 = 0.19$, indicates that we cannot formally conclude whether or not the Gaussian function provides a good description of the line profile. To obtain a less model-dependent estimate of the line width, we compute also the second moment of the emission spectrum, finding $\Delta V = 350\,\mathrm{km\,s^{-1}}$. Integrating over the line, we find $S_{CO}\,\Delta V = 0.42 \pm 0.07\,\mathrm{Jy\,km\,s^{-1}}$, where the error includes the (estimated) 15% uncertainty in our flux calibration.

To calculate the CO luminosity from the integrated flux, we apply the relations for L_{CO}

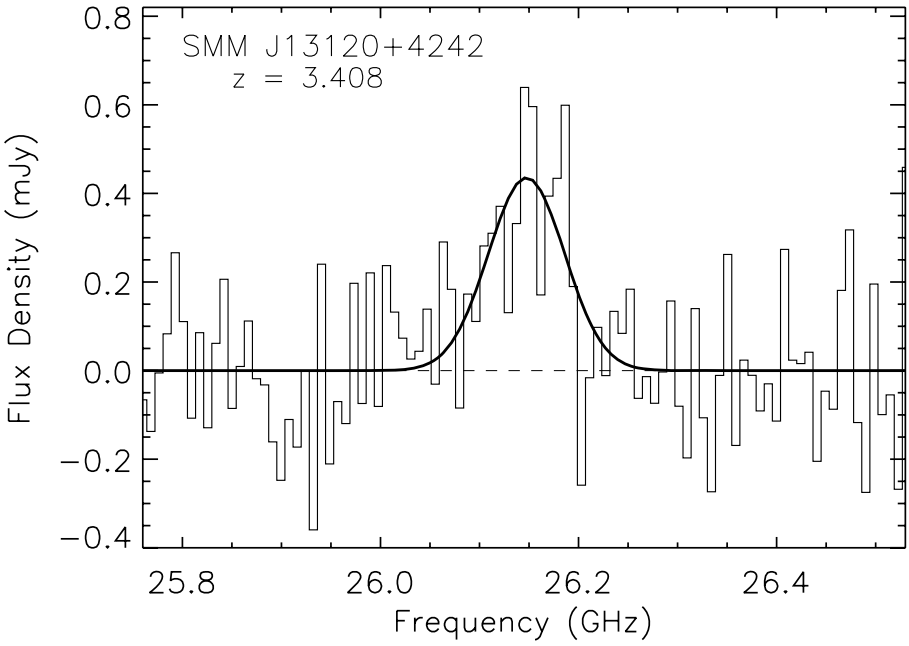

Figure 2.2 CO(1→0) spectrum of SMM 13120, produced by the $\alpha\mathrm{OFF}_1 + \beta\mathrm{OFF}_2$ method. A linear baseline has been subtracted from the spectrum post-calibration. The spectrum has been boxcar-smoothed to a velocity resolution of $94\,\mathrm{km\,s^{-1}}$ and re-binned so that each channel is independent. A Gaussian fit to the line with FWHM $1040\,\mathrm{km\,s^{-1}}$ is overplotted as the thick curve.

and L'_{CO} presented in Solomon, Downes, & Radford (1992):

$$L_{CO}(L_\odot) = 1.04 \times 10^{-3}\, S_{CO}\Delta V\, \nu_{\rm rest}\, (1+z)^{-1}\, D_L^2, \tag{2.9}$$

and

$$L'_{CO}({\rm K\,km\,s^{-1}\,pc^2}) = 3.25 \times 10^7\, S_{CO}\Delta V\, \nu_{\rm obs}^{-2}\, D_L^2\, (1+z)^{-3}, \tag{2.10}$$

where $S_{CO}\Delta V$ is in units of Jy km s^{-1}, $\nu_{\rm rest}$ and $\nu_{\rm obs}$ are the rest frequency and observed frequency of the CO(1→0) line and are in units of GHz, and D_L is the luminosity distance in units of Mpc. In this way, we obtain a CO luminosity of $L_{CO} = (1.0 \pm 0.2) \times 10^7\, L_\odot$ and $L'_{CO} = (2.0 \pm 0.3) \times 10^{11}$ K km s^{-1} pc^2. To calculate the H_2 mass from the CO luminosity, we use the relation

$$M(H_2) = \alpha \times L'_{CO}, \tag{2.11}$$

where α is the CO luminosity-to-H_2 mass conversion factor. We adopt the conversion factor $\alpha = 0.8 M_\odot\, ({\rm K\,km\,s^{-1}\,pc^2})^{-1}$, which is found by Downes & Solomon (1998) to be appropriate for molecular gas exposed to the intense ultraviolet (UV) radiation fields and strong tidal forces present at the centers of nearby ULIRGs, and estimate the total mass of low-excitation H_2 in SMM 13120 to be $M(H_2) = (1.6 \pm 0.3) \times 10^{11}\, M_\odot$. Note that the CO-to-$H_2$ mass conversion factor can vary depending on local gas conditions (e.g., Yao et al. 2003) and is thus highly uncertain for galaxies at high redshift. As a result, our absolute value of the molecular gas mass may have significant systematic error that is difficult to quantify. Should the gas in SMM 13120 be less dense and less excited than that of ULIRGs, the conversion factor for SMM 13120 should be larger, so we are underestimating the molecular gas mass; if the gas is more dense and more excited, the conversion factor may be too high, and we are overestimating the gas mass.

2.3.2 SMM 09431

SMM 09431 was identified by Cowie, Barger, & Kneib (2002) in deep submillimeter maps of the $z = 0.41$ galaxy cluster Abell 851 obtained with the SCUBA instrument on the JCMT. From subsequent 1.4 GHz observations, Ledlow et al. (2002) estimated $T_d = 38$ K and suggested that two individual radio sources, identified as H6 and H7, were associated with the SCUBA source. Optical follow-up observations showed H6 to be a narrow-line

Seyfert 1 galaxy at $z = 3.349$ (Ledlow et al. 2002), while the weaker radio source H7 has a redshift of $z = 3.347$ from O III (Takata et al. 2006). Both Neri et al. (2003) and Tacconi et al. (2006) detect CO(4→3) emission from H7 at $z = 3.3460 \pm 0.0001$ with a line width $\Delta V_{\rm FWHM} = 420 \pm 50\,{\rm km\,s^{-1}}$ and an integrated line flux $S_{CO}\,\Delta V = 1.1 \pm 0.1\,{\rm Jy\,km\,s^{-1}}$. H6 has not been definitively detected in CO. Assuming a CO to H_2 conversion factor $\alpha = 0.8\,M_\odot\ ({\rm K\,km\,s^{-1}\,pc^2})^{-1}$, Neri et al. (2003) infer a molecular gas mass $M({\rm H_2}) = (2.1 \pm 0.2) \times 10^{10}\,M_\odot$. SMM 09431 is lensed by the foreground galaxy cluster by a modest factor of 1.2 (Cowie et al. 2002); this factor has been included in all stated values of mass and luminosity.

We do not detect CO(1→0) emission from SMM 09431, which is apparent in the object's final calibrated spectrum displayed in Figure 2.1. Our observations yield a single-channel RMS of 0.41 mJy, which in turn corresponds to a statistical 3σ upper limit to the integrated flux density at 26.523 GHz of $0.056\,{\rm Jy\,km\,s^{-1}}$, assuming the CO(1→0) line follows the CO(4→3) line FWHM of $420\,{\rm km\,s^{-1}}$ and that the line has a Gaussian profile. However, due to the uncertainties associated with the GBT spectral baselines and the flux calibration, we feel that the value of the error in the integrated flux, $\sigma_{S\,\Delta V}$, found for SMM 09431 through application of the statistical error formula is probably an underestimate and thus will result in unrealistically low upper limits on the CO line luminosity and molecular gas mass. Consequently, we estimate an alternate value of $\sigma_{S\,\Delta V}$ for SMM 09431 from the error in the integrated flux of SMM 13120, noting that the single-channel RMS values of our final spectra of both objects are nearly identical (0.41 mJy for SMM 09431, 0.42 mJy for SMM 13120) and that the objects were observed in similar conditions on the same day at nearly the same sky frequency. We scale the error in $S_{CO}\,\Delta V$ of SMM 13120 ($\sigma_{S\,\Delta V} = 0.07\,{\rm Jy\,km\,s^{-1}}$, see §2.3.1) by $[\Delta V_{\rm FWHM}({\rm SMM\,09431})/\Delta V_{\rm FWHM}({\rm SMM\,13120})]^{1/2}$ to account for the difference in CO line width between the two objects, and thus obtain the more conservative 3σ upper limit of $S_{CO}\,\Delta V < 0.13\,{\rm Jy\,km\,s^{-1}}$ for SMM 09431. For the sake of completeness, we provide the 3σ upper limits of CO line luminosity and $M({\rm H_2})$ that result from both the statistical upper limit on the integrated line flux and our alternative upper limit. From $S_{CO}\,\Delta V < 0.056\,{\rm Jy\,km\,s^{-1}}$, we obtain the upper limits to the CO luminosity of SMM 09431 of $L_{CO} < 1.1 \times 10^6\,L_\odot$, or $L'_{CO} < 2.2 \times 10^{10}\,{\rm K\,km\,s^{-1}\,pc^2}$. Assuming the CO-to-$H_2$ conversion factor $\alpha = 0.8\,M_\odot\,({\rm K\,km\,s^{-1}\,pc^2})^{-1}$, the 3σ upper limit on $M({\rm H_2})$ for SMM 09431 is then $M({\rm H_2}) < 1.8 \times 10^{10}\,M_\odot$. For the conservative estimate $S_{CO}\,\Delta V < 0.13\,{\rm Jy\,km\,s^{-1}}$, the

corresponding upper limits are $L_{CO} < 2.5 \times 10^6\,L_\odot$, $L'_{CO} < 5.1 \times 10^{10}\,\mathrm{K\,km\,s^{-1}\,pc^2}$, and $M(\mathrm{H_2}) < 4.1 \times 10^{10}\,M_\odot$, which we believe to be more reasonable than the statistical upper limits. If we were to assume a broader CO(1→0) line, the upper limit will be still larger and therefore less restrictive.

2.4 Analysis & Discussion

2.4.1 CO Line Ratios and Gas Excitation

With detections in multiple CO lines for SMM 13120, one of which is from CO(1→0), we can use the ratio of the brightness temperatures of the different transitions to extract some clues about the globally-averaged conditions of its molecular gas. The task is made easier because SMM 13120 is not known to be strongly gravitationally lensed, so the effects of differential lensing on the line fluxes are not likely to complicate our interpretation. Defining r_{43} as the ratio of the area/velocity averaged brightness temperature of the CO(4→3) and CO(1→0) lines, and assuming all of the CO emission is from a single object, we find $r_{43} = 0.26 \pm 0.06$ for SMM 13120. This value of r_{43} is notably lower than the ratio that is expected from a thermalized (i.e., relative level populations described by principles of local thermodynamic equilibrium), optically thick source, $r_{43,LTE} = 1.0$, implying that the $J = 4$ level of CO is not thermalized in SMM 13120. As a consequence, $M(\mathrm{H_2})$ estimates for SMM 13120 calculated from $J_{upper} \geq 4$ CO lines, assuming the lines are fully thermalized and optically thick, will underestimate the mass of low-excitation gas in the galaxy. This is exactly what we find from our CO(1→0) detection of SMM 13120: our estimate of the molecular gas mass in §2.3.1, $M(\mathrm{H_2}) = 1.6 \times 10^{11}\,M_\odot$, is a factor of ~ 4 greater than the mass implied by the CO(4→3) observations if constant brightness temperature is assumed, $M(\mathrm{H_2}) = 4.2 \times 10^{10}\,M_\odot$. Moreover, the lack of a dominant population of thermalized high-excitation gas in SMM 13120 suggests that the CO luminosity-to-$\mathrm{H_2}$ mass conversion factor we use in §2.3.1 may be incorrect for this galaxy. Downes & Solomon (1998) derive that conversion factor for the central starbursts in ULIRGs, and from observations of the central IR-luminous starburst region of M82 (e.g., Weiß et al. 2005b) we expect the CO excitation in a starburst region to be thermalized at least to the CO $J = 4$ level. Since the $J = 4$ level is observed to not be thermalized when averaging over SMM 13120, the CO-to-$\mathrm{H_2}$ conversion factor of Downes & Solomon (1998) is likely too low for SMM 13120, and the total molecular gas

mass is likely to be even larger than the $1.6 \times 10^{11}\,M_{\odot}$ we calculate in §2.3.1.

Such low values of r_{43} as we find in SMM 13120 are not unknown: in the Milky Way, r_{43} ranges with position between ~ 0.1 and 0.2 (Fixsen, Bennett, & Mather 1999). The line ratio r_{43} we find for SMM 13120 is also reminiscent of the CO(5→4)/CO(1→0) ratio of 0.1 found in the ERO/SMG HR 10 by Greve et al. (2003), another high-z object in which the high-J CO emission does not trace the low-excitation gas. That SMM 13120 and HR 10 are similar is somewhat surprising, however, because HR 10 is not known to harbor an active nucleus, while SMM 13120 clearly does. On the other hand, the ratio r_{43} in SMM 13120 is significantly smaller in comparison to those of the other high-z active galaxies with CO(1→0) detections. PSS 2322+1944, APM 08279+5255, and 4C 60.07 are two QSOs and a radio galaxy, respectively, and have values of r_{43} of 1.4, 1.5, and 0.7, indicating that the molecular gas they contain is nearly thermalized and that molecular gas masses derived from CO(4→3) and CO(1→0) emission will be roughly similar, which is found to be true (Carilli et al. 2002b; Papadopoulos et al. 2001; Greve et al. 2004a). Since SMM 13120 hosts an AGN, we might expect its gas conditions to be more like those of the high-z active galaxies than galaxies lacking active nuclei; however, note that the active nucleus in SMM 13120 is probably significantly less luminous than those found in PSS 2322+1944 and APM 08279+5255 because, in its rest-frame UV spectrum, the AGN lines are weak and interstellar absorption features indicative of a starburst are also clearly visible (Chapman et al. 2005). It is possible that the less-powerful active nucleus in SMM 13120 could influence the gas properties of the host galaxy in a different way than would a high-luminosity AGN, causing the global CO line ratios to differ between the SMG and the QSOs. It may thus be inappropriate to use the mere presence of an AGN as a factor in predicting global CO line ratios.

From our measurement of r_{43} in SMM 13120 we can obtain quantitative constraints on the average kinetic temperature and density of the molecular gas in this system. To this end, we assume the CO(1→0) and (4→3) emission result from a single gas phase and use a large velocity gradient (LVG) model (based on Richardson et al. 1985) to fit the observed line ratio. Data from only two CO lines generally do not provide enough information to place strong constraints on the excitation; however, since one of the lines is from the 1→0 transition, we can place strong lower limits on the column and number density of CO, and by extension, on the density of H_2. A standard LVG code, assuming a typical Galactic

value for the [CO/H_2] abundance $X_{CO} = 10^{-4}$, velocity gradient $dV/dr = 1\,\mathrm{km\,s^{-1}\,pc^{-1}}$, and $T_{CMB} = (2.73\,\mathrm{K})(1+z)$, finds a best-fit density for SMM 13120 of $n(\mathrm{H_2}) > 300$ cm^{-3} for a range of gas kinetic temperatures $T_k = 42 - 54\,\mathrm{K}$. This solution is robust, such that the model finds no candidate solutions at other densities. However, in kinematically violent regions with intense UV radiation fields, such as we expect to find in ULIRGs and SMGs, the [CO/H_2] abundance is likely to be lower, so we also calculate the kinetic temperature and density limits for $X_{CO} = 10^{-5}$ to cover a range of possible values. Leaving the assumed values of dV/dr and T_{CMB} unchanged, we obtain a slightly higher limit on the molecular gas density of $n(\mathrm{H_2}) > 10^3$ cm^{-3} for a somewhat lower gas temperature range of $T_k = 34 - 46\,\mathrm{K}$. Both of these sets of temperature and density limits point to low-density gas in SMM 13120, although we would guess that the solution for $X_{CO} = 10^{-5}$ is closer to reality. Also, both of the model fits result in kinetic temperatures that are in good agreement with the dust temperature of SMM 13120 found by Chapman et al. (2005), corrected by a factor of 13% as suggested by Kovács et al. (2006): that is, $T_d = 42\,\mathrm{K}$. $T_k \simeq T_d$ would be expected for an interstellar medium in which the gas and dust are well mixed and thermally coupled. Encouraged by these similar values, we adopt a fixed value of $T_k = T_d = 42\,\mathrm{K}$, leave $X_{CO}/(dv/dr)$ free to vary, and once more use the LVG model to calculate the density of the molecular gas in SMM 13120, obtaining $n(\mathrm{H_2}) > 10^3$ cm^{-3} and $X_{CO}/(dv/dr) = 10^{-5}\,(\mathrm{km\,s^{-1}\,pc^{-1}})^{-1}$, consistent with the results of the previous fits. Therefore, the general constraints we can place on the globally-averaged gas properties of SMM 13120 are $n(\mathrm{H_2}) > (3-10) \times 10^2\,\mathrm{cm^{-3}}$ and $T_k = 34 - 54\,\mathrm{K}$, for a realistic range of $X_{CO}/(dv/dr) = 10^{-5} - 10^{-4}\,(\mathrm{km\,s^{-1}\,pc^{-1}})^{-1}$. The mean gas density is thus likely to be relatively low in this system. In addition, it is interesting to note that, if we assume that the galaxy is a uniform-density sphere, our density limits imply a small upper limit to the radius of SMM 13120 in the range 0.9–1.4 kpc, which is consistent with the median upper limit on SMG source size that Tacconi et al. (2006) derive from their high-resolution images of high-J CO emission from eight SMGs.

The diffuse, warm, and low excitation gas we find in SMM 13120 has been observed in local ULIRGs (Solomon et al. 1997) and at high redshift in HR 10 (Greve et al. 2003). In contrast, previous CO(1→0) detections of other $z > 3$ active galaxies have implied lower limits on the cold gas density nearly an order of magnitude larger. PSS 2322+1944, APM 08279+5255, and 4C 60.07 have cold gas densities derived from r_{43} and LVG models

in the range $n(\mathrm{H_2}) > 10^3 - 10^4$ cm^{-3} (Carilli et al. 2002b; Papadopoulos et al. 2001; Greve et al. 2004a).

For SMM 09431, we can use our 3σ upper limit calculations to place only a lower limit on r_{43}. We find $r_{43} > 1.2$ for $S_{CO}\,\Delta V < 0.056\,\mathrm{Jy\,km\,s^{-1}}$, or $r_{43} > 0.53$ for $S_{CO}\,\Delta V < 0.13\,\mathrm{Jy\,km\,s^{-1}}$. Both limits on r_{43} suggest SMM 09431 has higher excitation, on average, than SMM 13120, although whether SMM 09431 is more similar to the high-z QSOs and radio galaxy with CO(1→0) detections than SMM 13120 is unclear.

To examine the excitation of SMM 13120 and SMM 09431 in another way, we plot in Figure 2.3 the integrated line luminosities for different CO lines (hereafter referred to as the CO ladder), normalized to CO(1→0), for SMM 13120 and SMM 09431, as well as those of the other similarly-luminous high-z galaxies with CO(1→0) detections. For SMM 09431, we use our conservative 3σ upper limit of $S_{CO}\,\Delta V < 0.13\,\mathrm{Jy\,km\,s^{-1}}$ in Figure 2.3. In addition, we include the CO data of Weiß et al. (2005a) for SMM J16359+6612 at $z_{CO} = 2.517$: this galaxy lacks CO(1→0) data and is an order of magnitude less luminous than the other high-z sources, but it has the most complete CO ladder of any SMG and thus provides an interesting comparison. In place of a CO(1→0) detection for this galaxy we use the CO(1→0) flux implied by the LVG fit from Weiß et al. (2005a). Also for comparison purposes, we include in Figure 2.3 less IR luminous (by 2-3 orders of magnitude) local galaxies commonly used as templates representative of quiescent galaxies (the Milky Way) and starbursts (the center of M82). Assuming that all the CO emission comes from a single object, the CO ladder of SMM 13120 appears to rise much more slowly with increasing J than the ladders of the other high-z active galaxies, SMM 16359+6612, and M82's central region. The shallow rise of the CO ladder of SMM 13120 more closely resembles the CO ladders of the Milky Way and HR 10, and suggests excitation conditions in SMM 13120 somewhat between those of the inner ($2\overset{\circ}{.}5 < |l| < 32\overset{\circ}{.}5$) and the outer ($|l| > 32\overset{\circ}{.}5$) disk of the Milky Way. The shape of the CO ladder of the Milky Way (slow rise and turnover at lower J than the other sources) is caused by significant sub-thermal excitation, which is any molecular excitation process not governed by the principles of local thermodynamic equilibrium that causes the excitation temperature derived by comparing the population of different energy levels to be lower than the kinetic temperature of the emitting gas. While we cannot yet say that the CO ladder of SMM 13120 turns over in a similar way as the Milky Way, the slow rise and low values of r_{43} suggest that sub-thermal excitation is important

in both SMM 13120 and HR 10. The existence of sub-thermal excitation in these objects would imply that observations of high-J emission lines can provide only a lower limit to the molecular gas mass.

Our findings for SMM 13120, along with the results of Greve et al. (2003) for HR 10, highlight the need for observations of low-J CO emission to measure the entire molecular gas reservoir in high-z galaxies. Although it is true for some high-z galaxies that $J \geq 3$ CO lines can trace low-excitation gas molecules as well as the highly excited gas, such a conclusion seems not to apply to SMM 13120 and HR 10. In addition, some dispersion clearly exists in the gas properties of galaxies hosting active nuclei at high redshift, since SMM 13120 has both at least a weak AGN and a significant quantity of molecular gas not apparent in observations of high-J CO transitions.

2.4.2 Star Formation Timescales and Efficiency

One of the important issues to address in understanding the role of SMGs in the large-scale picture of galaxy formation and evolution is the duration of star formation. We can use our new estimate of the total molecular gas mass in SMM 13120 from CO(1→0) to calculate the length of time the major star formation epoch will last from its respective SFR, assuming the SFR is constant. We define this characteristic star formation timescale as

$$t_{\rm SF} = M({\rm H_2})/{\rm SFR}. \tag{2.12}$$

We calculate the SFR from the far-IR luminosity $L_{\rm FIR}$ using Equation 4 of Omont et al. (2001),

$${\rm SFR} = \delta_{MF}(L_{\rm FIR}/10^{10}\,L_{\odot})\,M_{\odot}\,{\rm yr}^{-1}, \tag{2.13}$$

where δ_{MF} is a function of the stellar initial mass function (IMF). We use as $L_{\rm FIR}$ the value of L_{bol} found by Chapman et al. (2005) for SMM 13120, multiplied by the correction factor of 0.5 implied by the results of Kovács et al. (2006), and assume a Salpeter IMF to obtain $\delta_{MF} = 0.8$. The resulting SFR and $t_{\rm SF}$ we obtain, and the $L_{\rm FIR}$ used in the calculation of the quantites, are listed in Table 1. Assuming that all the far-IR emission is a result of star formation, we thus obtain a short characteristic star formation timescale $t_{\rm SF} \sim 200\,{\rm Myr}$, consistent with the brief burst needed to form the old spheroids and elliptical galaxies

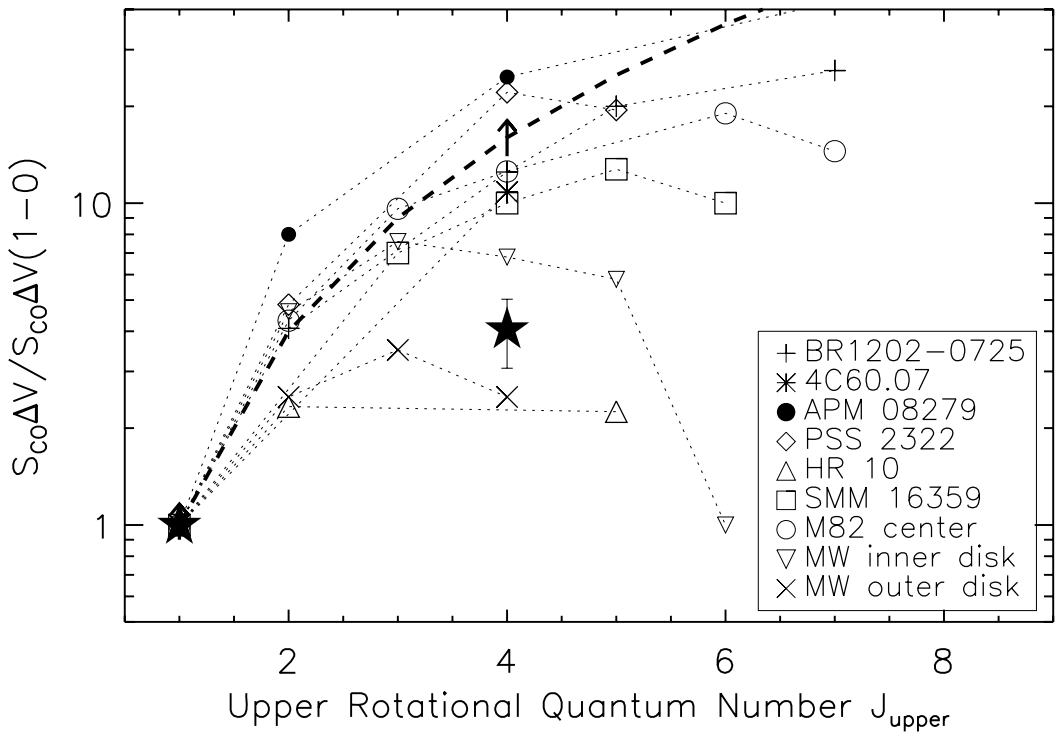

Figure 2.3 CO line ladder for high-z galaxies and local templates, normalized to the integrated CO(1→0) flux. The data points for SMM 13120 and SMM 09431 are the filled stars and the upward arrows, respectively. The thick dashed line represents the effect of constant brightness temperature on the CO line ratios. The CO transition data sources for BR 1202-0725 are Omont et al. (1996) and Carilli et al. (2002a); for 4C 60.07 Greve et al. (2004a) and Papadopoulos et al. (2000); for APM 08279+5255 Downes et al. (1999) and Papadopoulos et al. (2001); for PSS 2322+1944 Carilli et al. (2002b) and Cox et al. (2002); for HR 10 Andreani et al. (2000) and Greve et al. (2003); for SMM 16359+6612 Weiß et al. (2005a) and Kneib et al. (2005); for M82 Mao et al. (2000) and Weiß et al. (2005b); and for the Milky Way Fixsen et al. (1999).

we observe at $z \sim 0$, and in agreement with the duration of SMG star formation bursts estimated by Smail et al. (2004) from modeling the rest-frame optical broad-band colors of SMGs (100-200 Myr). Even though the value of $t_{\rm SF}$ we find for SMM 13120 is short, it is significantly longer than the star formation timescale calculated from the mass implied by the galaxy's CO(4→3) emission and the assumption of a constant brightness temperature, which is only 50 Myr. The CO(1→0) emission clearly indicates that there is more cold gas available in SMM 13120 to fuel star formation than is suggested by observations of CO(4→3) and the assumption of $r_{43} = 1$.

The continuum-to-line ratio $L_{\rm FIR}/L'_{CO}$ provides another means of investigating the evolutionary progression of SMM 13120, because it is commonly used to estimate the efficiency with which molecular gas is converted to stars, independent of the assumed value of the CO-to-H_2 conversion factor. For SMM 13120, we calculate $L_{\rm FIR}/L'_{CO}$ using again the value of L_{bol} from Chapman et al. (2005), corrected as suggested by Kovács et al. (2006), for $L_{\rm FIR}$, and we assume that all of the CO(1→0) emission comes from a single object. If we assume that all the far-IR emission is a consequence of star formation, we obtain an upper limit to the $L_{\rm FIR}/L'_{CO}$ ratio of $\sim 51\,L_\odot\,({\rm K\,km\,s^{-1}\,pc^2})^{-1}$, significantly less than the value ($\sim 190\,L_\odot\,({\rm K\,km\,s^{-1}\,pc^2})^{-1}$) obtained with the $J = 4 \rightarrow 3$ line.

In Table 2.1 we also list limits on $t_{\rm SF}$ and $L_{\rm FIR}/L'_{CO}$ for SMM 09431. We use the value of $L_{\rm FIR}$ from Neri et al. (2003) with our CO(1→0) upper limits to estimate the continuum-to-line ratio, finding $t_{\rm SF} < 15$ Myr and $L_{\rm FIR}/L'_{CO} > 680\,L_\odot\,({\rm K\,km\,s^{-1}\,pc^2})^{-1}$ for the statistical upper limit $S_{CO}\,\Delta V < 0.056\,{\rm Jy\,km\,s^{-1}}$, and $t_{\rm SF} < 34$ Myr and $L_{\rm FIR}/L'_{CO} > 290\,L_\odot\,({\rm K\,km\,s^{-1}\,pc^2})^{-1}$ for the more conservative limit $S_{CO}\,\Delta V < 0.13\,{\rm Jy\,km\,s^{-1}}$. The values found from our conservative limit are consistent with the results from CO(4→3).

Local LIRGs and ULIRGs are known to trace a scaling relation between L'_{CO} and $L_{\rm FIR}$, in which galaxies with higher IR luminosities have higher CO luminosities (e.g., Young et al. 1986). Yao et al. (2003) find a median value of $L_{\rm FIR}/L'_{CO}$ for LIRGs of $50 \pm 30\,L_\odot\,({\rm K\,km\,s^{-1}\,pc^2})^{-1}$, while Solomon et al. (1997) obtain a median value for ULIRGs of $160 \pm 130\,L_\odot\,({\rm K\,km\,s^{-1}\,pc^2})^{-1}$. The high-redshift QSOs and radio galaxies with CO(1→0) detections have continuum-to-line ratios $L_{\rm FIR}/L'_{CO} \sim 200 - 300\,L_\odot\,({\rm K\,km\,s^{-1}\,pc^2})^{-1}$ from both the CO(1→0) and CO(4→3) lines, which is larger than that of SMM 13120, but comparable to SMM 09431. However, in HR 10, $L_{\rm FIR}/L'_{CO} = 130\,L_\odot\,({\rm K\,km\,s^{-1}\,pc^2})^{-1}$ from CO(1→0), nearly an order of magnitude smaller than the continuum-to-line ratio calcu-

Table 2.1. Physical Parameters of Observed SMGs

Source	z_{CO}	μ_L[a]	$L_{\rm FIR}$ ($10^{13}\,L_\odot$)	SFR[b] ($M_\odot\,{\rm yr}^{-1}$)	r_{43}	CO Trans	$M({\rm H_2})$ ($10^{10}\,M_\odot$)	$t_{\rm SF}$[c] (Myr)	$L_{\rm FIR}/L'_{CO}$ ($L_\odot\,({\rm K\,km\,s^{-1}\,pc^2})^{-1}$)	Reference
SMM 13120	3.408	1.0	1.0	810	0.26 ± 0.06	1→0	16 ± 3	200	51	(1),(2),(3)
						4→3	4.2 ± 0.7	50	190	
SMM 09431[d]	3.346	1.2	1.5	1200	> 0.53	1→0	< 4.1	< 34	> 290	(1),(4)
						4→3	2.1 ± 0.2	18	560	

[a]Gravitational lensing magnification factor applied to $L_{\rm FIR}$ and L'_{CO}, and thus included in all quantities calculated from those luminosities.

[b]Derived from $L_{\rm FIR}$ according to Equation 2.13 in the text.

[c]Calculated using Equation 2.12 in the text.

[d]"Conservative" CO(1→0) limits from §2.3.2 used in all calculations.

References. — (1) Greve et al. 2005; (2) Chapman et al. 2005; (3) Kovács et al. 2006; (4) Neri et al. 2003

lated from its CO(5→4) line. Thus, the continuum-to-line ratio $L_{\rm FIR}/L'_{CO}$ in SMM 13120 resembles local star-forming galaxies and HR 10, suggesting similar star formation efficiencies among them, whereas SMM 09431 appears more like the other high-z systems observed in CO(1→0).

It thus seems that the physical conditions in the interstellar medium of SMM 13120, while similar to another SMG (HR 10), are different than the high-z QSOs, 4C 60.07, and SMM 09431. Several possibilities could explain the different conditions. It is possible that the QSOs and 4C 60.07 truly have higher star formation efficiencies than HR 10 and SMM 13120. Also, the optically- or radio-luminous high-z galaxies and SMM 09431 could have more significant contributions to $L_{\rm FIR}$ from dust heated by their active nuclei, causing an overestimation of the star formation efficiency when calculated from the continuum-to-line ratio. However, it should be considered that the $L_{\rm FIR}$–L'_{CO} relation appears to be non-linear at high values of $L_{\rm FIR}$. Gao & Solomon (2004a,b) suggest that, for this reason, the ratio $L_{\rm FIR}/L'_{CO}$ is not a good indicator of the efficiency of star formation in the most far-IR-bright galaxies such as high-z QSOs and SMGs. They argue that HCN emission is a better tracer of the dense gas associated with star formation and IR emission than CO due to its higher critical density for excitation ($\sim 10^5\,{\rm cm}^{-3}$), and since they find $L_{\rm FIR}$ and $L'_{\rm HCN}$ are linearly correlated over 3 orders of magnitude in $L_{\rm FIR}$, they suggest that the ratio $L_{\rm FIR}/L'_{\rm HCN}$ may be a better indicator of star formation efficiency than $L_{\rm FIR}/L'_{CO}$. In this light, it may be more appropriate to use $L_{\rm FIR}/L'_{\rm HCN}$ ratios or even $L_{\rm FIR}/L'_{CO}$ ratios derived from $J \geq 3$ CO transitions, which trace higher-density gas than CO(1→0), to compare the star formation efficiencies of the similarly luminous PSS 2322+1944, APM 08279+5255, and 4C 60.07 to SMM 13120 and HR 10.

2.4.3 A Merger in SMM 13120?

In §2.3.1, we found the velocity width of the Gaussian fit to the CO(1→0) line profile of SMM 13120 to be $\Delta V_{\rm FWHM} = 1040 \pm 190\,{\rm km\,s^{-1}}$, which deviates significantly from the FWHM fitted to the CO(4→3) line by Greve et al. (2005), $530 \pm 50\,{\rm km\,s^{-1}}$. Such a discrepancy is not typically expected; in general, we expect that the line profiles of CO transitions of different J will be of similar widths, from observations of nearby galaxies (e.g., Yao et al. 2003). However, as mentioned in §2.3.1, our data are not of sufficient quality to be certain that a Gaussian profile is an appropriate model for the line shape, so it may be

misleading to compare the Gaussian FWHM velocity widths. To determine the reality of the factor of ~ 2 difference in velocity width from the fits, we instead directly compare the CO(1→0) spectrum of SMM 13120 with the CO(4→3) spectrum from Greve et al. (2005) in Figure 2.4, where the amplitude of the 1→0 spectrum has been multiplied by a factor of 5 in both panels for ease of comparison. In panel (a), we compare the spectra smoothed to the same velocity resolution shown in Greve et al. (2005), $58\,\mathrm{km\,s^{-1}}$, and it is apparent that the low S/N ratio of both spectra preclude detailed comparison. Thus, in panel (b), we further smooth and re-bin the line profiles of both CO transitions to $170\,\mathrm{km\,s^{-1}}$ and find that the CO(4→3) line is nearly as wide as the CO(1→0) line, which suggests that the CO(4→3) line FWHM measurement may have been underestimated in Greve et al. (2005). However, in panel (b) of Figure 2.4, we observe that the CO(1→0) line extends to a lower velocity region of the spectrum than the CO(4→3) line, suggesting that there exists blueshifted (relative to the central system redshift) molecular gas in SMM 13120, which is less excited than the molecular gas at more positive velocity offsets.

Possible explanations of this excitation variation with velocity arise from both of the dynamical scenarios discussed by Tacconi et al. (2006) to explain the double-peaked CO line profiles they observe from other SMGs: a rotating disk and a merger of several galaxy components. If SMM 13120 were a single rotating disk, the blueward extension of the CO(1→0) line profile could indicate a physically distinct region of cold gas within the disk not symmetrically distributed about the more highly excited region represented by the CO(4→3) emission, such as a single giant molecular cloud complex. On the other hand, in a rotating disk the rotation curve should flatten away from the center of the galaxy. In such a case, when the CO line profiles are observed averaged over the entire galaxy, the width of the CO(1→0) profile would not increase over the CO(4→3) profile even if the lower excitation gas comes from an extended region as compared with the location of the CO(4→3) emission. Alternatively, if SMM 13120 is an interaction or a merger of several subcomponents separated by several hundred $\mathrm{km\,s^{-1}}$ in velocity space, the CO(1→0) line profile could be different from the CO(4→3) profile if the merging components possess different excitation conditions.

Continuum observations of SMM 13120 at different wavelengths seem to support a scenario involving an interaction or merger of galaxy components. In Figure 2.5 we show previously unpublished optical, near-infrared, and radio continuum images of SMM 13120,

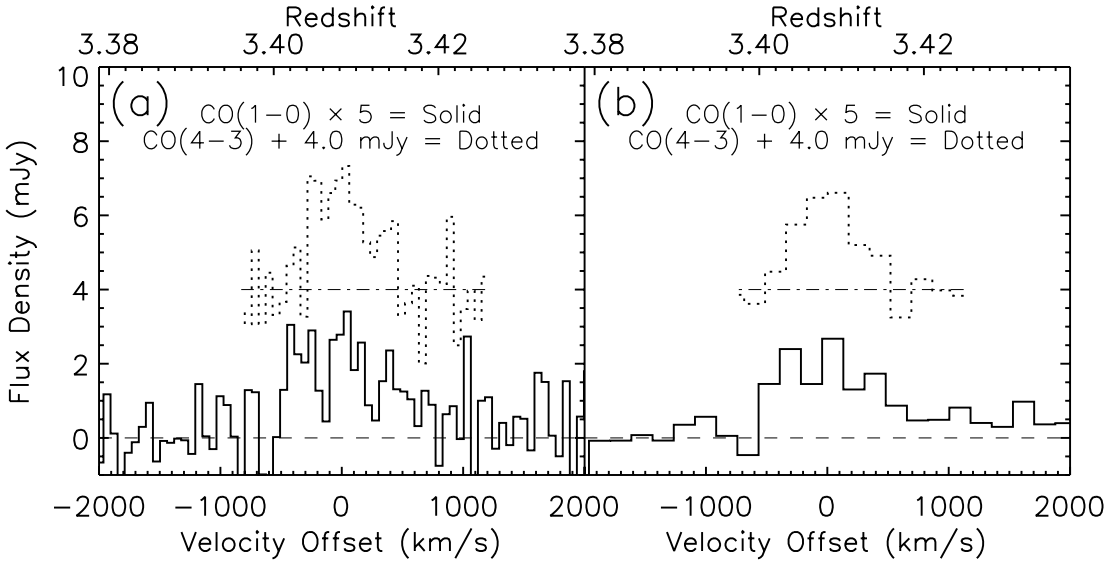

Figure 2.4 Comparison of CO(1→0) (solid line) and CO(4→3) spectra (dotted line). The CO(4→3) spectrum has been provided by T. Greve. For clarity, the amplitude of the CO(1→0) spectrum has been multiplied by a factor of 5, and the CO(4→3) spectrum has been offset from zero by 4 mJy. The spectra are smoothed to a common velocity resolution of 58 km s^{-1} in panel (a) and 170 km s^{-1} in panel (b).

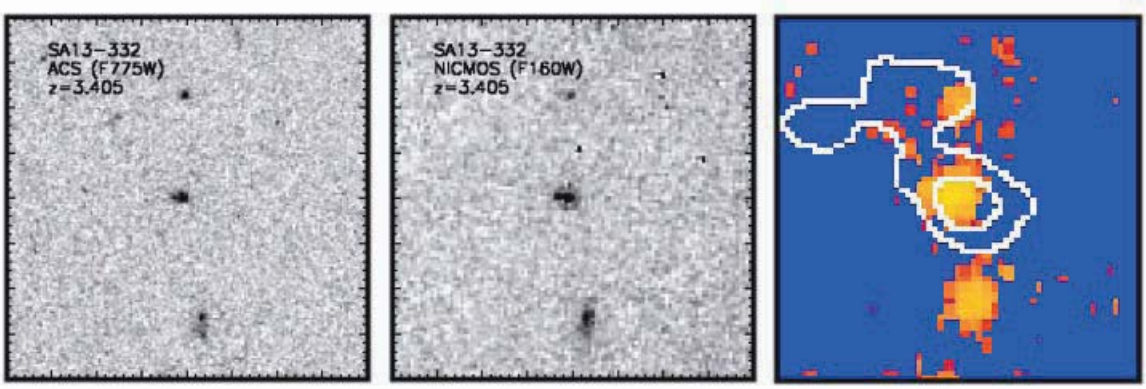

Figure 2.5 $8'' \times 8''$ images centered on the radio position of SMM 13120 ($\alpha_{J2000} = 13^h12^m01\overset{s}{.}172$, $\delta_{J2000} = 42^d42^m08\overset{''}{.}39$). *Left Panel*: $8'' \times 8''$ HST-ACS F775W-band (i') image (Borys et al. 2006, in preparation). *Center Panel*: HST-NICMOS F160W-band image (Borys et al. 2006, in preparation). *Right Panel*: VLA 1.4 GHz contours plotted over a Subaru-SUPRIMECam R-band image (Fomalont et al. 2006, private communication). The VLA data were obtained in A-array, with synthesized beam size $1.5''$, and the contour levels in the image are 15 and 30 μJy.

from Borys et al. (2006, in preparation) and Fomalont et al. (2006, private communication).

At the position of the 1.4 GHz emission peak the HST F775W- and F160W-band images show a compact, close-separation ($\sim 0\overset{''}{.}2$) double source. Plus, the radio continuum emission appears to be extended on the scale of $\sim 3''$ (at P.A. $\simeq 42°$), significant at the 4σ level. In fact, the northern source $\sim 2.5''$ away in the HST images appears to be associated with this extended radio emission. The radio continuum indicates significant activity (from black hole accretion or star formation) outside the radio/optical core of SMM 13120, and is suggestive of a galaxy interaction or merger. However, it is not necessarily associated with the blueward-extending CO(1→0), since the activity causing the extended radio emission would likely cause increased CO excitation. Obtaining high-accuracy redshifts of the optical sources around the optical/radio core and/or interferometric imaging at high spatial resolution of the CO emission lines can verify the merger/interaction scenario: if the optical/radio sources are found to have redshifts corresponding to the center and outer regions of the CO(1→0) and CO(4→3) lines, then the sources may indeed be interacting galaxies.

More data are clearly needed to determine the structure and energetics of the major gas component(s) in SMM 13120, and SMGs as a class. In particular, spatially- and spectrally-resolved images and spectra of CO(1→0) and high-J emission will be the most revealing,

along with HCN observations, and new instruments and facilities planned for the future will help provide these. In the near future, the new Ka-band correlation receiver at GBT will cover the frequency range to which CO(1→0) is redshifted for galaxies in the range $2 < z < 3$ (26–40 GHz), and thus will aid the detection of CO(1→0) in many more SMGs in a modest integration time (~ 6 hr or less). The GBT will also be important in obtaining HCN data for SMM 13120 and SMGs in general, in a few years assisted by the Expanded Very Large Array (EVLA)[3]. Looking farther into the future, the Atacama Large Millimeter Array (ALMA)[4] will be instrumental in understanding the nature of SMM 13120 and other SMGs, since it will provide spatial resolution comparable to HST at submillimeter wavelengths and allow us to determine if and where there are multiple components contributing to the far-IR continuum emission. ALMA will also enable high-quality imaging of many CO and HCN transitions in SMGs, so that the spatial dependence of excitation conditions can be explored.

Acknowledgments We would like to thank R. Maddalena and A. Minter at NRAO-Green Bank in developing tools to calibrate the GBT K-band data. We also thank C. Borys for providing HST images of SMM 13120 and E. Fomalont for providing VLA and Subaru images of SMM 13120.

[3]Information on the EVLA project is available at http://www.aoc.nrao.edu/evla/.
[4]Information on ALMA may be obtained from http://www.alma.nrao.edu/.

Chapter 3

Spitzer Near- and Mid-IR Observations of the Chapman et al. (2005) Sample of Submillimeter-Selected Galaxies

Submillimeter-selected galaxies (SMGs) are very faint at optical wavelengths and near-IR wavelengths ranging from less than $0.1\,\mu$Jy to $\sim$a few μJy (e.g., Ivison et al. 2002; Chapman et al. 2005), and are often detected only in very deep optical images. This faintness at optical wavelengths is attributed to strong dust obscuration in rest-frame UV and optical wavelengths. However, in the mid-IR, ground-based imaging cannot reach these depths due to atmospheric emission and technological limitations, and until recently a broad characterization of SMGs in the mid-IR wavebands was not practically possible. The *Spitzer Space Telescope* is the first mid-IR observatory with sufficient sensitivity in mid-IR instruments to detect SMGs and permit characterization of their rest-frame near-IR properties, wavelengths where the extinction from dust and effects of recent star formation have less impact on the observed stellar emission. *Spitzer* has two main imaging instruments, the Infrared Array Camera (IRAC; Fazio et al. 2004), which observes at wavelengths of 3.6, 4.5, 5.8, and $8.0\,\mu$m, and the Multiband Imaging Photometer for *Spitzer* (MIPS; Rieke et al. 2004), which has detectors for imaging at 24, 70, and $160\,\mu$m. IRAC is capable of imaging to sub-μJy levels in all bands, though in the 3.6 and $4.5\,\mu$m bands source confusion limits the sensitivity below $\sim 0.6\,\mu$Jy. MIPS is capable of imaging to 3σ depths of $\sim 10\mu$Jy and $\sim$ 1 mJy at $24\,\mu$m and $70\,\mu$m, respectively, below which they are limited by faint source confusion; however, the sensitivity of the $160\,\mu$m detector is quite limited and is

not frequently used to observe faint, high-redshift objects. Given the range of optical flux densities for SMGs and the mJy flux densities in the submm bands, the instruments on *Spitzer* are well-suited to studies of SMGs and other faint galaxies.

In this chapter, we describe new observations with *Spitzer* and data reduction for the radio-detected SMG sample of Chapman et al. (2005), which is the largest sample of SMGs with spectroscopic redshifts. In the next chapters, we will use the results of our mid-IR *Spitzer* observations described here to study the near and mid-IR properties of radio-detected SMGs, as well as constrain the total IR luminosities of these galaxies, examine their rest-frame UV/optical through far-IR spectral energy distributions (SEDs), and estimate their stellar masses and stellar population characteristics, all of which require accurate spectroscopic redshifts for proper characterization. We begin in §3.1 by describing the SMG sample of Chapman et al. (2005) and how it represents the population of SMGs in general. We proceed to describe the IRAC observations of this sample in §3.2, discuss the reduction of IRAC images, and present the results and tabulated IRAC fluxes for the sample in §3.3. In §3.4 we describe the MIPS 24 μm and 70 μm observations of the sample and discuss the processing of the MIPS images, and in §3.5 we present the results of the MIPS imaging and tabulate the fluxes we measure for the SMGs in both MIPS bands.

3.1 The Chapman et al. (2005) Sample of Submm-Selected Galaxies

Chapman et al. (2005, C05 hereafter) have compiled the largest sample to date of SMGs with spectroscopic redshifts. Prior to the efforts of C05, spectroscopic identifications of SMGs proceeded slowly due to the difficulty in determining the correct optical counterpart to a Submillimeter Common-User Bolometer Array (SCUBA) source, as discussed in Chapter 1. To connect submm sources detected by SCUBA with optical counterparts for spectroscopy, C05 required that the submm sources be detected in very deep (RMS noise $\sim 4--15\,\mu$Jy), high-resolution Very Large Array (VLA) maps at 1.4 GHz, where the source density on the sky is much lower than in the optical bands. The radio-detected sources were then observed with the Low Resolution Imaging Spectrometer (LRIS) multi-object spectrograph on the Keck I telescope, without preference for optical brightness.

In this way, C05 obtained spectroscopic redshifts for 73 SCUBA sources in 7 different

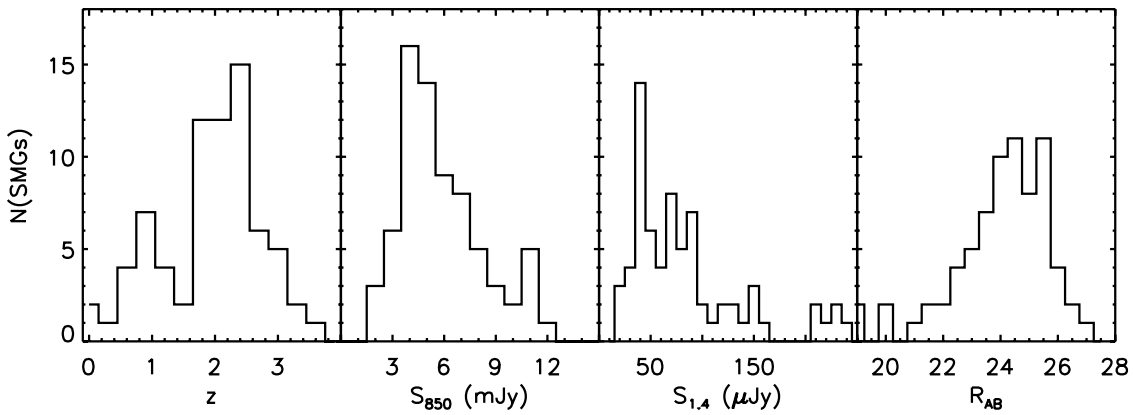

Figure 3.1 Distributions of redshift, $S_{850\mu\mathrm{m}}$, $S_{1.4\,\mathrm{GHz}}$, and R magnitude for the Chapman et al. (2005) sample of radio-detected SMGs.

"blank" fields on the sky. For reference, we list these 7 fields in Table 3.1. The redshift, 1.4 GHz flux, 850 μm flux, and R magnitude distributions for the spectroscopic sample are shown in Figure 3.1; C05 find medians for these distributions of $z = 2.2$, $S_{1.4} = 78 \pm 106\,\mu$Jy, $S_{850} = 5.7 \pm 3.0$ mJy, and $R_{\mathrm{AB}} = 24.6 \pm 1.7$. For 25% of the sample, C05 find spectral signatures of AGN in the rest-frame UV spectra, while 40% have spectral characteristics of star-forming galaxies; the rest of the spectra are difficult to classify. A large fraction of the redshifts have been independently verified through one or more of near-IR spectroscopy (e.g., Hα identification, Swinbank et al. 2004; Takata et al. 2006), mid-IR spectroscopy (Menéndez-Delmestre et al. 2007; Valiante et al. 2007), and CO rotational line spectroscopy (e.g., Greve et al. 2005, see also Chapter 2).

The spectroscopic SMG sample of C05 is the most complete and representative sample of this population and has been invaluable to the characterization of SMGs at all wavelengths, especially for studies of their bolometric luminosity, their evolution, their relation to other high-redshift populations, and the role of SMGs in the stellar mass assembly history of the Universe. However, it suffers from non-negligible selection biases. The spectroscopic redshift sample is slightly biased toward galaxies brighter in the optical bands although the radio and submm flux distributions of the galaxies with successful redshifts are not significantly different from those galaxies observed for which redshifts could not be identified. The more important selection biases are those resulting from the flux limits of the submm and radio surveys (~ 5 mJy and $\sim 30\,\mu$Jy, respectively) and the requirement that the submm sources

Table 3.1. Sky Fields in the Spectroscopic Redshift Survey of SMGs of Chapman et al. (2005)

Field Name	Center R.A. (J2000.0)	Center Dec. (J2000.0)	1.4 GHz Depth, 1σ (μJy)	N(SMGs)
CFRS–03h	03 02 40.9	+00 09 08	10	5
Lockman	10 52 00.1	+57 18 10	5	12
HDF-N/GOODS-N	12 37 07.2	+62 14 02	8	21
SSA–13	13 12 16.5	+42 41 21	4	11
CFRS–14h/Groth-Westphal	14 17 49.4	+52 30 23	14	7
ELAIS–N2	16 36 50.0	+40 57 35	15	8
SSA–22	22 15 15.1	+00 13 55	8	9

Note. — Units of right ascension are hours, minutes, and seconds. Units of declination are degrees, arcminutes, and arcseconds.

be detected in the radio to be included in the sample. Only 65–70% of bright ($S_{850} > 5\,\mathrm{mJy}$) SMGs have been detected in the radio (e.g., Ivison et al. 2002; Borys et al. 2004), despite the fact that the remaining $\sim 30\%$ span the same range in $S_{850\mu\mathrm{m}}$ as the radio-detected sample. Thus, in requiring a radio detection, C05 limit their study to a sub-sample of the full SMG population.

Which sub-population is missing is a matter of great debate. C05 advocate that the radio-faint SMGs are at similar redshifts to the rest of the population, but have colder dust temperatures. This possibility is illustrated in Figure 3.2, taken from C05, in which template SEDs from Dale & Helou (2002) of similar redshift but different dust temperatures are shown. As the dust temperature of the SED is lowered from 45 K to 25 K, the SEDs shift so that the submm fluxes do not change much, but the radio fluxes drop by nearly an order of magnitude. However, the effects of redshift and dust temperature are highly degenerate (Blain 1999b), and the same effect can be achieved by redshifting the SEDs to higher z since at radio frequencies the K correction is strongly positive. Thus, it is also possible that the galaxies not detected in the radio are at higher redshifts, as advocated by Eales et al. (2003).

Resolving the debate over the nature of the radio-faint SMG population is beyond the scope of this thesis. Accordingly, the conclusions we draw in studying the C05 sample of radio-detected SMGs must properly be restricted to apply only to radio-detected SMGs.

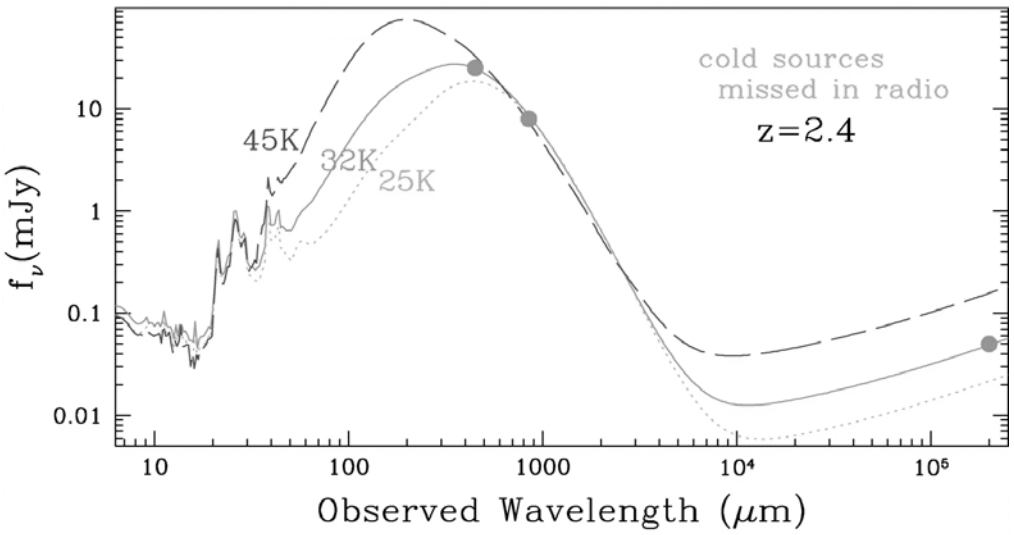

Figure 3.2 Illustration of the effect of changing dust temperature on SED shape for FIR-luminous galaxies, taken from C05. As the dust temperature decreases by only 20 degrees, the radio flux drops by an order of magnitude. However, redshifting the SED will have a similar effect on the radio flux due to the unfavorable K correction at radio wavelengths.

3.2 *Spitzer*-IRAC Observations of the Chapman Sample of Radio-Detected SMGs

We have obtained observations with the IRAC instrument on *Spitzer* for all 7 SMG fields in C05 in all 4 wavelength channels (3.6, 4.5, 5.8, and 8.0 μm) from General Observer (GO) programs led by A. Blain with the specific goal of imaging SMGs as well as from publicly-available data from various Legacy and Guaranteed Time Observation (GTO) programs obtained through the SSC archive. In Table 3.2 we detail the data sources for each SMG field as well as the sky coverage and typical depth of the images in each IRAC band. The depth of imaging coverage varies significantly between fields and also within fields, especially in the cases in which imaging from multiple observing programs and P.I.'s has been utilized, so we list the median integration time per pixel and the median 3σ point source sensitivity. For the majority of cases, the median integration time and sensitivity are essentially identical to the mode. The exception is the Lockman East Field, in which the different programs from which we have obtained data are imaged to very different depths. In this case, a small ($\sim 6' \times 6'$) portion of our final mosaic is deeper than the rest of the

area covered.

Each channel of IRAC images an area on the sky of size $5\farcm2 \times 5\farcm2$; since the SMGs in the C05 sample tend to be spread over larger areas than the detector size, the IRAC images of the SMG fields were taken in mapping mode utilizing a grid pattern of several columns by several rows. At each point (column X, row Y) on the grid, it was typical to take at least 5 dithered exposures using the medium- or large-scale random dither pattern, which offsets the telescope by typically one-fifth to one-third of the detector size. Typical exposures (referred to as frame times in the language of IRAC) were 100 or 200 seconds in IRAC channels 1, 2, and 3, and in Channel 4 two(four) 50-second exposures were taken for every single 100(200)-second exposure in the first 3 channels. Below, we describe our processing of this IRAC data into image mosaics and our methods of source extraction.

3.2.1 Data Processing, Artifact Removal, and Mosaicking

We began reduction of the IRAC data for all of the SMG fields except the GOODS-N field with the Basic Calibrated Data (BCD) images produced by version 14.0 (v14.0) of the Spitzer Science Center (SSC)'s IRAC Data Reduction Pipeline. We have excluded from all further processing the first 2 frames in each imaging sequence in each IRAC band (DCENUMs 0 and 1) since these frames have shorter times between data frames. Because the DC levels in the instrument are known to change as a function of the time elapsed between frames, these images cannot be calibrated correctly (this is known as the first-frame effect).

Pipeline v14.0 processing includes dark subtraction, detector linearization, flat fielding, cosmic ray detection, and flux calibration to units of $\mathrm{MJy\,sr^{-1}}$. However, pipeline v14.0 did not correct image artifacts such as column pull-down, which is a downward shift in the intensities of an entire column of the channel 1 and 2 arrays when a bright star or cosmic ray saturates a pixel in that column. Another form of image artifact which is not corrected in pipeline v14.0 is multiplexer bleed ("muxbleed"), which occurs in the channel 1 and 2 arrays and is triggered by bright stars, hot pixels, or cosmic ray hits, causing a decaying trail of pixels across a row of the array which repeats every 4 columns as well as a pinstripe pattern below the affected row. Persistent images, which are caused by a previous observation of a very bright star, are not corrected by the pipeline, nor is scattered light from sources out of the field of view of the detector and ghost images caused by internal

Table 3.2. Data Sources for IRAC Imaging of SMGs

Field Name	Center R.A.[a] (J2000.0)	Center Dec.[a] (J2000.0)	PID	PI	Field Size[b] arcmin × arcmin	$S_{lim,3.6\mu m}$ [c] (μJy)	$S_{lim,4.5\mu m}$ [c] (μJy)	$S_{lim,5.8\mu m}$ [c] (μJy)	$S_{lim,8.0\mu m}$ [c] (μJy)
CFRS–03h	03 02 44.7	+00 07 39	3473	A. Blain	10.0 × 10.9	0.5	0.6	3.4	4.4
Lockman	10 52 22.3	+57 24 54	81	G. Rieke	20.2 × 22.2	0.6	0.7	4.4	3.8
			1077	H. Dole					
HDF-N/GOODS-N	12 36 54.9	+62 14 19	169	M. Dickinson	16.5 × 10.0	0.1	0.1	0.4	0.4
SSA–13	13 12 26.1	+42 39 10	64	G. Fazio	17.5 × 14.9	0.9	1.3	6.4	6.5
CFRS–14h	14 17 45.3	+52 29 08	8	G. Fazio	8.3 × 7.1	0.3	0.4	1.5	1.9
ELAIS–N2	16 36 47.1	+41 00 35	3473	A. Blain	14.2 × 10.7	0.5	0.7	3.3	3.8
SSA–22	22 18 07.9	+00 17 27	3473	A. Blain	11.8 × 8.6	0.5	0.8	3.6	5.6
	22 17 30.9	+00 13 40	64	G. Fazio	5.5 × 5.5	0.3	0.4	1.9	2.3

Note. — Units of right ascension are hours, minutes, and seconds. Units of declination are degrees, arcminutes, and arcseconds.

[a]Coordinates of center of field imaged in all 4 IRAC channels.

[b]Size of field imaged in all 4 IRAC channels.

[c]Median 3σ point source sensitivity in combined mosaic.

reflections within the filters. In the top panel of Figure 3.3 we show an example IRAC channel 1 (3.6 μm) BCD image from our ELAIS-N2 data set, which is affected by column pull-down, muxbleed, and filter ghost images. In addition, some of the IRAC datasets for the SMG fields (CFRS-03h, ELAIS-N2, and SSA 22) were taken using in-place repeats, in which the telescope takes several exposure frames in a row without dithering. Because the telescope is not moved between frames, the frames have a much shorter delay interval from the preceding image between them, and since the DC levels vary quickly as a function of time, the first-frame effect for the repeat frames is not well-calibrated. This effect is most prominent in channel 3 and causes a distinct residual bias pattern over the BCD images.

Many of our BCD images suffered from at least some of these possible artifacts, and since we expected our target objects to be at the faintest flux levels in the images, it was necessary to remove the artifacts to improve our detection sensitivity and prevent the association of a target source with spurious detections. To accomplish this, we used the IDL IRAC Artifact Mitigation scripts[1] written by S. Carey at the SSC to remove column pull-down and muxbleed from all of our images. We used the Muxstripe Corrector[2], written by J. Surace at the SSC, to remove the pinstriping associated with muxbleed (iterating the script for the number of 2MASS stars in the image). In the bottom panel of Figure 3.3 we show the same image as in the top panel of the figure after running the artifact correction script. As is evident in the figure, the column pull-down was usually well-removed, as was muxbleed from fainter sources. However, because the SSC has not been able to model all forms of muxbleed, artifacts of this type caused by bright sources were not always completely removed. In cases where muxbleed could not be removed, we masked the remaining affected pixels. The pixels in the uncertainty images corresponding to the pixels affected by artifacts were modified to reflect uncertainties in the corrections applied. For the SMG fields in which in-place repeats were used in the data-taking process, we modified the Repeat-Delta-Dark script written in IDL by S. Carey[3] to remove the residual bias patterns from channel 3 BCD images.

Image artifacts caused by stray light and persistent images are difficult to remove reliably since they can vary in shape and intensity. As a result, we simply masked the pixels affected

[1]The IRAC Artifact Mitigation procedures are available from the website http://spider.ipac.caltech.edu/staff/carey/irac-artifacts/.

[2]The Muxstripe Corrector script can be downloaded from http://ssc.spitzer.caltech.edu/irac/automuxstripe/.

[3]The original version of the Repeat-Delta-Dark script is available from the SSC website at http://ssc.spitzer.caltech.edu/irac/deltadark/.

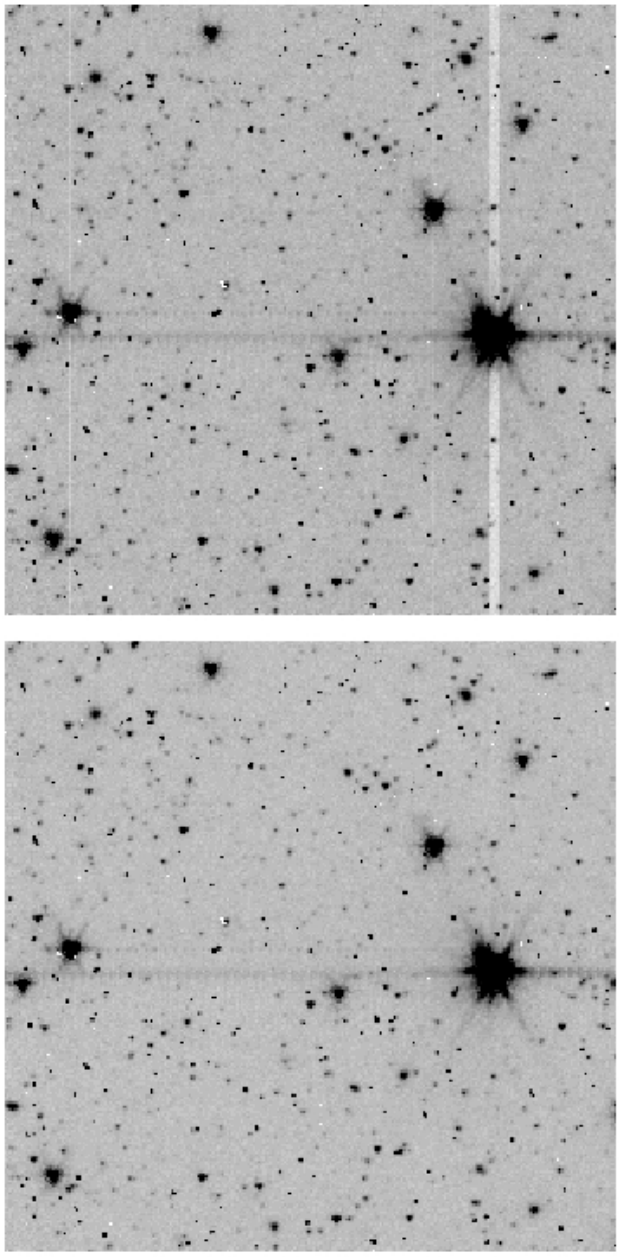

Figure 3.3 *Top Panel*: Example IRAC BCD image affected by column pull-down, muxbleed, and first-order filter ghosts, a 3.6 μm image from our ELAIS-N2 data set. Column pull-down is indicated by the white columns above and below the position of a saturated star. Muxbleed can be seen from the same stars causing column pull-down, where there is a decaying trail of pixels across a row affecting every fourth column and a faint pin-striping noticeable below the row of enhanced pixels. The optical filter ghost is visible for the brightest star as the asymmetry at the upper left of the star's diffraction spikes. *Bottom Panel*: Same image, after best-effort corrections carried out. Note that the column pull-down and pinstriping are well-removed, but residual trails of muxbleed across rows remain.

by these phenomena and did not measure a target source if it was affected in all of the BCDs which covered the target's position. To carry out the stray light masking, we used the Stray Light Masker written in IDL by M. Lacy and R. Arendt at the SSC,[4] which determines which pixels in a BCD will be affected by stray light based on the geometry of the array covers responsible for the scattering and the positions of 2 Micron All-Sky Survey (2MASS) sources near the area being imaged.

After artifact mitigation, and before constructing mosaics for each field, we carried out two more processing steps. First, we constructed "superflats" from our own data for each field by masking out 2MASS sources brighter than $K \sim 13$ in individual BCDs and taking the median of the masked images. The normalized superflats were then applied to all BCDs to remove higher-order effects and some persistent images.

We created mosaic images for each IRAC channel for each SMG field using the MOPEX software package (Makovoz & Marleau 2005) designed specifically for use with *Spitzer* data. After creating a common coordinate and geometric frame for all the artifact-corrected BCD images in all of the IRAC channels, we carried out absolute pointing refinement of the individual BCD frames, aligning each frame to the 2MASS system using bright ($K < 14$) 2MASS point sources in each image, to facilitate the co-addition of overlapping images in the mosaic. Pointing refinement was generally successful in channels 1 and 2; however, in channels 3 and 4, there were not always enough bright 2MASS stars visible for the pointing solution to be derived. Thus, if the absolute pointing refinement failed, we performed relative pointing refinement. Afterward, we equalized the background of individual median sky-subtracted BCD images, interpolated the background-matched frames into the common grid using the "drizzling" interpolation method with a drizzling factor of 0.8, and corrected the images for optical distortion. To improve the image quality of the mosaics, we identified and masked deviant pixels (e.g., due to cosmic ray hits, bad array pixels, or image artifacts) with spatial and temporal filtering. The combination of outlier rejection based on spatial and temporal filtering proved more effective than either method alone, since most of the data sets had variable coverage over the imaged fields and lacked the high redundancy required for temporal filtering only. Finally, the interpolated science images and uncertainty images were co-added into separate mosaics using the masks of rejected pixels, weighting pixels by exposure time. The final mosaics have pixels of size $0\farcs6$ in all fields, including the GOODS-

[4]The Stray Light Masking Software can be downloaded from http://ssc.spitzer.caltech.edu/irac/straylight/.

N field. We list the details of the IRAC mosaics for each field in Table 3.2, giving the center of the sky field mapped, the median integration time per pixel, and the median 3σ point source sensitivity for each IRAC channel. We have given the median integration time because the coverage varies within each mosaic, usually deeper in the center than at the edges.

For the GOODS-N field, the already-reduced and mosaicked IRAC images were downloaded from the GOODS *Spitzer* Legacy Project's website[5]. The processing and mosaicking of this data is described in Dickinson et al. (in preparation), and is very similar to that performed for the rest of the SMG fields. The final mosaic has $0\farcs6$ pixels, and its astrometry has been tied to the *Hubble Space Telescope*-Advanced Camera for Surveys (HST-ACS) and VLA images of the GOODS-N field.

3.2.2 Source Extraction

We have detected and extracted fluxes for the SMGs in each field in each IRAC channel using SExtractor version 2.3.2 (Bertin & Arnouts 1996). The point spread function (PSF) of IRAC tends to scatter light to radii as large as $\sim 1'$, especially in the longer-wavelength channels (c.f. IRAC Data Handbook), so a large-diameter aperture is required to measure the total flux from a source. However, the source density in the IRAC images, especially in the shorter-wavelength channels, is sufficiently high that large apertures will be frequently contaminated by other sources. Thus, we measure fluxes through $4''$-diameter apertures in each IRAC channel, centered on the IRAC counterpart of the SMG (identified through the position of the SMG's radio counterpart, not from the SCUBA position). We then apply aperture corrections to a $12''$-radius aperture, the size of which was determined by a curve-of-growth analysis of isolated 2MASS point sources in each field to obtain the radius enclosing the total flux in all channels. The $12''$-radius aperture also matches the IRAC absolute calibration aperture. Most of the SMGs have no neighbors within the $4''$ aperture to contaminate the photometry; we note in Appendix A galaxies which contain another object in its photometry aperture.

We expect the measured source fluxes to be accurate to better than 10% for IRAC channels 1 and 2, including flux calibration errors (typically 3%, see IRAC Data Handbook), aperture correction errors (typically 2-3%), errors due to uncorrected IRAC data artifacts

[5]http://data.spitzer.caltech.edu/popular/goods/

(e.g., pixel phase correction in channel 1), and errors due to color corrections (usually less than 1% for sources with spectra of shape $F_\nu \propto \nu^{-2}$). In channels 3 and 4, we expect the fluxes to be accurate to $\sim 10\%$ since errors in the aperture corrections tend to be larger at the longer wavelengths. The positions of the detected sources should be accurate to better than $1''$ in channels 1 and 2 since the absolute pointing has been aligned to the accuracy of 2MASS ($\sim 0\farcs15$) with an RMS of typically $0\farcs3$. We expect that the dominant position error in these channels comes from centroiding due to the under-sampled PSF. In channels 3 and 4, where absolute pointing refinement was unsuccessful, the source position errors have a more significant contribution from the blind pointing error of IRAC ($\sim 0\farcs5$), so we conservatively estimate that the positions are likely to be accurate to $\sim 1''$.

3.3 Results of IRAC Imaging of SMGs

3.3.1 Identification of SMG Counterparts in IRAC Images

As discussed in Chapter 1, identification of submm sources at optical and near-IR wavelengths is problematic due to the large SCUBA beam size and error circle at 850 μm and the faintness of SMGs at optical wavelengths. Statistical methods based on the probability of finding a source at a given distance from the submm position are often used to determine search radii for SMG counterparts at other wavelengths; however, in the optical and near-IR bands several possible counterparts frequently lay within the search radius, and it is unclear which sources, if any, are associated with the submm source. However, with precise radio positions, like those available for the SMGs in the sample of C05, much of the ambiguity is removed in counterpart selection, and one does not have to resort to statistical methods to identify most SMG counterparts.

Thus, here, we identify the SMGs in our IRAC imaging through their radio positions in C05. The sample of C05 has a typical position uncertainty of $0\farcs5$, comparable to the uncertainties of the positions of the IRAC detections. We add in quadrature the uncertainties in the radio positions and the uncertainties in the IRAC positions to determine the matching radius, obtaining $1\farcs1$. In several cases, which are noted in Appendix A, the optical counterpart identified by C05 is offset from the radio position, and we have allowed a larger offset between the IRAC and radio positions for these sources for consistency with C05.

We do not require detection in a particular IRAC band for counterpart identification, which would introduce additional selection effects on our sample. Rather, we identify counterparts for each SMG in all 4 IRAC channels separately, and when a source is detected in multiple IRAC bands, we have ensured that we consistently measure the same source in all bands.

3.3.2 Characteristics of SMGs in IRAC Images

The majority of the SMG sample of C05 is detected above a 3σ level in all of the IRAC bands. We detect 61 of 67 SMGs imaged at $3.6\,\mu$m, 63 of 67 with imaging at $4.5\,\mu$m, 53 of 67 with imaging at $5.8\,\mu$m, and 52 of 67 at $8.0\,\mu$m. The detected sources have typical flux densities of $\sim 1 - 100\,\mu$Jy. Over the 7 SMG fields with IRAC observations, 6 SMGs lack IRAC imaging in each channel, though not necessarily the same 6 objects in each channel since the field imaged by IRAC channels 1 and 3 is offset by $1\farcm5$ from the field observed by IRAC channels 2 and 4. Our IRAC map grids ensure that the central areas of the fields are covered in all 4 IRAC channels, but if a source happens to fall at the far edge of the mosaic field in channels 1 and 3 (or channels 2 and 4), it is often not in the mosaic field in channels 2 and 4 (or channels 1 and 3).

We show $20'' \times 20''$ postage stamp images of all SMGs in our sample with IRAC imaging in Figures 3.4, 3.5, 3.6, and 3.7, centered on the radio position of each object. In the images we see that, for the vast majority of the cases, only one source lies within the matching radius of $1''$, so source confusion is not typically a problem for counterpart identification. However, some SMGs have near neighbors which may contaminate photometry apertures, which we note in Appendix A. Nearly all of the SMGs appear as point sources in the IRAC images, so we are unable to comment on the rest-frame near-IR morphology of individual sources.

We list the positions of the IRAC counterparts and our measured flux density in each IRAC band for the all of the sources in the sample of C05, including those suspected of being low-z lenses and excluded from the analysis of C05, in Table 3.3. However, we exclude these low-z lenses from the remainder of our analysis here. The positions listed come from the bluest wavelength of detection, since for the 3.6 and $4.5\,\mu$m IRAC bands absolute pointing refinement was successful, and we expected the uncertainties in the positions to be smaller. The listed errors in each band include a 10% uncertainty to account for the uncertainty

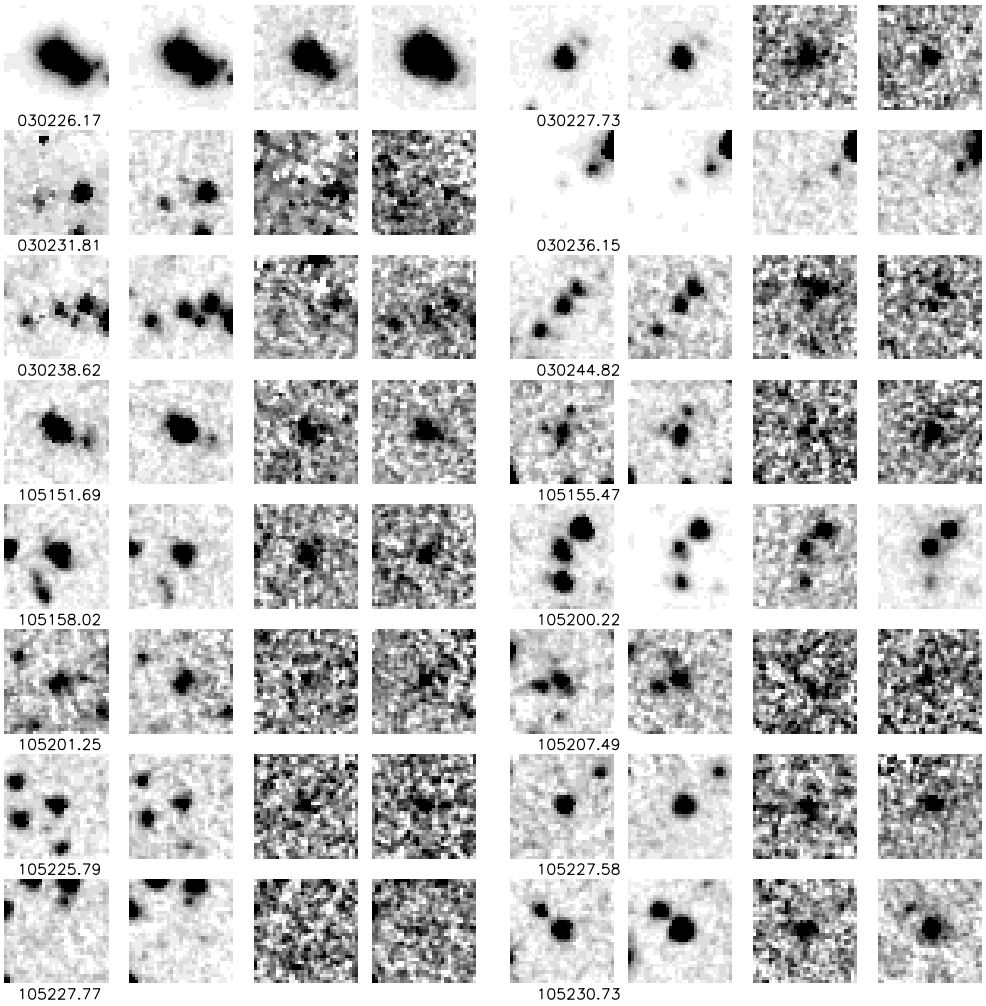

Figure 3.4 $20'' \times 20''$ postage stamp images of the radio positions of the SMGs in the sample of C05 for the 3.6, 4.5, 5.8, and 8.0 μm bands of IRAC, respectively. In each image, north is up, east is to the left.

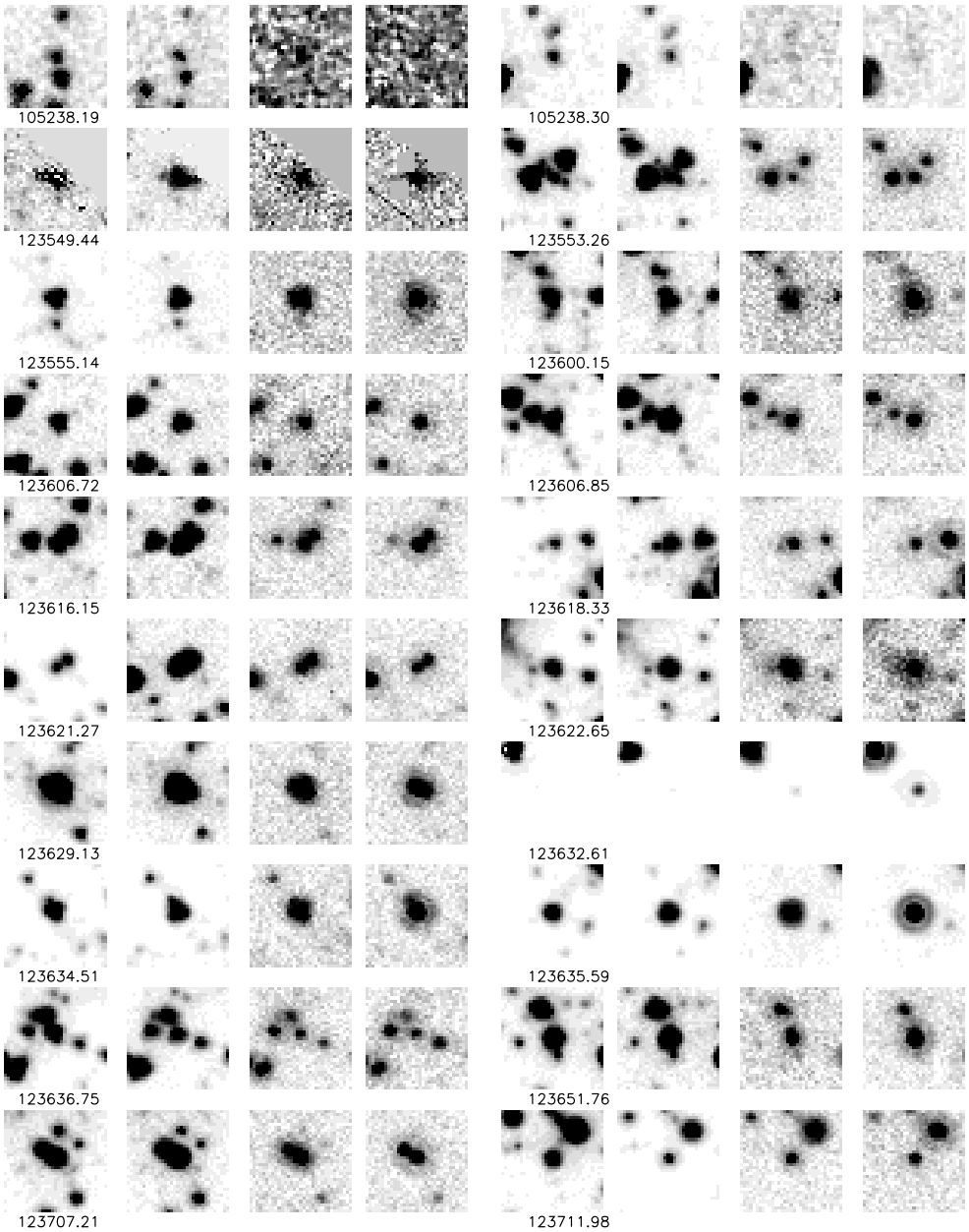

Figure 3.5 More $20'' \times 20''$ postage stamp images of the radio positions of the SMGs in the IRAC bands. Continued from Figure 3.4.

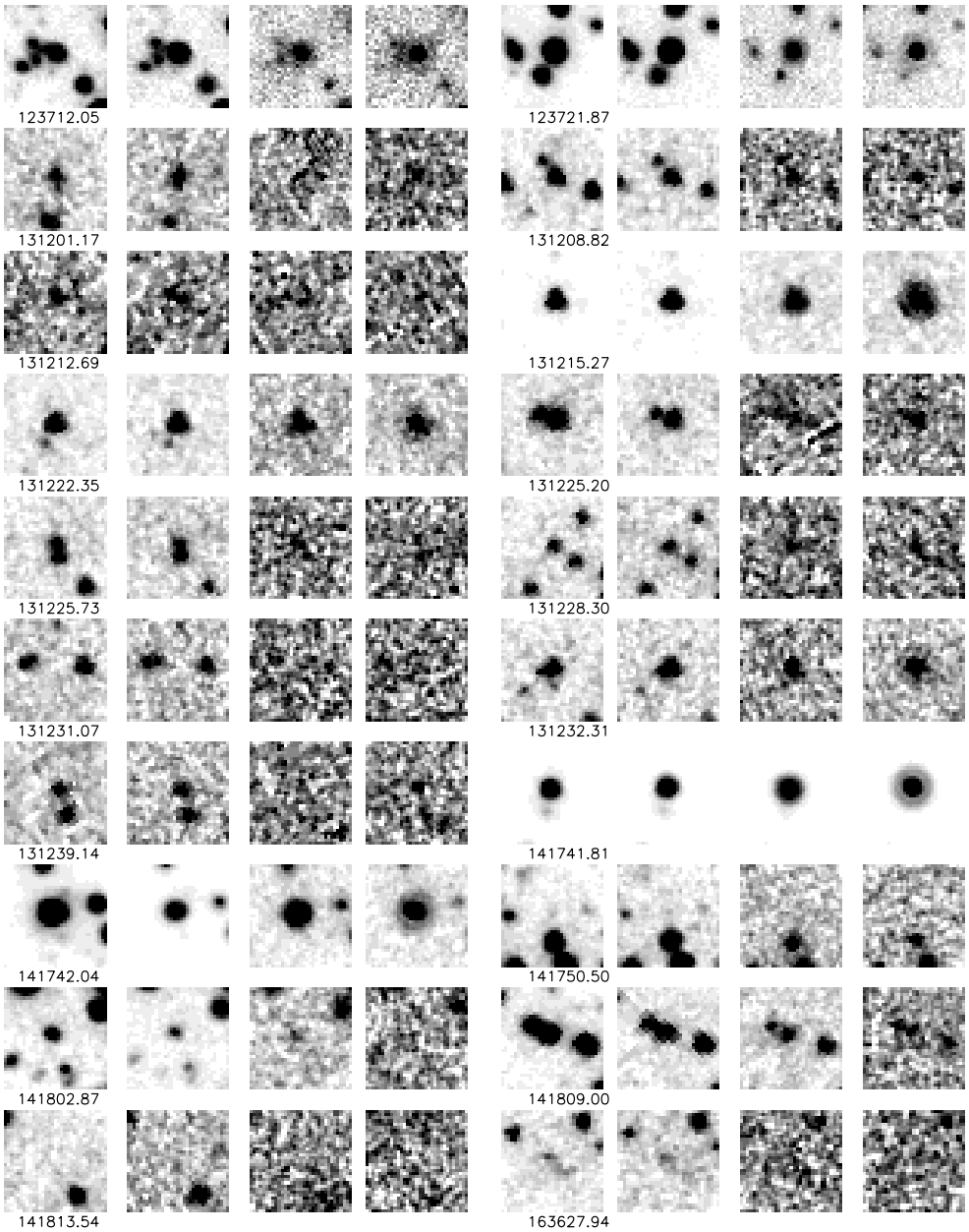

Figure 3.6 More $20'' \times 20''$ postage stamp images of the radio positions of the SMGs in the IRAC bands. Continued from Figures 3.4 and 3.5.

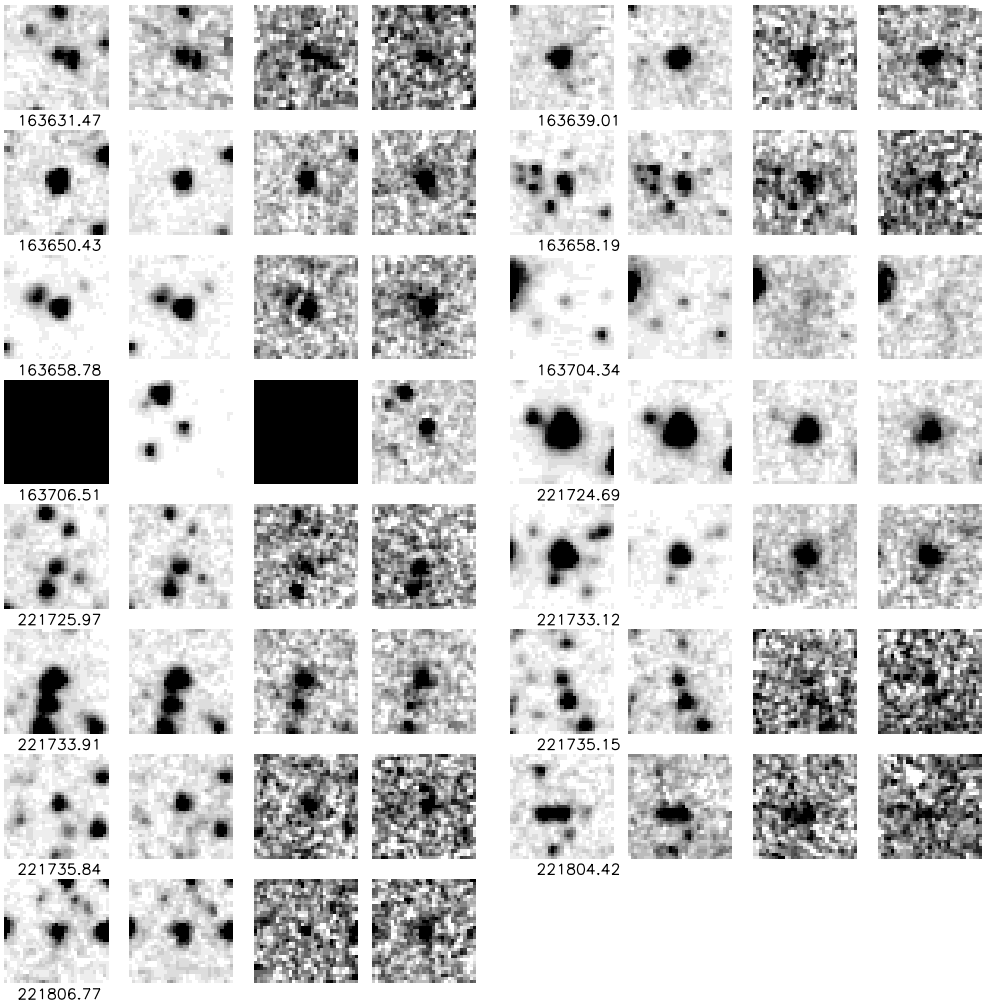

Figure 3.7 More $20'' \times 20''$ postage stamp images of the radio positions of the SMGs in the IRAC bands. Continued from Figures 3.4, 3.5, and 3.6. Black squares indicate that no imaging is available in that particular band.

in the absolute calibration, though this is likely an overestimate of the uncertainty for the measurements in the 3.6 μm and 4.5 μm channels. For undetected SMGs, we list 3σ point-source uncertainties/sensitivities as upper limits. For IRAC, the point source uncertainty is calculated according to the equation

$$\sigma = \mathrm{RMS}_{\mathrm{local}} \times \sqrt{N_i}, \tag{3.1}$$

where $\mathrm{RMS}_{\mathrm{local}}$ is the RMS per pixel in a 40×40-pixel box centered on the radio position of the SMG in units of $\mu\mathrm{Jy\,pixel}^{-1}$, and N_i is the number of noise pixels[6] in the image mosaic for IRAC channel i. By using the RMS of the pixels at the radio position of the undetected SMG the upper limits we calculate take into account the non-uniform coverage within the imaged fields and reflect more accurately the depth of imaging at the object's position. Blank entries in Table 3.3 indicate that the position of that particular object is not covered in our IRAC image mosaics.

We have compared our IRAC photometry to previously published values (Egami et al. 2004; Borys et al. 2005; Pope et al. 2006; Ashby et al. 2006) for cases in which we agree with the other studies in IRAC counterpart selection. Our photometry in all 4 IRAC bands agrees with both Borys et al. (2005) and Pope et al. (2006) to within 5% and with Ashby et al. (2006) to within 10–15%; however, our fluxes tend to be 10–30% higher than those of Egami et al. (2004), depending on the wavelength being compared. We suspect that the large differences between our photometry and that of Egami et al. (2004) arise because of the different ways we measure the sources. We have performed aperture photometry and applied aperture corrections, whereas Egami et al. (2004) uses PSF fitting to derive their fluxes, and they do not appear to apply any aperture corrections. However, as mentioned earlier, aperture corrections are very important when measuring IRAC fluxes since the PSF scatters light to large radii; thus, we feel our use of them is justified.

[6]The number of noise pixels is the equivalent number of pixels whose noise contributes to the flux of an extracted point source.

Table 3.3: IRAC Flux Densities for Chapman et al. (2005) SMG Sample

Chapman et al. (2005) ID	IRAC R.A. (J2000.0)	IRAC Dec. (J2000.0)	$S_{3.6\mu m}$ (μJy)	$S_{4.5\mu m}$ (μJy)	$S_{5.8\mu m}$ (μJy)	$S_{8.0\mu m}$ (μJy)
SMM J030226.17+000624.5[a]	03 02 26.17	+00 06 24.10	746.9 ± 75.0	502.1 ± 50.3	452.3 ± 45.9	2220.6 ± 224.1
SMM J030227.73+000653.5	03 02 27.74	+00 06 53.40	73.8 ± 7.4	79.3 ± 7.9	59.8 ± 6.3	61.6 ± 6.6
SMM J030231.81+001031.3	03 02 31.81	+00 10 31.30	< 0.7	1.6 ± 0.3	< 5.5	< 3.5
SMM J030236.15+000817.1	03 02 36.16	+00 08 16.80	7.7 ± 0.8	9.7 ± 1.0	14.9 ± 2.0	< 3.5
SMM J030238.62+001106.3	03 02 38.60	+00 11 05.40	16.6 ± 1.7	19.8 ± 2.0	< 5.1	< 3.8
SMM J030244.82+000632.3	03 02 44.84	+00 06 32.30	9.4 ± 0.9	7.7 ± 0.8	< 2.6	12.6 ± 2.2
SMM J105151.69+572636.0	10 51 51.71	+57 26 36.40	78.1 ± 7.8	89.2 ± 8.9	64.7 ± 6.9	63.3 ± 6.6
SMM J105155.47+572312.7	10 51 55.52	+57 23 12.20	5.1 ± 0.5	7.6 ± 0.8	13.1 ± 2.1	18.5 ± 2.0
SMM J105158.02+571800.2	10 51 58.03	+57 18 00.30	53.3 ± 5.3	55.5 ± 5.6	43.9 ± 5.1	53.0 ± 5.8
SMM J105200.22+572420.2	10 52 00.24	+57 24 21.20	22.5 ± 2.3	25.9 ± 2.6	40.8 ± 4.4	96.5 ± 9.7
SMM J105201.25+572445.7	10 52 01.19	+57 24 45.60	5.5 ± 0.6	8.7 ± 0.9	11.9 ± 2.2	14.8 ± 1.9
SMM J105207.49+571904.0	10 52 07.56	+57 19 04.10	10.1 ± 1.0	12.9 ± 1.3	< 4.8	< 5.6
SMM J105225.79+571906.4	10 52 25.81	+57 19 06.60	28.4 ± 2.9	22.3 ± 2.3	25.9 ± 3.7	37.3 ± 5.0
SMM J105227.77+572218.2	10 52 27.77	+57 22 18.20	< 0.5	< 0.3	< 4.9	< 1.8
SMM J105227.58+572512.4	10 52 27.55	+57 25 12.40	19.6 ± 2.0	25.6 ± 2.6	41.4 ± 4.9	28.5 ± 3.0
SMM J105230.73+572209.5	10 52 30.72	+57 22 09.40	33.4 ± 3.4	39.5 ± 4.0	56.5 ± 6.5	46.6 ± 4.7
SMM J105238.19+571651.1	10 52 38.18	+57 16 51.00	17.4 ± 1.8	18.8 ± 2.0	31.1 ± 4.3	< 7.6
SMM J105238.30+572435.8	10 52 38.30	+57 24 35.70	28.9 ± 2.9	32.7 ± 3.3	29.8 ± 4.6	< 57.2
SMM J123549.44+621536.8[b]	12 35 49.44	+62 15 36.40	$\cdots$	< 0.2	$\cdots$	< 1.5
SMM J123553.26+621337.7	12 35 53.25	+62 13 37.50	9.2 ± 1.3	14.6 ± 1.7	18.1 ± 1.9	24.7 ± 2.7
SMM J123555.14+620901.7	12 35 55.16	+62 09 01.50	42.5 ± 4.9	61.5 ± 7.0	79.5 ± 8.3	93.8 ± 10.2
SMM J123600.10+620253.5	12 36 00.10	+62 02 53.10	$\cdots$	$\cdots$	$\cdots$	$\cdots$
SMM J123600.15+621047.2	12 36 00.16	+62 10 47.30	12.6 ± 1.5	14.8 ± 1.7	27.0 ± 2.8	61.9 ± 6.4

Table 3.3 – Continued

Chapman et al. (2005) ID	IRAC R.A. (J2000.0)	IRAC Dec. (J2000.0)	$S_{3.6\mu m}$ (μJy)	$S_{4.5\mu m}$ (μJy)	$S_{5.8\mu m}$ (μJy)	$S_{8.0\mu m}$ (μJy)
SMM J123606.72+621550.7	12 36 06.73	+62 15 50.40	9.6 ± 1.4	13.2 ± 1.6	19.4 ± 2.1	26.3 ± 2.9
SMM J123606.85+621021.4	12 36 06.87	+62 10 21.40	27.8 ± 3.0	31.0 ± 3.3	35.5 ± 3.7	28.1 ± 3.1
SMM J123616.15+621513.7	12 36 15.99	+62 15 14.40	20.0 ± 2.3	15.0 ± 1.7	39.8 ± 4.1	46.8 ± 4.9
SMM J123618.33+621550.5	12 36 18.38	+62 15 50.30	15.0 ± 1.9	19.9 ± 2.2	27.3 ± 2.8	20.0 ± 2.2
SMM J123621.27+621708.4	12 36 21.12	+62 17 08.90	20.4 ± 2.3	27.3 ± 2.9	34.4 ± 3.5	24.5 ± 2.6
SMM J123622.65+621629.7	12 36 22.78	+62 16 29.50	19.8 ± 2.2	27.6 ± 2.9	35.3 ± 3.6	26.4 ± 2.8
SMM J123629.13+621045.8	12 36 29.08	+62 10 45.70	93.1 ± 9.6	87.0 ± 9.0	75.8 ± 7.7	72.0 ± 7.4
SMM J123632.61+620800.1	12 36 32.57	+62 07 59.80	21.2 ± 2.5	27.8 ± 3.0	50.7 ± 5.2	114.3 ± 11.7
SMM J123634.51+621241.0	12 36 34.54	+62 12 41.10	64.4 ± 6.7	72.5 ± 7.4	59.2 ± 6.0	73.6 ± 7.5
SMM J123635.59+621424.1	12 36 35.60	+62 14 23.90	65.0 ± 6.7	100.0 ± 10.1	175.8 ± 17.6	300.5 ± 30.2
SMM J123636.75+621156.1	12 36 36.79	+62 11 56.10	22.6 ± 2.5	16.2 ± 1.8	14.4 ± 1.5	13.4 ± 1.6
SMM J123651.76+621221.3[a]	12 36 51.72	+62 12 20.60	21.1 ± 2.3	21.1 ± 2.2	17.7 ± 1.8	46.9 ± 4.8
SMM J123707.21+621408.1	12 37 07.34	+62 14 08.60	19.4 ± 2.1	26.3 ± 2.8	36.0 ± 3.7	28.2 ± 2.9
SMM J123711.98+621325.7	12 37 12.00	+62 13 25.80	9.3 ± 1.1	11.5 ± 1.3	15.7 ± 1.6	12.1 ± 1.3
SMM J123712.05+621212.3[c]	12 37 12.07	+62 12 12.00	...	...	20.8 ± 2.1	23.0 ± 2.4
SMM J123716.01+620323.3	12 37 16.01	+62 03 22.90	...	...	...	...
SMM J123721.87+621035.3	12 37 21.86	+62 10 35.70	70.9 ± 7.3	53.9 ± 5.6	43.8 ± 4.4	44.3 ± 4.6
SMM J131201.17+424208.1	13 12 01.18	+42 42 08.30	10.6 ± 1.1	15.1 ± 1.6	24.1 ± 3.7	29.3 ± 4.1
SMM J131208.82+424129.1	13 12 08.81	+42 41 29.20	27.3 ± 2.8	37.3 ± 3.8	33.4 ± 4.4	26.9 ± 4.0
SMM J131212.69+424422.5	13 12 12.72	+42 44 23.30	4.6 ± 0.6	7.2 ± 1.0	< 8.2	< 10.2
SMM J131215.27+423900.9	13 12 15.22	+42 39 01.00	249.9 ± 25.1	296.5 ± 29.7	481.1 ± 53.5	831.4 ± 85.1
SMM J131222.35+423814.1	13 12 22.39	+42 38 13.80	63.2 ± 6.3	80.1 ± 8.0	148.2 ± 16.2	267.2 ± 27.4
SMM J131225.20+424344.5	13 12 25.18	+42 43 45.10	60.7 ± 6.1	48.3 ± 4.9	35.3 ± 4.6	53.1 ± 6.1
SMM J131228.30+424454.8	13 12 28.27	+42 44 54.90	11.3 ± 1.2	13.9 ± 1.4	21.7 ± 3.3	26.5 ± 3.5
SMM J131231.07+424609.0	13 12 31.07	+42 46 09.00	< 0.6	< 1.0	< 5.1	< 6.3
SMM J131225.73+423941.4	13 12 25.70	+42 39 40.30	21.1 ± 2.1	20.2 ± 2.1	< 4.9	< 5.7

Table 3.3 – Continued

Chapman et al. (2005) ID	IRAC R.A. (J2000.0)	IRAC Dec. (J2000.0)	$S_{3.6\mu m}$ (μJy)	$S_{4.5\mu m}$ (μJy)	$S_{5.8\mu m}$ (μJy)	$S_{8.0\mu m}$ (μJy)
SMM J131232.31+423949.5	13 12 32.31	+42 39 49.50	26.9 ± 2.7	42.6 ± 4.3	76.3 ± 8.9	191.4 ± 19.8
SMM J131239.14+424155.7	13 12 39.11	+42 41 55.90	9.3 ± 1.0	10.3 ± 1.1	< 7.7	15.9 ± 3.6
SMM J141742.04+523025.7	14 17 42.10	+52 30 26.20	153.2 ± 15.3	126.1 ± 12.6	140.4 ± 14.1	152.6 ± 15.3
SMM J141741.81+522823.0	14 17 41.87	+52 28 23.70	518.7 ± 51.9	851.5 ± 85.2	1313.4 ± 134.2	1961.9 ± 197.1
SMM J141800.40+512820.3	14 18 00.40	+51 28 20.30	...	...	...	...
SMM J141809.00+522803.8	14 18 09.11	+52 28 05.00	43.7 ± 4.4	56.7 ± 5.7	60.8 ± 6.4	40.8 ± 5.3
SMM J141802.87+523011.1	14 18 02.94	+52 30 12.50	5.0 ± 0.5	5.4 ± 0.6	5.7 ± 0.7	< 2.0
SMM J141750.50+523101.0	14 17 50.50	+52 31 01.00	< 0.3	< 0.3	< 1.3	< 1.8
SMM J141813.54+522923.4	14 18 13.54	+52 29 23.40	< 0.2	< 0.5	< 2.1	< 3.8
SMM J163627.94+405811.2	16 36 27.98	+40 58 11.30	3.7 ± 0.4	5.1 ± 0.6	< 3.8	< 4.1
SMM J163631.47+405546.9	16 36 31.42	+40 55 47.00	9.5 ± 1.0	17.0 ± 1.8	23.5 ± 3.0	19.5 ± 2.6
SMM J163639.01+405635.9	16 36 39.06	+40 56 35.60	23.0 ± 2.3	29.3 ± 2.9	33.5 ± 3.6	40.0 ± 4.2
SMM J163650.43+405734.5	16 36 50.41	+40 57 34.30	31.0 ± 3.1	36.9 ± 3.7	50.5 ± 5.2	65.0 ± 6.6
SMM J163658.19+410523.8	16 36 58.13	+41 05 23.10	14.9 ± 1.5	21.2 ± 2.1	28.1 ± 3.1	29.0 ± 3.5
SMM J163658.78+405728.1	16 36 58.75	+40 57 27.80	67.5 ± 6.8	66.6 ± 6.7	48.8 ± 5.2	61.7 ± 6.3
SMM J163704.34+410530.3[d]	16 37 04.30	+41 05 30.80	...	12.5 ± 1.3	< 5.7	< 5.5
SMM J163706.51+405313.8	16 37 06.47	+40 53 14.20	...	31.5 ± 3.2	...	62.0 ± 6.3
SMM J221724.69+001242.1[a]	22 17 24.70	+00 12 41.80	188.0 ± 18.8	146.4 ± 14.6	131.8 ± 13.4	128.0 ± 12.9
SMM J221733.12+001120.2	22 17 33.16	+00 11 20.10	87.9 ± 8.8	66.5 ± 6.7	78.8 ± 8.1	66.1 ± 6.7
SMM J221804.42+002154.4	22 18 04.43	+00 21 52.90	9.1 ± 0.9	13.4 ± 1.4	19.5 ± 2.3	< 6.5
SMM J221806.77+001245.7	22 18 06.75	+00 12 45.40	19.8 ± 2.0	25.8 ± 2.6	10.1 ± 3.1	36.3 ± 4.1
SMM J221735.84+001558.9	22 17 35.84	+00 15 59.00	6.9 ± 0.7	11.1 ± 1.1	12.6 ± 1.5	17.7 ± 2.0
SMM J221735.15+001537.2	22 17 35.16	+00 15 37.20	4.2 ± 0.4	6.1 ± 0.6	< 1.9	8.6 ± 1.3
SMM J221733.91+001352.1	22 17 33.96	+00 13 52.00	21.1 ± 2.1	26.6 ± 2.7	28.6 ± 3.0	38.9 ± 4.0

Table 3.3 – Continued

Chapman et al. (2005) ID	IRAC R.A. (J2000.0)	IRAC Dec. (J2000.0)	$S_{3.6\mu m}$ (μJy)	$S_{4.5\mu m}$ (μJy)	$S_{5.8\mu m}$ (μJy)	$S_{8.0\mu m}$ (μJy)
SMM J221725.97+001238.9	22 17 26.00	+00 12 36.50	5.9 ± 0.6	7.6 ± 0.8	9.0 ± 1.2	14.6 ± 1.7
SMM J221733.02+000906.0	22 17 33.02	+00 09 06.00	···	···	···	···
SMM J221737.39+001025.1	22 17 37.39	+00 10 25.10	···	···	···	···

Units of right ascension are hours, minutes, and seconds. Units of declination are degrees, arcminutes, and arcseconds.

[a] This object was identified by Chapman et al. (2005) as a low-z lens unassociated with the submillimeter source. It has been excluded from the analysis presented here.

[b] This object lies on the edges of the IRAC images in all fields but is clearly detected.

[c] This object is detected in all IRAC bands, but confused with another source at 3.6 and 4.5 μm such that SExtractor could not measure it separately in these bands.

[d] This object is detected in the 3.6 μm channel of IRAC but falls within a column affected by column pull-down and with resulting large uncertainties cause it to be formally undetected.

3.4 *Spitzer*-MIPS Observations of the Chapman Sample of SMGs

We have compiled imaging observations for the C05 SMG sample in the 24μm and 70μm bands of MIPS from a variety of observing programs. Data for the CFRS-03h and SSA-22 fields were obtained through a GO program undertaken by A. Blain, while data for 4 of the remaining 5 SMG fields come from *Spitzer* Legacy Projects and GTO programs available in the SSC data archive. The SSA-13 field has no MIPS observations available. The depth of imaging coverage varies significantly between fields and also within fields, especially in the cases in which imaging from multiple observing programs and P.I.'s has been utilized. In Tables 3.4 and 3.5 we detail the data sources, sky coverage, and typical integration times for the MIPS 24 μm and 70 μm data, respectively, for each of the SMG fields.

At 24 μm, MIPS can image a 5.′4 square field, while the 70 μm detector images a $2.'5 \times 5'$ field of view. Since the SMGs are typically spread over areas larger than these detectors, mosaics of MIPS pointings were observed to cover the necessary area on the sky. Much of the 24 μm and 70 μm imaging was taken in large-field photometry mode, in which the scan mirror is used to take images with small offsets from a central telescope pointing, and the telescope is moved between cycles of scan mirror positions in order to cover the desired field. When photometry mode is employed, the effective exposure times of individual frames at 24 μm are either 10 s or 30 s, and 10 s at 70 μm. For some of the fields for which we obtained data from GTO or Legacy programs, the data were taken in ScanMap mode, where the telescope constantly scans along one direction while the scan mirror compensates and freezes images on the data arrays. In these cases, the effective integration time per frame at both 24 μm and 70 μm is smaller, either 3 s or 10 s, and the data are less sensitive overall due to the properties of the MIPS detectors for small frame times.

3.4.1 24 μm Data Processing

For all of the imaged SMG fields except the HDF/GOODS-N field, we began reduction of the 24 μm MIPS data with the BCD images produced by version 14.4.0 (v14.4) of the SSC's MIPS Data Reduction Pipeline. We have excluded from all processing the first frame in each imaging sequence (those with DCENUM=0) since these frames have a shorter exposure time than the rest and response that is depressed by 10–15%.

Table 3.4. Data Sources for 24μm MIPS Imaging of SMGs

Field Name	Center R.A.[a] (J2000.0)	Center Dec.[a] (J2000.0)	PID	PI	Field Size[b] arcmin × arcmin	Median t_{int}[c] sec	3σ depth [d] μJy
CFRS–03h	03 02 34.2	+00 09 09	3473	A. Blain	12.7 × 13.3	1308	93
Lockman	10 52 15.0	+57 21 44	81	G. Rieke	22.1 × 13.6	1771	84
			1077	H. Dole			
			142	C. Lonsdale			
HDF-N/GOODS-N	12 36 54.9	+62 14 19	169	M. Dickinson	18.8 × 13.4	29757	66
CFRS–14h	14 17 44.0	+52 30 25	8	G. Fazio	9.7 × 8.6	681	109
ELAIS–N2	16 36 47.1	+40 59 32	183	C. Lonsdale	17.6 × 16.5	154	143
SSA–22	22 18 07.4	+00 17 33	3473	A. Blain	10.8 × 11.5	1227	100
	22 17 30.3	+00 13 48	64	G. Fazio	7.5 × 8.2	542	131

Note. — Units of right ascension are hours, minutes, and seconds. Units of declination are degrees, arcminutes, and arcseconds.

[a]Coordinates of center of combined MIPS 24μm mosaic.

[b]Size of combined mosaic.

[c]Median integration time per pixel in combined mosaic.

[d]Median 3σ point source sensitivity in combined mosaic.

Table 3.5. Data Sources for 70μm MIPS Imaging of SMGs

Field Name	Center R.A.[a] (J2000.0)	Center Dec.[a] (J2000.0)	PID	PI	Field Size[b] arcmin × arcmin	Median t_{int}[c] (sec)	Median 3σ Depth[d] (mJy)
CFRS–03h	03 02 34.6	+00 08 50	3473	A. Blain	13.3 × 7.8	195	10.9
Lockman	10 52 14.7	+57 21 38	81	G. Rieke	17.4 × 11.2	970	4.6
			1077	H. Dole			
			142	C. Lonsdale			
HDF-N/GOODS-N	12 38 59.1	+62 34 36	3325	D. Frayer	10.0 × 10.0	10600	1.5
			81	H. Dole	85.0 × 27.2	600	6.3
CFRS–14h	14 17 37.1	+52 28 06	8	G. Fazio	13.0 × 7.5	303	7.4
ELAIS–N2	16 36 48.1	+40 58 53	183	C. Lonsdale	14.1 × 13.8	74	8.8
SSA–22	22 18 07.8	+00 17 20	3473	A. Blain	10.9 × 6.2	215	11.8
	22 17 31.1	+00 13 30	64	G. Fazio	7.6 × 2.7	653	7.8

Note. — Units of right ascension are hours, minutes, and seconds. Units of declination are degrees, arcminutes, and arcseconds.

[a]Coordinates of center of combined MIPS 70μm mosaic.

[b]Size of combined mosaic.

[c]Median integration time per pixel for combined mosaic.

[d]Median 3σ point source sensitivity for combined mosaic.

Pipeline v14.4 processing includes data linearization, removal of time-dependent responsivity variations, dark subtraction, flat-fielding to remove pixel-to-pixel gain variations and stimulator flash illumination patterns, flagging of pixels affected by cosmic rays and saturation, and flux calibration to units of $\mathrm{MJy\,sr^{-1}}$ (Gordon et al. 2005). However, image artifacts, such as long-term latent images from previous observations of bright sources and residual gradients at the few percent level due to imperfect flat-field corrections (which depend on the instrument's scan mirror position), persist in the 24 μm BCDs and add noise, complicating the detection of faint sources (Fadda et al. 2006). To mitigate the effects of such artifacts and improve the sensitivity of the BCD images, we applied the self-calibration procedure described in the MIPS Data Handbook, v. 3.2.1. In this process, for each Astronomical Observing Request (AOR) a normalized median of all the images, excluding very bright pixels, is constructed from primary array BCDs (PRIMEARR=1). The individual BCDs in that AOR are subsequently divided by this normalized median image.

The median-calibrated primary array BCD images from all AORs available for a given SMG field were next combined into a single 24 μm mosaic using the MOPEX software package. In a similar procedure to that used to create the mosaics of IRAC BCD images, we created a common coordinate and geometric grid for all of the BCD frames of a field and then equalized the background in overlapping frames. Unlike the mosaicking for the IRAC images, however, the 24 μm BCDs did not require drizzling since the PSF is nearly Nyquist-sampled. Thus, we interpolated them into the common grid with a simple bi-linear method, correcting the individual images for optical distortion. Deviant pixels (e.g., due to cosmic ray hits or bad array pixels) were identified and masked with the same method as used for the IRAC mosaics. The interpolated science images and uncertainty images were finally co-added and combined into a single science mosaic and a single uncertainty mosaic, again weighting pixels by exposure time. The final mosaics have $1\farcs275$ pixels. In Table 3.4 we list the centers of the combined mosaics and median effective integration time per pixel.

For the GOODS-N field, the already-reduced and mosaicked 24 μm images were downloaded from the GOODS-N *Spitzer* Legacy Project's website. The processing of this data is described in Chary et al. (in preparation). The final mosaic has $1\farcs2$ pixels, and its astrometry has been tied to the HST/ACS images of the GOODS-N field through the IRAC data of the same field.

3.4.2 24 μm Source Extraction

The high source density at 24 μm in deep images (Papovich et al. 2004) combined with the large point response function (PRF)[7] of MIPS (full width at half maximum [FWHM] = 5.″9 at 24 μm) causes significant source blending, especially as the image depth increases. Also, a significant fraction of a point source's flux at 24 μm ($\sim 50\%$) is found in the Airy rings. As a result, reliable photometry measurements require flux profile fitting for each source. We used the APEX package included within MOPEX in single-frame mode to perform source detection and extraction through PRF fitting for all of the 24 μm mosaics of the SMG fields, including GOODS-N.

An empirical PRF for each mosaic was created in a multi-step, iterative process, modified from that described in Fadda et al. (2006). In the first step, a theoretical PRF generated from STinyTim, the *Spitzer* version of the PSF modeling program TinyTim developed for HST, was used with a high detection threshold to extract several tens of bright, relatively uncrowded point sources (no neighbors within 20″) from which a preliminary empirical PRF was subsequently constructed. Next, this preliminary PRF was used to subtract the first bright Airy ring (at a radius of ~ 9 pixels) around the brightest sources (S/N ≥ 15) in the mosaic image, since this ring caused false detections to be made at low flux levels around bright sources. Point source detection to detect all sources was then carried out using the ringless mosaic image and a much lower detection threshold than first used. Following this step, we add an additional step to the PRF estimation process not used in Fadda et al. (2006): the empirical PRF was refined by improving the profile determination at large radii, an important step since significant flux is contained in the diffraction rings. We subtracted all neighbors found in the full detection list within 36″ of the bright sources used for PRF estimation from the original mosaic image using the empirical PRF. A new, improved PRF was then estimated from the bright, isolated sources in the neighbor-subtracted image. This final version of the PRF was normalized to the flux contained within 12 mosaic pixels (15.″3).

We used the new PRF in the fitting and extraction of all point sources from the original image with S/N > 3 which were detected in the ringless image. Finally, an aperture correction of 1.153 was applied to the extracted fluxes to account for the normalization of the PRF flux within a 15″ radius. This aperture correction was derived by Fadda et al.

[7] A PRF is a derivative of the PSF: the PRF is the convolution of the PSF with the pixel response function of the detector.

(2006) from a curve-of-growth analysis of a bright star in the 24 μm mosaic from the *Spitzer* First Look Survey (FLS) and is likely to be approximately correct for our dataset as the image processing, mosaicking, and source extraction procedures are very similar.

For several sources in the GOODS-N field, our source extraction method could not converge and failed to extract blended sources. For these sources, we use the fluxes from the GOODS-N 24 μm source catalog (Chary et al., in preparation) if they were available. The sources for which we used the fluxes in the GOODS-N catalog are SMM J123600.15+621047.2, SMM J123606.72+621550.7, SMM J123632.61+620800.1, and SMM J123634.51+621241.0.

The absolute source fluxes measured in our source extraction process are likely to be accurate to better than 10% for bright sources (S/N $>$ 20), including the uncertainty in the absolute flux calibration (4%; Engelbracht et al. 2007) and uncertainties in the extraction process and aperture correction. For fainter sources (5 $<$ S/N $<$ 10) there is likely an additional systematic $\sim 10 - 15\%$ uncertainty in the flux measurements introduced by the extraction procedure (Fadda et al. 2006). At low S/N levels, extracted sources are biased toward higher fluxes since they are preferentially detected by APEX if they lie above positive fluctuations in the background noise. We do not include in any flux uncertainty estimates the possible errors due to non-negligible color corrections needed for sources with SEDs that are not of the form $\nu F_\nu = constant$ (the form of SED assumed for *Spitzer* flux calibration). For a power-law SED at 24 μm, such corrections would be less than 4%; however, for high-redshift sources, redshifted emission and absorption features passing into the 24 μm band (e.g., mid-IR PAH features) cause the color corrections to vary dramatically with redshift and mid-IR spectrum. Consequently, we have chosen not to apply systematic color corrections to the catalogs of sources extracted at 24 μm.

The absolute positions of extracted 24 μm sources are expected to be accurate to within 2$''$. Because we did not perform pointing refinement on the 24 μm mosaics (excepting the GOODS-N mosaic, which was aligned to the VLA reference frame by Chary et al.) due to a lack of a significant number of bright 2MASS point source counterparts at 24 μm, the uncertainties in the source positions are dominated by the blind pointing uncertainty of MIPS at 24 μm ($1\sigma = 1\farcs2$). Fadda et al. (2006) show through extractions of simulated sources that a component of uncertainty resulting from the extraction process, which is dependent on S/N, also becomes important for sources with S/N $<$ 10. This extraction error, due to difficulty in centering the PRF for faint objects occupying relatively few pixels,

can be as much as $\sim 1''$ for sources with S/N < 7 and becomes negligible for S/N > 20 (Fadda et al. 2006). Thus, position uncertainties for bright sources should be better than the stated $2''$, while $2''$ is generous enough to account for errors in the positions of low S/N sources.

3.4.3 70 μm Data Processing

Processing of the 70 μm MIPS data for all SMG fields followed the procedures described in Frayer et al. (2006a). Similarly to the 24 μm MIPS data processing, the first frame in all data collection sequences (those with DCENUM=0) has been excluded from processing due to depressed response in this first frame. The basic data reduction pipeline run by the SSC calculates the slope of the data ramps in each pixel, rejecting cosmic rays and correcting nonlinearities, and calibrates the slope image by performing dark subtraction, flat-fielding, and absolute flux calibration. However, image artifacts due to residual background drifts over time and latent images from internal stimulator flashes remain in the 70 μm BCD images after pipeline processing. To mitigate these artifacts, the SSC pipeline filters the 70 μm BCDs in the spatial and time domains, by which the sky background is also subtracted. While this filtering improves the sensitivity of 70 μm BCDs by as much as a factor of 2, information is lost about the extended background in an image, so filtered images are only appropriate for analysis of point sources (Frayer et al. 2006a).

Because none of the SMG fields contain bright or extended sources at 70 μm, we began our reduction of all fields except the GOODS-N field with the filtered 70 μm BCD images produced by v14.4 of the SSC MIPS Data Pipeline. The filtered BCDs for the primary array (PRIMEARR=1) were next combined into a single image mosaic for each SMG field using MOPEX. The individual filtered BCD frames were corrected for distortion and interpolated to a common sky grid in a similar way to the 24 μm images. Bad array pixels were identified through temporal filtering only and masked prior to image co-addition. All of the 70 μm image mosaics have square pixels of size $4''$. The centers, sizes, and median 3σ point source depths of the 70 μm mosaics are listed in Table 3.5. The 70 μm mosaics tend to cover less area on the sky than the 24 μm mosaics, and thus fewer SMGs have imaging available at 70 μm.

The reduced 70 μm mosaic of the GOODS-N field was provided by D. Frayer. A description of the data and reduction for this field can be found in Frayer et al. (2006b). The

inner $10' \times 10'$ area of this field has significantly deeper data than the rest of the image (exposure time of 10.6 ks versus 600 s), and most of the radio-detected SMGs are located within the deep area.

3.4.4 70 μm Source Extraction

Frayer et al. (2006a) find that fitting a PRF to 70 μm sources to obtain flux measurements provides more reliable results than aperture photometry, especially for faint sources. Since the K-correction at 70 μm is positive for high-redshift, cool sources, and only 2 SMGs have yet been detected at 70 μm (Huynh et al. 2007), we expect SMGs to be faint if detected at all in our sample of 70 μm images. Thus, we used flux profile fitting techniques to detect and extract fluxes for 70 μm sources in the mosaics of the SMG fields, even though the source density in the 70 μm images is significantly lower than in the 24 μm images. We performed PRF fitting on the 70 μm images of all the SMG fields, including the GOODS-N field, using APEX. However, due to a lack of bright sources in the images, we could not construct a PRF from them. Instead, we used an empirical PRF constructed by Frayer et al. (2006a) from 70 μm point sources detected in the *Spitzer* Extragalactic First Look Survey (xFLS) to extract all S/N > 3 sources in the SMG fields. The resulting flux densities were multiplied by a color correction factor of 1.09, the factor appropriate for converting from a constant νF_ν SED to a power law SED $F_\nu \propto \nu^{-\alpha}$, where $\alpha \sim 0 - 2$, which is the typical range of slopes for galaxies.

The absolute source fluxes extracted in the above procedure are expected to be accurate to $\sim 10\%$, including the uncertainty in the absolute flux conversion factor (7%; Gordon et al. 2007) and uncertainties in color corrections. The absolute positions of detected sources are expected to have an accuracy of $\sim 4''$, including the blind pointing uncertainty of MIPS at 70 μm ($1\farcs7$; MIPS Data Handbook) and uncertainty in the positions of low S/N extracted sources ($\sim 3''$; Frayer et al. 2006a).

3.5 Results of MIPS Imaging of SMGs

3.5.1 Identification of SMG Counterparts at 24 μm and 70 μm

As mentioned in § 3.3.1, the sample of radio-detected SMGs in C05 has a typical radio position uncertainty of $0\farcs5$, which is smaller than the position uncertainty of the MIPS

sources ($\sim 2''$ and $\sim 4''$ at 24 and 70 μm, respectively). Accordingly, to pick out MIPS counterparts for the C05 sample, we used a search radius of size equal to the positional uncertainty at the wavelength in question, $2''$ at 24 μm and $4''$ at 70 μm. In 4 cases (SMM J123618.33+621550.5, SMM J123621.27+621708.4, SMM J123707.21+621408.1, and SMM J123712.05+621212.3) a position error of up to $4''$ was permitted at 24 μm to account for centroiding differences, because the 24 μm counterpart clearly covered the radio position.

3.5.2 Source Blending and SMG Detection in 24 μm Images

Due to the large PRF of MIPS at 24 μm, we caution that the detection of a 24 μm source at the radio SMG position does not conclusively indicate an association with the submm source. The $\sim 6''$ FWHM of a 24 μm point source is sufficiently large that in cases where the submm sources have ambiguous radio or optical counterparts, or nearby neighbors, the counterparts can be blended at 24 μm, and thus it becomes hard to verify that the SMG is responsible for the 24 μm source or even to separate the contributions of the different objects to the total 24 μm flux. There are several objects in the C05 sample with near neighbors in high resolution images (optical, IRAC, or radio), and some of these SMGS are either known to be significantly blended or suspected to be blended with other sources at 24 μm: SMM J105200.22+572420.2, SMM J105207.49+571904.0, SMM J123553.26+621337.7, SMM J123606.85+621021.4, SMM J123616.15+621513.7, SMM J123621.27+621708.4, SMM J123629.13+621045.8, and SMM J123707.21+621408.1 (see Appendix A for notes on individual sources). For the blended sources from the GOODS-N field, we have either taken the source fluxes from Pope et al. (2006), if available, or from the 24 μm source catalog of Chary et al. (in preparation) for the GOODS-N field. The 24 μm measurements in the GOODS-N field from both Pope et al. (2006) and Chary et al. were made using the GOODS-N IRAC source catalog as input to de-blend 24 μm sources and produce estimates of the 24 μm flux for individual IRAC sources. However, we caution that the de-blended flux estimates for these sources have larger uncertainties than formally calculated, considering that neither the redshift nor the mid-IR SED for the components were used to separate the contributions from the blended sources. For the blended SMGs in the Lockman field, SMM J105200.22+572420.2 and SMM J105207.49+571904.0, estimates of the fluxes of components of blended sources have been made in a similar way to those in the GOODS-N field by Egami et al. (2004), and we use these fluxes here with the same note of caution regarding

the uncertainties as mentioned for the sources in the GOODS-N field.

3.5.3 Characteristics of SMGs in 24 μm and 70 μm Images

Of the 58 SMGs in the C05 sample with imaging available at 24 μm, 40 are detected at $> 3\sigma$ significance (69%). In Figure 3.8 we show $20'' \times 20''$ postage stamp 24 μm images centered at the SMG radio positions for all SMGs with imaging coverage at that wavelength. In all cases when a 24 μm counterpart is detected, only one source is located within the search radius, and that source is always point-like. For the majority of the SMGs detected at 24 μm, the 24 μm counterparts are located within $1''$ of the radio position.

At 70 μm, a much smaller fraction of the C05 SMG sample is detected, 4 out of 58 with imaging. In Figure 3.9, $64'' \times 64''$ 70 μm postage stamp images are shown for only the SMGs detected at 70 μm. Again, the 70 μm counterparts appear as point sources.

3.5.4 MIPS Flux Measurements for Chapman SMGs

In Table 3.6 we present the positions and flux measurements for the counterparts of the C05 SMGs at 24 μm and 70 μm. The stated errors for each object detected at each wavelength include the $\sim 10\%$ absolute calibration uncertainty estimate. For non-detections at 24 μm we list a 3σ upper limit on the point-source flux, which is calculated using the equation

$$\sigma = \mathrm{RMS}_{\mathrm{local}} \times N, \tag{3.2}$$

where $\mathrm{RMS}_{\mathrm{local}}$ is the RMS per pixel in a 20×20-pixel box centered on the radio position of the SMG in units of $\mu\mathrm{Jy\,pixel}^{-1}$, and N is the theoretical number of noise pixels in the 24 μm mosaic. Similarly, for SMGs not detected at 70 μm, we list the 3σ upper limit on point-source flux as an upper limit. To calculate the 70 μm point-source flux upper limit, we use the empirical determination of the conversion factor between point-source noise and pixel surface brightness noise for $4''$ pixels from Frayer et al. (2006b) and the local RMS per pixel for each object in a box centered on the radio position of the SMG:

$$\sigma = \mathrm{RMS}_{\mathrm{local}} \times 10.9\,\mathrm{mJy}\,(\mathrm{MJy\,sr}^{-1})^{-1}. \tag{3.3}$$

In the cases in which we have SMGs in common with the samples of Pope et al. (2006)

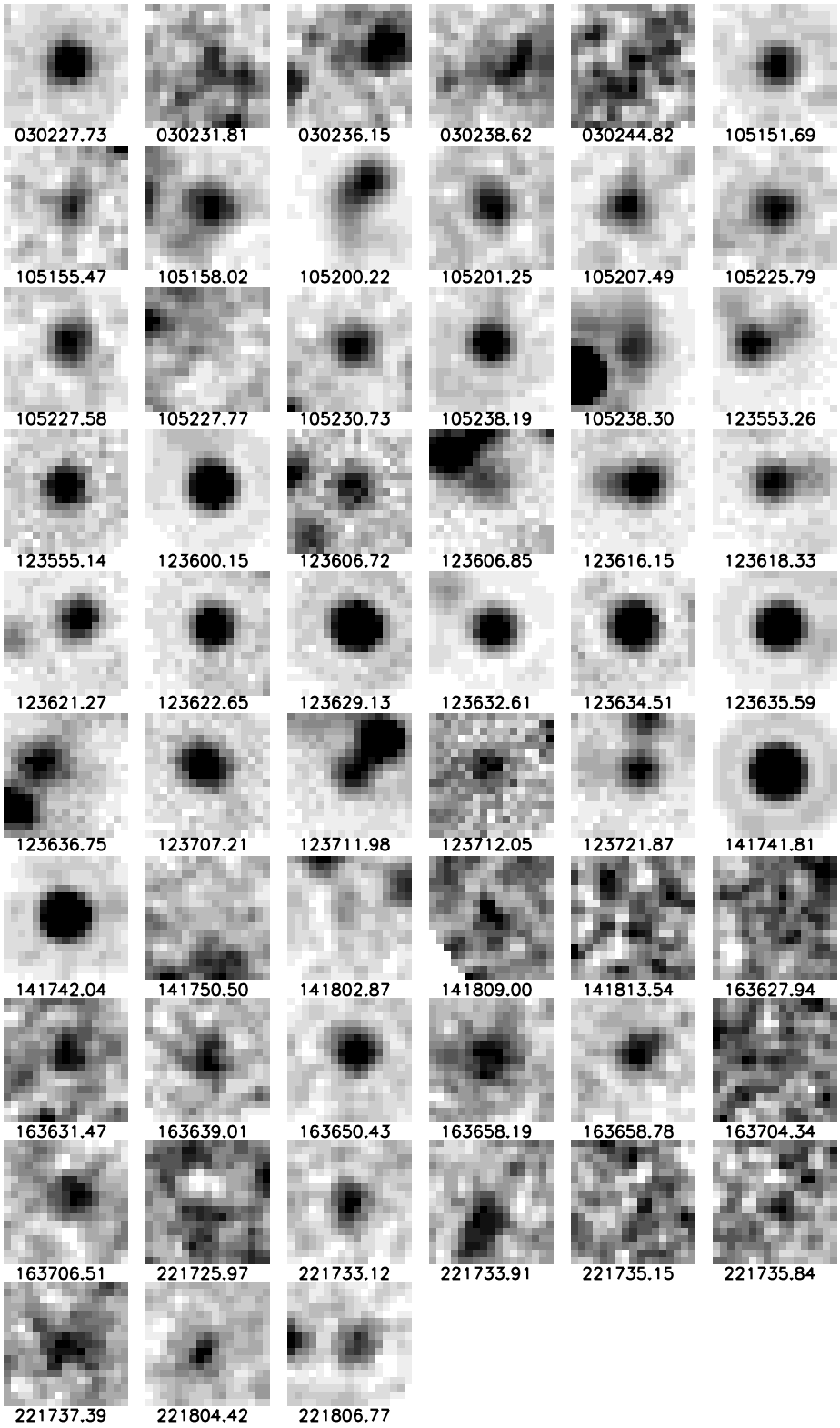

Figure 3.8 24 μm postage stamp images of SMGs, centered at the radio position published in C05. Each image is $20'' \times 20''$ in size. North is up, east is to the left.

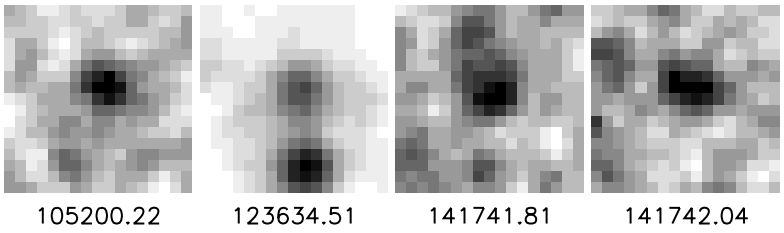

Figure 3.9 70 μm postage stamp images of SMGs, centered at the radio position published in C05. Each image is $64'' \times 64''$ in size. North is up, east is to the right.

(7), Egami et al. (2004) (4), and Ivison et al. (2004) (3), which are detected at 24 μm, we have compared our flux measurements to those of the other authors. We find that our flux measurements agree to within 10% with those of Pope et al. (2006) (usually better than 10%) and to within 12% with those of Egami et al. (2004) and Ivison et al. (2004) with the exception of one source, SMM J105155.47+572312.7, which is of low S/N. However, the separate measurements of this SMG agree within the stated errors. At 70 μm, we have one source in common with Huynh et al. (2007), SMM J123634.51+621241.0, for which our measurements are identical.

Table 3.6: MIPS 24 μm and 70 μm Results for Chapman et al. (2005) SMG Sample

Chapman et al. (2005) ID	z_{spec}	24μm R.A. (J2000.0)	24μm Dec. (J2000.0)	70μm R.A. (J2000.0)	70μm Dec. (J2000.0)	$S_{24\mu m}$ (μJy)	$S_{70\mu m}$ (mJy)
SMM J030226.17+000624.5[c]	0.080	03 02 26.15	+00 06 23.8	03 02 26.02	+00 06 27.1	2224.5 ± 114.2	30.1 ± 7.5
SMM J030227.73+000653.5	1.408	03 02 27.74	+00 06 53.5	···	···	498.9 ± 33.1	< 13.6
SMM J030231.81+001031.3	1.316	···	···	···	···	< 110.7	< 14.8
SMM J030236.15+000817.1	2.435	···	···	···	···	< 78.2	< 10.0
SMM J030238.62+001106.3	0.276	···	···	···	···	< 107.5	< 12.7
SMM J030244.82+000632.3	0.176	···	···	···	···	< 83.7	< 10.4
SMM J105151.69+572636.0	1.147	10 51 51.67	+57 26 35.7	···	···	342.4 ± 24.0	< 4.2
SMM J105155.47+572312.7	2.686	10 51 55.45	+57 23 12.8	···	···	99.0 ± 15.9	< 3.6
SMM J105158.02+571800.2	2.239	10 51 58.08	+57 18 00.2	···	···	241.1 ± 21.1	< 4.1
SMM J105200.22+572420.2[a,b]	0.689	···	···	10 52 00.16	+57 24 22.7	< 65.1	6.2 ± 1.3
SMM J105201.25+572445.7	2.148	10 52 01.27	+57 24 45.9	···	···	172.5 ± 16.3	< 3.7
SMM J105207.49+571904.0	2.689	10 52 07.63	+57 19 04.4	···	···	190.9 ± 14.8	< 3.2
SMM J105225.79+571906.4	2.372	10 52 25.81	+57 19 06.2	···	···	178.6 ± 14.4	< 3.2
SMM J105227.77+572218.2	1.956	···	···	···	···	< 63.9	< 4.1
SMM J105227.58+572512.4	2.142	10 52 27.60	+57 25 12.8	···	···	226.3 ± 17.4	< 4.5
SMM J105230.73+572209.5	2.611	10 52 30.72	+57 22 09.3	···	···	184.2 ± 17.9	< 4.1
SMM J105238.19+571651.1	1.852	10 52 38.21	+57 16 51.3	···	···	498.3 ± 29.6	< 3.9
SMM J105238.30+572435.8	3.036	10 52 38.43	+57 24 36.5	···	···	335.6 ± 19.4	< 6.4
SMM J123549.44+621536.8	2.203	12 35 49.38	+62 15 36.8	···	···	178.7 ± 31.4	< 4.1
SMM J123553.26+621337.7[a]	2.098	···	···	···	···	< 70.9	< 2.1
SMM J123555.14+620901.7	1.875	12 35 55.21	+62 09 01.4	···	···	333.5 ± 22.2	< 2.0
SMM J123600.10+620253.5	2.710	···	···	···	···	···	< 5.5
SMM J123600.15+621047.2	1.994	12 36 00.18	+62 10 47.3	···	···	1270.8 ± 64.0	< 3.8

Table 3.6 – Continued

Chapman et al. (2005) ID	z_{spec}	24μm R.A. (J2000.0)	24μm Dec. (J2000.0)	70μm R.A. (J2000.0)	70μm Dec. (J2000.0)	$S_{24\mu m}$ (μJy)	$S_{70\mu m}$ (mJy)
SMM J123606.72+621550.7	2.416	12 36 06.73	+62 15 50.6	···	···	124.0 ± 8.6	< 3.2
SMM J123606.85+621021.4[a]	2.509	···	···	···	···	< 113.5	< 3.9
SMM J123616.15+621513.7	2.578	12 36 16.18	+62 15 14.6	···	···	319.1 ± 17.8	< 2.0
SMM J123618.33+621550.5	1.865	12 36 18.57	+62 15 50.1	···	···	343.8 ± 18.8	< 3.6
SMM J123621.27+621708.4	1.988	12 36 21.10	+62 17 09.5	···	···	346.5 ± 20.6	< 2.2
SMM J123622.65+621629.7	2.466	12 36 22.68	+62 16 29.9	···	···	368.5 ± 20.7	< 2.7
SMM J123629.13+621045.8	1.013	12 36 29.07	+62 10 45.7	···	···	664.8 ± 34.2	< 1.8
SMM J123632.61+620800.1	1.993	12 36 32.60	+62 07 59.7	···	···	849.0 ± 43.3	< 2.4
SMM J123634.51+621241.0	1.219	12 36 34.51	+62 12 41.0	12 36 34.71	+62 12 40.5	464.6 ± 23.8	13.9 ± 2.1
SMM J123635.59+621424.1	2.005	12 36 35.57	+62 14 24.2	···	···	1445.1 ± 72.8	< 2.8
SMM J123636.75+621156.1[a]	0.557	···	···	···	···	< 127.8	< 5.3
SMM J123651.76+621221.3[c]	0.298	12 36 51.72	+62 12 20.8	···	···	107.0 ± 9.9	< 1.6
SMM J123707.21+621408.1	2.484	12 37 07.40	+62 14 09.0	···	···	232.8 ± 15.1	< 1.6
SMM J123711.98+621325.7	1.992	12 37 12.04	+62 13 25.6	···	···	250.7 ± 15.2	< 1.5
SMM J123712.05+621212.3	2.914	12 37 12.23	+62 12 12.1	···	···	31.0 ± 8.2	< 1.5
SMM J123716.01+620323.3	2.037	···	···	···	···	···	< 6.0
SMM J123721.87+621035.3	0.979	12 37 21.88	+62 10 35.5	···	···	245.6 ± 15.9	< 3.0
SMM J141742.04+523025.7	0.661	14 17 42.08	+52 30 25.3	14 17 42.10	+52 30 29.0	1090.1 ± 56.8	16.9 ± 4.0
SMM J141741.81+522823.0	1.150	14 17 41.84	+52 28 23.0	14 17 41.67	+52 28 23.1	5741.6 ± 288.5	18.7 ± 3.5
SMM J141809.00+522803.8	2.712	···	···	···	···	< 142.0	< 13.4
SMM J141802.87+523011.1	2.127	···	···	···	···	< 93.2	< 6.9
SMM J141750.50+523101.0	2.128	···	···	···	···	< 88.8	< 6.7
SMM J141813.54+522923.4	3.484	···	···	···	···	< 169.0	< 9.0
SMM J163627.94+405811.2	3.180	···	···	···	···	< 123.8	< 6.7
SMM J163631.47+405546.9	2.283	16 36 31.49	+40 55 47.7	···	···	240.2 ± 41.5	< 9.4

Table 3.6 – Continued

Chapman et al. (2005) ID	z_{spec}	24μm R.A. (J2000.0)	24μm Dec. (J2000.0)	70μm R.A. (J2000.0)	70μm Dec. (J2000.0)	$S_{24\mu m}$ (μJy)	$S_{70\mu m}$ (mJy)
SMM J163639.01+405635.9	1.495	16 36 39.06	+40 56 35.2	···	···	321.4 ± 38.6	< 7.8
SMM J163650.43+405734.5	2.378	16 36 50.42	+40 57 34.8	···	···	886.5 ± 58.8	< 9.1
SMM J163658.19+410523.8	2.454	16 36 58.21	+41 05 24.3	···	···	343.5 ± 46.8	< 7.9
SMM J163658.78+405728.1	1.190	16 36 58.77	+40 57 28.1	···	···	463.0 ± 42.0	< 6.0
SMM J163704.34+410530.3	0.840	···	···	···	···	< 174.7	< 11.6
SMM J163706.51+405313.8	2.374	16 37 06.43	+40 53 14.9	···	···	390.3 ± 50.7	< 9.5
SMM J221724.69+001242.1[c]	0.510	22 17 24.74	+00 12 41.0	···	···	618.1 ± 45.0	···
SMM J221733.12+001120.2	0.652	22 17 33.19	+00 11 19.1	···	···	516.9 ± 45.6	< 10.9
SMM J221804.42+002154.4	2.517	22 18 04.48	+00 21 52.5	···	···	346.7 ± 38.8	< 23.8
SMM J221806.77+001245.7	3.623	22 18 06.74	+00 12 45.3	···	···	475.2 ± 44.0	< 18.5
SMM J221735.84+001558.9	3.089	···	···	···	···	< 132.8	···
SMM J221735.15+001537.2	3.098	···	···	···	···	< 112.1	···
SMM J221733.91+001352.1	2.864	···	···	···	···	< 98.1	< 6.2
SMM J221725.97+001238.9	3.094	···	···	···	···	< 113.9	< 6.3
SMM J221733.02+000906.0	0.926	···	···	···	···	···	···
SMM J221737.39+001025.1	2.614	···	···	···	···	< 176.7	< 12.1

Units of right ascension are hours, minutes, and seconds. Units of declination are degrees, arcminutes, and arcseconds.

[a] This object is likely detected at 24 μm but is blended with another nearby source.

[b] The 70 μm source may be blended with a nearby source.

[c] This object was identified by Chapman et al. (2005) as a low-z lens unassociated with the submillimeter source. It has been excluded from the analysis presented here.

3.6 Summary

We have presented near- and mid-IR observations of radio-detected SMGs in the sample of Chapman et al. (2005) obtained with the IRAC and MIPS instruments on board the *Spitzer Space Telescope*. We detect over 90% of the SMG sample at 3.6 and 4.5 μm and $\sim$ 80% of the sample at 5.8 and 8.0 μm, bands which sample the rest-frame near-IR emission from SMGs. Typical flux densities of SMGs detected in the IRAC bands range from $\sim$ a few to 100 μJy. We detect $\sim$ 70% of our SMG sample with MIPS at 24 μm, obtaining typical flux densities of several hundred μJy. The detection fraction of our SMG sample at 70 μm is much lower than in the IRAC and 24 μm bands, with only 7% detected.

Acknowledgments We wish to thank R. Chary, M. Salvato, and D. Frayer for their very helpful advice in reducing IRAC and MIPS data and D. Frayer for providing the unpublished 70 μm image mosaic of the GOODS-N field. The *Spitzer Space Telescope* is operated by the Jet Propulsion Laboratory at the California Institute of Technology, under contract with NASA.

Chapter 4

The Infrared Spectral Energy Distributions and Luminosities of Submillimeter-Selected Galaxies

In order to determine the contribution of submillimeter-selected galaxies (SMGs) to the star formation history of the universe, it is vital to know the typical infrared (IR) luminosity ($L_{\rm IR}$) of the population. As mentioned in Chapter 1, the 850 μm detections of SMGs, combined with their observed faintness at optical wavelengths, imply that the majority of the bolometric luminosity of these objects is emitted in the rest-frame far-IR wavebands. However, in the past the sensitivity of far-IR instruments (e.g., the *Infrared Astronomical Satellite* [*IRAS*], the *Infrared Space Observatory* [*ISO*]) has not been nearly sufficient to detect objects with far-IR fluxes similar to that predicted for SMGs based on models of thermal dust emission ($\sim$ a few to tens of mJy), so we have not been able to verify the prediction. The *Herschel Space Telescope*, with a 3.5-m aperture, imaging instruments observing bands centered at 75, 160, 250, 350, and 500 μm, and spectrometers covering the same range of wavelength will be capable of observing sources as faint as 3–5 mJy in only one hour, and will fill in crucial gaps in our knowledge of the far-IR spectral energy distributions (SEDs) of SMGs. Until then, however, we must rely on other means to estimate the IR luminosity of SMGs and other high-redshift galaxies.

Thus far, the IR luminosities of SMGs have most frequently been inferred using 850 μm flux measurements and SED templates appropriate for local ultraluminous IR galaxies (ULIRGs; Chapman et al. 2005; Pope et al. 2006; Huynh et al. 2007) or by applying the correlation between far-IR emission and radio emission observed in local galaxies (e.g., Condon 1992) to radio-detected SMGs. Chapman et al. (2005) find a median IR luminosity of

$8.5 \times 10^{12}\,L_{\odot}$ for their sample of 73 SMGs with spectroscopic redshifts, whereas Pope et al. (2006) find a median of $L_{\rm IR} = 6.0 \times 10^{12}\,L_{\odot}$ for the SMGs in the GOODS-N field using a different set of SED templates. The accuracy of such estimates hinges on the assumption that the IR spectral shape of SMGs, which is determined by the properties of the emitting dust such as temperature and emissivity, is the same as that of ULIRGs. However, small changes in characteristic dust temperature (T_d) for a given emissivity can change the luminosity estimate significantly because $L \propto T^{4+\beta}$ (e.g., Blain 2002; Blain et al. 2003); thus, if local ULIRGs have systematically different characteristic dust temperatures than high-z SMGs, SMG luminosity estimates based on ULIRG templates will be systematically in error. Indeed, recent studies (e.g., Chapman et al. 2005; Kovács et al. 2006; Pope et al. 2006; Huynh et al. 2007) suggest that, in reality, SMGs at $z > 1$ are cooler than local ULIRGs.

Yet, the lack of IR data for SMGs precludes detailed comparison between the IR SEDs of SMGs and ULIRGs besides hindering direct estimates of SMG luminosity. Specifically, observations at the peak and on the Wien side of the peak of the IR SED are required for SMGs. Kovács et al. (2006) used 350 μm observations of 21 SMGs from the SHARC-II instrument at the Caltech Submillimeter Observatory (CSO) to constrain the far-IR SED peak and make the first direct estimate of dust temperatures in this class of objects, finding an average dust temperature of 35 ± 3 K, which is the typical value for IR-luminous sources at high redshifts inferred from fits to $z < 1$ galaxy number counts from *IRAS* and *ISO*. Adding mid-IR data to the set of SED constraints is still necessary, however: Frayer et al. (2004) find that measurements with the *Spitzer Space Telescope* at 24 and 70 μm are sensitive to hot dust emission in high-z objects and may help separate the contributions to the total IR luminosity of dust heated by a central active galactic nucleus (AGN) and dust heated by star formation in addition to constraining the total IR luminosity.

In this chapter we analyze deep *Spitzer* imaging of the radio-selected SMG sample of Chapman et al. (2005) at 24 and 70 μm. With this data, which fill in important gaps in the IR SEDs of SMGs, we calculate revised estimates of $L_{\rm IR}$ and characteristic dust temperature for the radio-selected SMGs. We then use our new luminosity estimates to constrain the $L - T_d$ relation and the far-IR–radio correlation for SMGs. The outline of the chapter is as follows. In §4.1 we discuss the models which we use to derive IR luminosities and dust temperatures for all of the galaxies and present revised estimates of these quantities

for our SMG sample. In §4.2 we investigate the effects of our new $L_{\rm IR}$ estimates on the $L_{\rm IR}-T_d$ relation for IR-luminous galaxies and its implications for submm-radio photometric redshifts for submm sources. In §4.3 we present a composite SED of all the objects in our sample and examine its features, attempting to determine if SMGs consist of a uniform population of galaxies which can be described by a single SED. Finally, in §4.4 we discuss the implications for the far-IR–radio correlation in SMGs from our new results.

4.1 IR Luminosities of Radio-Detected SMGs

By using the *Spitzer*-MIPS fluxes measured for the C05 sample of radio-detected SMGs with spectroscopic redshifts presented in Chapter 3, we can now place constraints on the Wien side of the IR SED peak for these objects and estimate the IR luminosity and characteristic dust temperature T_d with improved accuracy over the estimates published for this same sample in C05. Despite the limited information provided by 24 μm observations in high-z galaxies due to mid-IR spectral features, and having only upper limits for most SMGs at 70 μm, such measurements are still extremely valuable to constrain the mid-IR slope of the SED since they can rule out both very hot dust temperatures and very cold dust temperatures. The availability of the spectroscopic redshifts for this sample of SMGs is also vital in the determination of luminosities and dust temperature because the effects of changing T_d for an SED are degenerate with the effects of changing z (Blain et al. 2002), and changes in $L_{\rm IR}$ are very sensitive to changes in T_d. Knowing the redshift accurately *a priori*, we eliminate this degeneracy and can constrain the characteristic dust temperature to within several degrees Kelvin. In this section we first describe the model we use to estimate the IR luminosities of SMGs, followed by a discussion of the results of our SED modeling, and finally we compare our IR luminosity estimates to those estimated from mid-IR data only.

4.1.1 SED Model Used to Derive $L_{\rm IR}$

To derive the integrated IR luminosity of a high-redshift galaxy, one must approximate its IR SED and then integrate over it. The far-IR SED of any galaxy is likely to result from a complicated mixture of many different emitting components with distinct temperatures, masses, and geometries. However, the number of data points available to constrain the

far-IR SED for any single galaxy is small; thus, the capability to constrain complex models of dust emission does not exist. Accordingly, it is preferable to fit SED models with as few free parameters as possible. There are a variety of models in the literature from which to choose, including semi-empirical SED templates derived from observations and models of low redshift IR-luminous galaxies (e.g., Chary & Elbaz 2001; Dale & Helou 2002), multi-temperature radiative transfer models (e.g., Efstathiou et al. 2000; Siebenmorgen & Krügel 2007), two-temperature modified blackbody models (Dunne & Eales 2001), and single-temperature graybody models (e.g., Blain 1999a; Dunne et al. 2000; Kovács et al. 2006). Our preference is to not use templates based on low-redshift galaxies, however; the spread in mid-IR spectral slopes for local ULIRGS is at least a factor of 50 (Armus et al. 2007), and thus using templates based on these galaxies leads to significant uncertainty when applied to high-z sources.

We prefer instead to use the simplest model that will adequately fit the data since we have few points to constrain the model (usually 3–4 detections), and thus choose to fit the single-temperature, optically thin graybody models with power-law Wien tails used by Blain (1999a) and Blain et al. (2003). In this model, the Rayleigh-Jeans side of the SED peak is modeled as a blackbody of a single temperature T_d, modified by a frequency-dependent emissivity term:

$$S(\nu, T_d) = \epsilon_\nu \, B(\nu, T_d) \propto \nu^\beta \, B(\nu, T_d). \tag{4.1}$$

We approximate the full emissivity term $[1 - \exp(\nu/\nu_0)^\beta]$ as ν^β for the optically thin limit $\nu_{obs} \ll \nu_0$, since on the Rayleigh-Jeans side of the spectrum we are far from the frequency at which the optical depth increases significantly. On the Wien side of the IR SED peak we describe the SED as a power law, where

$$S(\nu) \propto \nu^{-\alpha}. \tag{4.2}$$

The substitution of the Planck function with a power law at higher frequencies is necessary to match the observed near-IR SEDs of local galaxies, which do not show an exponential drop similar to the Planck function behavior at mid-IR wavelengths (e.g., see Blain et al. 2003). The power law and graybody function are joined at the frequency ν' where the

logarithmic gradient of the long-wavelength SED steepens beyond α:

$$\frac{d \ln S(\nu')}{d \ln \nu'} = -\alpha. \tag{4.3}$$

Thus, three parameters describe the fitted SED model: T_d, α, and β. The temperature T_d describes the peak of the SED and provides a characteristic temperature for the dust population, α is the slope of the SED in the mid-IR and indicates the contribution of warm dust, and β is the power-law index of the SED in the Rayleigh-Jeans regime. Since T_d and β are highly correlated parameters in the SED fitting (Blain et al. 2003), we choose to use a fixed value $\beta = 1.5$ in our SED fitting and luminosity estimates, which is typical of dust in active star-forming galaxies in the local universe (Dunne et al. 2000), to reduce the size of the parameter space, .

To place the most constraints on the IR SED and thus derive the most accurate $L_{\rm IR}$ values possible for the SMG sample of C05, we have compiled data for the sample at mid-IR through radio wavelengths. *Spitzer*-IRAC data has been excluded from the analysis since, at the high redshifts typical of SMGs, the IRAC bands are primarily detecting stellar emission from the galaxies, which contributes only minimally to the total IR luminosity in these objects (see Chapter 6). We combine the *Spitzer*-MIPS data with 850 μm and 1.4 GHz measurements from C05, 1100 μm and 1200 μm data on the SMGs in the Lockman Hole field from Laurent et al. (2006) and Greve et al. (2004b), respectively, 1200 μm data for the ELAIS–N2 field from Greve et al. (2004b), and 350 μm observations of 21 galaxies in the Chapman sample from Kovács et al. (2006). The 350 μm observations are especially important, as they are closest to the peak of the SMGs' IR SED, and those galaxies with 350 μm data will have the most accurate $L_{\rm IR}$.

4.1.2 Results of SED Fitting: $L_{\rm IR}$ Results for SMGs in the C05 Sample

We fit the model described above to all mid-IR to radio data and compute IR luminosities for the SMGs in the sample of C05 for which we have observations in both of the *Spitzer*-MIPS bands, or which have detections at 350 μm if the MIPS information is missing, a total of 55 objects. Our IR luminosity is generally defined as the integral under the best-fit SED model from rest-frame 1 μm to 1 mm. In Table 4.1 we list the IR luminosity and best-fit values of T_d and α for each SMG analyzed. In Figure 4.1 we show the fits to the SEDs of

the SMGs for which 350 μm data are available. It is clear in the SED plots that the 350 μm data point is nearly always close to the peak of the SED, and is thus extremely important.

4.1.2.1 IR Luminosities

The median value of $L_{\rm IR}$ we find for our radio-selected SMG sample is $L_{\rm IR} = 5.4 \times 10^{12}\,L_{\odot}$ with an inter-quartile range of $6.9 \times 10^{12}\,L_{\odot}$, confirming that most of the radio-detected SMGs are highly luminous. Our median result is nearly 40% lower than the median for the sample found by C05 ($8.5 \times 10^{12}\,L_{\odot}$), who obtain $L_{\rm IR}$ using the templates of Dale & Helou (2002) and the local far-IR–radio correlation. However, some of the SMGs included in the median by C05 are not included in the current sample. When we re-calculate the median $L_{\rm IR}$ of C05, leaving out the galaxies lacking MIPS data for which we have not, in the current study, calculated $L_{\rm IR}$, we obtain $L_{\rm IR} = 8.1 \times 10^{12}\,L_{\odot}$; thus, the source of the discrepancy is not the difference in samples. There is no noticeable trend of luminosity difference with redshift between our new estimates and those of C05, either. We do employ a slightly different definition of $L_{\rm IR}$ from C05, though since we integrate over a greater range of wavelength one would expect our values of $L_{\rm IR}$ to be slightly higher. Our revised median $L_{\rm IR}$ is also slightly lower than, but consistent with, Pope et al. (2006), who fit modified Chary & Elbaz (2001) templates to 24 μm, 850 μm, and 1.4 GHz data and find a median $L_{\rm IR}$ of $6.7 \times 10^{12}\,L_{\odot}$. Our new typical $L_{\rm IR}$ is also consistent with Kovács et al. (2006), who fit graybody models similar to ours, though without the Wien tail, and obtain a median $L_{\rm FIR}$ of $4.7 \times 10^{12}\,L_{\odot}$. Comparing on a galaxy-to-galaxy basis, we find that, on average, our $L_{\rm IR}$ estimates are systematically lower than C05 by 22%, but systematically higher than those of Kovács et al. (2006) by 52%. However, Kovács et al. (2006) explicitly calculate $L_{\rm FIR}$ since the SED model they use decreases very steeply on the Wien side of the SED peak, which could explain some of the difference. Kovács et al. (2006) suggest that the IR luminosities calculated by C05 are overestimated by a factor of 2. Our results indicate, as well, that the estimates of C05 are too high, but only by $\sim 30\%$.

C05 use their sample of radio-detected SMGs with spectroscopic redshifts to calculate the bolometric luminosity density of the population of radio-detected SMGs and estimate the contribution these galaxies make to the evolution of the cosmic star formation rate density (SFRD) with redshift. They find that the evolution of the luminosity density of the

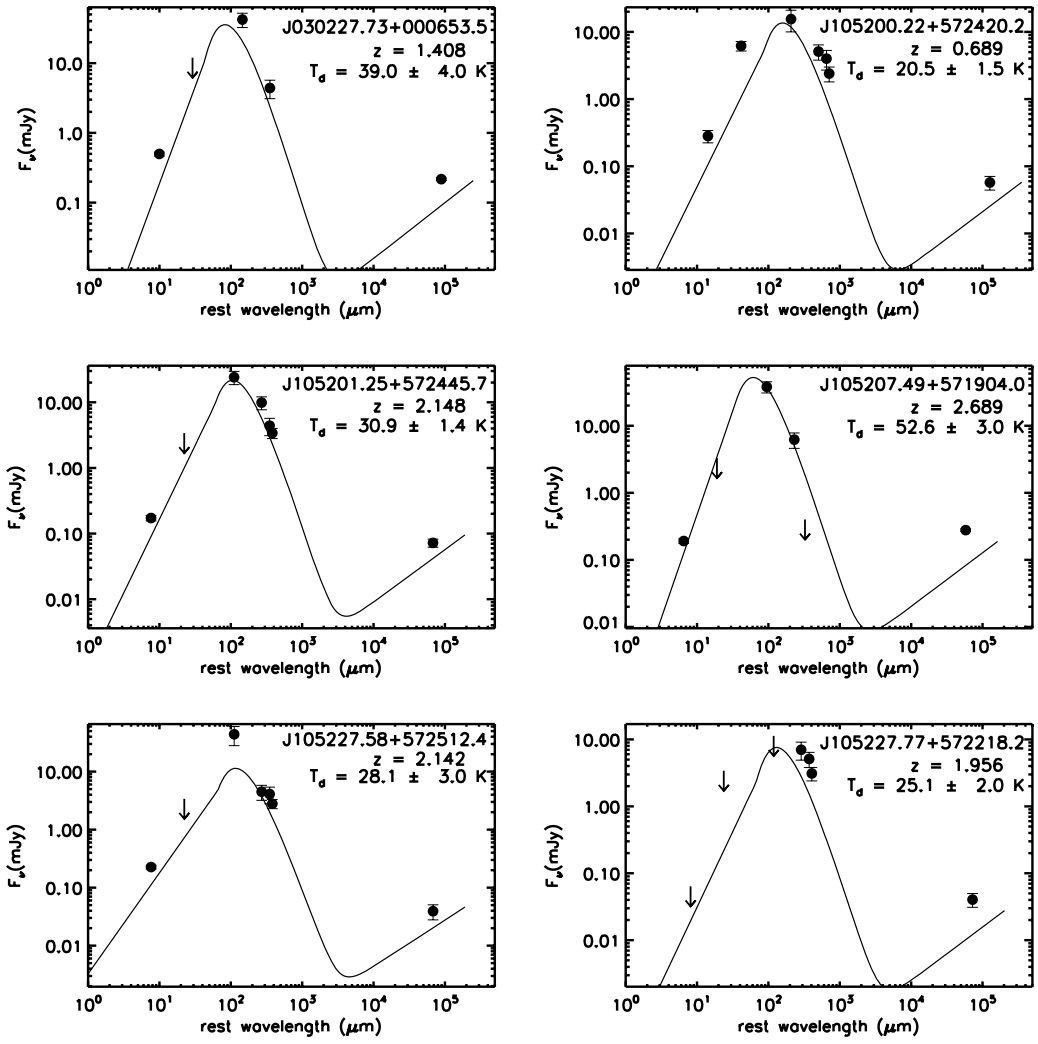

Figure 4.1 IR SED fits to Radio-Detected SMGs with 350 μm data from Kovács et al. (2006). Filled circles indicate detections, downward pointing arrows indicate upper limits. The solid line represents the best-fit graybody SED.

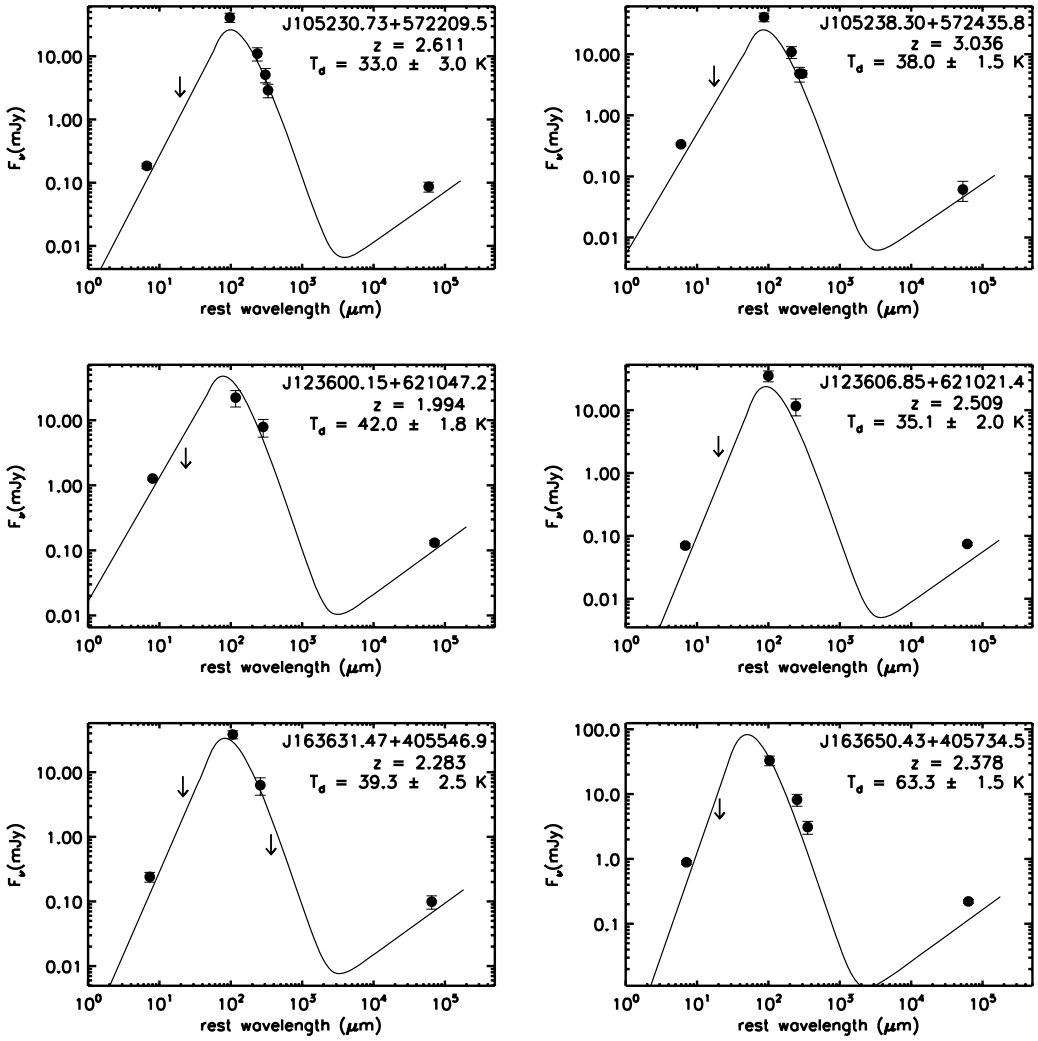

Figure 4.2 IR SED fits to Radio-Detected SMGs with 350 μm data from Kovács et al. (2006). Continued from Figure 4.1.

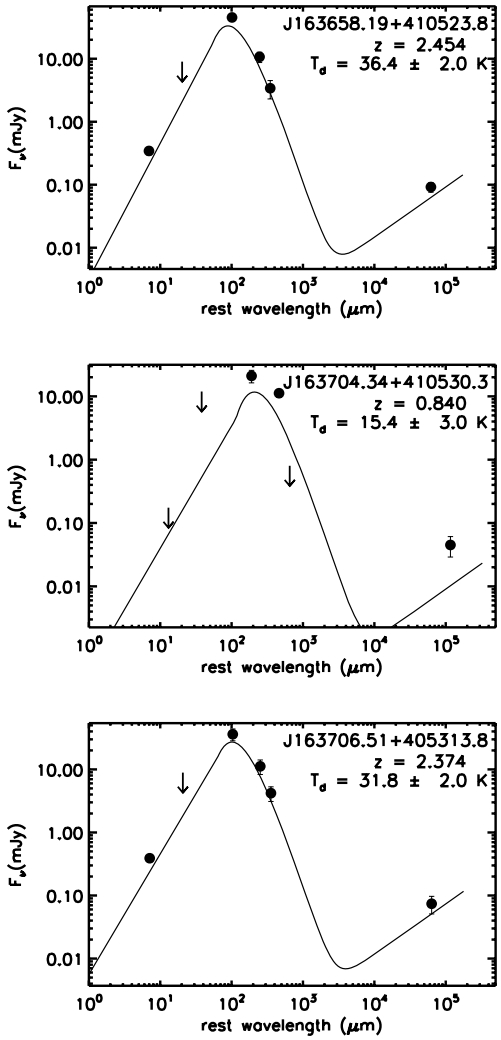

Figure 4.3 IR SED fits to Radio-Detected SMGs with 350 μm data from Kovács et al. (2006). Continued from Figures 4.1 and 4.2.

SMGs is similar to that of quasars but not UV-selected high-z galaxies, and estimate that SMGs contribute $\sim 0.05\,M_{\odot}\,\mathrm{yr}^{-1}\,\mathrm{Mpc}^{-3}$ at $z \sim 2$, suggesting that SMGs are the dominant sources of star formation activity in the Universe at $z \sim 2-3$. However, to arrive at this conclusion, C05 must make several assumptions: (1) they estimate that 30% of the total IR luminosity of SMGs arises from AGN activity; (2) the radio-undetected SMGs have a redshift distribution that significantly overlaps with that of the radio-detected sources; and (3) submm sources below their survey's flux limit have the same redshift distribution as found in their observations and contribute nearly two-thirds of the total luminosity density of all high-z submm sources. Since we find that the IR luminosities calculated by C05 are likely overestimated by $\sim$ 30%, with no trend in redshift, the total luminosity density of SMGs will be similarly 30% lower at each redshift. This adjustment is not large enough, though, to significantly lessen the estimated contribution of SMGs to the cosmic SFRD in light of the assumptions made to derive it. Nor will our current findings significantly alter the shape of the IR luminosity function of SMGs derived by C05 if the central locations of the luminosity function bins are shifted to values 30% lower.

4.1.2.2 Characteristic Dust Temperatures

The median T_d resulting from our SED fits to the radio-detected SMGs in the C05 sample is 33 K with inter-quartile range 12 K, while the mean and standard deviation for the sample are 35 ± 12 K. Our result is consistent with the result of Kovács et al. (2006), who obtain a mean T_d of 35 ± 3 K. Yet, Pope et al. (2006) obtain a cooler typical T_d for their sample of SMGs with spectroscopic redshifts, which comes from the best-fit template SED model to the composite SED of their sample.

In Figure 4.4 we compare the distribution of T_d we find for our sample of radio-detected SMGs from our new SED model fits to the distributions of T_d for galaxies with $L_{\mathrm{IR}} < 10^{11}\,L_{\odot}$ from the IRAS Bright Galaxy Sample in the sample of Dunne et al. (2000, denoted here as ordinary galaxies); galaxies with $10^{11}\,L_{\odot} < L_{\mathrm{IR}} < 10^{12}\,L_{\odot}$ (LIRGs) also from Dunne et al. (2000); and galaxies with $L_{\mathrm{IR}} > 10^{12}\,L_{\odot}$ (ULIRGs) from the sample of Stanford et al. (2000), in which the IRAS Faint Source Catalog was cross-correlated with sources from the Faint Images of the Radio Sky at Twenty Centimeter (FIRST) survey (Becker et al. 1995). All of the T_d values displayed in Figure 4.4, and L_{IR} values used to sort the samples have been calculated self-consistently, using our graybody SED model with a power-law substituted at

wavelengths shortward of the peak, to facilitate comparison. From Figure 4.4 it is apparent that the submm-selected objects are not a uniform population but rather a mix of low-redshift, very cold sources as well as high-redshift, very luminous sources with a range of dust temperatures. We have divided our SMG sample into two sub-samples and calculated separate T_d, one for SMGs with $L_{\rm IR} < 10^{12}\,L_\odot$ and the other with $L_{\rm IR} > 10^{12}\,L_\odot$. The range of T_d across the SMG sample is large, encompassing nearly all of the range spanned by the galaxies selected by IRAS. The lower-luminosity SMGs, usually in the low-redshift tail of the SMG z distribution, appear to have dust temperatures lower than the higher-luminosity SMGs. They also have lower T_d than is typical of the other infrared-selected samples shown, but similar to that of the Milky Way. The more luminous SMGs have a distribution of T_d which generally overlaps with the LIRGs and ordinary galaxies in the Dunne et al. (2000) sample as well as the cold end of the ULIRG distribution. However, the high-temperature tail of the luminous SMG distribution seems to extend through the higher-temperature end of the ULIRG distribution. This large range in T_d within the SMG sample suggests that the far-IR–radio correlation for SMGs will show intrinsic scatter between the colder and warmer sources, since their SEDs peak at different frequencies.

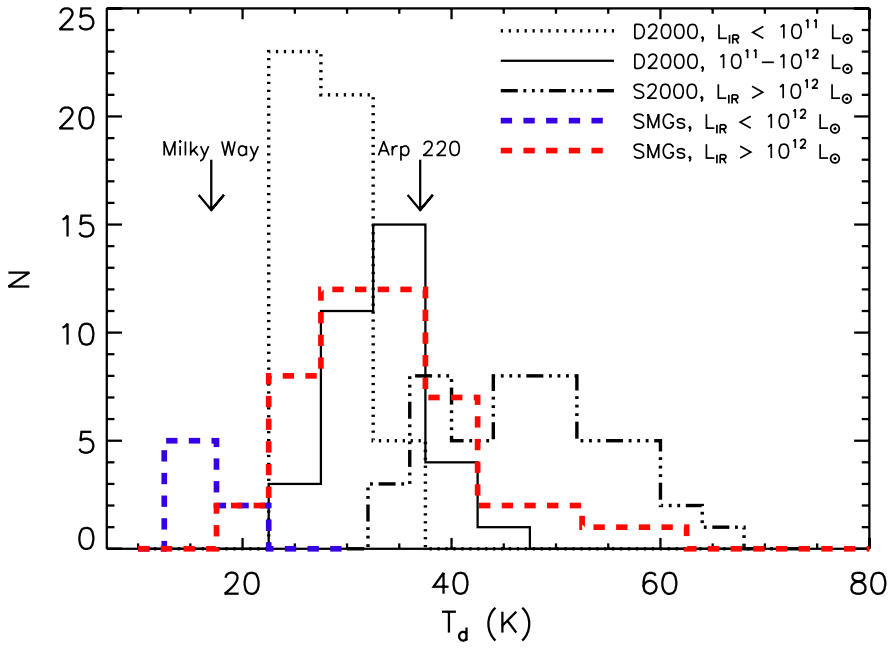

Figure 4.4 Comparison of the T_d distribution of SMGs with the T_d distributions of $L_{\rm IR} < 10^{12}\,L_\odot$ galaxies from Dunne et al. (2000) (D2000; dotted and solid black lines) and $L_{\rm IR} > 10^{12}\,L_\odot$ galaxies from Stanford et al. (2000) (S2000; dot-dashed black line). SMGs with $L_{\rm IR} < 10^{12}\,L_\odot$ are shown as the blue dotted line, while SMGs with $L_{\rm IR} > 10^{12}\,L_\odot$ are represented by the red dotted line. The temperatures for the samples of Dunne et al. (2000) and Stanford et al. (2000) have been derived using the same SED model as we have used for the SMGs.

Table 4.1: SED Fitting Results for Chapman et al. (2005) SMG Sample

Chapman et al. (2005) ID	T_d (K)	L_{IR} ($\times 10^{12}\,L_\odot$)	α
SMMJ030227.73+000653.5	39.0 ± 4.0	6.0 ± 0.5	2.8 ± 0.2
SMMJ030231.81+001031.3	23.6 ± 2.5	1.0 ± 0.2	2.3 ± 0.2
SMMJ030236.15+000817.1	40.4 ± 7.0	4.4 ± 1.7	2.6 ± 0.2
SMMJ030238.62+001106.3	24.5 ± 1.7	0.16 ± 0.02	4.5 ± 0.5
SMMJ030244.82+000632.3	19.2 ± 2.0	0.033 ± 0.005	3.9 ± 0.5
SMMJ105151.69+572636.0	27.1 ± 1.8	2.0 ± 0.2	2.4 ± 0.2
SMMJ105155.47+572312.7	32.2 ± 2.5	3.7 ± 0.6	2.3 ± 0.2
SMMJ105158.02+571800.2	37.5 ± 2.0	8.3 ± 0.5	2.4 ± 0.2
SMMJ105200.22+572420.2	20.1 ± 1.6	0.39 ± 0.05	2.0 ± 0.2
SMMJ105201.25+572445.7	30.9 ± 1.4	5.4 ± 0.5	2.2 ± 0.2
SMMJ105207.49+571904.0	52.6 ± 3.0	23 ± 4	3.1 ± 0.2
SMMJ105225.79+571906.4	51.0 ± 1.5	17 ± 2	3.2 ± 0.2
SMMJ105227.58+572512.4	28.1 ± 3.0	3.5 ± 0.8	1.8 ± 0.2
SMMJ105227.77+572218.2	25.1 ± 2.0	2.2 ± 0.2	2.3 ± 0.5
SMMJ105230.73+572209.5	33.0 ± 3.0	9.5 ± 1.0	2.2 ± 0.2
SMMJ105238.19+571651.1	32.7 ± 2.5	4.0 ± 0.3	1.8 ± 0.2
SMMJ105238.30+572435.8	36.6 ± 2.8	11 ± 1	2.1 ± 0.2
SMMJ123549.44+621536.8	31.5 ± 2.8	5.5 ± 0.3	2.2 ± 0.2
SMMJ123553.26+621337.7	28.4 ± 3.0	3.6 ± 0.5	2.5 ± 0.5
SMMJ123555.14+620901.7	41.4 ± 1.5	12 ± 2	2.9 ± 0.2
SMMJ123600.15+621047.2	42.0 ± 1.8	12 ± 1	1.9 ± 0.2
SMMJ123606.72+621550.7	27.5 ± 2.5	2.3 ± 0.2	1.8 ± 0.2
SMMJ123606.85+621021.4	31.6 ± 4.0	8.2 ± 0.6	2.0 ± 0.2
SMMJ123616.15+621513.7	30.4 ± 2.0	3.6 ± 0.4	1.8 ± 0.2
SMMJ123618.33+621550.5	37.9 ± 2.0	8.2 ± 0.6	2.5 ± 0.2
SMMJ123621.27+621708.4	37.3 ± 1.7	9.2 ± 0.6	2.5 ± 0.2
SMMJ123622.65+621629.7	35.3 ± 2.5	8.0 ± 0.6	1.9 ± 0.2
SMMJ123629.13+621045.8	23.8 ± 2.0	1.1 ± 0.1	1.8 ± 0.2
SMMJ123632.61+620800.1	35.4 ± 2.6	6.6 ± 0.5	1.7 ± 0.2
SMMJ123634.51+621241.0	42.8 ± 1.5	4.8 ± 0.5	3.2 ± 0.2
SMMJ123635.59+621424.1	35.4 ± 2.3	8.8 ± 0.3	1.4 ± 0.2
SMMJ123636.75+621156.1	16.1 ± 2.0	0.16 ± 0.03	2.3 ± 0.2
SMMJ123707.21+621408.1	35.4 ± 2.5	5.1 ± 0.4	1.9 ± 0.2
SMMJ123711.98+621325.7	32.9 ± 2.5	3.6 ± 0.4	2.0 ± 0.2
SMMJ123712.05+621212.3	26.5 ± 3.5	2.9 ± 0.4	2.2 ± 0.2
SMMJ123716.01+620323.3	40.5 ± 6.0	7.8 ± 1.5	2.5 ± 0.5
SMMJ123721.87+621035.3	16.1 ± 1.3	0.67 ± 0.08	1.9 ± 0.2
SMMJ141742.04+523025.7	32.2 ± 1.6	1.0 ± 0.1	2.5 ± 0.2

Table 4.1 – Continued

Chapman et al. (2005) ID	T_d (K)	L_{IR} ($\times 10^{12}\,L_\odot$)	α
SMMJ141741.81+522823.0	30.6 ± 5.0	5.7 ± 2.0	0.8 ± 0.1
SMMJ141750.50+523101.0	41.8 ± 17.0	4.3 ± 3.0	2.8 ± 0.5
SMMJ141802.87+523011.1	32.8 ± 8.0	2.4 ± 1.2	2.2 ± 0.5
SMMJ141809.00+522803.8	48.9 ± 10.0	11 ± 6	2.7 ± 0.5
SMMJ141813.54+522923.4	85.1 ± 12.0	74 ± 3	4.2 ± 0.5
SMMJ163627.94+405811.2	56.5 ± 12.0	27 ± 1	3.1 ± 0.5
SMMJ163631.47+405546.9	39.3 ± 2.5	9.8 ± 1.3	2.5 ± 0.2
SMMJ163639.01+405635.9	34.2 ± 2.0	4.6 ± 1.5	2.6 ± 0.1
SMMJ163650.43+405734.5	63.3 ± 1.5	49 ± 3	3.2 ± 0.2
SMMJ163658.19+410523.8	36.7 ± 3.0	10 ± 1.5	2.5 ± 0.2
SMMJ163658.78+405728.1	25.0 ± 1.9	1.4 ± 0.2	1.9 ± 0.1
SMMJ163704.34+410530.3	15.4 ± 3.0	0.40 ± 0.12	1.9 ± 0.2
SMMJ163706.51+405313.8	31.8 ± 2.0	8.0 ± 1.0	1.9 ± 0.2
SMMJ221733.12+001120.2	18.6 ± 1.3	0.41 ± 0.10	1.9 ± 0.1
SMMJ221737.39+001025.1	49.8 ± 4.5	18 ± 3	3.0 ± 0.2
SMMJ221804.42+002154.4	28.4 ± 1.5	6.0 ± 1.0	1.6 ± 0.1
SMMJ221806.77+001245.7	43.8 ± 3.4	21 ± 5	1.7 ± 0.2

4.1.3 Effects of Degeneracies in Model Parameters

Due to the degeneracy between the fitted SED parameters β and T_d, which arises because the location of the peak frequency of the SED scales as $\sim \beta/T_d$ (Blain et al. 2003), the differences in the distribution of T_d among SMGs and IRAS-selected galaxies seen in Figure 4.4 may not truly reflect the physical temperature distributions; rather, it reflects variation in overall SED shape. The variation in SED shape among the different galaxy types may be due to differences in temperature, but it could also be due to differences in the properties of the emitting dust grains. Hence, all discussions of temperature differences between populations should be regarded as tentative and thought of as differences in SED shape. In contrast, the parameter α in the SED model shows no significant degeneracy with T_d or β, and is thus well-determined (Blain et al. 2003).

Fortunately, the value of $L_{\rm IR}$ derived from the best-fit values of (T_d, β, α) found for each source and the frequency of the SED peak are not affected significantly as T_d and β are changed within their allowed parameter space, as shown by Blain et al. (2003). As a result, the interpretation of the values of $L_{\rm IR}$ we have calculated is straightforward.

4.1.4 Comparison to IR Luminosities Derived From Mid-IR Data

As SMGs are relatively bright in the far-IR and submm in comparison to high-z galaxies selected at optical and near-IR wavelengths, we have the luxury of being able to derive IR luminosities for SMGs from fitting SED models to submm data. However, at the current sensitivity and confusion limits of submm detectors ($\sim$ 2 mJy), most UV, optical, and near-IR selected galaxy samples have not been detected at those wavelengths (Chapman et al. 2000; Peacock et al. 2000; Webb et al. 2003; Knudsen et al. 2005; Dannerbauer et al. 2006). In local and $z < 1$ galaxies detected by *ISO*, Elbaz et al. (2002) find that the mid-IR luminosity of galaxies is well-correlated with total IR luminosity. Thus, with the improved mid-IR sensitivity of *Spitzer*, optically and near-IR selected galaxies have been detected at mid-IR wavelengths for the first time, and numerous authors (e.g., Reddy et al. 2006a; Daddi et al. 2007) have extrapolated the 24 μm fluxes to IR luminosities and finding agreement with estimates using data at other wavelengths. Marcillac et al. (2006) find that the rest-frame range 5–30 μm is a good tracer of total IR luminosity derived from the radio-far-IR correlation in a sample of galaxies detected by *ISO* at 15 μm and MIPS at 24 μm for galaxies at $z < 1.3$. Reddy et al. (2006a) find the $L_{5-8\mu{\rm m}}$ derived from MIPS 24 μm fluxes correlates with average X-ray luminosity derived from a stacking analysis of $z \sim 2$ optically-selected galaxies; thus, since X-ray luminosity is correlated with IR luminosity for local star-forming galaxies, Reddy et al. (2006a) infer that the mid-IR luminosity must also be correlated with total IR luminosity for optically selected galaxies at $z \sim 2$. However, since the luminosity of SMGs is dominated by far-IR emission, it is not entirely clear that the mid-IR luminosity is well-correlated with the total IR luminosity. In this section, we examine the results from extrapolation of 24 μm flux to $L_{\rm IR}$ for SMGs by comparing with our IR luminosities derived from fitting graybody models to the SEDs of SMGs.

One difficulty inherent in using the 24 μm flux as an indicator of total IR luminosity comes from the variation in mid-IR spectral line strengths between galaxies, possibly due to changes in the intensity of the UV radiation field (e.g., Dale et al. 2001), metallicity

(e.g., Engelbracht et al. 2005), or dust grain characteristics, which are redshifted into the 24 μm band for galaxies at $z \sim 1-3$ (e.g., see Figure 5.6). In an attempt to correct for these effects, we have K-corrected the MIPS 24 μm flux of our SMG sample to the 8 μm luminosity ($L_{8\mu\mathrm{m}}$), a wavelength which has little contamination from stellar light and at which the flux is dominated by dust emission. As a template to calculate K corrections, we have used the averaged mid-IR spectrum of the sample of 23 SMGs from Menéndez-Delmestre et al. (2007, in preparation), obtained with the Infrared Spectrograph (IRS) on *Spitzer*. While calculating K corrections from this composite spectrum will undoubtedly cause errors since the strength of the mid-IR spectral features varies between SMGs (see Menéndez-Delmestre et al. 2007; Valiante et al. 2007), we nonetheless feel that our method is preferable to using local galaxies as template spectra, whose similarity to the mid-IR spectrum of a particular SMG is poorly known. The composite SMG spectrum from IRS shows polycyclic aromatic hydrocarbon (PAH) emission features superposed on power-law continuum emission, so we predict that the most serious errors may arise for SMGs lacking PAH emission features in their mid-IR spectra.

After applying K corrections and calculating $L_{8\mu\mathrm{m}}$, we used the new empirical calibration of the conversion between 8 μm luminosity and total IR luminosity for galaxies from Caputi et al. (2007) to calculate $L_{\mathrm{IR},8\mu\mathrm{m}}$ for the SMGs:

$$L_{\mathrm{IR},8\mu\mathrm{m}}(L_{\odot}) = 1.91 \times \left[\frac{\nu L_{\nu}(8\mu\mathrm{m})}{L_{\odot}}\right]^{1.06}. \tag{4.4}$$

To illustrate the range in uncertainties in past calculations of L_{IR} from $L_{8\mu\mathrm{m}}$, we have also computed $L_{\mathrm{IR},8\mu\mathrm{m}}$ using the relation between $L_{8\mu\mathrm{m}}$ and total infrared luminosity derived from the luminosity-dependent templates of Chary & Elbaz (2001), which has often been used in the literature (e.g., Daddi et al. 2007):

$$\log\left(\frac{L_{\mathrm{IR},8\mu\mathrm{m}}}{L_{\odot}}\right) = 1.50 \times \log\left[\frac{\nu L_{\nu}(8\mu\mathrm{m})}{L_{\odot}}\right] - 4.31. \tag{4.5}$$

In Figure 4.5 we compare the L_{IR} we derive through our SED fits to the L_{IR} calculated from $L_{8\mu\mathrm{m}}$. The values of L_{IR} computed by the different methods diverge around $2 \times 10^{12}\,L_{\odot}$, at which point the scatter between points of similar luminosity as determined by the SED fitting method can be as much as an order of magnitude for the $L_{8\mu\mathrm{m}}$–L_{IR} conversions

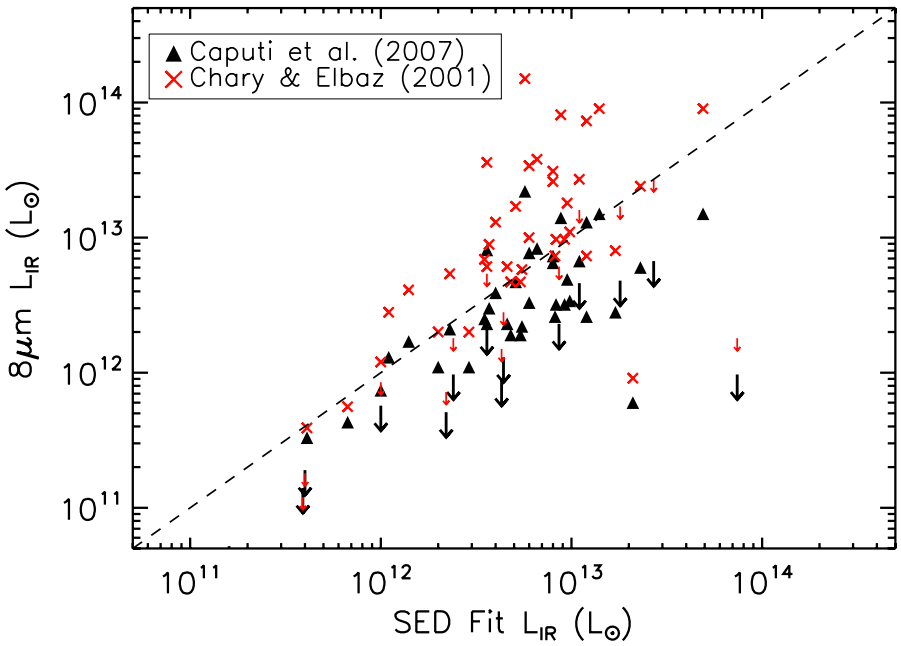

Figure 4.5 Comparison of $L_{\rm IR}$ derived from SED fits to $L_{\rm IR}$ derived from MIPS 24 μm flux for SMGs. Filled black triangles and red crosses represent galaxies with detections at 24 μm, while downward arrows represent galaxies with upper limits at 24 μm.

of both Caputi et al. (2007) and Chary & Elbaz (2001). The conversion of Caputi et al. (2007) gives slightly less scatter than the conversion of Chary & Elbaz (2001), though it systematically under-predicts the total IR luminosity; the conversion of Chary & Elbaz (2001) tends to over-predict $L_{\rm IR}$.

Dale et al. (2005) suggest that a factor of 10 should be taken as the minimum systematic uncertainty when $L_{\rm IR}$ is estimated from rest-frame 8 μm fluxes due to the variation in the ratio of 8 μm-to-total IR luminosity observed in the SEDs of local galaxies in the SINGS survey. The scatter produced when we compare $L_{\rm IR}$ derived from far and mid-IR SED fitting to $L_{\rm IR}$ extrapolated from 8 μm luminosity supports their argument. Some of the scatter may be due to error in the applied K corrections, so we estimate the range of errors possible in the K corrections. By using a range of mid-IR galaxy spectral templates, from quiescent galaxies to AGN, we find that the K corrections derived from the composite SMG spectrum are unlikely to be in error by more than a factor of 3. Thus, we suspect that much of the scatter in the values of $L_{\rm IR}$ predicted from mid-IR data is not arising from the K

corrections and, thus, that the mid-IR is simply not a good predictor of total IR flux. SED variation, as suggested by Dale et al. (2005), seems a likely explanation for why the $L_{\rm IR}$ predicted from the mid-IR disagrees with $L_{\rm IR}$ from SED fitting for SMGs but produces acceptable results for galaxies selected at other wavelengths. The total IR luminosity of SMGs is highly dependent on the characteristic dust temperature of a galaxy; however, for SMGs the 24 μm flux is not strongly correlated with T_d, possibly due to significant mid-IR spectral features. This could well be the root of the discrepancies.

Interestingly, Pope et al. (2006) find that total IR luminosities for SMGs predicted from MIPS 24 μm observations do not show significant disagreement with luminosities predicted from radio flux, 850 μm flux, and 24 μm flux with modified Chary & Elbaz (2001) SED templates, whereas we find that $L_{8\mu{\rm m}}$ frequently over-predicts $L_{\rm IR}$. However, our sample of SMGs with spectroscopic redshifts and new estimates of $L_{\rm IR}$ is approximately 3 times larger than that of Pope et al. (2006), and thus may include galaxies with a wider range of SED characteristics, which may explain our differing results.

4.2 Luminosity-Temperature Relation for Radio-Detected SMGs

The existence of a $L_{\rm IR}$-T_d relation for SMGs and the scatter within it highlights the intrinsic limits of our ability to estimate the redshift of a galaxy based on its submm-to-radio flux ratio (Blain et al. 2003). C05 find that radio-detected SMGs trace out a correlation between total IR luminosity and T_d; however, it is inconsistent with the local correlation for *IRAS* galaxies found by Chapman et al. (2003b). Using our new, improved determinations of $L_{\rm IR}$ and T_d for radio-detected SMGs, we can revise the $L_{\rm IR}$–T_d relation established for SMGs by C05 and reduce the observational scatter to get a better idea of the intrinsic scatter and thus the accuracy limit of submm-radio photometric redshifts for SMGs.

We show T_d versus $L_{\rm IR}$ for our sample of radio-detected SMGs with MIPS observations in Figure 4.6. We have also added to the plot the remaining radio-detected SMGs in the C05 sample for which MIPS data was not obtained, using the values of $L_{\rm IR}$ published in C05 lowered by 30% to reflect the average offset between our new values of $L_{\rm IR}$ and those of C05. For comparison, we over-plot T_d versus $L_{\rm IR}$ for the *IRAS*-selected sample of Dunne et al. (2000) and the faint *IRAS* sources selected at radio wavelengths from Stanford et al. (2000). As in the previous section, the values of T_d and $L_{\rm IR}$ for the Dunne et al.

(2000) and Stanford et al. (2000) samples have been derived using our SED model described earlier for consistency in comparison. In Figure 4.6 we see that our revised luminosity and temperature estimates for the radio-detected SMGs have not resulted in the SMG relation becoming consistent with that of the lower-redshift galaxy samples; rather, the separate $L_{\rm IR}$–T_d relations of the SMGs and lower redshift galaxies have become more apparent, and radio-detected SMGs are clearly more luminous in the IR at a given temperature, or, systematically cooler at a given luminosity. That the different galaxy samples lay in distinct parts of $L_{\rm IR}$–T_d plane can be attributed, in part, to the fact that the galaxies have been subject to different selection criteria, though true differences in the ISM conditions of the different samples may also be responsible (Blain et al. 2004a). Also, since T_d is not a truly physical temperature but rather a characterization of the peak of the IR SED, the different $L_{\rm IR}$–T_d relations imply significantly different SED characteristics between high-z SMGs and local galaxies.

The $L_{\rm IR}$–T_d relation for the radio-detected SMGs appears to be tight; however, both C05 and Blain et al. (2004a) propose that the shapes of the $L_{\rm IR}$–T_d relation for SMGs and galaxies selected at other wavelengths are determined more by their selection criteria than by similarity in properties within the samples. To illustrate this, on the figure we over-plot lines that show the effects of the selection at $850\,\mu$m and 1.4 GHz at redshifts of 0.5 and 2.5. Galaxies can be detected to the right of the line in each case; thus, in requiring a radio detection we will miss sources in the low-$L_{\rm IR}$ section of the plot, and the submm selection means that we tend to miss sources in the high-T_d, lower- $L_{\rm IR}$ portion of the plot. It is also interesting to note that for low redshift sources, we can in principle detect sources with both high $L_{\rm IR}$ and high T_d; yet, very few sources fall in this region. The galaxies from the Stanford et al. (2000) sample also indicate that such galaxies may be extremely rare.

In the context of submm-radio photometric redshifts, we point out that although the SMGs have a low formal scatter relative to a fitted $L_{\rm IR}$–T_d relation, from Figure 4.6 we see that the scatter in T_d for a given luminosity still spans ~ 10 K or more in the luminosity range $10^{12} - 10^{13}\,L_{\odot}$. This spread of a factor of ~ 1.4 implies that the highest accuracy possible in submm-radio photometric redshifts is $\Delta z \sim 1$ (Blain et al. 2003, 2004a) due to the temperature-redshift degeneracy. Thus, even with improved estimates of $L_{\rm IR}$ and T_d for SMGs from data with wider wavelength coverage than previously used, we are unable to support claims that the accuracy of submm-radio photometric redshifts is significantly

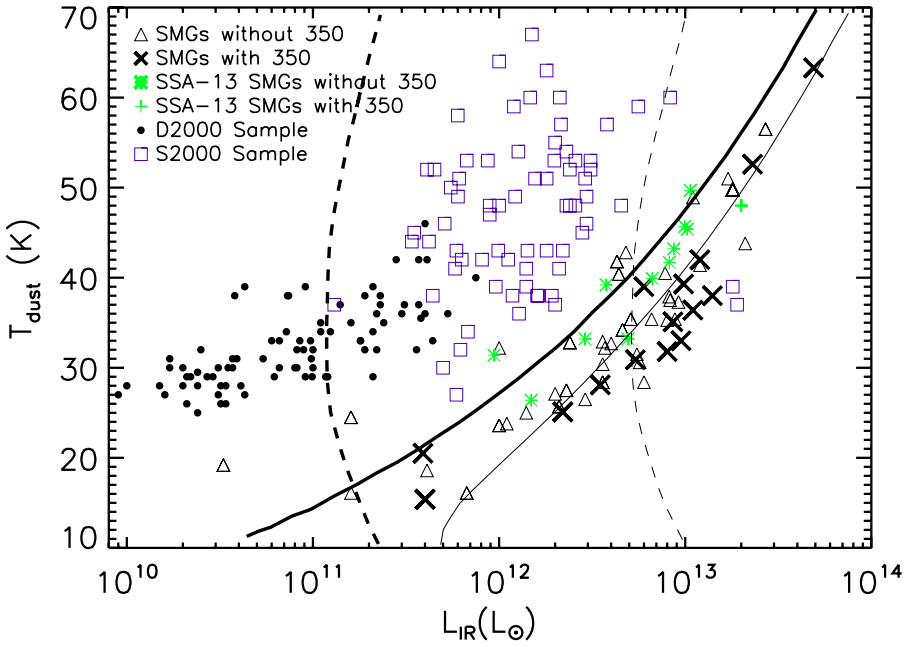

Figure 4.6 Characteristic dust temperature (T_d) versus IR luminosity for radio-detected SMGs. For comparison, the samples of local *IRAS*-selected galaxies of Dunne et al. (2000, D2000) and *IRAS*/radio-selected galaxies of Stanford et al. (2000, S2000) are over-plotted. The solid and dashed lines indicate the effects of the flux limits of the C05 survey at 850 μm (typically 5 mJy) and 1.4 GHz (faintest limit is $\sim 30\,\mu$Jy), respectively. The thicker solid and dashed lines represent limits for a galaxy at $z = 0.5$, while the thin solid and dashed lines represent limits for a galaxy at $z = 2.5$.

less than $\Delta z \sim 1$, in contrast to the recent study of Aretxaga et al. (2007), who find their photometric redshifts for SMGs in the SHADES survey have an accuracy of $\Delta z \simeq 0.2$. We note that we have not included the effects on the redshift uncertainty of using local IR-luminous galaxies as templates to derive submm-radio photometric redshifts in our discussion here; however, if SMGs are not well-represented by the templates of local galaxies, the accuracy of the photometric redshifts can be eroded further. The cumulative uncertainties in photometric redshifts for submm sources derived from far-IR, submm, mm, and radio data highlight the importance of obtaining spectroscopic redshifts for SMGs.

4.3 The IR Spectral Energy Distribution of Radio-Detected SMGs

Studies of the use of the far-IR/submm/radio spectral index, $\alpha_{1.4}^{850}$, as a redshift indicator for SMGs (e.g., Blain 1999b; Blain et al. 2003; Vlahakis et al. 2007) suggest that among the population significant SED variations exist. Since we have assembled the largest sample of mid-to-far IR measurements for radio-detected SMGs with accurate spectroscopic redshifts, we are in a unique position to examine their rest-frame IR SEDs. We can combine the data points for all of the SMGs, redshifted to their rest wavelength, on a single plot, and since the galaxies are spread in redshift, the points will fill in gaps in wavelength coverage that would appear in the SEDs of individual objects. In this way, one can examine the SED shape and determine if SMGs represent a homogeneous population. We can also compare the composite SED to local galaxies with well-measured SEDs. Egami et al. (2004) and Pope et al. (2006) have carried out similar analyses on small samples of SMGs with spectroscopic redshifts (3 and 9 objects, respectively) using IRAC 3.6–8.0 μm data, MIPS 24 μm data, SCUBA 850 μm data, and 1.4 GHz data. Egami et al. (2004), using photometric redshifts for the SMGs that lack spectroscopic data, find that 7 of their 10 SMGs have "cold" SEDs which are well-fit by the SED of Arp 220. Pope et al. (2006) find that high-z SMGs have different SED shapes from local galaxies of similar luminosity, tend to be cooler than low-redshift ULIRGs, and display variation in SED shape which causes scatter in the composite SED. Pope et al. (2006) also conclude that the 850 μm flux of SMGs is a good proxy for the far-IR luminosity of these objects. Using our 70 μm data, the 350 μm data from Kovács et al. (2006) and Laurent et al. (2006), plus the $\sim$ 1 mm data from Laurent et al. (2006) and

Greve et al. (2004b), in combination with IRAC, 24 μm, 850 μm, and 1.4 GHz measurements will give us a more complete picture of the SED shape of radio-detected SMGs than has been published previously.

We first plot the composite IR SED of our sample of SMGs in physical units in Figure 4.7, dividing the sample into three redshift bins: $z < 1.0$, $1.0 < z < 2.0$, and $z > 2.0$. Since the observed SEDs are dominated by the far-IR component and do not strongly resemble lower-luminosity star-forming galaxies nearby (e.g., Dale et al. 2005), we over-plot linear interpolations to the observed SEDs of local far-IR luminous galaxies frequently used as "cold" and "warm" ULIRG templates, Arp 220 and Mrk 231, respectively, for comparison. The data for Arp 220 and Mrk 231 have been taken from the NASA Extragalactic Database (NED)[1] and from the IRS spectra of Armus et al. (2007) and are interpolated only where there are data points; gaps indicate wavelength ranges where insufficient data are available. We show these interpolations of the SEDs of Arp 220 and Mrk 231 in Figure 4.8. In the composite SEDs in Figure 4.7, we omit the error bars on all of the SMG measurements for clarity, but note that for the majority of the points the error bars are the size of the points or smaller. The reason we have divided the galaxies into different redshift bins is immediately clear in Figure 4.7: there is a noticeable redshift dependence of SED shape. The SMGs in the $z < 1.0$ bin tend to be less luminous than Arp 220 and appear to be very cold, similar to low-z disk galaxies. The SMGs in the bin $1.0 < z < 2.0$ are more intermediate between Arp 220 and Mrk 231: they are more luminous than those in the lowest-z bin, and most are more luminous in the mid-IR than Arp 220 and do not display the heavy silicate absorption feature that Arp 220 shows. However, the SMG SED appears to peak longward of Arp 220 and Mrk 231. The SMGs in the highest redshift bin tend to be more luminous than the local template ULIRGs, but their SEDs may peak at similar wavelengths. The scatter in the mid-IR measurements and radio measurements is much larger than the scatter in the submm data points, perhaps reflecting a wide range in mid-IR and radio properties among these sources. In this redshift bin we see more SMGs appearing to be similar to Mrk 231 in the mid-IR.

In Figure 4.7 there are hints that there may be some luminosity dependence in the SED shape. To examine the SED shapes without luminosity dependence, we normalize the data points by the total IR luminosity in Figure 4.9. Significant SED shape variation across the

[1]The NED database can be found at http://nedwww.ipac.caltech.edu/.

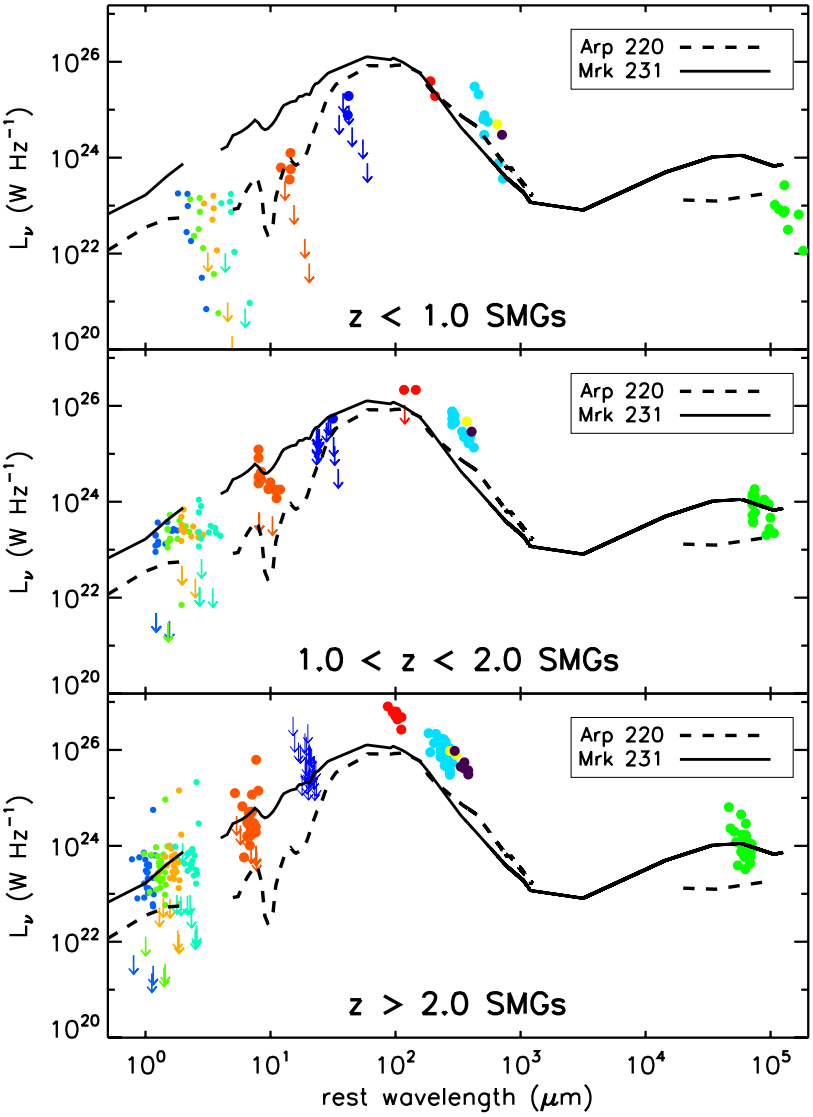

Figure 4.7 Composite IR SED for radio-detected SMGs in physical luminosity units, sorted into redshift bins $z < 1.0$ (top panel), $1.0 < z < 2.0$ (middle panel), and $z > 2.0$ (bottom panel) due to strong redshift dependence of SED shape. Data from different observed passbands are indicated in different colors or point sizes: small light blue, light green, light orange, and cyan points indicate IRAC data; large orange points are 24 μm data; large dark blue points represent 70 μm measurements; large red points are 350 μm data; large cyan points indicate 850 μm data; large yellow points represent 1100 μm data; large purple points are 1200 μm measurements; and large green points are 1.4 GHz data. Downward arrows indicate upper limits. The solid and dashed lines represent a linear interpolation to the observed SEDs of local "cold" and "warm" ULIRG template sources, Arp 220 and Mrk 231, respectively.

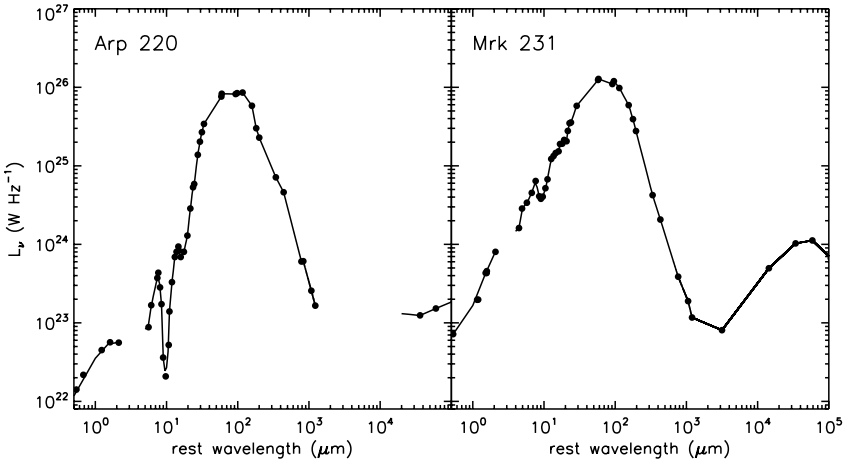

Figure 4.8 Interpolations to the SEDs of the local template ULIRGs Arp 220 and Mrk 231. Interpolation has only been performed in wavelength ranges where sufficient data exists to fairly represent the SED's appearance; blank regions indicate regions of insufficient data.

SMG class is apparent in the normalized composite SEDs, except at radio wavelengths. In all of the redshift bins, the scatter in the radio data points is significantly smaller when the SEDs are normalized by $L_{\rm IR}$, suggesting a correlation between IR and radio luminosity (see § 4.4). In the lowest redshift bin, the SEDs of the SMGs are clearly peaked longward of Arp 220 and are likely to be very cold. For some of these objects, we also see enhancement in the 24 μm point over that of Arp 220. In the $z = 1 - 2$ bin, the SMGs are clearly not as heavily absorbed around 10 μm as Arp 220 and seem to have some warm component in the observed 24 μm data point that not present in Arp 220. However, the SMGs do not seem to be as warm as Mrk 231. The galaxies in this redshift bin may also tend to have SEDs that peak at longer wavelengths than Arp 220, though it is difficult to tell due to the gap in wavelength coverage between the observed 70 μm and 350 μm points. In the highest redshift bin, the SED variation is quite large after luminosity is accounted for. In the mid-IR, data points scatter through an order of magnitude at the same redshift, as do the 350 μm points and the 850 μm points, perhaps reflecting a variety of dust conditions. The scatter at 850 μm is astonishingly large in all of the redshift bins, suggesting that the assertion of Pope et al. (2006) that the 850 μm flux is a good proxy for the total $L_{\rm IR}$ is incorrect. Instead, the radio luminosity appears to be a better indicator of $L_{\rm IR}$, at least for the radio-detected SMGs.

The effects of submm selection are very clear in the composite SEDs of SMGs shown here,

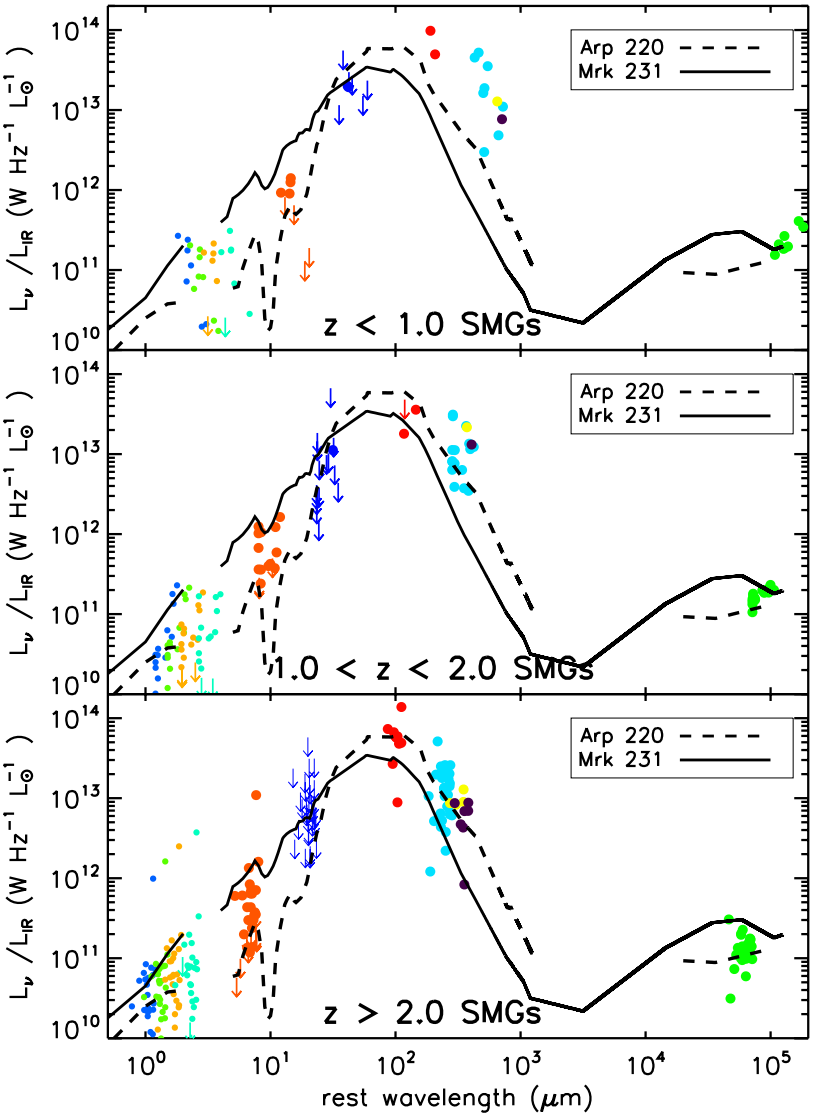

Figure 4.9 Composite IR SED for radio-detected SMGs, normalized to total $L_{\rm IR}$ and sorted into redshift bins as in Figure 4.7. Data points and line styles are the same as in Figure 4.7.

in that selection at submm wavelengths will detect very cold galaxies at lower redshifts and very luminous, but not as cold, galaxies at higher redshift. Selection effects aside, however, the composite SEDs presented here strongly indicate that SMGs are a "mixed bag" of objects. This is especially true within the $z > 2$ redshift bin, in which the scatter in the composite SED is large even after normalizing by total $L_{\rm IR}$, and when comparing the $z < 1$ bin and the $z > 2$ bin, as the SED shapes between these two bins are dramatically different.

Our findings here provide strong evidence that SMGs are not a uniform population and are certainly not well-described by a single SED template across all redshifts. It is also apparent that Arp 220 is not a good template for high-redshift SMGs due to its large silicate absorption, faintness in the mid-IR, and submm excess, nor is it a good template for low-z SMGs because of the location of the peak of its SED peak. In the mid-IR, high-z SMGs seem to fall somewhere between Arp 220 and Mrk 231, so neither galaxy would be a good template. For low-z SMGs, in which the SEDs appear to peak longward of the *IRAS* wavebands, it is likely that none of the *IRAS* galaxy-based templates are good approximations.

4.4 The IR-Radio Correlation for IR-Luminous Galaxies at High Redshift

A correlation between the far-IR emission and the radio emission of galaxies is well-established for local galaxies of all spectral types (e.g., Helou et al. 1985; Condon 1992; Yun et al. 2001). This correlation is nearly linear and extends over 5 orders of magnitude in $L_{\rm IR}$ for local galaxies (Yun et al. 2001). The physical processes causing the correlation are still unclear, but the standard explanation is that the correlation exists because both the far-IR emission and the radio emission from a galaxy are caused by high-mass stars: the far-IR emission arises from the stars' photons heating the dust, while the radio emission is synchrotron radiation from relativistic electrons in supernova remnants of high-mass stars.

This far-IR–radio correlation has been applied to estimate the luminosity of SMGs (e.g., C05) and, more recently, other populations of high-redshift galaxies (e.g., Daddi et al. 2007; Barger et al. 2007), since current technology permits observations of higher resolution and sensitivity at radio wavelengths with more ease than at far-IR and submm wavelengths. The far-IR–radio correlation has also been used to estimate redshifts for SMGs from the

submm-radio spectral index, $\alpha_{1.4}^{850}$, defined by Carilli & Yun (1999). However, until recently, it was not known if high-redshift sources followed the far-IR–radio correlation at all, or, if the correlation evolves with redshift. Garrett (2002) extrapolated from *ISO* observations at 15 μm with the SED templates of local galaxies, which hinted that the far-IR–radio correlation holds at redshifts greater than 1. But it was not until *Spitzer* that Appleton et al. (2004) found that the far-IR–radio correlation clearly holds for galaxies to $z \sim 1$ using 70 μm observations from *Spitzer*-MIPS from the *Spitzer* First Look Survey, after applying K-corrections to the observed fluxes based on the template SEDs of Dale et al. (2001) and the SED of M82. Kovács et al. (2006) used 350 μm observations with the SHARC-II camera at the CSO in combination with existing submm data to make the most convincing case yet that a nearly linear far-IR–radio correlation exists for SMGs at $z \sim 1-3$, using a sub-sample of 21 galaxies from the radio-detected SMG sample of C05.

We now build upon the work of Kovács et al. (2006) in refining the far-IR–radio correlation for radio-detected SMGs using our new SED model fits to mid-IR data from *Spitzer* and far-IR data from the SCUBA, SHARC-II, and MAMBO instruments at the JCMT, CSO, and IRAM 30-m telescope, respectively. In the upper panel of Figure 4.10 we show IR luminosity versus radio luminosity ($L_{1.4}$) for the 55 SMGs in our sample with MIPS observations and luminosities. We use our values of $L_{\rm IR}$ calculated in §4.1.2 as a proxy for $L_{\rm FIR}$, which is acceptable since in the previous section we established that the far-IR emission is the dominant component of the IR SED of radio-detected SMGs. We have calculated radio luminosities ($L_{1.4}$) for our sample from the 1.4 GHz measurements tabulated in C05, applying a K correction assuming that the radio spectrum is dominated by synchrotron emission and is thus described by a power law, $S_\nu \propto \nu^{-\alpha_r}$, where α_r is the radio spectral index. We assume $\alpha_r = 0.7$, typical of non-thermal radio emission from local galaxies (Condon 1992). The radio luminosity then can be calculated from the following simple analytic expression:

$$L_{1.4} = 4\pi D_L^2 \, S_{1.4} \, (1+z)^{\alpha_r - 1}. \tag{4.6}$$

A tight IR–radio correlation is apparent in the top panel of Figure 4.10, across nearly 4 orders of magnitude in $L_{\rm IR}$ with only a few outliers, consistent with Kovács et al. (2006). In this plot we have indicated SMGs with and without 350 μm data as separate symbols and SMGs with and without 70 μm detections in different colors to display that there is no

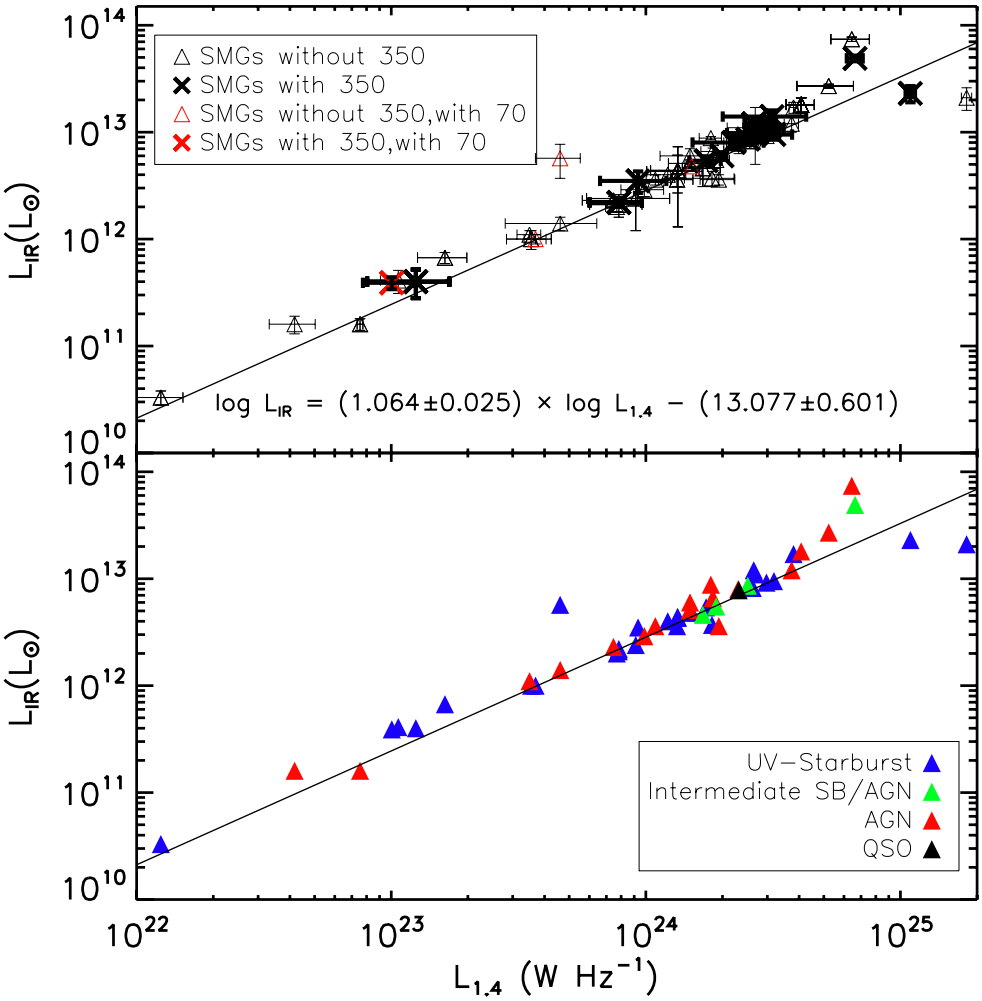

Figure 4.10 IR–radio correlation for radio-detected SMGs. IR luminosities are those presented in §4.1.2. *Top Panel:* SMGs with and without 350 μm data are plotted as triangles and crosses, respectively, and SMGs with and without 70 μm detections are plotted in red and black, respectively. *Bottom panel:* SMGs are separated into starburst (SB), AGN, and intermediate SB/AGN spectral classes using the classifications of Chapman et al. (2005); Swinbank et al. (2004); Takata et al. (2006); and Alexander et al. (2005).

change in the observed IR–radio correlation for SMGs with the additional data constraints. We use least-squares fitting to fit a power law function to the observed correlation, obtaining

$$\log\left(\frac{L_{\rm IR}}{L_\odot}\right) = (1.064 \pm 0.025)\,\log\left(\frac{L_{1.4}}{\rm W\,Hz^{-1}}\right) - (13.077 \pm 0.601), \tag{4.7}$$

where the stated errors are the 1σ uncertainties on the coefficients. Thus, the IR–radio correlation for SMGs is close to linear, but shows evidence for non-linearity similar to the low redshift far-IR–radio correlation (e.g., Yun et al. 2001). Our best fit IR–radio power law index is consistent with that found by Kovács et al. (2006), 1.02 ± 0.12, to within their measurement errors.

In the lower panel of Figure 4.10 we show the same data as in the top panel, but we separate the SMGs by spectral classes. The spectral classifications have been taken from the rest-frame UV results of C05, the rest-frame optical results of Takata et al. (2006) and Swinbank et al. (2004), and the X-ray results of Alexander et al. (2005). If a particular SMG has been denoted an AGN at any wavelength, it is plotted here as an AGN. If one has been denoted as an intermediate spectral type at any wavelength, it is plotted here as an intermediate type. In the figure we can see that spectral type appears to have no relation to the position of a SMG relative to the best-fit IR–radio correlation. We can also see that there are no clearly radio-loud galaxies in our MIPS sample, although that may be a relic of our MIPS observations (2 radio-loud SMGs are known in the SSA 13 field, which lacks MIPS coverage). We conclude from the bottom panel of Figure 4.10 that most radio-detected SMGs will lie on the IR–radio relation, regardless of whether or not it is known to contain an AGN.

To compare to the far-IR–radio correlation observed for local galaxies, we attempt to estimate the value of the far-IR–radio correlation parameter q, defined for local galaxies observed with *IRAS* by Helou et al. (1985) as

$$q = \log\left(\frac{\rm FIR\,(W\,m^{-2})}{3.75 \times 10^{12}\,\rm Hz}\right) - \log\left(\frac{S_{1.4}}{\rm W\,m^{-2}\,Hz^{-1}}\right), \tag{4.8}$$

where the FIR parameter is defined as

$$\rm FIR = 1.26 \times 10^{-14}(2.58 S_{60\mu m} + S_{100\mu m}), \tag{4.9}$$

and where the IRAS 60 μm and 100 μm fluxes $S_{60\mu\mathrm{m}}$ and $S_{100\mu\mathrm{m}}$ are in Jy. Lacking *IRAS* fluxes for our sample of SMGs, we interpolate q by convolving the *IRAS* 60 μm and 100 μm filter transmission profiles with the best-fit graybody SED model fits for each SMG and integrating. We caution that the values of q derived in this way are not highly accurate as a result. For our sample of radio-detected SMGs, we find a mean value of $q = 2.18$ with a standard deviation $\sigma_q = 0.13$, which is lower than that found by Yun et al. (2001) for bright ($S_{60\mu\mathrm{m}} > 1\,\mathrm{Jy}$), radio-identified *IRAS* galaxies, $q = 2.34$ with dispersion $\sigma_q = 0.33$. Our value is also slightly higher than the mean q found for some of the SMGs in our sample by Kovács et al. (2006), $q = 2.07$. However, the 2 radio-loud SMGs in the sample analyzed by Kovács et al. (2006), which tend to lower the average q value, are missing from our sample here since the sources have no MIPS data available. The inclusion of these radio-loud objects in their average may at least partially explain why the average q of Kovács et al. (2006) is lower than what we find here. Furthermore, the authors of that study note that simply by using radio flux values from Biggs & Ivison (2006) instead, q increases by 0.06 on average. Since even the uncertainty in the radio flux density can cause such a systematic difference in a mean value of q, we doubt that our values of q estimated from interpolation are precise enough to definitively say that the mean q for SMGs is systematically lower than that of local galaxies. The scatter seen in the values of q for local galaxies is certainly sufficient to place SMGs in the same approximate range as local IRAS sources.

Since the q parameter displays intrinsic scatter in local galaxies which is larger than the measurement errors (Condon 1992), which has been attributed to differences in dust temperatures and SEDs of galaxies (Yun et al. 2001), we prefer to compare the IR–radio correlation in SMGs to the IR–radio correlation in local galaxies in a different way. In Figure 4.11 we plot L_{IR} versus $L_{1.4}$ for our SMG sample as in Figure 4.10, but add to the plot local IRAS-selected galaxies with $L_{\mathrm{IR}} \sim 10^{11} - 10^{12} L_{\odot}$ from the sample of Dunne et al. (2000). For the galaxies in the Dunne et al. (2000), we have estimated L_{IR} using the same SED model used to derive the IR luminosities of the SMG sample, and to derive the radio luminosities we have taken fluxes for these galaxies from the NRAO-VLA Sky Survey (NVSS Condon et al. 1998) and K-corrected them to remove any uncertainties in the relation related to distance. Immediately in Figure 4.11 it can be seen that even though the galaxies from Dunne et al. (2000) are of lower luminosity than is typical of SMGs, the SMGs follow a very similar IR luminosity-radio luminosity relation as the galaxies in the

Dunne et al. (2000) sample. When we fit a power law separately to the sample of Dunne et al. (2000), we obtain

$$\log\left(\frac{L_{\rm IR}}{L_\odot}\right) = (1.048 \pm 0.013)\ \log\left(\frac{L_{1.4}}{\rm W\,Hz^{-1}}\right) - (12.614 \pm 0.282), \tag{4.10}$$

which is consistent to within the errors of the relation found for the SMGs. On the other hand, it appears from the figure that if we do not use the coldest, lowest-luminosity, low-z SMGs (which we know to have significantly different SEDs from the high-z SMGs) when fitting the correlations to the different galaxy samples, there may be a slight difference in the slopes of the local and high-z correlation. If there is a difference in slope between the local galaxies and the high-z galaxies, it is likely modest at best.

Thus, we conclude that high-z SMGs follow an IR–radio relation that is not very different from local IRAS galaxies. We note that the galaxies in the Dunne et al. (2000) sample significantly overlap in their distribution of T_d with the SMGs (see §4.1.2), which may explain why the local and high-z correlations agree fairly well. This does not necessarily mean that the local and high-z galaxies have the same physical dust temperatures, but at least their temperatures and emissivities cause the SEDs of the local and high-z galaxies to peak at similar wavelengths.

We further note that our finding that SMGs follow a IR–radio correlation similar to that of local IRAS galaxies contrasts with the prediction of Vlahakis et al. (2007) that the far-IR–radio relation is evolving with redshift. They find that the majority of high-z SMGs must be brighter at radio wavelengths than is predicted by redshifting the Carilli & Yun (1999) radio–submm spectral index $\alpha_{1.4}^{850}$ of local optically-selected and *IRAS*-selected galaxies, using the observed SEDs of the local galaxies as templates. However, Vlahakis et al. (2007) do not comment on the strength of the evolution that they suspect occurs; our results here for the high-z SMGs could be consistent with a small amount of evolution in the correlation with redshift. We point out, though, that Vlahakis et al. (2007) observe in their analysis that $\alpha_{1.4}^{850}$ for local galaxies varies with galaxy SED, and show that a wide range of values for the spectral index are possible, with *IRAS*-selected galaxies typically showing lower values of the spectral index. Since, as Vlahakis et al. (2007) point out, high-z SMGs are selected at rest-frame wavelengths longer than *IRAS*-selected galaxies, and the SMGs in the C05 sample show variation in their IR SEDs and display a large scatter in $\alpha_{1.4}^{850}$

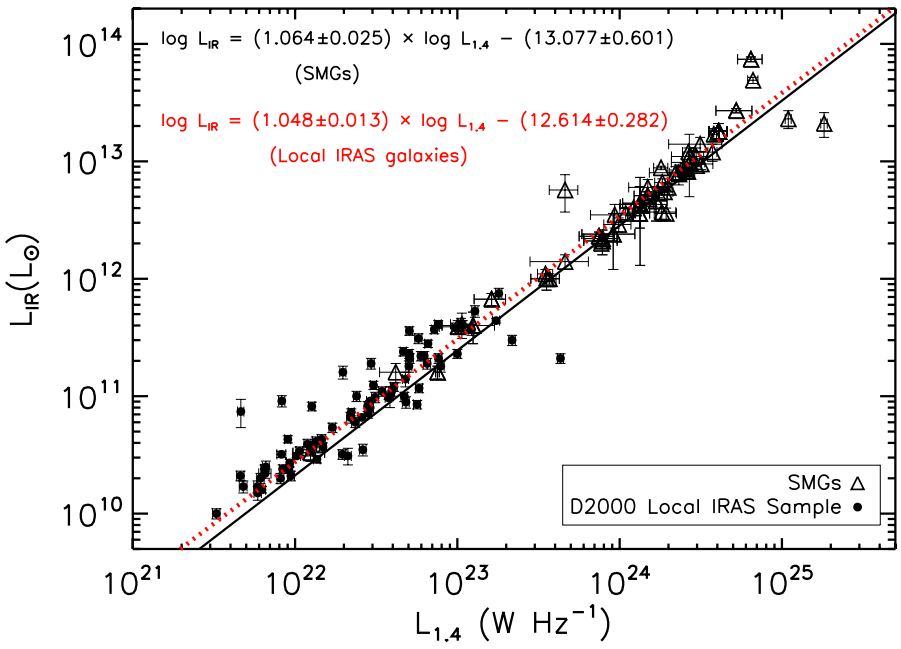

Figure 4.11 $L_{\rm IR}$–L_{radio} correlation for radio-detected SMGs and local *IRAS*-selected galaxies from the sample of Dunne et al. (2000). The values of $L_{\rm IR}$ have been derived for both galaxy samples using the graybody SED model described in §4.1.1. The solid line shows the best-fit power-law correlation to only the SMG sample, while the dotted red line shows the power-law correlation fit to only the local *IRAS* galaxies. The correlations appear to be the same to within the fitting errors.

at a particular redshift (C05), we find it more likely that differences in the SEDs of SMGs as compared to local galaxies are more likely the explanation for the lower-than expected values of $\alpha_{1.4}^{850}$ that Vlahakis et al. (2007) obtain.

On the other hand, our finding that local *IRAS* galaxies and SMGs follow IR luminosity–radio luminosity correlations that are not very different is dependent on our assumption that SMGs and local galaxies have the same radio spectral indices. The radio spectral indices of SMGs are essentially unknown, which is why we have assumed a typical local value for non-thermal radio emission to K-correct our 1.4 GHz fluxes. Future work on the IR–radio luminosity correlation in SMGs and other high redshift sources will benefit from radio observations of these galaxies at multiple radio continuum frequencies to determine radio spectral indices of these galaxies.

4.5 Conclusions

We have used deep *Spitzer*-MIPS imaging of the radio-detected SMGs in the spectroscopic sample of Chapman et al. (2005) to derive new estimates of the IR luminosity. Our *Spitzer* data constrain the Wien side of the SED peak of high-redshift SMGs, and thus are important indicators of the contribution of hot dust emission and total IR luminosity for this class of far-IR-luminous galaxies. From fitting graybody SEDs with power-law Wien tails to the individual galaxies in our sample, we find a median IR luminosity for the sample of $L_{\rm IR} = 5.4 \times 10^{12}\,L_{\odot}$ and that the IR luminosity estimates of Chapman et al. (2005) are approximately 30% too high on average, though this does not significantly affect the conclusion of Chapman et al. (2005) that SMGs may trace the dominant sites of star formation at $z \sim 2-3$. We find that SMGs tend to have different dust characteristics (the effects of temperature and emissivity combined) from some ULIRGs at lower redshifts, and that most of the SMGs, while being brighter in the mid-IR than the SED of Arp 220 would predict, do not contain dominant hot dust components. We also find that the IR SEDs of SMGs vary with redshift, show at least an order of magnitude variation in mid-IR properties at a given redshift, and are not well-described in the mid-IR by the SED of Arp 220. Finally, having enough IR data points to obtain the IR luminosity of SMGs without the use of radio data, we find the SMGs show a relatively tight, almost linear correlation between total IR luminosity and radio luminosity, which is similar to the $L_{\rm IR}$-radio correlation of local

IRAS-selected galaxies. Since the far-IR luminosity dominates the total IR luminosity in all the SMGs in our sample, we conclude that the high-redshift far-IR–radio correlation is not vastly different from the local far-IR–radio correlation.

Acknowledgments We wish to thank K. Menéndez-Delmestre for providing her unpublished composite IRS spectrum of SMGs for our study presented here. This research has made use of the NASA/IPAC Extragalactic Database (NED), which is operated by the Jet Propulsion Laboratory, California Institute of Technology, under contract with the National Aeronautics and Space Administration.

Chapter 5

The Rest-Frame Near and Mid-Infrared Properties of Submillimeter-Selected Galaxies and Their Relation to Other High-z Galaxy Populations

The rest-frame UV and rest-frame optical properties of submillimeter-selected galaxies (SMGs) have been well characterized in the studies of Chapman et al. (2005) and Smail et al. (2004). Chapman et al. (2005) found that $\sim 65\%$ of the SMGs in their sample with deep U data are quite blue and satisfy the BX/BM galaxy selection criterion, while 30% were too faint to be selected as Lyman break galaxies (LBGs) or BX/BM galaxies. From their rest-frame UV (observed-band optical) spectroscopy Chapman et al. (2005) found that $\sim 50\%$ of their sample display Ly-α emission lines, whereas two-thirds of LBGs and $\sim 40\%$ of BX/BM galaxies show Ly-α emission (Steidel et al. 2003, 2004). From observed frame near-IR imaging, Smail et al. (2004) found SMGs are somewhat redder than the field, with median $I-K$ and $J-K$ colors of 3.71 ± 0.16 and 1.73 ± 0.10, respectively, with the colors spanning 4 magnitudes and showing no trend with redshift. Smail et al. (2004) attribute the large variation in rest-frame optical colors to differing levels of extinction within SMGs and find it unlikely that the colors are dominated by old stellar populations. They further find that the observed-frame K-band (rest-frame V-band) light is only weakly coupled with the far-IR luminosity, such that SMGs, which are an order of magnitude more IR-luminous than LBGs and BX/BM galaxies, are only a factor of ~ 2 brighter in K than the UV-selected galaxies.

However, not until the advent of the *Spitzer Space Telescope* has there been sufficient sensitivity in near/mid-IR instruments to characterize the rest-frame near-IR properties of SMGs, wavelengths where the extinction from dust and effects of recent star formation have less impact on the observed stellar emission. Several authors (e.g., Egami et al. 2004; Pope et al. 2006; Ashby et al. 2006) have already shown that SMGs can be well-detected and studied with *Spitzer*, yet these studies have usually been restricted to small (10–20) numbers of SMGs in individual fields on the sky. None, so far, have analyzed a a representative sample of SMGs with spectroscopic redshifts. In this chapter, we carry out such an analysis by studying the near and mid-IR properties of the SMGs in the sample of Chapman et al. (2005) with *Spitzer* data presented in Chapter 3. We examine the near and mid-IR fluxes and colors of SMGs and compare them to the observed properties of several other populations of high-z galaxies selected at different wavelengths.

5.1 The Rest-Frame Near-IR Properties of the Chapman et al. (2005) SMG Sample from IRAC Imaging

In the rest-frame near-IR, the light from normal galaxies is dominated by starlight, from both cool, evolved giant stars and low-mass stars of all ages. Stellar emission peaks in the near-IR due to a maximum in thermal emission and a minimum in the opacity of the H^- ion, the dominant source of opacity in low-mass stars, causing a feature referred to as the 1.6 μm bump. In galaxies with heavily obscured, powerful active galactic nuclei (AGN), the rest-frame near-IR can also contain emission from small dust grains heated by the AGN, to temperatures near their sublimation temperatures (~ 1500 K). Also, the dust grains extinguishing light from young massive stars at optical wavelengths are much more transparent in the near-IR, so the light emerging from a galaxy at these wavelengths better reflects the number of stars present in the galaxy. Since strong extinction affects SMGs such that little blue light from stars can escape, the rest-frame near-IR offers the best opportunity to obtain information about the bulk of the stars in SMGs. At the same time, we may also be able to determine if SMGs contain powerful obscured AGN by looking at the rest-frame near-IR SED and colors.

The bands observed by IRAC correspond to the rest-frame near-IR (J, H, K) for galaxies at $z \sim 2$. Thus, here we use the results of the IRAC imaging of the Chapman et al. (C05

hereafter 2005) sample presented in Chapter 3 to examine the rest-frame near-IR properties of SMGs.

5.1.1 IRAC Flux Densities of SMGs

As mentioned in the previous chapter, the majority of the SMG sample of C05 is detected above a 3σ level in all of the IRAC bands, with typical flux densities of $\sim$ a few to $\sim 100\,\mu$Jy. We detect $> 90\%$ of SMGs with imaging at 3.6 and $4.5\,\mu$m, and $\sim 80\%$ of SMGs with imaging at 5.8 and $8.0\,\mu$m. In Figure 5.1 we show flux density versus redshift for our SMG sample for each IRAC band, illustrating the spread in flux density for the radio-detected SMGs in our sample. For the $z > 2$ SMGs, the IRAC fluxes vary over ~ 2 orders of magnitude in all channels when the undetected sources are included. At redshifts lower than 2, the variation in flux among the detected sources may appear somewhat smaller, but given the fewer number of sources overall compared the those at $z > 2$, it is difficult to discern if the reduced scatter is real.

It is interesting that the few sources not detected in the 3.6 and $4.5\,\mu$m images have fluxes so far below that of the sources that are detected in the flux versus redshift plots. From the postage stamp images in Figures 3.4, 3.5, 3.6, and 3.7, we see that the majority of our radio- detected SMGs are well-detected in the 3.6 and $4.5\,\mu$m bands. Most of the undetected sources in these bands seem to truly be extremely faint, since no trace of a source is seen in the postage stamps. In fact, the sources which are not detected are unusual enough and faint enough that they may indicate a problem with the counterpart identification. In the longer wavelength bands, which have lower sensitivity than the bluer bands, the undetected sources seem less anomalous. In general, it appears that much of the SMG population can be detected by IRAC without such extremely deep imaging as has been obtained for the GOODS fields; rather, integration times of 500–1000 sec will suffice for many of the SMGs.

5.1.2 Using IRAC Fluxes as a Redshift Indicator

Recently, Younger et al. (2007) suggested that flux in the IRAC bands, specifically the $3.6\,\mu$m band, can be used as an indication of redshift for SMGs, since they find that for cold, dusty $L_{\rm IR} \sim 10^{12} - 10^{13}\,L_{\odot}$ galaxies similar to the local ULIRG Arp 220 the observed $3.6\,\mu$m flux should be a strong function of redshift. They then proceed to argue that several radio-faint ($S_{1.4\rm GHz} < 60\,\mu$Jy) submilllimeter sources must lie at $z > 3$, because these

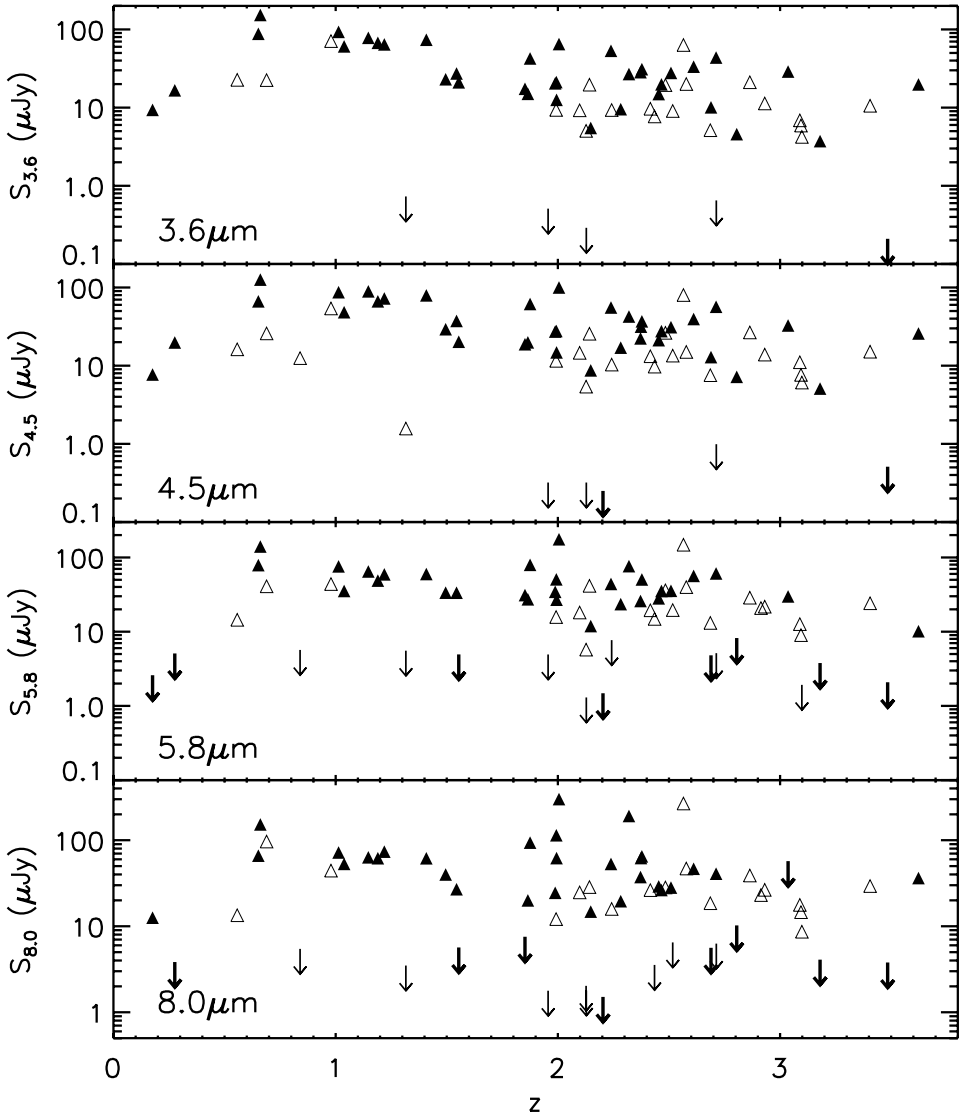

Figure 5.1 Flux density versus redshift in IRAC bands for radio-detected SMGs in the sample of C05. Triangles represent detected SMGs, while downward arrows indicate 3σ point-source upper limits for undetected objects. Filled triangles and thick arrows indicate "radio-bright" ($S_{1.4\mathrm{GHz}} > 60\,\mu$Jy) SMGs according to the criterion of Younger et al. (2007), while open triangles and thin arrows represent "radio-dim" SMGs of those authors ($S_{1.4\mathrm{GHz}} < 60\,\mu$Jy).

sources have low radio flux and low 3.6 μm flux densities (2–5 μJy). Since we now have the largest sample of IRAC observations of SMGs with spectroscopic redshifts, we can evaluate whether the 3.6 μm flux of SMGs is in fact a function of redshift. In looking at the detected SMGs in Figure 5.1, we see that there appears to be a correlation of 3.6 μm flux with redshift over the range $z = 0 - 3$, which a Spearman rank correlation test (applied only to detected sources) finds to be significant at a $\sim 3\sigma$ level. However, for $z > 2$, the scatter in the points is not indicative of a correlation at all; indeed, when we separate the SMG sample into bins of $z < 2$ and $z > 2$ and apply the Spearman rank test separately to detected sources in each bin, we find a marginal ($\sim 2\sigma$) correlation at best for the $z < 2.0$ bin, and no correlation of significance for the $z > 2$ bin. These results suggest that, above $z \sim 2$, a correlation between 3.6 μm flux density and redshift does not hold for SMGs. Thus, it is unlikely that the 3.6 μm fluxes reveal any information about redshift for sources above $z > 2$ and should not be used to distinguish a source at $z \sim 2$ from one at $z \sim 3 - 4$. The same results are obtained when we carry out a Spearman rank test on the 4.5 μm fluxes of detected sources versus redshift: a marginally significant correlation (at the $2 - 3\sigma$ level) can be found when all redshifts are considered and when only $z < 2$ sources are considered; however, for $z > 2$ sources, no significant correlation is evident. In the 5.8 and 8.0 μm bands, no significant correlations with redshift are indicated by the Spearman rank test. We conclude that the IRAC flux densities by themselves should not be taken as indicators of redshift for SMGs.

However, Younger et al. (2007) only apply the flux density as an indicator of redshift to their objects with $S_{1.4\mathrm{GHz}} < 60\,\mu$Jy (which they refer to as "radio-dim"), while we have used all radio-detected SMGs to determine that 3.6 μm flux is not a good redshift indicator. The C05 SMG sample contains numerous SMGs that are radio-dim by the criterion of Younger et al. (2007), contrary to the assertion of the authors of that paper that the sample of C05 is radio-bright, and we in Figure 5.1 we have divided the C05 sample of SMGs into a radio-bright sample ($S_{1.4\mathrm{GHz}} > 60\,\mu$Jy; filled triangles and thick arrows) and a radio-faint sample ($S_{1.4\mathrm{GHz}} < 60\,\mu$Jy; open triangles and thin arrows) to see if any correlation exists between IRAC flux and redshift for only radio-dim sources. From Figure 5.1 we note that such radio-dim SMGs are observed at both relatively low ($z < 1$) and high redshifts, as are radio-bright SMGs; thus, radio flux by itself does not indicate redshift. A Spearman rank correlation test fails to find any significant correlation between IRAC flux density and redshift in any IRAC band for the radio-dim SMGs that are detected.

Younger et al. (2007) also find that their 5 radio-dim sources have systematically lower $3.6\,\mu$m flux densities than galaxies in the C05 sample in the GOODS-N field and in the SSA22 field, which they also use as an indicator that the radio-dim sources lie at higher redshift. From Figure 5.1 it is not entirely clear that this is, in fact, true for SMGs in general; however, when we find the median $3.6\,\mu$m flux for the C05 sample which is detected at that wavelength, we obtain $\langle S_{3.6}\rangle = 9.7\,\mu$Jy for the radio-faint SMGs but $\langle S_{3.6}\rangle = 27.6\,\mu$Jy for the radio-bright sources. When we break the SMGs into two redshift bins, $z < 2$ and $z > 2$, we again obtain lower median $3.6\,\mu$m fluxes for the radio-faint SMGs as compared with the radio-bright sources in both redshift bins, $\langle S_{3.6,faint}\rangle = 22.6\,\mu$Jy versus $\langle S_{3.6,bright}\rangle = 34.9\,\mu$Jy for $z < 2$ and $\langle S_{3.6,faint}\rangle = 9.3\,\mu$Jy versus $\langle S_{3.6,bright}\rangle = 27.3\,\mu$Jy for $z > 2$ sources. Thus, it does appear that radio-dim SMGs, using the criterion of Younger et al. (2007), may be systematically fainter in the $3.6\,\mu$m band than SMGs that are brighter radio sources. However, the physical reason behind the difference is unclear because the $3.6\,\mu$m flux in SMGs primarily comes from the existing stellar component of the galaxies, while the radio emission is thought to arise from either regions of recent, massive star formation containing supernova remnants or from accretion onto an active nucleus. Nor does a systematically lower $3.6\,\mu$m flux in radio-dim sources justify assuming higher redshifts for them, considering that radio-dim sources occur at both low and high redshifts.

5.1.3 IRAC Colors of SMGs

With our IRAC measurements of the C05 sample of SMGs, we can now explore the rest-frame near-IR colors of radio-detected SMGs, which in galaxies without a strong AGN is a probe of the stellar emission from the galaxy. With smaller samples of SMGs in the GOODS-N and CFRS-14h/Groth-Westphal fields, Pope et al. (2006) and Ashby et al. (2006), respectively, found that SMGs tend to be redder than field galaxies in the colors formed from the various IRAC bands. Here, we extend the near-IR color analysis to include at least twice as many SMGs as Pope et al. (2006) and Ashby et al. (2006), for all of which we have spectroscopic redshifts and can thus look for any trends with redshift. Due to the possibility of increased AGN contribution and/or contamination from the $3.3\,\mu$m polycyclic aromatic hydrocarbon (PAH) emission feature in $z \sim 1.2-2$ galaxies, we try to avoid using the observed $8.0\,\mu$m band flux in our colors to better represent the stellar emission.

Scoville et al. (2000) use a NICMOS F110W-F160W versus F160W-F222M color-color diagram (essentially $J-H$ versus $H-K$), shown in Figure 5.2, to illustrate the effects in color space of aging a stellar population, reddening a stellar population, and the contributions to the near-IR colors of dust heated by an AGN. For galaxies at $z \sim 1.5-2.5$, the IRAC 3.6, 4.5, and 5.8 μm bands roughly approximate the J, H, and K filters, so in Figure 5.3 we plot the 4.5-3.6 μm flux ratio versus the 5.8-4.5 μm ratio for the SMGs with detections in the 3.6 and 4.5 μm bands (most of the sample) to see if we can separate out contributions from stars and hot dust. For comparison, we overplot a sample of field galaxies from the deep GOODS-N IRAC images. We have separated the SMGs into 4 redshift bins, indicated by different colors, to look for any redshift effects as well. The majority of field galaxies follow a well-defined track in the 4.5/3.6 μm–5.8-4.5 μm color-color space, which corresponds to stellar populations behind moderate extinction, over which 10 of the 14 $z < 1.5$ SMGs in our sample fall. Most of the $z > 1.5$ SMGs in the C05 sample, and three lower-z SMGs, are significantly redder in both the 4.5/3.6 and 5.8/4.5 colors than the field and $z < 1.5$ SMGs, indicating that the SEDs of much of the high-z SMGs are still rising through the 3.6, 4.5, and 5.8 μm IRAC bands. Such behavior makes sense if the near-IR emission of SMGs is dominated by stellar emission and rises toward the 1.6 μm stellar maximum (which falls into the 5.8 μm band at $z \sim 2.5$).

On the other hand, the color-color diagram of Scoville et al. (2000) suggests that the reddest colors could also arise from a powerful, obscured AGN. The diagram for local ultraluminous IR galaxies (ULIRGs) suggests the reddest SMGs in $S_{5.8}/S_{4.5}$ that are bluer in $S_{4.5}/S_{3.6}$ contain significant contributions from dust heated to $\sim 400-600$ K, while those that are redder in $S_{4.5}/S_{3.6}$ contain significant contributions from even hotter dust at ~ 1000 K. However, the region of the diagram populated by heavily extincted stellar populations lies fairly close to the tracks representing the colors of sources with significant contributions from hot dust, so the red IRAC colors still cannot conclusively distinguish between high-z stellar-dominated sources and AGN. There is a noticeable difference between the IRAC colors of lower and higher-z SMGs, but since there is not a smooth trend with redshift we suggest that the color difference implies that there is something fundamentally different about the lower-z sources causing them to be more blue; perhaps that these SMGs are less massive or less obscured than the galaxies at higher redshifts or do not contain significant contributions from hot dust but have high reddenings. A further interesting

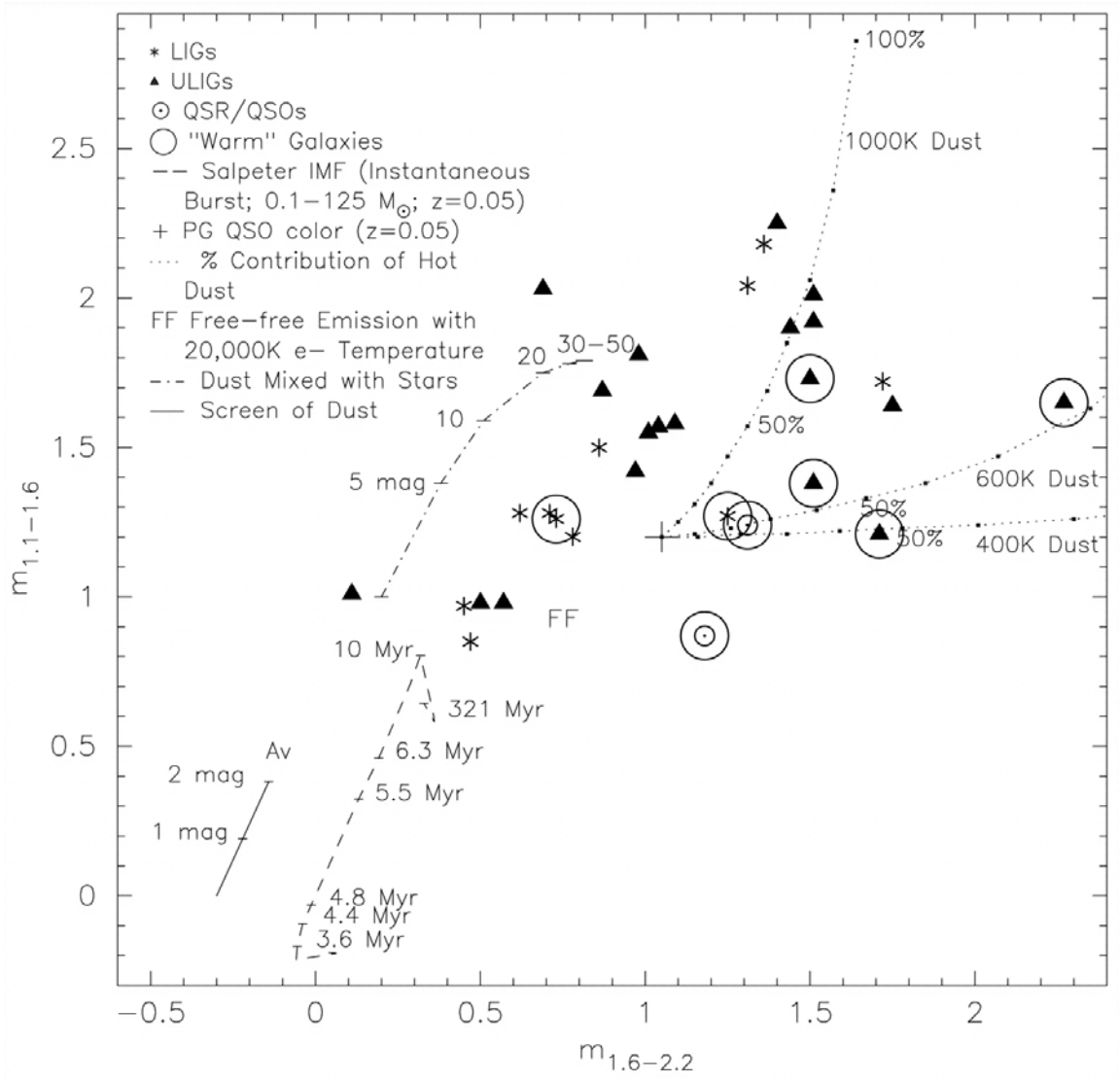

Figure 5.2 F110W-F160W versus F160W-F222M ($J-H$ vs. $H-K$) color-color diagram of Scoville et al. (2000), illustrating the effects of stellar populations and dust heating by AGN on near-IR colors of local ULIRGs. Reproduced with permission of the author.

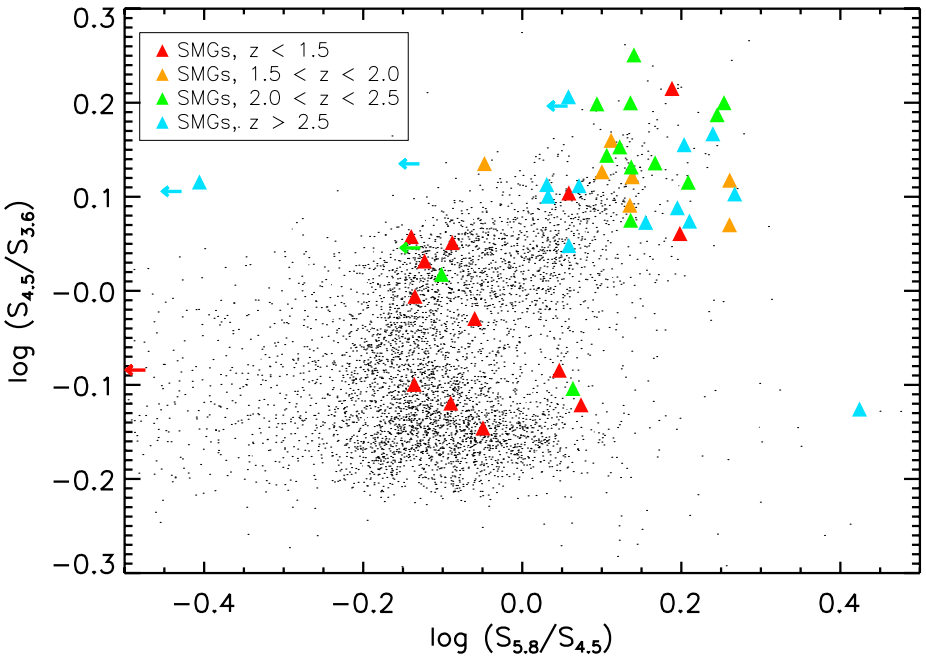

Figure 5.3 4.5μm/3.6μm vs. 5.8μm/4.5μm color-color diagram for radio-detected SMGs in the C05 sample and Field Galaxies. SMGs are indicated by filled triangles, color-coded by redshift, while field galaxies from the GOODS-N field are represented by black dots. Leftward-pointing arrows indicate SMGs which are detected at 3.6 and 4.5 μm but not at 5.8 μm. Error bars for the SMGs are approximately the size of the triangle points or smaller.

note is that our sample of IRAC-observed SMGs, especially the galaxies at $z > 1.5$, appears to avoid the region of color space around $(\log S_{5.8}/S_{4.5}, \log S_{4.5}/S_{3.6}) \sim (0, 0.03)$. This may simply be an effect of small-number statistics, but could also reflect some physical difference between the galaxies on either side of the gap.

Pope et al. (2006) suggest that a 5.8 μm versus 5.8-3.6 μm ratio color-magnitude diagram can be used to separate $z > 1.5$ SMGs from lower-z SMGs, even if a source contains an X-ray detected AGN, as well as indicate mid-IR counterparts to submm sources. With our large sample of SMGs with spectroscopic redshifts we can test this possibility. In Figure 5.4 we plot this color-magnitude diagram for field galaxies in the GOODS-N field and radio-detected SMGs from the C05 sample, color-coding the SMGs by redshift bin as in Figure 5.3. We have also indicated the region in which Pope et al. (2006) find that 11/11 SMGs in their sample have $z > 1.5$ by dashed lines. The demarcated region in color-magnitude space does tend to contain SMGs with $z > 1.5$, but there are exceptions. Some $z > 2$ SMGs are bluer and fainter than the region Pope et al. (2006) assign to $z > 1.5$ SMGs, while two $z < 1.5$ SMGs fall into the high-z portion of the plot. One of the lower-z SMGs falling in this region is SMM J105200.22+572420.2 ($z = 0.689$), which has been identified as a possible AGN based on its IRAC SED by Egami et al. (2004), and the contribution of an AGN to the near-IR emission could certainly cause redder 5.8-3.6 μm color in this object than would be expected based other SMGs at similar redshifts. The other lower-z SMG falling in the high-z region in Figure 5.4, SMM J163639.01+405635.9, lies at $z = 1.488$ and is thus right at the $z \sim 1.5$ dividing line, so it is not really out of place in the high-z region. On the whole, it does appear that the location of a SMG in the 5.8 μm versus 5.8-3.6 μm color-magnitude diagram is a reasonable method of separating low-z sources from high-z sources; yet, it is not a foolproof redshift indicator for sources with an AGN visible in the near-IR or bluer-than-expected colors.

On another note, our IRAC data for an expanded SMG sample generally supports the observation of Pope et al. (2006) that SMGs tend to be brighter at 5.8 μm than the field for a given color, which could indicate that they are more massive or more obscured than the field galaxies, that they contain powerful AGN, or that we are sampling closer to the maximum of their SED than for field galaxies. The SMGs are frequently significantly redder in 5.8/3.6 μm color than the field as well. The flux and color of the SMGs tend to make them stand out from the field sample, which lends support to the hypothesis that they

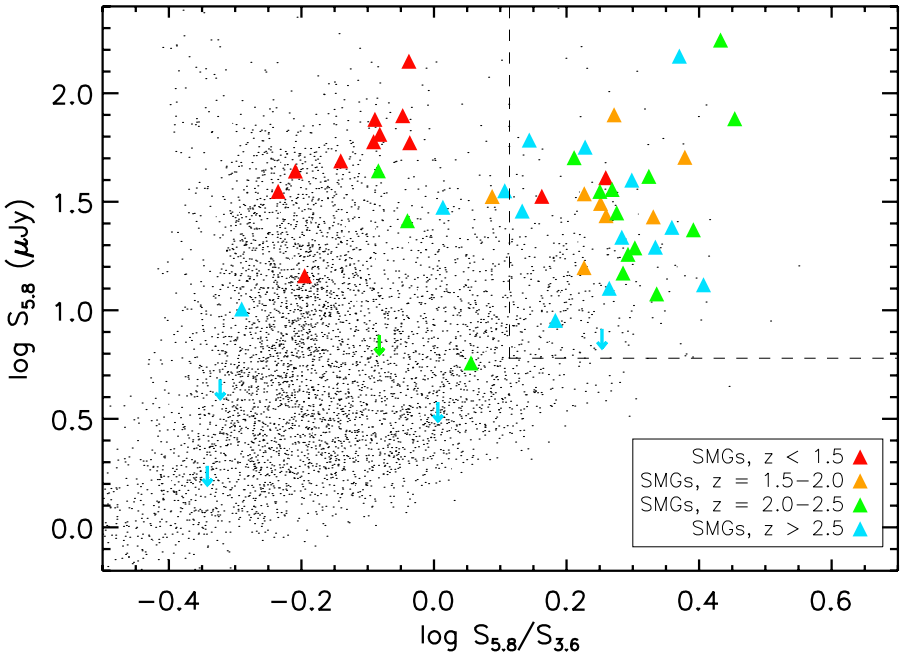

Figure 5.4 5.8 μm vs. 5.8μm/3.6μm color-magnitude diagram for radio-detected SMGs in the C05 sample and Field Galaxies. SMGs are indicated by filled triangles, color-coded by redshift, while field galaxies from the GOODS-N field are represented by black dots. Downward-pointing arrows indicate SMGs which are detected at 3.6 μm but not at 5.8 μm. Dashed lines indicate the region of the plot identified by Pope et al. (2006) as containing SMGs at $z > 1.5$. Error bars for the SMGs are approximately the size of the triangle points or smaller.

are extreme objects in some form, and could help identify the IR counterparts to SMGs as suggested by Pope et al. (2006). Many of the $z > 1.5$ SMGs do lie in the region where $S_{5.8}/S_{3.6} > 1.3$ and $S_{5.8} > 6\,\mu$Jy, and a possible SMG counterpart which fell in this region of the color-magnitude diagram has an increased likelihood of being the correct counterpart than one which does not. Yet, enough SMGs lie outside the selected region of the color-magnitude diagram that possible SMG counterparts should not be ruled out simply because they do not satisfy the $5.8\,\mu$m flux and $S_{5.8}/S_{3.6}$ color requirements.

In none of the IRAC colors have we noticed a trend of color with redshift, except that $z < 1.5$ SMGs tend to fall in different areas of color-color and color-magnitude space than $z > 1.5$ SMGs. However, this difference may not be due solely to redshift effects; rather, it may reflect some form of evolution in the population causing the $z < 1.5$ SMGs to be intrinsically different objects than the $z > 1.5$ SMGs. In Figure 5.5 we explicitly plot near-IR colors versus redshift to see if any of the colors can help indicate redshifts of SMGs. With the possible exception of $z < 1.5$ SMGs in the $3.6\,\mu\mathrm{m}/K$ color, no significant trends of near-IR color with redshift are visible for the SMGs, though the $z > 2$ SMGs may be systematically slightly redder in $S_{5.8}/S_{3.6}$ and $S_{5.8}/S_{4.5}$. In fact, the spread in the IRAC colors of the radio-detected SMGs, especially those at $z > 2$, is remarkably low, less than an order of magnitude; the spread in the $S_{4.5}/S_{3.6}$ color is especially small. We find the means and standard deviations of the different near-IR colors to be $\langle S_{3.6}/S_K \rangle = 2.48 \pm 1.49$, $\langle S_{4.5}/S_{3.6} \rangle = 1.23 \pm 0.25$, $\langle S_{5.8}/S_{3.6} \rangle = 1.61 \pm 0.62$, and $\langle S_{5.8}/S_{4.5} \rangle = 1.29 \pm 0.40$ for the SMGs in our sample which have IRAC detections. Such small scatter in the IRAC colors is in marked contrast with the observed $I - K$ and $J - K$ colors for this same sample of SMGs found by Smail et al. (2004), which span 4–5 magnitudes. That SMGs appear more uniform in their rest-frame near-IR colors than in their rest-frame optical colors reflects the waning influence of dust obscuration in the near-IR as compared with the effects of extinction at optical wavelengths. It may also indicate that SMGs commonly host significant existing stellar populations on top of the burst producing the enormous IR luminosity of these systems. While it is possible that some selection bias towards bluer objects exists in our sample due to the requirement of a spectroscopic redshift from optical wavelengths, we note that the range of rest-frame optical colors in these objects indicate that we are already dealing with galaxies of varying extinction, and given the similarity of the near-IR colors across the range of optical extinction, it is unlikely that our selection bias will affect the

trends in the near-IR colors.

In summary, we find that most of the 67 radio-detected SMGs in our IRAC-imaged sample are detected as point sources with flux densities $> 1\,\mu$Jy. SMGs at $z > 2$ show no correlation in IRAC flux density with redshift, while SMGs at lower redshifts show evidence for marginal correlation with redshift in the $3.6\,\mu$m and $4.5\,\mu$m IRAC bands. We do not observe a significant trend of the rest-frame near-IR colors of SMGs with redshift, though we find these colors to be much more uniform across the sample as compared with the rest-frame optical colors. Our sample of SMGs are typically brighter in the $5.8\,\mu$m IRAC band than faint field galaxies, and the $z > 1.5$ SMGs tend to be redder in their IRAC colors than both field galaxies and lower redshift SMGs.

5.2 The Rest-Frame Mid-IR Properties of Radio-Selected SMGs at $24\,\mu$m

We now shift from discussion of the rest-frame near-IR properties of SMGs, which are mostly due to emission from underlying populations of older, low-mass stars, and possibly hot dust emission from a powerful obscured AGN, to their rest-frame mid-IR properties. The MIPS $24\,\mu$m instrument samples the rest-frame mid-IR for $z \sim 2$ galaxies, a wavelength regime in which the emission from stars falls off steeply and emission from small dust grains dominates the spectral energy distribution. The dust can be heated by starlight, an AGN, or both, producing both continuum and emission lines. In Figure 5.6 we show for reference the spectrum of M82 with the redshifted $24\,\mu$m filter bandpass plotted over it, indicating what spectral features can fall into the filter at different redshifts.

In this section we discuss the results of the $24\,\mu$m observations of SMGs presented in Chapter 3 in the context of dust temperature and emission features.

5.2.1 Detection Rates and $24\,\mu$m Fluxes

As we mentioned in Chapter 3, we detect $\sim$ 70% of the SMGs in the C05 sample at $> 3\sigma$ significance. The $24\,\mu$m detection rate we find across the entire Chapman sample is somewhat lower than found in previous studies of SMGs in individual fields. Previous studies of samples of radio-selected SMGs with *Spitzer*-MIPS at $24\,\mu$m have resulted in nearly 100% detection rates: Egami et al. (2004) find that 6 of 7 SCUBA sources with radio

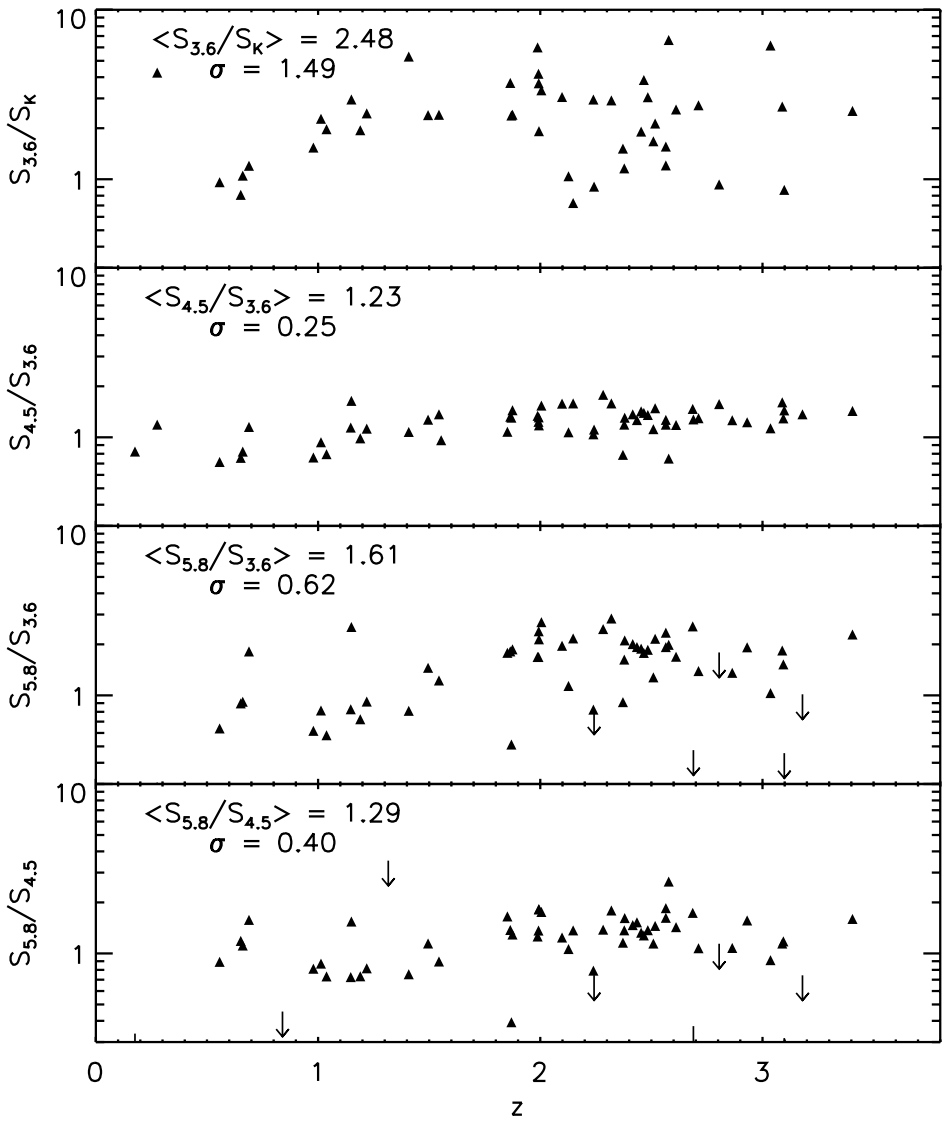

Figure 5.5 Rest-frame near-IR colors versus redshift for the C05 sample of radio-detected SMGs. SMGs detected in both wavelengths of a particular color are indicated by filled triangles, while downward-pointing arrows represent objects which are detected in only one band. Error bars for the points are approximately the size of the points.

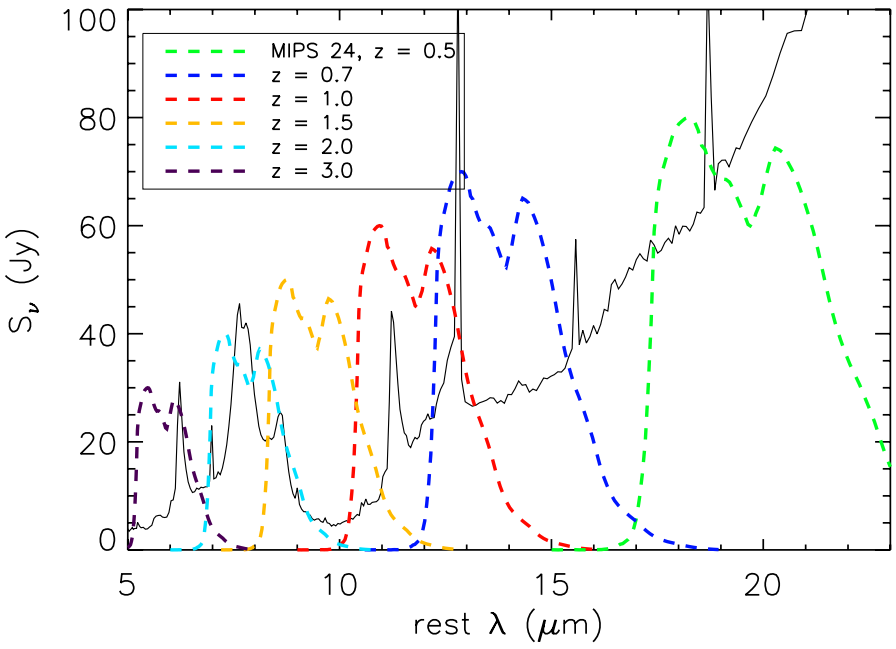

Figure 5.6 Rest-frame wavelength coverage of the MIPS 24 μm band at redshifts where SMGs are found. The different colored dashed lines indicate the portion of the rest-frame mid-IR spectrum transmitted through the 24 μm filter for the corresponding redshift, where the transmission profiles are arbitrarily normalized for clarity. The mid-IR spectrum of M82 from ISO (Sturm et al. 2000), shown as the black curve, is used to show typical emission and absorption features in galaxy spectra in the mid-IR to give a sense of what information 24 μm filter measurements may convey.

detections in their study of SCUBA sources in the Lockman Hole are detected at 24 μm, while Ivison et al. (2004) report the same detection fraction in looking at radio-detected MAMBO-selected sources in the same field. Frayer et al. (2004) detect 7 of $7 > 3\sigma$ SCUBA sources with radio detections in the *Spitzer* xFLS, and Pope et al. (2006) find that 20 of 21 SMGs with securely identified radio counterparts are detected at 24 μm. However, it is important to note from Table 3.4 that the depth of coverage between different SMG fields is highly variable, so a lack of detection of a particular SMG does not necessarily indicate that it is intrinsically different from the rest of the sample. The field with the highest 24 μm detection rate, GOODS-N, has by far the deepest data, suggesting that deeper 24 μm observations in the other SMG fields are likely to detect those sources not yet detected. Indeed, several of the postage stamp images in Figure 3.8 of SMGs with upper limits at 24 μm are suggestive of a source just beyond the detection limit at that position, so deeper imaging may prove fruitful.

To illustrate the range of 24 μm fluxes for the radio-selected SMGs, we show in Figure 5.7 a plot of the measured 24 μm fluxes versus redshift. From the figure it is apparent that 24 μm flux is not a strong function of redshift for this sample of SMGs. The SMGs span almost 2 orders of magnitude in 24 μm flux and more than an order of magnitude at any particular redshift. This variation is most likely because the MIPS 24 μm band samples various redshifted mid-IR emission lines (e.g., PAHs) and absorption features (e.g., 9.7 μm silicate feature), shown in Figure 5.6, as well as thermal dust continuum emission. The scatter in Figure 5.7 suggests that the radio-selected SMGs show significant variation in their mid-IR spectral features. For example, at $z \sim 1.5$, one might expect to see low fluxes or non-detections in the 24 μm band, based on the mid-IR spectrum M82, since the 24 μm band is dominated by the 9.7 μm silicate absorption feature at this redshift. Yet, in the radio-detected SMG sample, at $z \sim 1.5$, 2 of the 3 SMGs have strong 24 μm detections, while the third is not detected. Similarly, at $z \sim 2$, where the 7.7 μm PAH feature falls in the MIPS band, one might expect to see an enhancement in the 24 μm flux. However, among the $z \sim 2$ SMGs, the largest range in 24 μm flux of any particular redshift is observed.

Given the variation in 24 μm flux we observe for our sample of SMGs, it is clear that mid-IR spectra of these objects is required to understand the mid-IR emission in individual objects. The Infrared Spectrograph (IRS) instrument on *Spitzer* has produced spectra for several SMGs so far (e.g., Lutz et al. 2005; Menéndez-Delmestre et al. 2007; Valiante

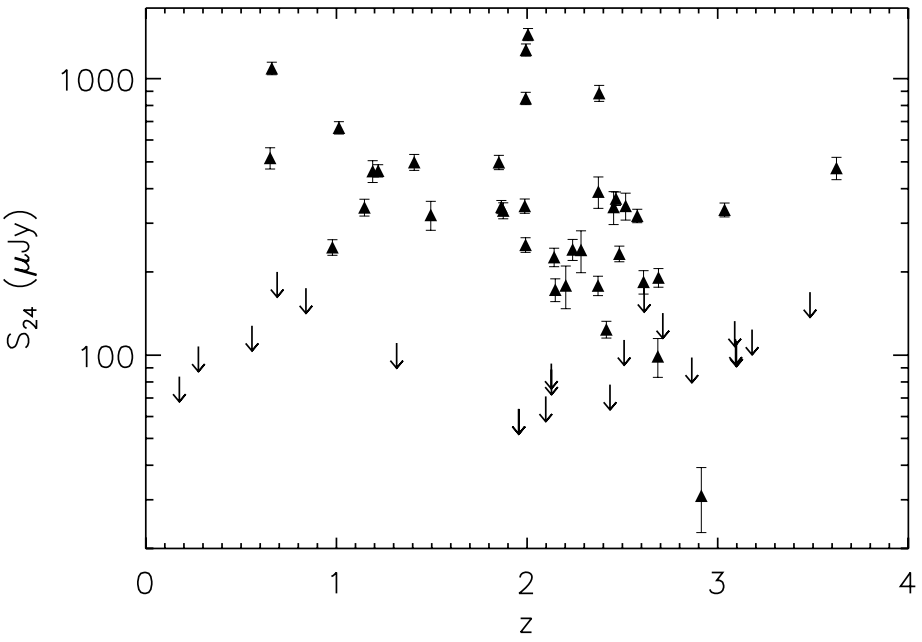

Figure 5.7 24 μm flux as a function of z for radio-detected SMGs in the C05 sample. Filled triangles represent detections, while downward arrows indicate upper limits.

et al. 2007) which show a variety of combinations of PAH emission features and mid-IR continuum, and thus indicate that use of a single template mid-IR spectrum can lead to misleading conclusions. We thus prefer to avoid extensive interpretation of the 24 μm data for the SMGs until spectra are available for more sources. We merely note that it is likely that the observed 24 μm fluxes are likely to result from varying combinations of continuum and spectral features in most objects.

5.2.2 Using 24μm–IRAC Colors to Separate AGN from Starbursts in SMGs

An important issue in determining the contribution of SMGs to the star formation history on the Universe which is unresolved is the contribution to the far-IR emission of SMGs from active nuclei. The first step in studying the relative contributions of star formation and AGN activity to the total IR luminosity is to identify which SMGs contain AGN. This is not a trivial step, even with spectroscopic data, as the studies of C05, Swinbank et al. (2004), and Takata et al. (2006) have shown. With the advent of *Spitzer*, numer-

ous authors (e.g., Lacy et al. 2004; Ivison et al. 2004; Sajina et al. 2005; Weedman et al. 2006) have proposed methods of separating AGN from strongly star forming galaxies in the general galaxy population based on mid-IR colors and fluxes. Several authors (e.g., Egami et al. 2004; Ivison et al. 2004; Ashby et al. 2006) have suggested that such mid-IR techniques can be used to identify powerful AGN in SMGs as well. In particular, Ivison et al. (2004) proposed using a diagram of the ratio $S_{24\mu\mathrm{m}}/S_{8\mu\mathrm{m}}$ plotted versus the ratio $S_{8\mu\mathrm{m}}/S_{4.5\mu\mathrm{m}}$ to distinguish star-forming galaxies from AGN-dominated sources and possibly even distinguish redshift. The idea is based on the observation that the SEDs of two relatively nearby ULIRGs, Arp 220 and Mrk 231, which are frequently used as templates for "Starburst ULIRGs" and "AGN-dominated ULIRGs," cause the two galaxies to follow well-separated tracks in $S_{24\mu\mathrm{m}}/S_{8\mu\mathrm{m}}$–$S_{8\mu\mathrm{m}}/S_{4.5\mu\mathrm{m}}$ color space as the SEDs are redshifted to larger distances. Since we now have both MIPS-24 μm and IRAC data for most of the radio-detected SMGs in the C05 sample, many of which have separate UV and optical spectral classifications, we can test the effectiveness of Ivison et al. (2004)'s color-color diagram in exposing AGN. Since we have secure spectroscopic redshifts for our sample, we can also test the use of the color-color diagram as a redshift indicator.

We plot the color-color diagram of Ivison et al. (2004) in Figure 5.8, including only the SMGs with 24 μm observations, which means we lack information for the galaxies in the SSA 13 field. In the diagram we have color-coded the SMG points by redshift as in previous figures, and those objects known to show AGN features in their rest-frame UV, optical, or IR spectra, and also any classified as an AGN from X-ray observations, are circled in black. Objects with intermediate starburst/AGN spectral signatures are outlined with black squares. We have also plotted the color-color tracks for Arp 220 and Mrk 231 for redshifts corresponding to $z = 0 - 3$, marking the location corresponding to $z = 1$ with a large diagonal cross, the location of $z = 2$ with a large plus sign, and the location of $z = 3$ with a large asterisk.

At first glance, it is apparent that the diagram will not be a good way to distinguish the redshift of SMGs; galaxies of all redshifts appear in any portion of the plot and do not appear to make a clean sequence as the tracks of Arp 220 and Mrk 231 would suggest. Our findings support the suggestion of Sajina et al. (2005) that because of large variations in 24 μm flux (as the 7.7 μm PAH feature enters and leaves the bandpass) high values of the ratio $S_{24\mu\mathrm{m}}/S_{8\mu\mathrm{m}}$ do not necessarily indicate low redshifts. On the other hand, the

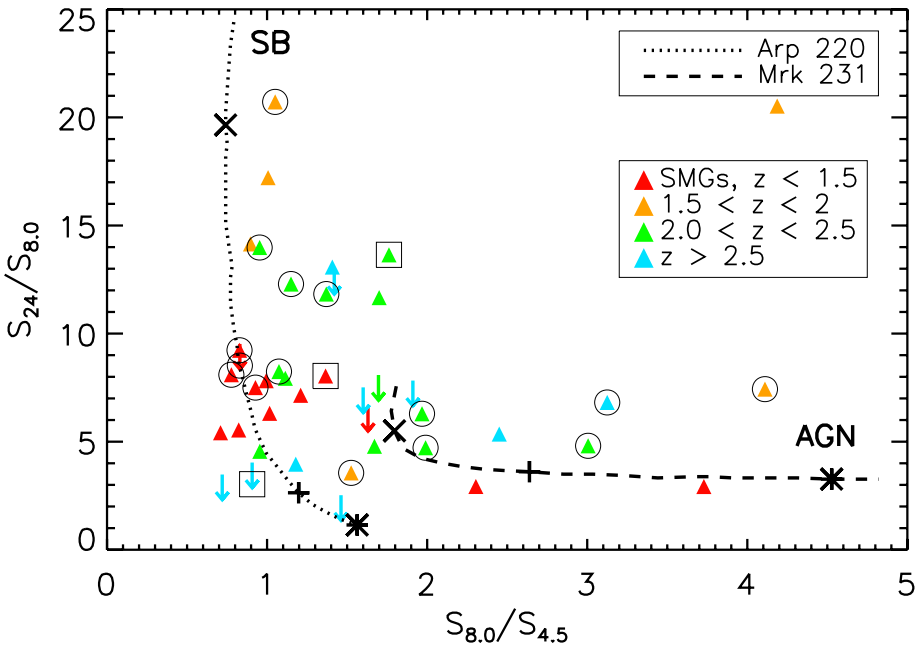

Figure 5.8 The $S_{24\mu\mathrm{m}}/S_{8\mu\mathrm{m}}$ vs. $S_{8\mu\mathrm{m}}/S_{4.5\mu\mathrm{m}}$ color-color plot proposed by Ivison et al. (2004) to separate powerful AGNs from strongly star-forming systems for SMGs. The SMGs from the sample of C05 with MIPS observations are plotted as triangles for 24 μm detections and downward arrows for sources not detected at 24 μm, and are color-coded according to redshift. The dotted line represents the color-color track of Arp 220 as its SED is redshifted, while the dashed line represents the same track for Mrk 231. Points along these tracks corresponding to the observed colors when the SEDs are redshifted to $z = (1, 2, 3)$ are represented by the large black diagonal crosses, the large black plus signs, and the large black asterisks, respectively. SMGs with AGN spectral classifications in the literature at any wavelength are outlined by black circles, and SMGs with intermediate starburst/AGN classifications are outlined by black squares.

diagram may indeed be useful to identify AGN: 5 SMGs classified as AGN do fall on the AGN track, along with several SMGs not identified as AGN. (Note that a lack of an AGN classification in this sample does not automatically indicate that it is a starburst, since for most of our sample the classifications are only available from rest-frame UV spectra, a region in which AGN spectral diagnostics are not as clearly defined as in the optical bands). One of the previously unidentified AGNs is SMM J105200.22+572420.2; both Egami et al. (2004) and Ivison et al. (2004) suggest that it should be called an AGN on the basis of its mid-IR colors. SMM J141741.81+522823.0 is picked out as an AGN in the diagram as well; Ashby et al. (2006) suggested this object to be an AGN based on its brightness and lack of PAH features in its IRS spectrum. SMM J105155.47+572312.7 is selected out as an AGN in this diagram as well, a classification also made by Egami et al. (2004) on the basis of its "warm" SED.

However, it is important to point out that not all of the SMGs with identified AGN fall on the AGN color track. At least 7 SMGs with AGN identifications fall on the starburst track, and still more fall in between the starburst and the AGN track. The interpretation of their location in the diagram is unclear for all of these sources. One possible scenario is that the SMGs on the starburst track with spectroscopically-identified AGN are galaxies with weak, non-dominant AGN and substantial populations of low-mass stars which swamp the AGN light in the near-IR. If this were the case, we might then be able to suggest that AGN strength increases across the plot from $S_{8\mu\mathrm{m}}/S_{4.5\mu\mathrm{m}} \sim 1-5$. The SMGs falling between the starburst and AGN tracks could then be interpreted as having AGNs with power intermediate between the galaxies on the starburst track and those on the AGN track, and we could conclude that most of our SMG sample is not dominated by a powerful, obscured AGN, even if an AGN is present.

However, Sajina et al. (2005) provide a different interpretation of the $S_{24\mu\mathrm{m}}/S_{8\mu\mathrm{m}}$ vs. $S_{8\mu\mathrm{m}}/S_{4.5\mu\mathrm{m}}$ color-color plot from their simulations of mid-IR color plots based on linear combinations of a mid-IR continuum spectrum from an AGN, a PAH emission spectrum, and a stellar continuum spectrum. The results of the simulations explain the $S_{24\mu\mathrm{m}}/S_{8\mu\mathrm{m}}$–$S_{8\mu\mathrm{m}}/S_{4.5\mu\mathrm{m}}$ color-color diagram as an extinction sequence at high redshift in which both PAH-dominated objects and continuum-dominated objects are shifted to redder $S_{8\mu\mathrm{m}}/S_{4.5\mu\mathrm{m}}$ colors as the optical depth along the line of sight is increased. Under this scenario, some of the SMGs on the AGN track which have not been identified as AGN

could possibly be PAH-dominated sources with large extinction. We might then interpret the SMGs with identified AGN which lie on the starburst track as less obscured sources than the identified AGN on the AGN sequence.

Given the different interpretations of the $S_{24\mu\mathrm{m}}/S_{8\mu\mathrm{m}}$ vs. $S_{8\mu\mathrm{m}}/S_{4.5\mu\mathrm{m}}$ diagram and the ambiguities caused by identified AGN which lie in the starburst region, we suggest that more investigation of the factors determining the $S_{24\mu\mathrm{m}}/S_{8\mu\mathrm{m}}$ and $S_{8\mu\mathrm{m}}/S_{4.5\mu\mathrm{m}}$ colors is needed before this particular method of separating AGN-dominated from starburst galaxies can be widely utilized. We also suggest that the near-IR may not be the best place to separate out starbusts, since the near-IR emission of galaxies is sensitive to emission from both recently-formed stars and old, evolved stars.

5.3 Properties of Radio-Selected SMGs at 70 μm

The 70 μm band of MIPS samples the rest-frame 24 μm emission from galaxies at $z \sim 2$, and thus will be sensitive to warm dust at these redshifts. However, the instrument is limited by practical considerations as well as by confusion limits, such that it can only detect objects with flux greater than $\sim$ 1 mJy at a 3-sigma level (Frayer et al. 2006b). Detections of $z \sim 2$ SMGs in this band of $\sim$a few mJy would likely indicate a somewhat flat SED and the presence of a strong AGN. Detections of $z < 1$ SMGs at 70 μm at similar flux levels, however, will not necessarily indicate a strong AGN; rather, they will be consistent with very cold SEDs. Here, we discuss the 70 μm data for the C05 sample of SMGs presented in Chapter 3.

We mentioned in Chapter 3 that at 70 μm, a much smaller fraction of the C05 SMG sample are detected than in the IRAC bands or at 24 μm. The four radio-selected SMGs detected at 70 μm, SMM J105200.22+572420.2 ($z = 0.689$), SMM J123634.51+621241.0 ($z = 1.219$), SMM J141742.04+523025.7 ($z = 0.661$), and SMM J141741.81+522823.0 ($z = 1.150$), lie in the low-redshift tail of the radio-detected SMG redshift distribution (see Chapter 3), which is consistent with the results of Huynh et al. (2007). Even in the GOODS-N field, which has the deepest observations of all the SMG fields at 70 μm, no high-redshift sources are detected, so it is unlikely that the variation in coverage depth between SMG fields is entirely responsible for the low detection rate.

To obtain an idea of the average 70 μm flux for the SMGs not detected at that wave-

length, we have stacked $84'' \times 84''$ cutouts from the $70\,\mu$m mosaics centered on the radio positions of the SMGs undetected at $70\,\mu$m, in which all sources with S/N > 3 have been subtracted. We employ a process similar to that of Huynh et al. (2007): we first subtract the median of its pixels from each cutout in the stack to improve the local background removal and then rotate each cutout by 90° relative to the image before it in the stack before coadding the images in the stack. The coaddition weights each cutout image by the RMS of its pixels. For comparison, we have also constructed a coadded, stacked image of random positions within the mosaics. To effectively represent the different depths of imaging between fields in the random stack, we have used in the random stack the same number of random cutouts from a particular field as the number of undetected SMGs in that field.

In the stacked image of 50 SMG source positions, we find a 3.4σ source with a flux density of $0.48 \pm 0.14\,\mu$Jy. In comparison, in the stack of random image positions, no sources with S/N > 2 are found, suggesting that the source in the stacked SMG image is real. However, given the range of redshift of our undetected SMG sources ($0.2 < z < 3.5$) and the behavior of the K-correction, it is unclear if the flux density of the source should be interpreted as typical for all of the undetected SMGs or just a particular subset. Huynh et al. (2007) find in their stacking analysis of SMGs at $70\,\mu$m that the $\sim 3\sigma$ source found in their stacked image is dominated by galaxies with $z < 2$. Accordingly, we divide our stack into separate stacks for sources with $z < 2$ and $z > 2$ for comparison. Unlike the findings of Huynh et al. (2007), no sources are detected above a S/N ~ 2 level in either of our low or high-z stacks, but given the non-uniform depth of the $70\,\mu$m mosaics and that a significant number of the low-z sources in the low-z stack come from fields with less deep coverage than the GOODS-N field, it is unclear that the stack of our low-z SMGs are any different than that of Huynh et al. (2007).

5.4 Comparison of SMG Near and Mid-IR Properties to Other High-z Galaxy Populations

The various populations of high-redshift galaxies discussed in Chapter 1, which are selected at different wavelengths, might seem to have little in common, since at the wavelengths at which they are selected the physical mechanisms responsible for their emission are different. Also, as discussed in Chapter 1, the overlap between the galaxy populations tends to be

small. Yet, all of the galaxy populations obviously have one characteristic in common which may prove to be the key to understanding how the populations relate to one another: stars. It is thus plausible that comparing the properties of the different high-z populations at wavelengths where stellar emission dominates and the effects of dust are at a minimum will be very useful towards understanding the relationships between the different types of galaxies. With observations for the largest sample of SMGs with spectroscopic redshifts from the IRAC instrument of *Spitzer*, we can now make more representative comparisons between the near and mid-IR properties of radio-detected SMGs and other high-redshift galaxy populations. We can also compare the MIPS properties of the different types of galaxies to attempt to learn about any differences in dust properties.

Here, we choose to compare SMGs to several different types of high-z galaxies which span a range of mass, luminosity, and nuclear activity, hoping to shed some light on physical reasons behind any observed differences between the galaxy types. We prefer to use galaxies with spectroscopic redshifts for our comparison, so we construct our comparison sample from the catalog of LBG and BX/BM galaxies of Reddy et al. (2006b) in the GOODS-N field, galaxies which represent stellar-dominated star forming galaxies with low obscuration; the sample of 24 μm-selected galaxies from the *Spitzer*-xFLS presented by Yan et al. (2007, spectra) and Sajina et al. (2007, photometry), which represent a different type of highly IR-luminous galaxy other than SMGs; and the sample of powerful, massive high-z radio galaxies (HzRGs) from Seymour et al. (2007), which represent highly obscured, radio-loud AGN. In addition, we have separated out the galaxies in the sample of Reddy et al. (2006b) which satisfy the distant red galaxy (DRG) criteria of Franx et al. (2003), which we treat separately as another comparison set of galaxies; these DRGs also satisfy BX/BM or LBG criterion, which means they are likely to be star-forming DRGs instead of passive DRGs. Also, when available, we include published statistics of larger DRG and BzK galaxy samples to give a better representation of these near-IR selected galaxies; however, since the samples themselves tend to be unpublished, they are not included in plots.

5.4.1 Comparisons of IRAC Properties

5.4.1.1 IRAC Detection Rates

In comparing the galaxy samples, we immediately notice a significant difference in the detection rates of the different galaxy types in the various IRAC bands. Earlier, we found that $> 90\%$ of our radio-detected SMG sample were detected in the 3.6 and 4.5 μm bands of IRAC, while $\sim 80\%$ of the sample were detected in the 5.8 and 8.0 μm bands. The high-z radio galaxy sample and 24 μm-selected sample have similarly high rates of detection in the IRAC bands as the SMGs. However, the LBGs, BX/BM galaxies, and DRGs from Reddy et al. (2006b) have much lower detection fractions in the 5.8 and 8.0 μm bands than the SMGs, radio galaxies, and 24 μm galaxies, despite the fact that the IRAC measurements of these sources come from one of the deepest IRAC data sets available (GOODS-N). The BX/BM and DRG samples are detected only $\sim 60 - 65\%$ of the time at 5.8 μm and $\sim 40\%$ of the time at 8.0 μm, although they have detection fractions at 3.6 and 4.5 μm similar to those of the SMGs ($> 90\%$). The LBGs have an even lower detection fraction at 5.8 and 8.0 μm of $\sim 33\%$, a point noted by Rigopoulou et al. (2006), and their detection fraction at 3.6 and 4.5 μm is also slightly lower than for the BX/BM-selected sample. There are several possible explanations to the lower detection rate of the UV/optical-selected galaxies in the longer wavelength IRAC bands. One is that the SMGs, HzRGs, and 24 μm-selected types may typically have larger stellar masses than the optically-selected sources, causing an increase in luminosity in the region of the stellar peak at rest wavelength 1.6 μm. Alternatively, the galaxies not selected at optical wavelengths could have a more significant contribution, for some reason, from stars in the highly-luminous thermally pulsating asymptotic giant branch (TP-AGB) phase (Maraston 2005; Maraston et al. 2006). It is also possible that SMGs, HzRGs, and 24 μm galaxies could have significant contributions from AGN in the near-IR which are not present for the galaxies selected in the rest-frame UV and optical. We require additional information, however, before we can distinguish the effects. Thus, we compare the near-IR colors of the galaxies below, to see if we can shed any light on the contributions from stars and hot dust.

5.4.1.2 Comparison of IRAC Colors

In Figure 5.9 we recreate the color-color diagram shown in Figure 5.3 for each of the different samples of high-z galaxies. Each panel plots a different galaxy type over a sample of field sources from the GOODS-N field, and the points for each galaxy type are color coded by redshift in the same manner as in Figure 5.3. Sources in all of the galaxy samples must have detections in the 3.6 and 4.5 μm IRAC bands to be included in this plot; however, as discussed in the previous paragraph, we will lose only $\sim 10\%$ of the sources from each sample through this requirement, and thus our results will still be representative of the different populations.

The different high-z populations do tend to have different distributions in the $S_{4.5}/S_{3.6}$–$S_{5.8}/S_{4.5}$ color space, though none stand out so much that they can be cleanly separated from the other types. The most noticeable aspect of Figure 5.9 is that the distribution of SMGs in the color space most resembles that of the powerful high-z radio galaxies, as both the SMGs and HzRGs are frequently found to be red in both $S_{4.5}/S_{3.6}$ and $S_{5.8}/S_{4.5}$, but also show some objects which are blue in $S_{5.8}/S_{4.5}$. The high-z radio galaxies are all powerful, obscured AGN: does the similarity in colors indicate that $z > 1.5$ SMGs are also dominated by powerful AGN? We suspect that it is not necessarily true that the IR, or at least near-IR, luminosity of SMGs is dominated by AGN, since Seymour et al. (2007) find that half of their sample of HzRGs observed by both IRAC and MIPS are dominated by starlight in the rest-frame near-IR, while for another 20% of their sample 60–90% of the rest-frame near-IR luminosity can be attributed to starlight. This contradictory-seeming situation (stellar light dominating the light of a powerful AGN) can be attributed to the orientation of the central AGN under AGN unification scenarios (e.g., Antonucci 1993). Thus, the near-IR colors of the radio-loud galaxies may not be entirely reflecting an active nucleus. However, the color-color diagram of Scoville et al. (2000) suggests that the position of the high-z radio galaxies implies significant contribution from dust at 1000 K, so it is unclear what the actual contributions of stars and AGN are. The color similarity between SMGs and radio-loud galaxies may indeed indicate that the two have similarly massive underlying stellar populations, a possibility we explore further in Chapter 6 when we calculate stellar masses for our SMG sample.

Another observation of interest in Figure 5.9 is that a large number of the BX/BM

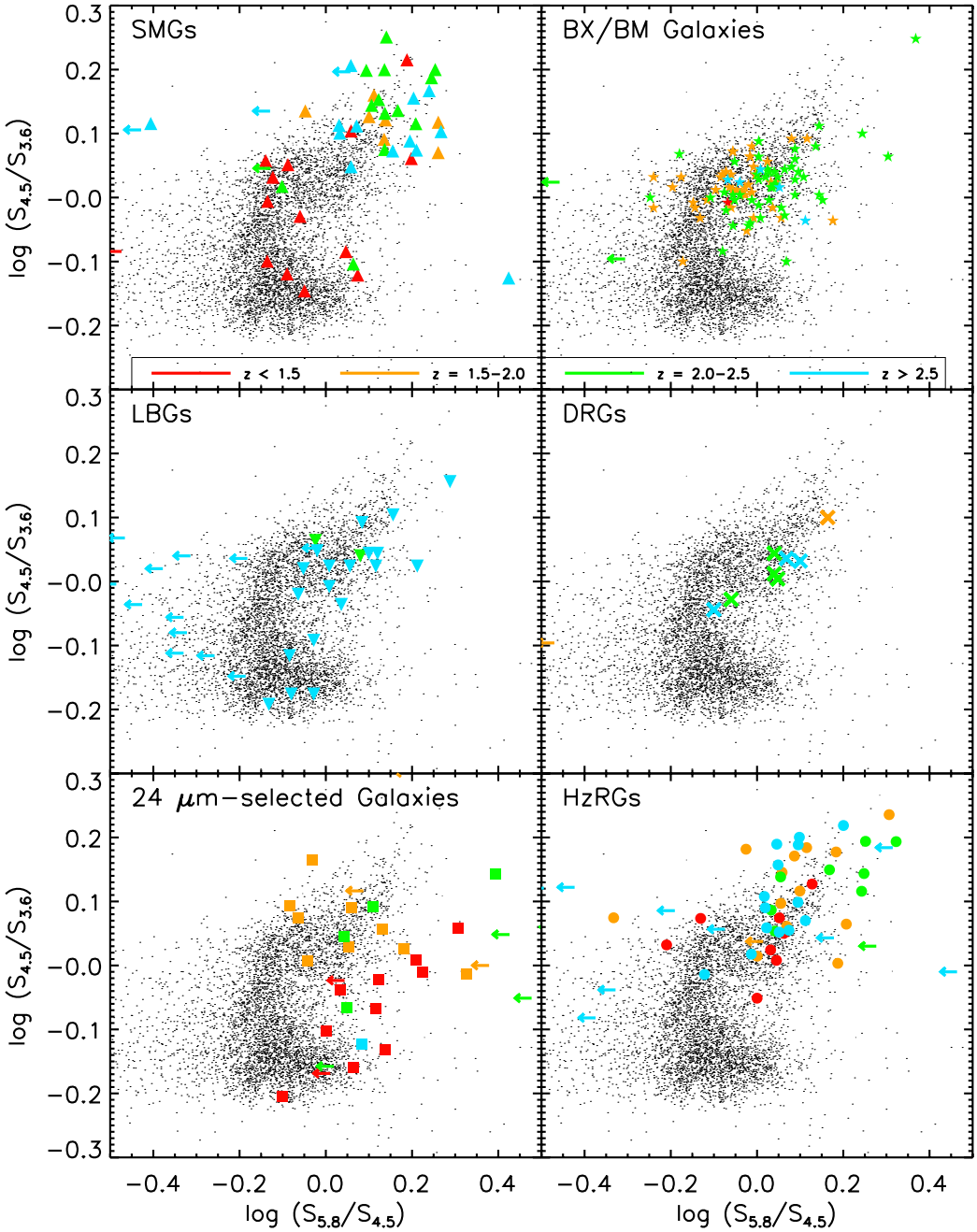

Figure 5.9 4.5μm/3.6μm vs. 5.8μm/4.5μm color-color diagrams comparing radio-detected SMGs in the C05 sample to field galaxies and samples of BX/BM galaxies, LBGs, DRGs, 24 μm-selected galaxies, and high-z radio galaxies. The redshift color coding is the same as in Figure 5.3. Field galaxies from the GOODS-N field are represented by black dots. Leftward-pointing arrows indicate galaxies which are detected at 3.6 and 4.5 μm but not at 5.8 μm.

galaxies and some LBGs fill in the "gap" seen in the SMGs' color-color distribution near $(\log S_{5.8}/S_{4.5}, \log S_{4.5}/S_{3.6}) \sim (0, 0.03)$, which we pointed out in §5.1.3, and do not overlap a great deal in color space with SMGs at similar redshifts. Much of the overlap of the SMGs with the optically-selected galaxies appears to be in the low-redshift SMGs which lie on the field sequence, though there are some fairly blue high-z SMGs which coincide with the blue tail of the LBGs and BX/BM sources. The BX/BM galaxies and LBGs tend to be less red in both $S_{4.5}/S_{3.6}$ and $S_{5.8}/S_{4.5}$ than the majority of the SMGs at similar redshifts, but there are at least 10 BX/BM galaxies and LBGs which share the very red colors of the $z > 1.5$ SMGs. These very red optically-selected galaxies may represent the IR-luminous LBGs (LBGs detected at 24 μm) suggested by Huang et al. (2005) as possible bridges between LBG and SMG population.

The 24 μm-selected galaxy sample does not overlap a great deal with SMGs or any of the other galaxy populations represented in Figure 5.9 in the $S_{4.5}/S_{3.6}$–$S_{5.8}/S_{4.5}$ color space. The observed difference may simply be due to our small sample sizes, though it will be interesting to do this color comparison when larger samples of both SMGs and 24 μm galaxies with spectroscopic redshifts are available. From the currently available data, it seems that the 24 μm galaxies at $z < 1.5$ are redder in $S_{5.8}/S_{4.5}$ than SMGs at similar redshifts and that the higher-z 24 μm galaxies are somewhat bluer in $S_{4.5}/S_{3.6}$. One possible explanation for these colors is that a higher fraction of the lower-z 24 μm galaxies host obscured active nuclei than SMGs at similar redshifts.

Another color-color diagram discussed in the literature is the $S_{8.0\mu\mathrm{m}}/S_{4.5\mu\mathrm{m}}$–$S_{5.8\mu\mathrm{m}}/S_{3.6\mu\mathrm{m}}$ diagram, which was suggested by Lacy et al. (2004) as a way to discriminate obscured AGNs from bluer field objects. In the $S_{8.0}/S_{4.5}$–$S_{5.8}/S_{3.6}$ color space, most of the objects in an observed field will fall into a clump in the range [-0.5,0] in both axes. Two plumes are observed to extend redward in $S_{8.0}/S_{4.5}$, one which is more blue in $S_{5.8}/S_{3.6}$ and one which is more red. Lacy et al. (2004) identify this red plume with obscured AGN and demarcate a region in color-color space which they use to identify AGN. In Figure 5.10 we plot the $S_{8.0}/S_{4.5}$–$S_{5.8}/S_{3.6}$ color-color diagram for field galaxies in the GOODS-N field and over-plot the different galaxy populations we have been examining: SMGs, BX/BM galaxies, LBGs, DRGs, 24 μm-selected galaxies, and high-z radio galaxies, using the objects which have detections in all 4 IRAC bands. In Figure 5.10 we also indicate with dotted lines the region in color space that Lacy et al. (2004) associate with obscured AGN. Perhaps not

surprisingly, nearly all of the high-z radio galaxies fall in the AGN region, which is also noted by Seymour et al. (2007). What is surprising is that most of the rest of the high-z galaxy populations also fall in the AGN region, including much of the BX/BM and LBG populations, which are not thought to host powerful obscured AGN. Our findings support the arguments of Sajina et al. (2007), who showed that the $S_{8.0}/S_{4.5}$–$S_{5.8}/S_{3.6}$ critera are unreliable at $z > 2$ because the host galaxies can dominate the AGN near the location of the stellar bump at $1.6\,\mu$m. Thus, we should not necessarily assume that any of these galaxies have powerful AGN simply because they fall into the AGN region of the $S_{8.0}/S_{4.5}$–$S_{5.8}/S_{3.6}$ color-color plot.

We compare the different galaxy samples in another way in Figure 5.11, using the same color-magnitude diagram as shown in Figure 5.4. Again, the different high-z populations tend to occupy different regions of color-magnitude space, but are not distinct enough to be able to cleanly separate each one from the others. The SMGs are clearly brighter on average at $5.8\,\mu$m and more red in $S_{5.8}/S_{3.6}$ than the optical and UV-selected galaxies, but are typically fainter than the high-z radio galaxies at the same wavelength. The SMG sample may also be typically fainter than the $24\,\mu$m-selected sample, though there are many upper limits in the $24\,\mu$m-selected sample which make it difficult to say with certainty that the $24\,\mu$m galaxies are brighter. If the 5.8μm flux of SMGs is dominated by starlight, this color-magnitude diagram indicates that SMGs are more massive (or contain a larger fraction of TP-AGB stars) than BX/BM galaxies, LBGs, and DRGs. The optically-selected galaxies appear to overlap the moderately faint, red field galaxy population, with the exception of several bright LBGs.

We have also indicated in Figure 5.11 the region Pope et al. (2006) found to contain only $z > 1.5$ SMGs, just to see if the region will also pick out other high-z redshift galaxy populations. Doing so will test to see if this color-magnitude diagram can be used to identify SMG counterparts in IRAC bands from other galaxies. It is evident that most optically-selected high-z galaxies will not be sufficiently bright or red to fall into the demarcated region, though a few will. On the other hand, most of the high-z radio galaxies fall into the region, as do some $24\,\mu$m-selected galaxies. However, high-z radio galaxies are more rare on the sky than SMGs, so when trying to identify a SMG counterpart through this color-magnitude diagram it is unlikely that a high-z radio source and an SMG will be in such close proximity that they could both be counterparts to a particular submm source. The

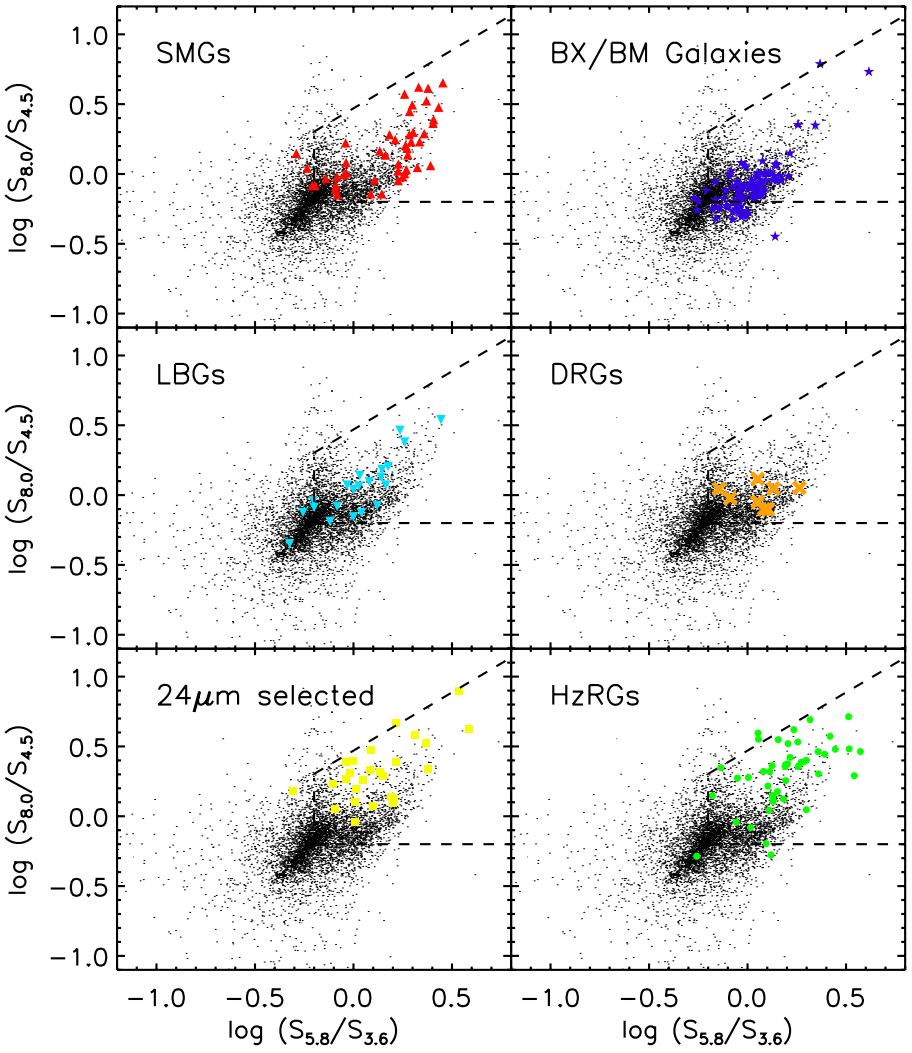

Figure 5.10 $S_{8.0\mu\mathrm{m}}/S_{4.5\mu\mathrm{m}}$ vs. $S_{5.8\mu\mathrm{m}}/S_{3.6\mu\mathrm{m}}$ color-color diagram for field sources and high-z galaxy populations. Field galaxies are represented by black dots, while high-z galaxies are the colored points. Dashed lines mark off the region which Lacy et al. (2004) identified with obscured AGN.

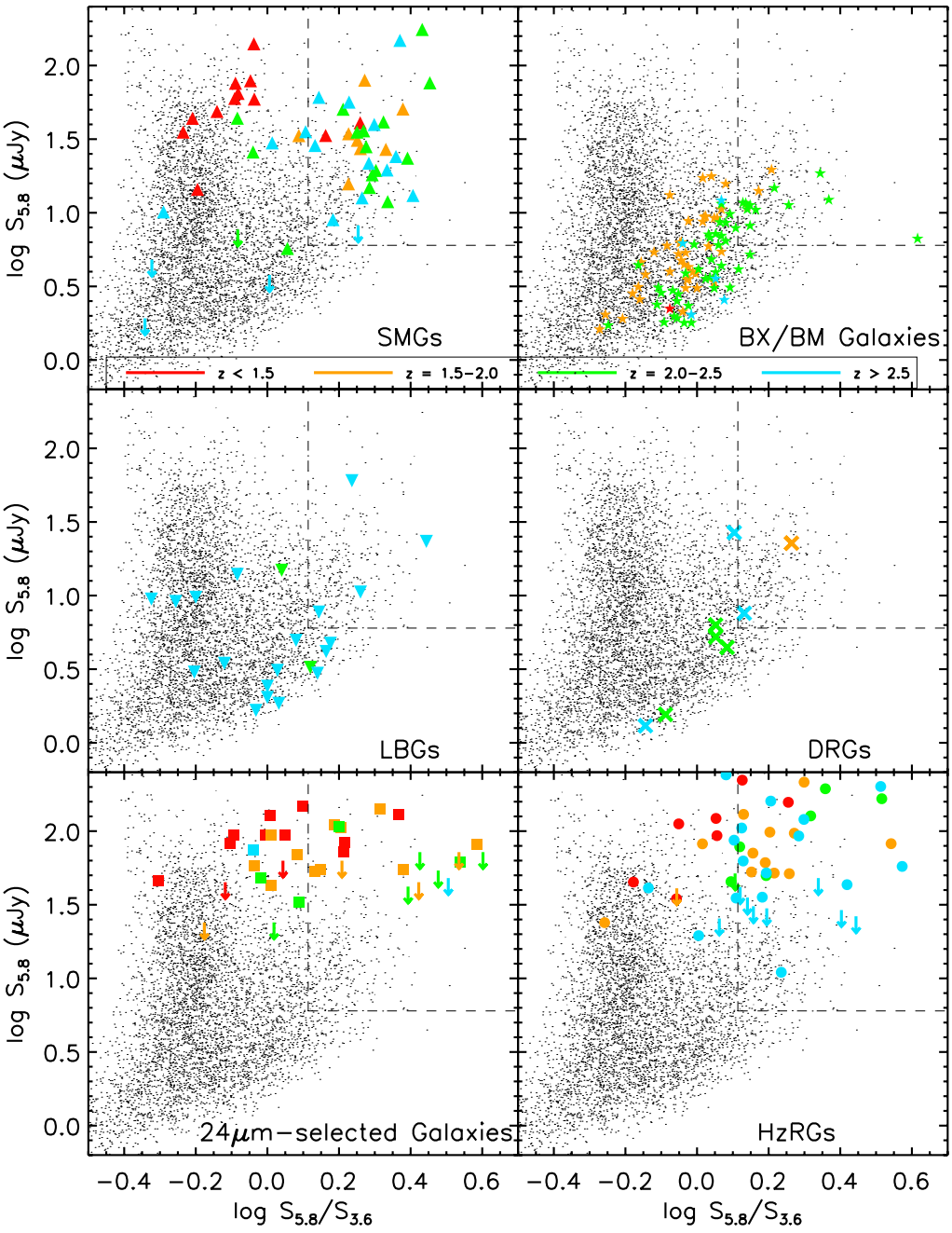

Figure 5.11 5.8 μm vs. 5.8μm/3.6μm color-magnitude diagram for radio-detected SMGs in the C05 sample, BX/BM galaxies, LBGs, DRGs, 24 μm-selected galaxies, and high-z radio galaxies. Field galaxies from GOODS-N are plotted as small dots for reference. The high-z galaxy points are color-coded according to redshift as in Figure 5.9. Downward-pointing arrows indicate galaxies which are detected at 3.6 μm but not at 5.8 μm. Dashed lines indicate the region of the plot identified by Pope et al. (2006) as containing SMGs at $z > 1.5$.

24 μm galaxies may be more of a problem to separate from SMG counterparts through this particular diagram, but it may be possible to incorporate other data to separate out a SMG counterpart from a 24 μm selected galaxy. All of these findings tend to support the use of the $S_{5.8}$–$S_{5.8}/S_{3.6}$ color-magnitude diagram to help select SMG counterparts in the mid-IR. However, the main problem for using this color-magnitude diagram to identify high-z SMG counterparts remains: a possible counterpart cannot be excluded simply because it does not lie in the upper right of the color-magnitude diagram. More field galaxies will lie outside the designated region than within it, which means it will still be difficult to determine a counterpart for a SMG through this diagram when the SMG does not fall in the marked off region of the diagram.

5.4.2 Comparison of MIPS Properties

In the MIPS bands, disparities in detection rate among the different galaxy samples emerge once more, though not in the 24 μm band, where most of the galaxy samples seem to have rather similar detection rates. We found in §3.5.3 that for our SMG sample with MIPS observations, we detected $\sim 70\%$ at 24 μm. Among the BX/BM galaxies from the catalog of Reddy et al. (2006b), 65% are detected by MIPS at 24 μm, while 53% of the LBGs from the same catalog are detected at 24 μm. Roughly half of the DRG sample of Papovich et al. (2006) is detected above 50 μJy at 24 μm, while 62% of the UV-selected galaxies meeting the DRG criteria in the catalog of Reddy et al. (2006b) are detected at at 24 μm as well. Among another common optically-selected population, the star forming BzK galaxies (sBzK), Daddi et al. (2007) obtain a higher detection rate, from 65–100% depending on K-band magnitude. For the 24 μm-selected sample of Yan et al. (2007) the detection rate at 24 μm is, of course, 100%, and for the HzRG sample of Seymour et al. (2007) the detection rate among sources with MIPS observations is 84%.

In the 70 μm band, where 7% of our SMG sample is detected, the major differences appear. For UV and optically-selected sources, 70 μm measurements are difficult to find, probably because the sensitivity of the 70 μm band causes it to be unlikely that the majority of UV and optically-selected galaxies would be detected in the deepest observations. Papovich et al. (2007) report detections of 4 DRGs with photometric redshifts between $z = 1.5$ and $z = 2.5$; however, these detections represent $< 1\%$ of their total sample, illustrating the low probability of detection for optically-selected high-z sources at 70 μm. On the other

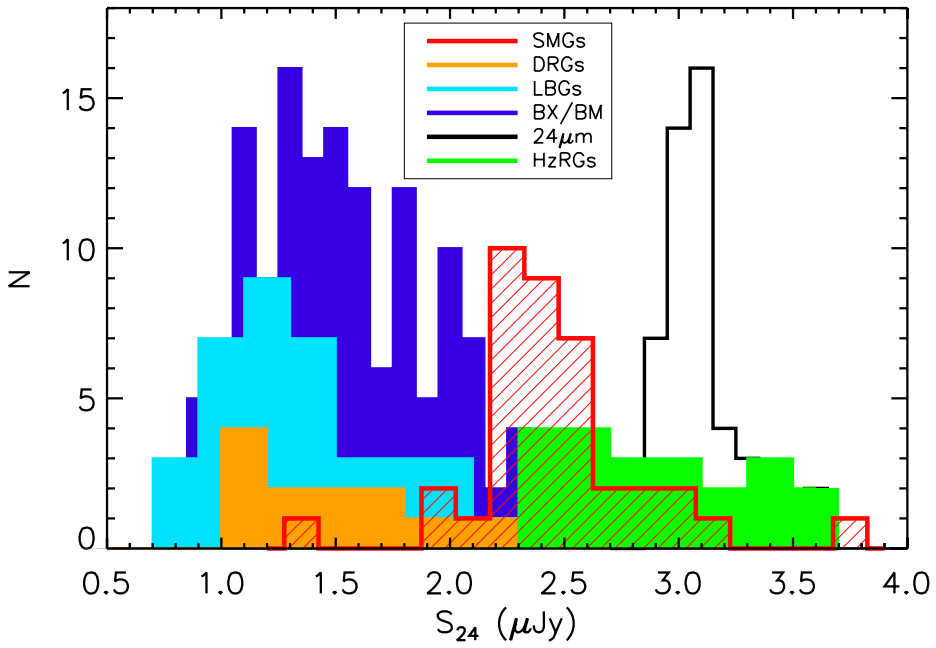

Figure 5.12 Distribution of 24 μm flux density for detected sources for SMGs (red hatched histogram), BX/BM galaxies (dark blue histogram), LBGs (light blue histogram), DRGs (orange histogram), 24 μm-selected galaxies (black histogram), and high-z radio galaxies (green histogram). The histograms have bin sizes of $\Delta \log S_{24} = 0.1$ (BX/BM, 24 μm-selected galaxies), $\Delta \log S_{24} = 0.15$ (SMGs), and $\Delta \log S_{24} = 0.2$ (LBGs, DRGs, HzRGs) for ease of viewing.

hand, the 24 μm-selected galaxies have a detection rate at 70 μm of 69%, and the high-z radio galaxies are detected 21% of the time. We note that the sources which are brightest at 24 μm among the SMGs, 24 μm galaxies, and HzRGs tend to be those which are also detected at 70 μm.

The distributions of 24 μm fluxes in Figure 5.12 show that SMGs peak in the middle of the overall range of high-z galaxy fluxes, though its distribution has tails out to the lowest and highest ends of the range. On average, the BX/BM galaxies, LBGs, and DRGs tend to be much fainter than the SMGs at 24 μm, as their flux density distributions tend to peak an order of magnitude or more lower than the SMG distribution. When the non-detections of the UV/optically-selected galaxies are taken into account, these galaxies are much more faint on average at 24 μm. However, the BX/BM galaxies show a high-flux tail that extends out to the location of the peak of the SMGs' distribution, implying the

existence of a segment of that population which is infrared luminous and likely similar to the IR-luminous LBGs described by Huang et al. (2005). Though not shown in Figure 5.12, the sBzK galaxies in the sample of Daddi et al. (2007) overlap with both the BX/BM and SMG populations at 24 μm, with 24 μm fluxes ranging from 10 to 1000 μJy. The majority of the sample of sBzK galaxies falls below $S_{24} = 100\,\mu$Jy, but a significant fraction fall in the 100–500 μJy range. In comparison to the UV-selected sources, SMGs must have more dust continuum and/or brighter PAH features; however, SMGs may have similar mid-IR properties to optically-selected high-z sources. The 24 μm-selected galaxies and HzRGs fill out the upper end of the range of 24 μm flux and are clearly much brighter, on average, than SMGs at 24 μm, indicating that they harbor significantly more hot dust than SMGs or have much stronger PAH features (or both). However, the HzRGs show variation of up to an order of magnitude in 24 μm flux density, and the fainter tail of their flux distribution overlaps the higher end of the SMG distribution, which suggests some variation in the dust temperatures in these objects.

Next, we turn our attention to the 24 μm colors of the different types of galaxies. In Figure 5.13 we plot the $S_{24}/S_{8.0}$–$S_{8.0}/S_{4.5}$ color-color diagram from Ivison et al. (2004), comparing SMGs, BX/BM galaxies, 24 μm-selected galaxies, and high-z radio galaxies. While we have overplotted the color tracks of Arp 220 and Mrk 231 as in Figure 5.8, we are not explicity looking to separate AGN from starbursts in this plot; the tracks are merely reference points. We have once more color-coded the galaxy points by redshift, using the same scheme as in Figure 5.9. The different types of galaxies have somewhat different distributions in color space. Unlike the other galaxy populations shown in the plot, the BX/BM galaxies with 24 μm detections follow the color-color track of Arp 220 rather closely, with only 2 objects falling near the Mrk 231 track. Some BX/BM display AGN signatures in their rest-frame UV/optical spectra, so it would not be unexpected to find some galaxies with Mrk 231-like colors. Moving on to the HzRGs, we see a rather similar distribution in color space to that of the SMGs, in that some objects fall near the Arp 220 track (though again, the redshifts of the HzRGs falling near the track do not correspond to the redshift Arp 220 would have at this point in color-color space), while some of the HzRGs fall near the Mrk 231 track, and some fall between the two tracks. The 24 μm-selected galaxies, on the other hand, appear to be totally different from the other galaxy types in the $S_{24}/S_{8.0}$–$S_{8.0}/S_{4.5}$ color space. The 24 μm galaxies cover the same range

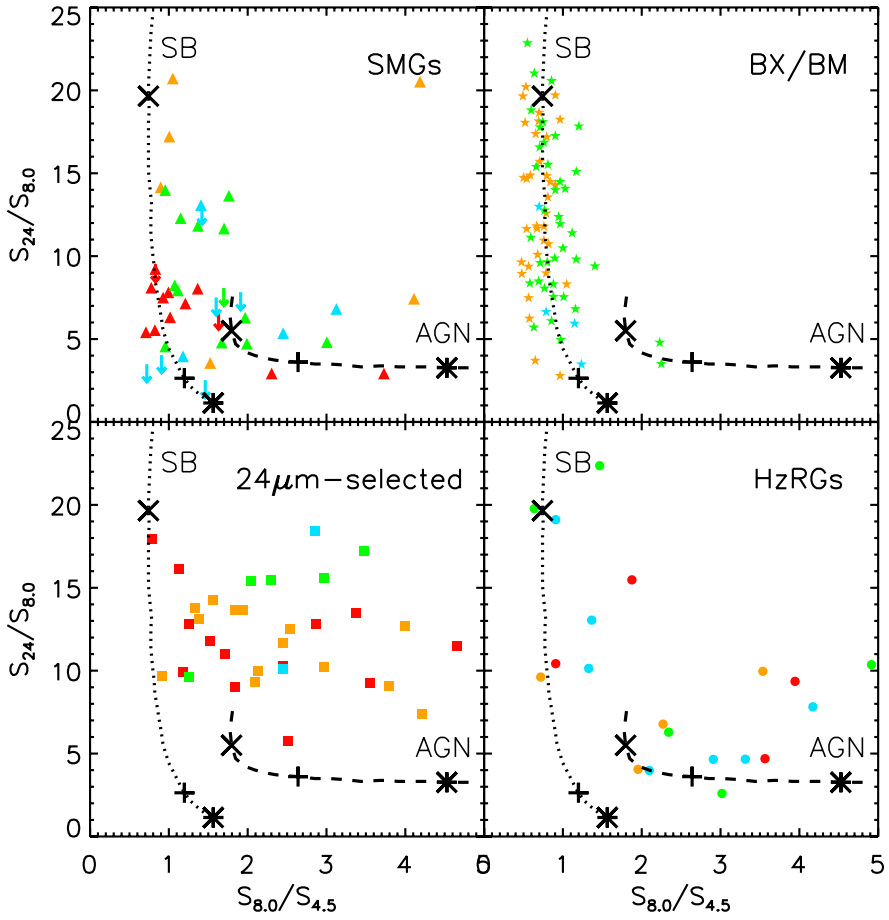

Figure 5.13 Comparison of $S_{24}/S_{8.0}$–$S_{8.0}/S_{4.5}$ color-color plots for different high-z galaxy populations. The points are color-coded by redshift as in Figure 5.11.

in $S_{8.0}/S_{4.5}$, yet their $S_{24}/S_{8.0}$ flux ratio at a given value of $S_{8.0}/S_{4.5}$ tends to be larger. That this should necessarily be the case because the 24 μm-selected sample is bright at 24 μm by definition is not true: it could happen that these galaxies would have 8.0 μm flux densities that would scale with the 24 μm flux, resulting in similar colors to the SMGs and HzRGs. But this is clearly not the case. For some reason, the 24 μm- selected galaxies are systematically fainter at 8 μm than we might expect from their 24 μm fluxes.

In comparing the different populations, the suggestion of Sajina et al. (2005) that the trends in this diagram might be a function of extinction at high redshift seems plausible. We see that the BX/BM galaxies, which are known to have low extinction since we observe their rest-frame UV light, lie consistently on the far left of the plot. The 24 μm-selected galaxies, which must contain significant dust, move toward the right of the plot and scatter

significantly more. We observe the HzRGs scattered towards the red end and high extinction, which is consistent with their nature of being highly obscured active galaxies. Under this interpretation, the SMGs could be seen as having varying quantities of extinction since we see the galaxies all over the plot.

The 24 μm-selected galaxies are clearly different in the MIPS bands from SMGs at the same redshifts. The higher mid-IR luminosities of the 24 μm galaxies imply that they contain either a continuum component that most SMGs lack, presumably from an AGN, or have significantly brighter PAH features than SMGs. Both powerful AGNs and strong PAHs are observed in the mid-IR spectra of the 24 μm galaxies (Yan et al. 2007), so it is difficult to determine which effect (or both?) has more influence. Detailed comparison of SMGs with 24 μm-selected galaxies may shed light on how star formation and AGN contribute to the dust heating in both types of systems, and while it is beyond the scope of our present discussion, it will be valuable in the future to carry out such a study.

5.5 Summary

In this chapter, we have examined the near and mid-IR properties of the Chapman et al. (2005) sample of radio-detected SMGs observed with the IRAC and MIPS instruments of *Spitzer*. We have found that SMGs have red IRAC colors indicating that their near-IR SEDs continue to rise through at least the first three bands and show remarkably little scatter when compared with the rest-frame optical colors. The IRAC colors also indicate contributions from both low-mass stars and dust emission in many $z > 2$ SMGs. SMGs appear to be brighter at 5.8 μm and redder than faint field galaxies. In the 24μm band of MIPS, we find that the fluxes of SMGs scatter over 2 orders of magnitude and are not obviously correlated with redshift, which may be an effect of mid- IR spectral features passing in and out of the 24 μm bandpass at different redshifts. In the 70 μm MIPS band, we detect only a few SMGs, all of which lie in the low-redshift tail of the redshift distribution of SMGs.

We also compare the IRAC and MIPS properties of SMGs to those of high-redshift UV-selected galaxies, 24 μm-selected galaxies, and powerful high-z radio galaxies in this chapter, finding:

- In the IRAC bands, which sample the region near the peak of stellar emission in

galaxies and also extremely hot dust ($\sim 500 - 1500\,\mathrm{K}$) from obscured AGN:

  - SMGs are brighter and redder than UV-selected galaxies, suggesting they have higher dust content, higher stellar mass, or higher AGN contribution, or some combination of these factors.
  - The near-IR colors of SMGs are most similar to those of high-z radio galaxies, objects which are known to contain powerful, obscured AGN.

- In the $24\,\mu$m MIPS band, which traces emission from warm dust and PAH molecules:
  - SMGs are brighter at $24\,\mu$m than UV-selected galaxies, but have a similar range in flux to DRG and BzK star-forming galaxies.
  - SMGs are much fainter than $24\,\mu$m-selected galaxies at similar redshifts and somewhat fainter than high-z radio galaxies, suggesting that the dust in SMGs has lower temperature than the dust in the $24\,\mu$m-selected galaxies and high-z radio-bright galaxies.

For future studies, we suggest that detailed comparisons of $24\,\mu$m-selected galaxies with SMGs may reveal valuable information on how AGN and star formation contribute to the luminosity of ultraluminous IR galaxies at high redshift.

Chapter 6

The Stellar Mass Content of Submillimeter-Selected Galaxies

The high star formation rates of submillimeter-selected galaxies (SMGs) implied by their IR luminosities suggest that these galaxies may be forming a large mass of stars in a very short time, leading to the hypothesis that the population may represent the formation phase of the most massive spheroids (e.g., Smail et al. 2002, 2004). While it appears from molecular gas observations that SMGs contain enough gas to form a massive stellar system at some point in their evolution, whether or not they contain enough mass to form a giant elliptical galaxy depends on the mass of their underlying stellar populations. However, our knowledge of the underlying, evolved stellar content of SMGs is limited.

The stellar mass of a galaxy, while one of its most fundamental characteristics, is one of the most difficult to determine directly. While dynamical masses and gas masses can be estimated through spectroscopic observations of emission lines from galaxies, stellar masses must be inferred from the total light we observe from the galaxy. Studies of open star clusters in the Milky Way indicate that the integrated light from a population of stars is a strong function of age and metallicity, which complicate our ability to estimate a mass from the integrated emission of a galaxy. Extinction of starlight due to dust is also a significant problem in determining stellar mass from the light we observe, causing the mass to be significantly underestimated if the data are not corrected for the effects of reddening.

Brinchmann & Ellis (2000) introduced the technique of estimating the stellar mass ($M_\star$) of galaxies of known redshift through fitting evolutionary population synthesis models to an object's optical-band and near-IR photometry. The underlying argument the technique exploits is that the near-IR luminosity of a $z < 1$ galaxy is a better indicator of the total

stellar mass of a galaxy than the optical luminosity due to the increased sensitivity of the optical bands to recent episodes of star formation (e.g., over a range of ages in which the rest-frame V-band luminosity varies by a factor of 10, the rest-frame near-IR luminosity varies by only a factor of 2; Leitherer et al. 1999; Bruzual & Charlot 2003). By fitting population synthesis models of different ages, extinctions, and metallicities to the observed SED of a galaxy to determine the best-fit normalization and, thus, $M_\star$, Brinchmann & Ellis (2000) proposed that they could correct relative $M_\star$ estimates for the uncertainty in the age of a galaxy's stellar population, the dominant uncertainty when inferring $M_\star$ from luminosity. This SED fitting method has since been modified (e.g., Kauffmann et al. 2003; Bundy et al. 2005) and applied to large samples of galaxies at low redshift, e.g., $\sim 10^5$ $z < 0.2$ Sloan Digital Sky Survey galaxies (Kauffmann et al. 2003), and intermediate redshift, e.g., AEGIS galaxies at $0.7 < z < 1.1$ (Noeske et al. 2007), as well as select populations of high-redshift galaxies (e.g., Shapley et al. 2005; Yan et al. 2006), enabling large studies of the evolution in stellar mass density in the Universe.

The SED fitting method will be the best way to estimate the stellar mass of SMGs; yet, the spectral energy distributions (SEDs) of SMGs in the rest-frame optical and near-IR have, until recently, been poorly constrained. With the *Spitzer* near- and mid-IR data for the Chapman et al. (2005) sample presented in Chapter 3, we can now constrain the rest-frame near-IR SEDs for a large sample of SMGs, which will assist in the fitting of stellar population synthesis models to their rest-frame UV to near-IR SEDs.

Hence, in this chapter, we will analyze the rest-frame UV to near-IR SEDs of the Chapman et al. (2005) sample of 67 SMGs with spectroscopic redshifts and *Spitzer*-IRAC observations to derive stellar masses for each individual SMG, and attempt to determine stellar population characteristics of the whole sample. Borys et al. (2005) have already completed an initial study with *Spitzer*-IRAC data for 13 X-ray detected SMGs with spectroscopic redshifts in the GOODS-N field, and in this chapter we will expand the sample size of SMGs with stellar mass estimates by a factor of 6 over the work of Borys et al. (2005). In §6.1 of the chapter, we describe the optical, near-IR, and mid-IR data sample we use to construct the SEDs of the SMGs. In §6.2 we discuss the procedure we use to fit population synthesis models to the observed SEDs and present the rest-frame UV–near-IR SEDs of the C05 sample. In §6.3 we calculate the stellar masses for the SMGs using the results of §6.2 and discuss the impact of systematic uncertainties on the stellar mass estimates. In §6.4 we compare

the stellar mass estimates to gas mass and dynamical mass estimates from observations of CO rotational transitions. In §6.5 we discuss prospects for photometric redshifts of SMGs based on the stellar SEDs, the stellar mass results in the context of the stellar populations in SMGs and the evolution of SMGs, and compare to other populations of high-z galaxies.

6.1 Optical, Near-IR, and Mid-IR Data for the Chapman SMG Sample

As mentioned earlier, Smail et al. (2004) found that they could place only weak constraints on the stellar properties of individual SMGs using (observed-frame) optical and near-IR data. Because the near-IR luminosity is much less dependent on past star formation history than, for example, the optical-band luminosity (e.g., Kauffmann & Charlot 1998), IRAC near/mid-IR data provides the rest-frame near-IR wavelength coverage necessary for the best determinations of total stellar mass. The rest-frame near-IR is also less affected by reddening than optical-band data, and thus will be beneficial when looking at SMGs which suffer from extinction in the rest-frame UV and optical bands. However, Borys et al. (2005) and Shapley et al. (2005) note that the IRAC data alone are not sufficient to constrain the SED fitting. The best representation of the stellar component of SMGs hence requires data across the range of rest-frame wavelengths at which starlight dominates. Thus, for our present study we combine observed-frame optical and near-IR measurements for the Chapman et al. (2005, hereafter C05) sample from literature sources with our new IRAC measurements presented in Chapter 3.

We have compiled optical data from a variety of sources to obtain the most wavelength coverage possible for all of the sky fields in the C05 survey. The photometric bands available vary for each field, though each field has R-band data tabulated in C05. In the CFRS-03h field, we use here UBV data from Clements et al. (2004), which have 3σ depth limits of 26.98, 26.38, and 26.40 magnitudes (AB), and R data from C05, with a depth limit of 26.2 mag_{AB}. For the Lockman East field, we use the B data when available from C05, and R data from Ivison et al. (2005), which has a 3σ depth of 27.5 mag_{AB}. In the HDF/GOODS-N field (hereafter simply the GOODS-N field), we use the optical photometry catalog of Capak et al. (2004), which contains measurements in U, B, V, R, I, and z' with 3σ depths 27.6, 27.4, 27.4, 27.2, 26.2, and 26.0 mag_{AB}, respectively. The SMGs in the SSA-13 field have B and

R measurements in C05, with 3σ depths 27.0 and 26.1 mag_{AB}, plus z band measurements from Fomalont et al. (2006) with 3σ depth 24.9 mag_{AB}. In the Groth-Westphal field we use the B and R measurements from C05, which have 3σ depth limits of 27.5 and 26.0 mag_{AB}. For the ELAIS-N2 field, we take our optical data from Ivison et al. (2002), in B, V, and R. The 3σ depth limits for this data are 26.5, 25.9, and 26.1 mag_{AB}, respectively. B and R data for the SSA-22 field come from C05 and have respective 3σ depth limits of 27.0 and 27.2 mag_{AB}.

We take all of the near-IR data (I, J, K) from the study of Smail et al. (2004) for all of the fields, with two exceptions. In the GOODS-N field, we use the I data of Capak et al. (2004) instead of that of Smail et al. (2004). The second exception is the ELAIS-N2 field, which has no J-band data. The 3σ IJK data sensitivity limits vary by field and within fields and are listed in Smail et al. (2004); they are typically ~ 26, ~ 22.5, and 22 mag_{AB}.

We analyze here only the SMGs for which IRAC imaging is available to be able to improve over past studies. Fortunately, only 6 SMGs in the C05 have not been observed by IRAC. We also exclude sources which have less than 3 detections across the range of observed wavelengths (optical–mid-IR), since it is difficult to place meaningful constraints on the SED with so few detections.

6.2 The Rest-Frame UV–Near-IR SEDs of SMGs

In this section we have compiled all of the broadband optical through mid-IR photometry for our sample of SMGs with spectroscopic redshifts, and have constructed their stellar SEDs. With the largest sample of SEDs of SMGs of any previous study, we will discuss common SED features and fit stellar population synthesis models to the data to determine ages, extinction, and absolute magnitudes to be used in the next section for the estimation of stellar masses.

6.2.1 Stellar Population Modeling Procedure

We follow procedures similar to those of Borys et al. (2005) and Shapley et al. (2005) in fitting the observed SEDs of our sample of SMGs. We use the HYPER-Z photometric redshift software package (Bolzonella et al. 2000) to fit evolutionary population synthesis models to the optical–mid-IR SEDs of our sample, restricting the code to fit the SEDs

at the spectroscopic redshift. We use the population synthesis models of both Bruzual & Charlot (2003, using the Padova 1994 stellar tracks) and Maraston (2005) in our fitting, selecting from both authors models with solar metallicity and Salpeter (1955) IMF. We use solar metallicity in the absence of metallicity information for high-z SMGs, but note that it is not an unreasonable choice since the models of, for example, Frayer & Brown (1997), predict that solar metallicity in the gas phase can be attained in young, strongly star-forming galaxies on timescales of $\sim$ a few $\times$ 100 Myr. We have also chosen to use a Salpeter IMF because it facilitates comparison between the BC03 and Maraston (2005) models, as these are the IMFs which the authors have in common. For both sets of models, we investigate the impact on the stellar population results of using a variety of star formation histories: an instantaneous star formation burst model, a continuous star formation model, and exponential star formation histories of the form

$$\mathrm{SFR}(t) \propto \exp(-t/\tau), \tag{6.1}$$

where $\tau = 0.01, 0.05, 0.1, 0.250, 0.5, 1, 2$, and 5 Gyr. We have chosen to not use more complex star formation histories such as short bursts on top of an exponential star formation history because, as we discuss later, the data are insufficient to constrain even simple star formation histories.

In our SED fitting we allow the extinction (A_V) to vary within a range of $A_V = 0 - 3$, and we assume the Calzetti et al. (2000) extinction law for starbursts to account for dust extinction. We also correct for reddening along the line of sight to each SMG field due to the Milky Way using the dust maps of Schlegel et al. (1998).

6.2.2 Systematic Uncertainties in SED fitting of SMGs

HYPER-Z fits evolutionary population synthesis models to the optical-to-mid-IR SEDs of our sample through χ^2 minimization, finding the values of A_V, age (really time from start of star formation), and normalization resulting in the best χ^2 for each star formation history. We constrain the ages to be less than the age of the universe at the redshift of each SMG, though as we discuss later, it is not always successful in doing so. In principle, we could then find the combination of star formation history, A_V, age, and normalization which produce the lowest value of χ^2 overall, which would then provide us with constraints

on the stellar population in the galaxies.

However, in practice we find that the overall best-fitting combination of star formation history, A_V, age, and normalization is rarely significantly better at fitting the data than any other set of parameters: the values of χ^2 are nearly identical between the best-fit parameters of all the star formation histories used. For example, in Figures 6.1 and 6.2 we show the observed SEDs of two SMGs in the GOODS-N field, one at $z \sim 1$ and one at $z \sim 2.5$, fit by a range of different star formation histories, using models of both BC03 (black line) and Maraston (2005, green dotted line). The figures show that, even with a broad range of photometric data (both galaxies have measurements in $UBVRIz'JK$, plus all 4 IRAC channels), all of the star formation histories can produce acceptable fits of nearly identical χ^2, with ages varying from $\sim 10\,\mathrm{Myr}$ to $\sim 2\,\mathrm{Gyr}$, since a young burst model has a similar shape to older, extended star formation models. Thus, we are clearly unable to constrain even simple star formation histories through fitting stellar population models, as Shapley et al. (2001, 2005), Papovich et al. (2001), and Erb et al. (2006) find for UV-selected high-redshift galaxies with similar broadband photometric data. Since the best-fit ages are strongly dependent on the assumed star-formation history, we are thus also unable to effectively constrain the ages of the stellar population in the SMGs.

Some of our inability to constrain the star formation history and the stellar population ages stems from our observational data. The determination of age relies heavily on the shape of the Balmer break in the SED, which reflects the relative fractions of O/B and A stars. Since we usually do not have enough photometric data points in the critical area of the Balmer break to define the shape of the break, we are able to fit the observed SED with models of varying age. For most of our SMGs, we can rule out photometric errors as significant sources of ambiguity, though systematic errors in some data sets may change the shape of the observed SED.

Also, some of the difficulty in constraining stellar population ages arises from the application of relatively simple stellar models to what is likely a complex mix of stellar populations of differing metallicity, reddening, and age. As can be seen in Figures 6.1 and 6.2, that all the simple model star formation histories can fit the data similarly well, indicating that the use of more complex star formation histories is not justified. The heavy reddening at the blue end of the SED in principle will also hinder the determination of age from population synthesis models, since the reddening of a young population of stars produces the same

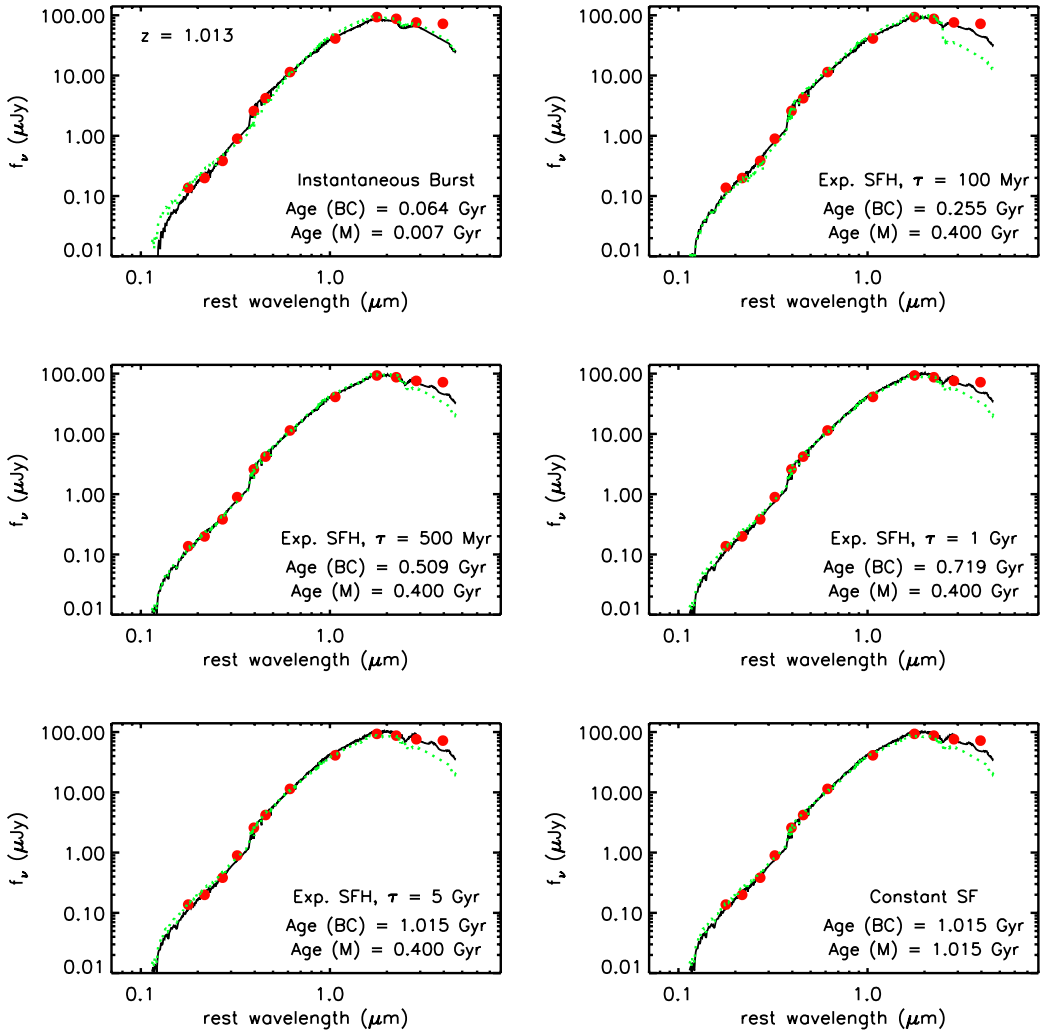

Figure 6.1 Fits of several different stellar population models of different star formation history to the observed SED of SMM J123629.13+621045.8 (red points). The best-fit BC03 model spectrum is over-plotted as the black line, while the best-fit Maraston (2005) model is represented by the green dotted line.

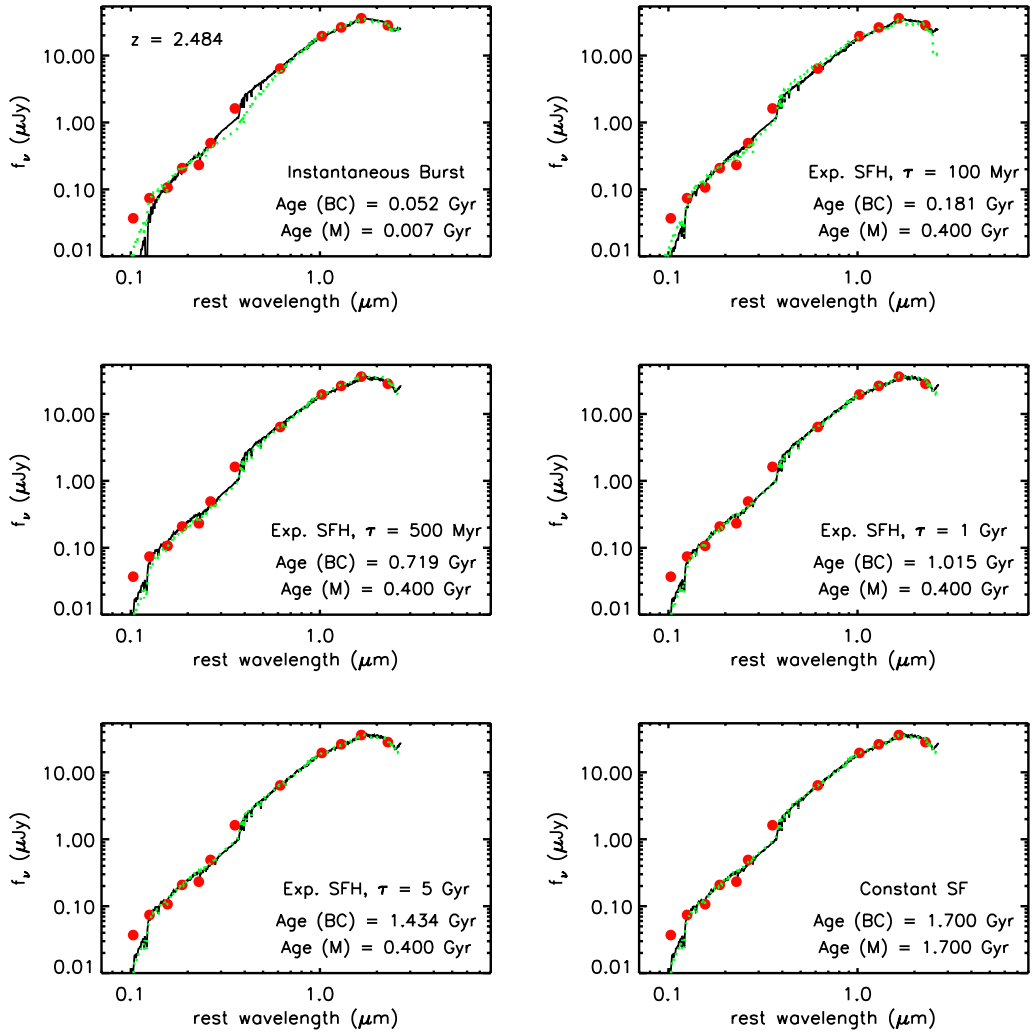

Figure 6.2 Fits of several different stellar population models of different star formation history to the observed SED of SMM J123707.21+621408.1 (red points). The best-fit BC03 model spectrum is over-plotted as the black line, while the best-fit Maraston (2005) model is represented by the green dotted line.

effect in the models as aging the stellar population.

6.2.3 Results of SED Fitting

We present the rest-frame optical to near-IR SEDs of the C05 sample of radio-detected SMGs in Figures 6.3–6.10. In looking at the SEDs of the SMG sample, we see some variety in shape, though the majority follow a noticeable pattern in which objects are significantly brighter in the rest-frame near-IR than in the rest-frame UV and optical, with steep near-UV to optical spectral slopes indicating the presence of significant extinction. However, there is a minority (~ 8 SMGs) for which the UV–near-IR spectral shape is fairly flat (data points span ~ 1 order of magnitude or less across the observed wavelength range). 4 of these flat-spectrum sources show obvious active galactic nucleus (AGN) or QSO features in their optical spectra (C05) and lie at $z > 2.4$, and a likely explanation for the flat SED is that AGN emission is dominating the optical spectrum. Two of the flat-spectrum sources are at $z < 1$ and show no AGN features in their UV/optical spectra; it is possible that these SMGs contain very young starbursts or are less reddened than the higher redshift sources. The remaining flat spectrum sources are at $z \sim 1.5 - 3$ and do not show clear AGN features in their rest-frame UV spectra; however, none of these sources have rest-frame optical spectroscopic data, which may yet reveal AGN characteristics; on the other hand, they may contain young starbursts as well.

Flat-spectrum objects aside, the other common feature in the UV–near-IR SEDs of our sample of SMGs is the peak in emission around $\sim 1.6\,\mu$m, seen also in the SEDs of the sample of Borys et al. (2005). This peak in the SED corresponds to the frequency minimum of the opacity of the H^- ion in stellar photospheres and represents the frequency of maximum emission from stars. The presence of the $1.6\,\mu$m peak provides additional support for the redshifts of C05 as well; as an aside, we note that nearly all of the observed rest-frame UV to near-IR SEDs of our sample are consistent with their redshifts in C05.

Only in 8–10 SMGs in our sample do we see clear indication of a break in the continuum near 4000 Å, which could be due to the Balmer discontinuity in young stars or the 4000 Å break seen in evolved stellar populations. In some cases there are hints of a break, but more data points in the region are needed to establish its presence conclusively. Indeed, the objects in the SMG field with photometry in the largest number of optical/near-IR bands, those in the GOODS-N field, show the best evidence for continuum breaks at 4000 Å.

Well-sampled optical SEDs are important to define the Balmer break, partly because it tends to be smaller in amplitude than the Lyman continuum break. The lower number of photometric data points available for the other SMG fields may explain why Borys et al. (2005) finds clear indications of spectral breaks in much of their sample (which are all from the GOODS-N field), and here we do not. We note that there may be continuum breaks in all of the SMGs; we merely do not have sufficient data to say so.

6.2.4 Emission Lines and Color Excess in SMG SEDs

Broadband photometric measurements of galaxies can contain emission lines as well as continuum for galaxies which have active nuclei or very active star formation. When the broadband measurements contain emission lines, the data points will appear anomalous when SEDs are constructed from the broadband data, and can interfere with fitting SED models to the data points. This is frequently seen for UV-selected galaxies (e.g., Shapley et al. 2005; Erb et al. 2006), and the emission line contamination must be removed for appropriate SEDs to be fit. Similarly, excess continuum emission, frequently due to AGN light, can hinder the fitting of SEDs and determination of stellar masses. Here, we briefly discuss the incidence of emission lines and continuum excess in the SEDs of our SMG sample.

Among our SMG sample, we see evidence of excess emission at various points across the SED for perhaps a third of the objects, though in most cases the general shape remains consistent with the majority pattern. In a few cases, we see evidence of contamination of broadband measurements by emission lines, notably Hα and Hβ/[O III], and possibly even [O II]. 6 SMGs in the sample appear to have slightly significant UV excesses, though the stellar population models we use may simply not be adequate to describe the UV SEDs of these objects properly. Much more frequently, however, we see significant excess emission at the red end of the SED, which is suggestive of an obscured AGN. 13 of the 67 SMGs in our sample show these red upturns, some of which were noted in Borys et al. (2005). 4 of the red-upturn galaxies have previously been identified as AGN by their UV/optical spectral features. It is also possible that for some galaxies the apparent excess in the longest-wavelength IRAC bands arises from a strong 3.3 μm polycyclic aromatic hydrocarbon (PAH) feature. In any case, it is important to note that since we have chosen to estimate stellar mass from the rest-frame H magnitude, the red upturn in many of these sources has little

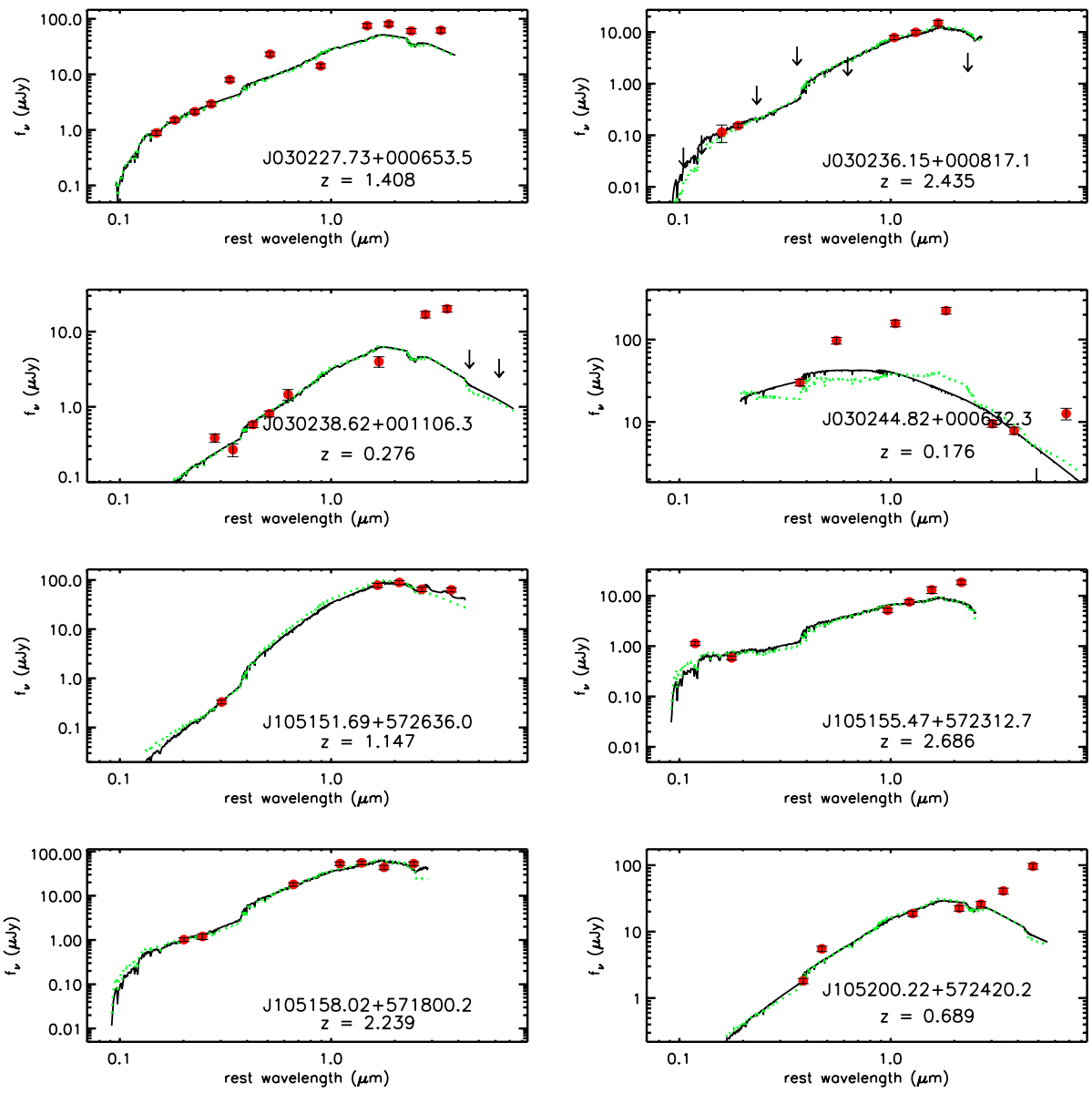

Figure 6.3 Rest-frame optical through near-IR SEDs of radio-detected SMGs in the sample of C05 which have been observed by IRAC. Observed data points are in red, while non-detections are indicated by downward arrows originating from the measured upper limit. The best-fit CSF model of BC03 is over-plotted as the black line, while the best-fit CSF model of Maraston (2005) is represented by the dotted green line.

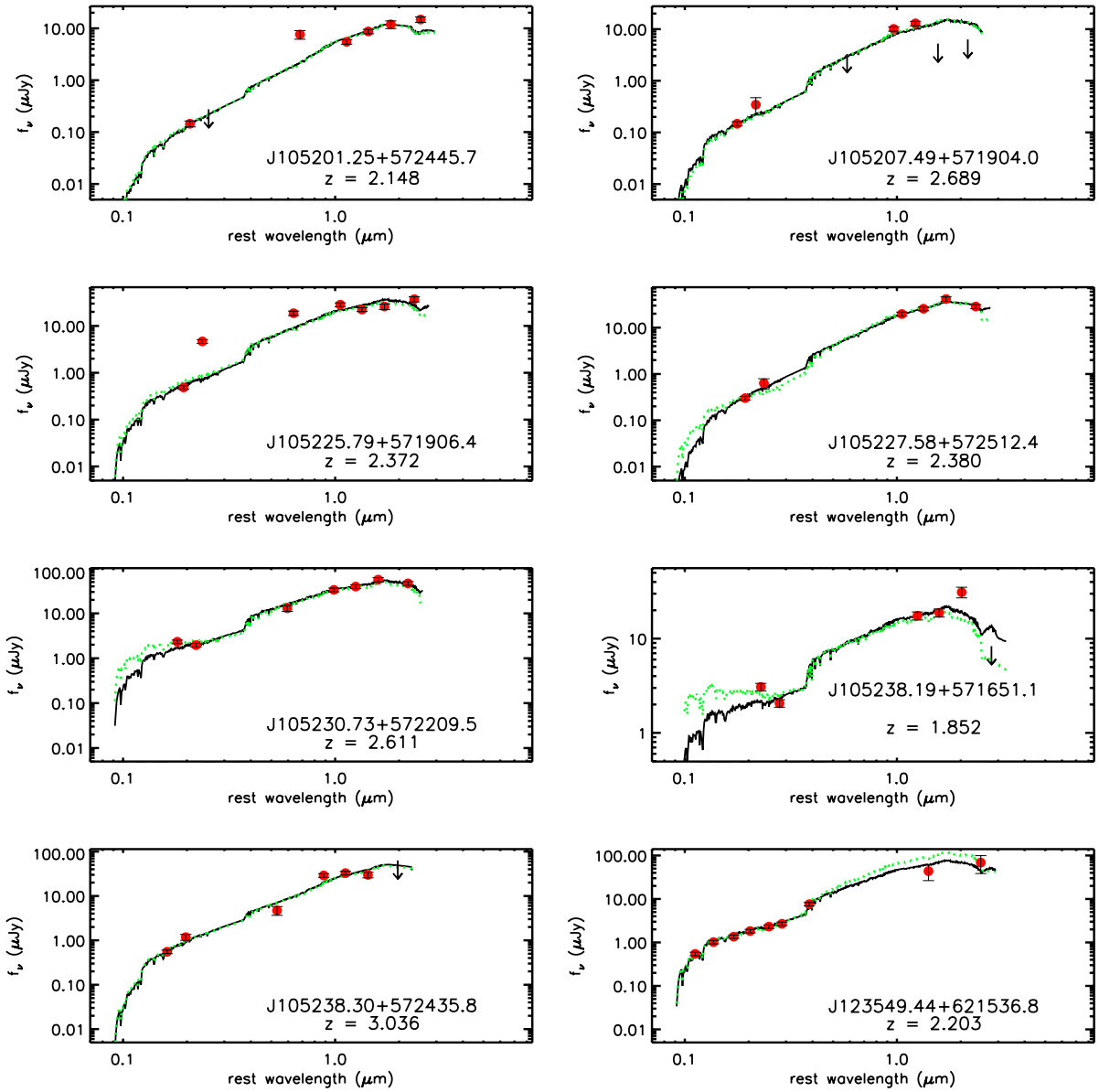

Figure 6.4 More rest-frame optical through near-IR SEDs of radio-detected SMGs from the sample of C05. Data points and lines are as in Figure 6.3.

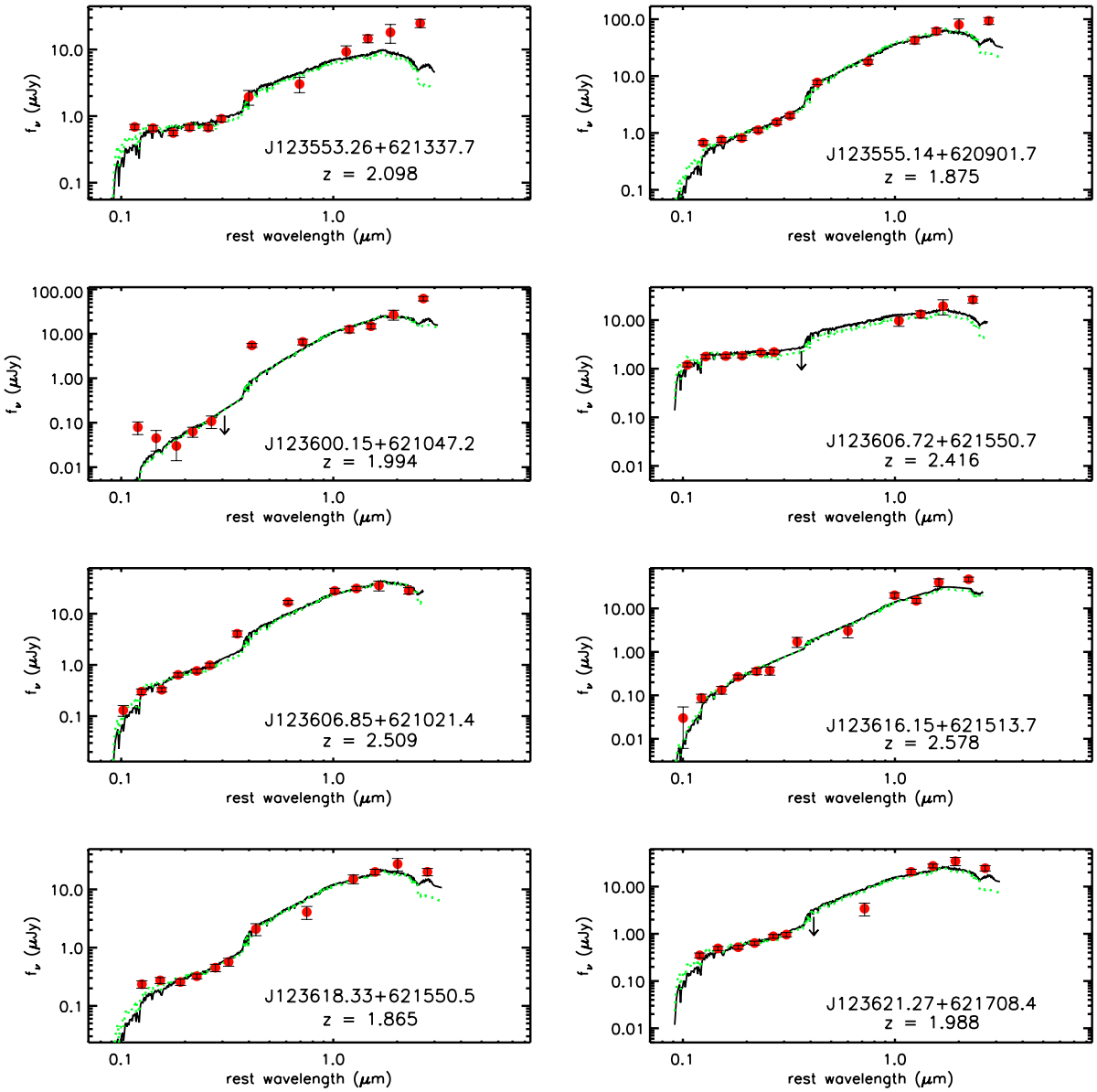

Figure 6.5 More rest-frame optical through near-IR SEDs of radio-detected SMGs from the sample of C05. Data points and lines are as in Figure 6.3.

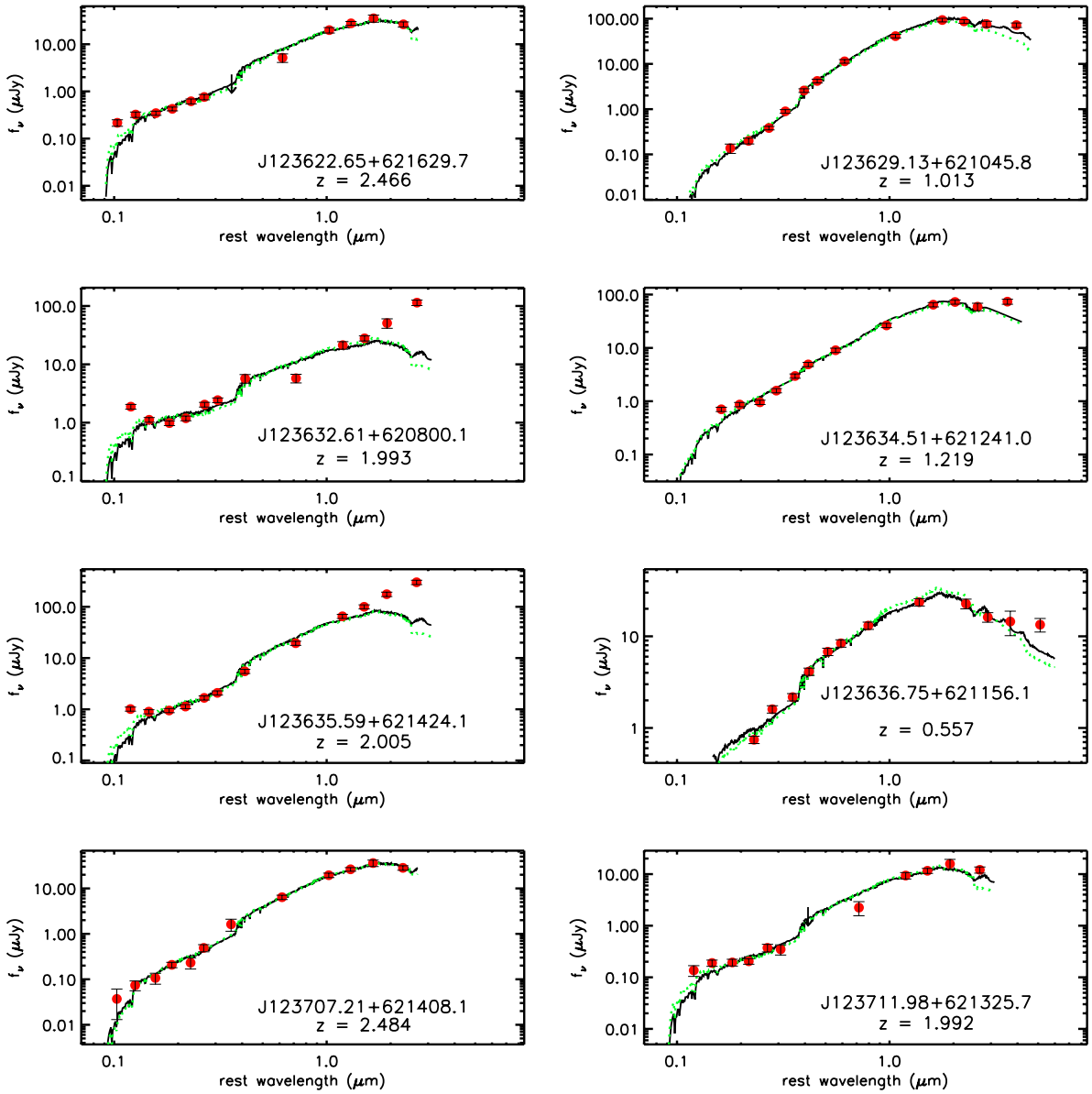

Figure 6.6 More rest-frame optical through near-IR SEDs of radio-detected SMGs from the sample of C05. Data points and lines are as in Figure 6.3.

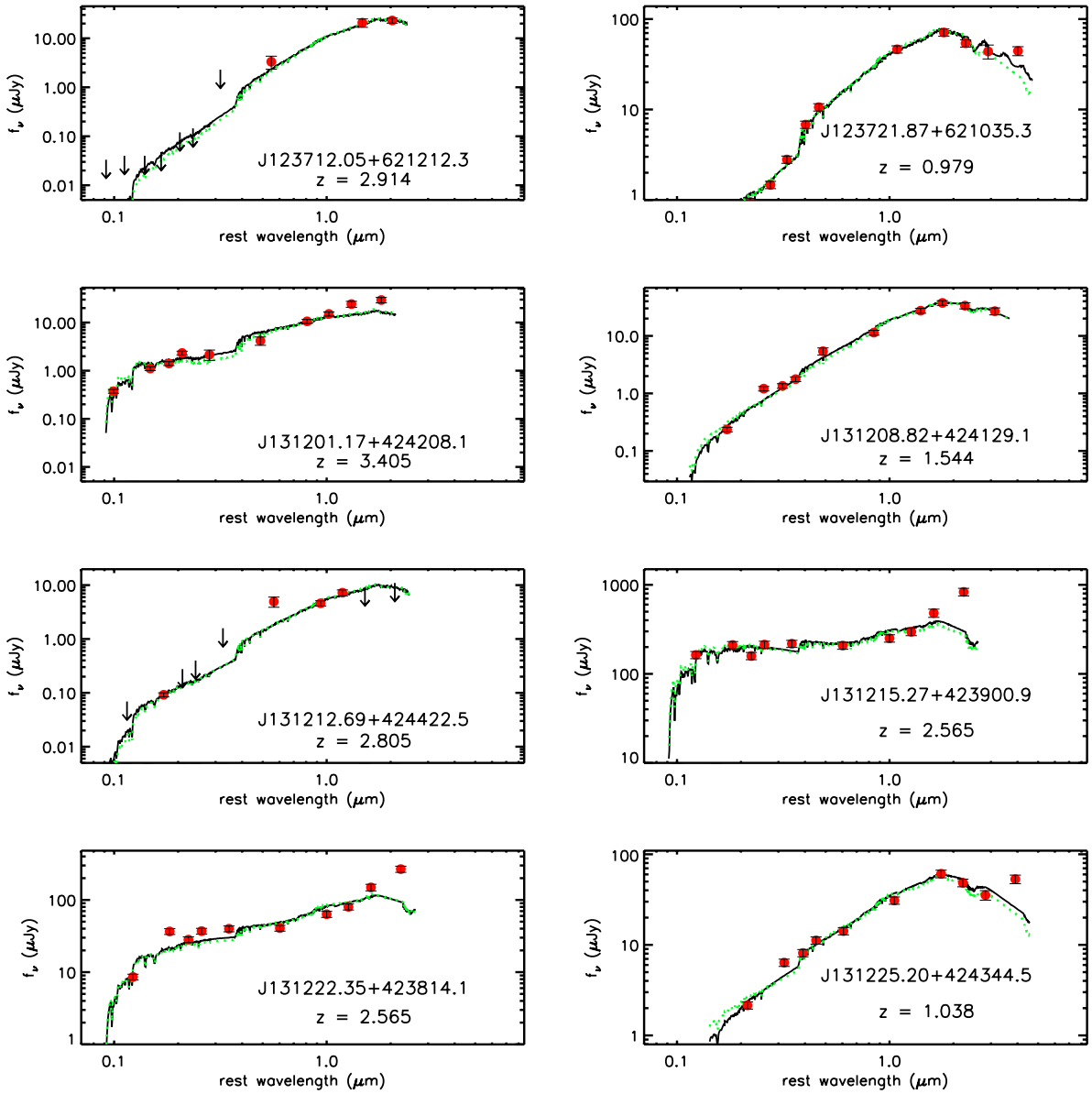

Figure 6.7 More rest-frame optical through near-IR SEDs of radio-detected SMGs from the sample of C05. Data points and lines are as in Figure 6.3.

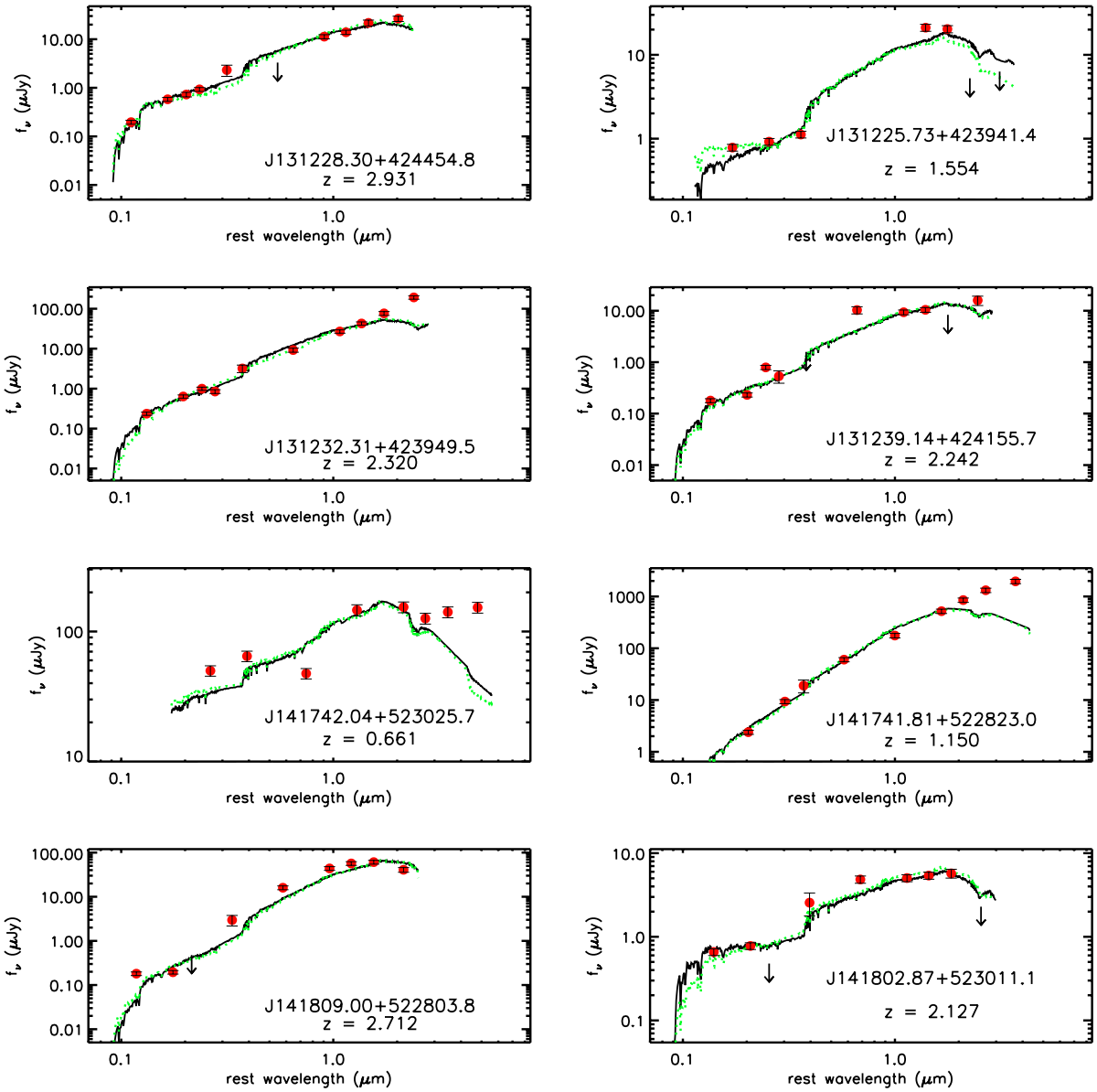

Figure 6.8 More rest-frame optical through near-IR SEDs of radio-detected SMGs from the sample of C05. Data points and lines are as in Figure 6.3.

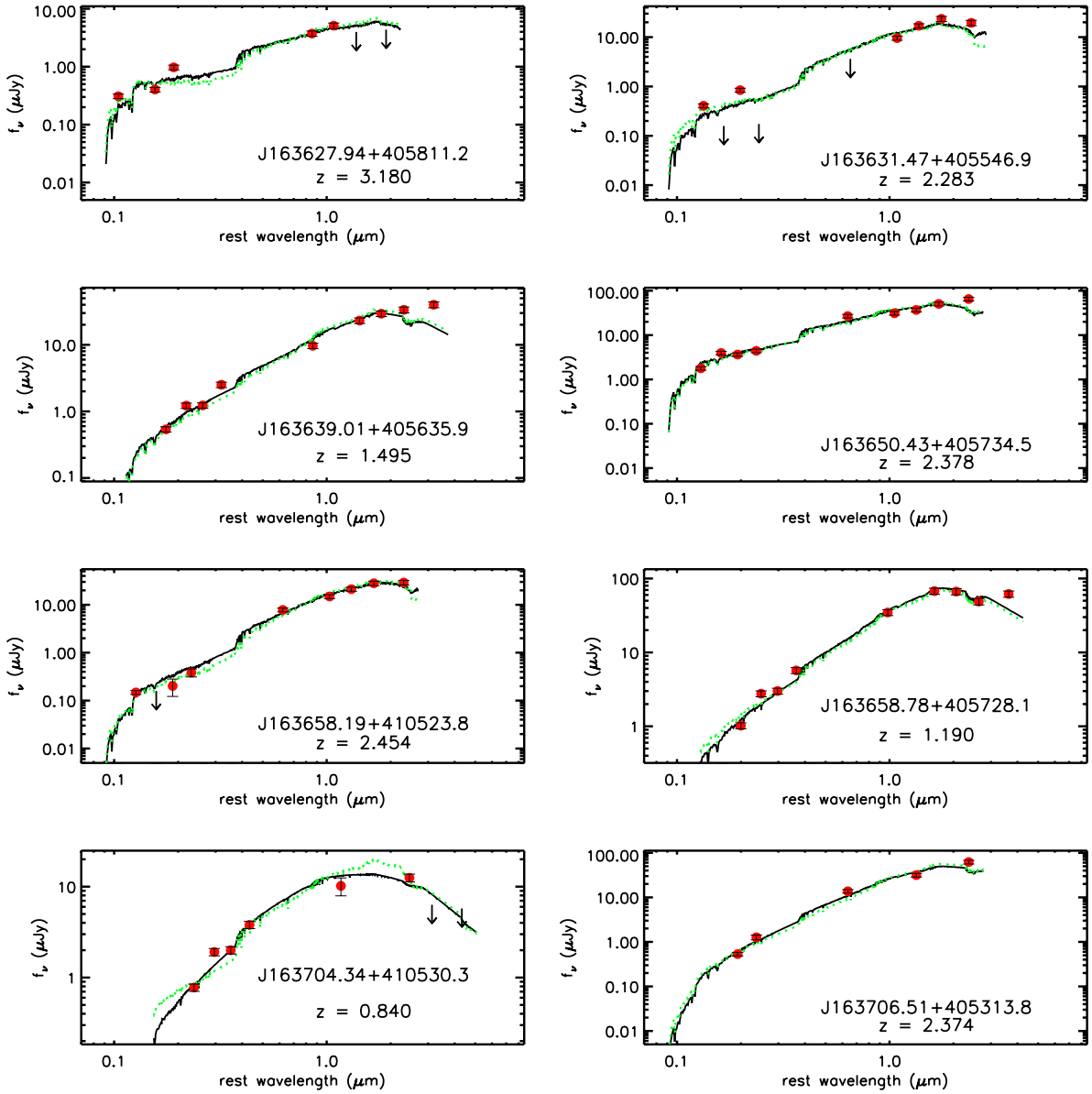

Figure 6.9 More rest-frame optical through near-IR SEDs of radio-detected SMGs from the sample of C05. Data points and lines are as in Figure 6.3.

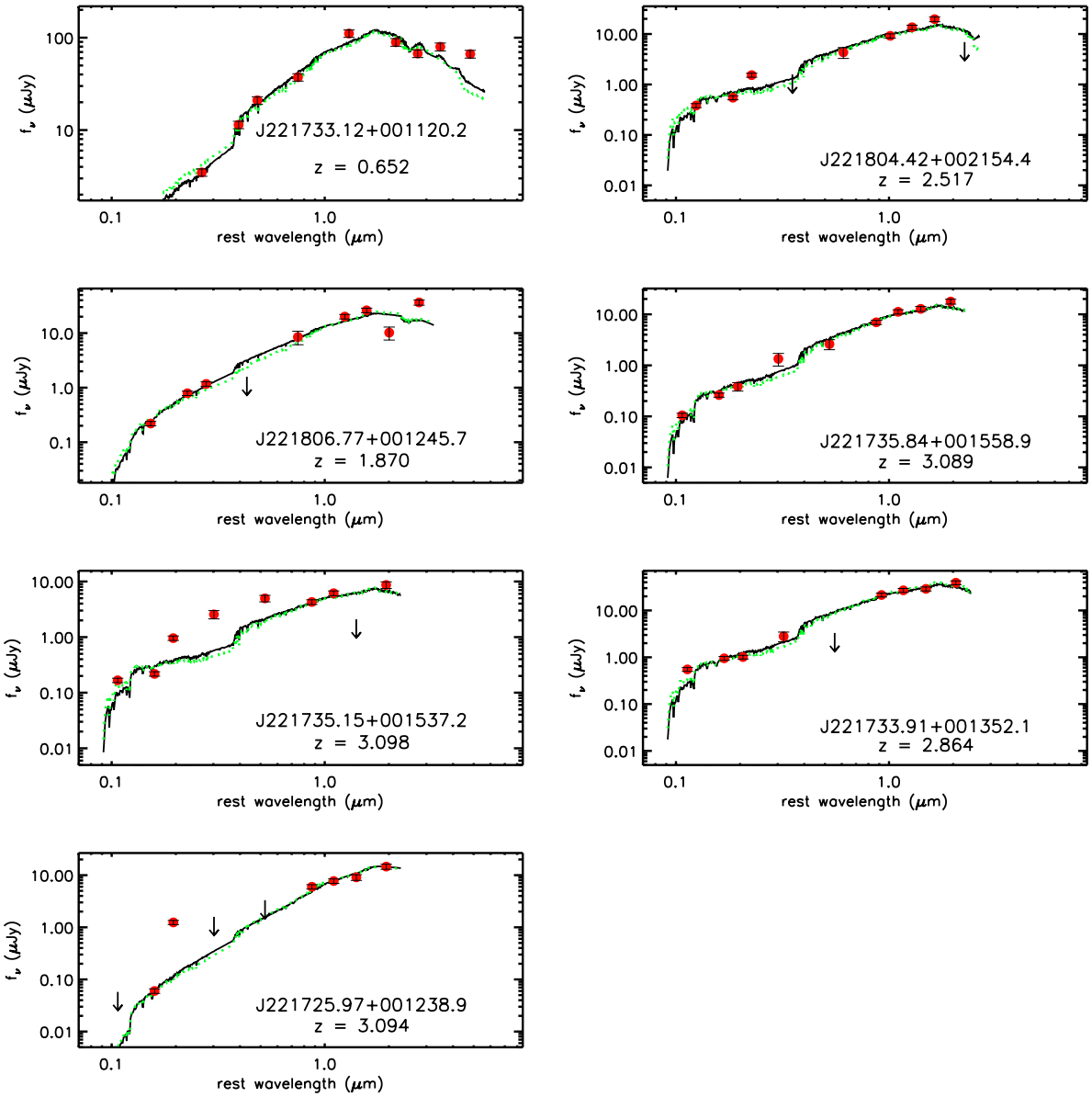

Figure 6.10 More rest-frame optical through near-IR SEDs of radio-detected SMGs from the sample of C05. Data points and lines are as in Figure 6.3.

impact on the value of $M_\star$ we calculate.

6.2.5 Comparison of Model SED Fits of Bruzual & Charlot (2003) and Maraston (2005)

Recent discussions in the literature about the importance of the contributions of very luminous giant stars to the integrated near-IR light of galaxies (e.g., Maraston 2005; Maraston et al. 2006) highlighted how the use of different sets of stellar models can influence the results of stellar mass studies and conclusions about mass assembly at high redshift. Thus, we have chosen in this chapter to use two popular population synthesis models, those of BC03 and Maraston (2005), to model the SEDs of SMGs and estimate stellar masses. Here, we compare the fits to the SMG SEDs of the models of the different authors in an effort to determine if one set of models should be preferred over the other.

We plot the best-fit CSF models of BC03 (black line) and Maraston (2005) (green line) over the observed data points in Figures 6.3–6.10, noting that the fits of the burst models are similar so the CSF models are representative of the fits of the different star formation histories. For the most part, the fits of the BC03 and Maraston (2005) models appear very similar, though they almost always correspond to different ages and, thus, reddenings. In the burst model fits, the ages agree to within 10 Myr for $\sim 50\%$ of our SMG sample, but differ by more than an order of magnitude only $\sim 10\%$ of the time. When the ages agree to within 10 Myr, the reddening values are usually within 0.3 mag of each other, and the reddenings inferred from the BC03 tend to be higher than those inferred from the Maraston (2005) model even when the BC03 age is older. In the CSF model fits, the ages agree to within 1 Gyr for $\sim 60\%$ of the sample and differ by more than an order of magnitude in only $\sim 10\%$ of cases; similar to the burst models, the reddening values inferred are typically within 0.3 of each other when the ages are similar, with BC03 reddenings tending to be larger. Thus, it seems that the BC03 models tend to require more reddening to match the SEDs of SMGs. However, as mentioned earlier, we do not find that one set of models gives systematically lower ages than the other, overall.

We note that both sets of models give ages older than the age of the universe for $\sim 25\%$ of the sample using the CSF models, which in most cases can be attributed to the low time resolution of the age grids at ages above 2 Gyr. In computing average ages, in cases where the fitted age is greater than the age of the Universe at the redshift of the galaxy, we have

substituted the age of the Universe at that redshift in place of the fitted age.

Also worthy of note is that the models of the different authors fitted to the SMG SEDs differ most at the extreme blue and red ends of the SED. When there is a clear difference, the model of Maraston (2005) is usually brighter at the blue end of the SED and fainter at the red end. This behavior occurs when the BC03 model fit gives a higher reddening than the Maraston (2005) model fit, but the ages from the different models are similar, signaling that the BC03 models tend to be more blue than the Maraston (2005) models and, thus, require higher reddening to produce the observed ratio of near-IR to UV/optical light.

For the most part, the fits of both sets of models match the data reasonably well, even though the formal χ^2 values per degree of freedom of the fits are frequently greater than 1, a result also found by Papovich et al. (2001) when fitting the optical-to-near-IR SEDs of Lyman break galaxies (LBGs). The high values of χ^2 imply that one or more of the following are true: (1) the photometric errors on the measurements have been underestimated, (2) the distribution in the errors of the fitted parameters is not Gaussian, or (3) the models used do not adequately describe the SEDs of the SMGs. It is certainly likely that the stellar population models are insufficient to describe the observed SEDs, since, for example, we assume a single metallicity for all galaxies, we use only simple star formation histories, and we assume a single extinction model for galaxies which are likely to have a range of extinction characteristics. However, it is also possible that the photometric errors have been underestimated, especially in the IRAC data, because mosaic image pixels within a given region have correlated noise properties due to drizzling. To check if the photometric errors were at the root of the high χ^2 values, we re-fit the observed SEDs, including extra 5-15% systematic uncertainties in all of the photometric data. However, the changes in the χ^2 distributions of the fitted parameters were relatively insignificant when the extra uncertainty was included, suggesting that it is more likely that the models are not good descriptions for all of the data.

For several objects (e.g., SMM J030244.82+000632.3), the best-fitting models from both BC03 and Maraston (2005) are clearly poor fits to the observed data, and as a result, the interpolated absolute magnitude that results from the fit is much lower than the observed data points would suggest. Since the absolute magnitudes in these cases may be in serious error, we exclude them from the sample averages of age and absolute magnitude.

6.3 The Stellar Masses of Radio-Detected SMGs

With the results of the rest-frame UV through near-IR SED fitting for the C05 SMG sample in hand, we can now estimate the stellar masses of the SMGs. We first describe our method for estimating the masses, in which we attempt to take into account the systematic uncertainties discussed in §6.2.2. We then discuss the systematic uncertainties associated with the mass estimates, which are in addition to those occurring in the SED fitting process. Afterward, we present the results of the stellar mass calculations and discuss briefly the impact of our new results on the observed black hole mass–stellar mass correlation for SMGs.

6.3.1 Stellar Mass Estimation Procedure

The stellar mass for each galaxy can be computed after fitting its SED using the absolute magnitude in a given observed band and the mass-to-light (M/L) ratio for that band corresponding to the star formation history used and the fitted age of the model. K-band light is frequently used for $z < 1$ galaxies because of its low sensitivity to previous star formation history (e.g., Bundy et al. 2005). For the same reason, and due to the lessened effects of dust obscuration, Borys et al. (2005) use the rest-frame K band for their stellar mass estimates of SMGs. We instead choose to use the rest-frame H band to estimate $M_\star$ for our sample of SMGs to benefit from the low extinction of the near-IR bands while minimizing the possible contribution from very hot dust heated by a central, obscured AGN which can fall in the rest-frame K band (e.g., Borys et al. 2005; Seymour et al. 2007). There are two more benefits to using H, one of which is that for our highest-redshift ($z > 3$) SMGs, the longest-wavelength IRAC observations (8.0 μm) do not quite sample rest-frame K, so calculations of the absolute K magnitude (M_K) for these sources are not observationally constrained. The second benefit derives from the increasing influence of thermally pulsating asymptotic giant branch (TP-AGB) stars on the model M/L ratio in the Maraston (2005) stellar population models in the K-band. By going to a slightly bluer band, we reduce the uncertain influence of TP-AGB stars to the integrated galaxy light and M/L ratios: in H-band, the change in M/L ratio induced by the appearance of a dominant solar-metallicity TP-AGB population at ages of $\sim 0.5 - 1.5$ Gyr is a factor of ~ 2, while in the K-band, the change in M/L at the same time is nearly a factor of 4.

The star formation history and model ages that should be used in calculating $M_\star$ are less clear. As shown in §6.2.2, we are unable to adequately constrain the age and star formation history for individual SMGs through SED fitting, in that models with ages of a few Myr to several Gyr fit similarly well to the observations. The choice of star formation history has a direct impact on the age, since the instantaneous burst models tend to produce the youngest ages, and the CSF models tend to produce the oldest ages (the exponential models tend to produce ages somewhere between the burst history and the CSF history). The fitted stellar population ages affect the stellar mass estimates significantly because the values of the M/L ratio used to calculate the stellar masses are determined by the ages. Thus, our lack of ability to constrain the ages and star formation histories of the SMGs can introduce extra systematic uncertainties into the stellar mass calculations, on top of any resulting from the stellar models themselves.

Fortunately, the importance of the stellar population ages on the mass estimates is not dire, as we illustrate in Figure 6.11 by showing the effects of age and star formation history on the H-band M/L ratios of the BC03 and Maraston (2005) solar-metallicity models, using the inverse form $L_H/M_\star$ for easier viewing. The light-to-mass (L/M) ratios at all ages vary much less than the ages themselves, generally spanning a factor of 5–10 at all reasonable ages of the stellar population. At ages above 50 Myr, the different ages implied by the different star formation histories are not major concerns either: the L/M ratio of a younger instantaneous burst population differs by no more than a factor of 2 from the L/M of an old, CSF population, so the inferred masses will be in error at most by a factor of 2, which may even be smaller than the systematic errors in the light-to-mass ratios. Thus, neglecting systematic errors in the L/M ratios, the stellar masses derived from them will be much better constrained than the ages.

In the absence of any indication of which star formation history is most appropriate, and with the knowledge that (a) the age estimates of individual galaxies in our SMG sample are not well constrained; (b) the SED fits of the different star formation histories are correlated; and (c) the ages implied by the different star formation histories will give similar L/M ratios to within a factor of a few, we elect to use a similar method to that of Borys et al. (2005) to estimate $M_\star$ for our SMG sample. We use the averages of the fitted ages from each of the instantaneous burst and CSF models to determine a single $L_H/M_\star$ ratio for each model, average the $L_H/M_\star$ ratios of the two models, and apply this average ratio to the absolute

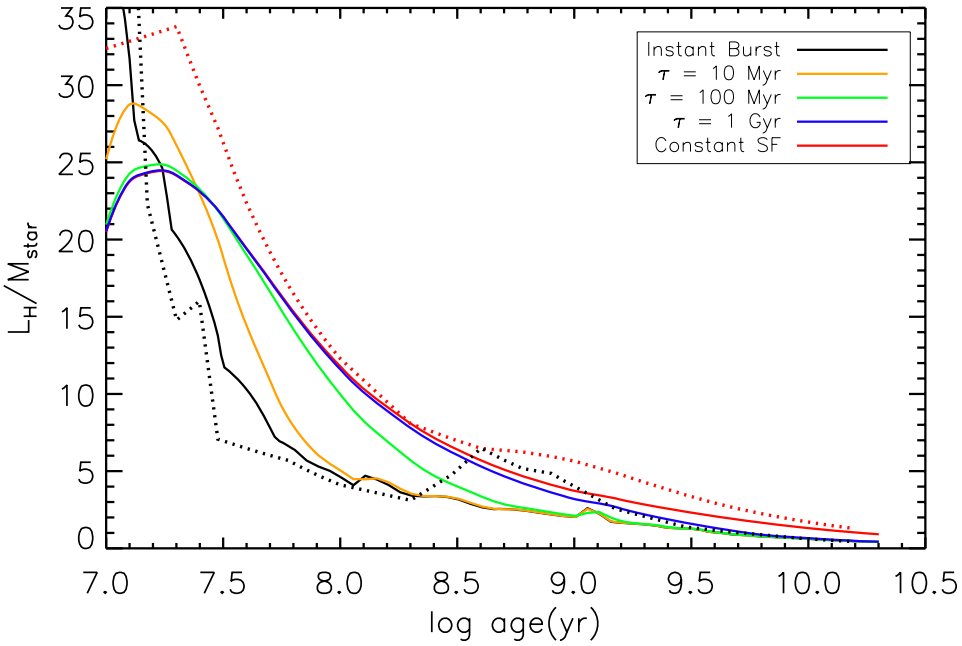

Figure 6.11 $L_H/M_\star$ vs. time since onset of star formation for solar-metallicity population synthesis models of BC03 and Maraston (2005). Solid lines represent models of BC03, while dotted lines represent the models of Maraston (2005). The increase in $L_H/M_\star$ near $\log \mathrm{age} = 8.5$ in the Maraston (2005) burst model marks the onset of the TP-AGB phase.

H magnitude for each individual galaxy to calculate $M_\star$ for all the SMGs in our sample individually, according to the equation

$$M_\star = \frac{10^{(H_\odot - M_H)/2.5}}{L_H/M_\star}, \tag{6.2}$$

where $H_\odot = 3.3\,\mathrm{mag}$ is the absolute H magnitude of the Sun on the Vega system. We calculate separate mass estimates for the BC03 and Maraston (2005) models and do not average them.

From fitting the instantaneous burst models to the SMGs, we obtain an average age of $0.073 \pm 0.14\,\mathrm{Gyr}$ for the BC03 burst model and $0.10 \pm 0.64\,\mathrm{Gyr}$ for the burst model of Maraston (2005). From fitting the CSF models, we obtain means and standard deviations of $1.4 \pm 1.2\,\mathrm{Gyr}$ and 1.4 ± 1.4 for BC03 and Maraston (2005), respectively. The BC03 average burst age of 73 Myr corresponds to $L_H/M_\star = 5.6\,L_\odot/M_\odot$ in that set of models, while the BC03 CSF age of 1.4 Gyr indicates $L_H/M_\star = 3.3\,L_\odot/M_\odot$. The average ages of the Maraston (2005) models result in $L_H/M_\star = 4.1\,L_\odot/M_\odot$ for the instantaneous burst model and $L_H/M_\star = 5.1\,L_\odot/M_\odot$ for the CSF model. We note that at the average age of the CSF model for Maraston (2005), the contribution of TP-AGB stars to the near-IR light of the stellar population is still significant and increases the $L_H/M_\star$ ratio over that predicted by BC03.

We calculate the absolute H magnitude for each galaxy by averaging the M_H values calculated from the SED fits of burst and CSF models for both BC03 and Maraston (2005) since the numbers are very similar; thus, 4 different estimates of M_H are averaged to produce one final number for each galaxy. We estimate the uncertainty on this average magnitude as half of the difference between the highest estimate of M_H and the lowest estimate of M_H.

We estimate the uncertainty in the masses by propagating the errors calculated for the absolute magnitude and the uncertainty in the $L_H/M_\star$. We take the uncertainty in the L/M ratio to be half the difference between the CSF and instantaneous burst light-to-mass ratios, since these values tend to represent the maximum and minimum values of the light-to-mass ratio of the different star formation histories. We have thus tried to represent both random fitting errors and systematic errors in the ages and L/M ratios in our uncertainty estimates; however, systematic errors still exist for our mass estimates, as we discuss below.

6.3.2 Sources of Systematic Uncertainty in $M_\star$

Numerous systematic uncertainties plague stellar mass estimates from broadband photometry, as pointed out by many authors (e.g., Papovich et al. 2001; van der Wel et al. 2006; Borys et al. 2005). One of the most significant sources of uncertainty, i.e., our inability to constrain the star formation history and age of the dominant stellar population of individual galaxies, has already been discussed in both §6.2.2 and §6.3.1, so in this section we briefly discuss the other sources of systematic uncertainty in our mass estimates for SMGs.

One significant source of uncertainty comes from our choice of IMF. We chose to use a Salpeter IMF primarily for ease of analysis. However, the Salpeter IMF places more emphasis on low-mass stars than is observed locally; if we overestimate the contribution of low-mass stars, we obtain a lower L/M ratio than should be used. Thus, we have also carried out our mass estimation procedure on our sample using the alternate IMFs available with the stellar models: the Chabrier (2003) IMF for the BC03 models and the Kroupa (2001) IMF with the Maraston (2005) models. We find that use of the Chabrier (2003) IMF with the BC03 models resulted in masses which are lower by a factor of 1.7 on average, while using the Kroupa (2001) IMF with the models of Maraston (2005) gives masses that are lower by a factor of 1.9.

Our choice to use solar metallicity also affects our stellar mass estimates. The metallicities of SMGs are not well-constrained, so we have little guide for our choice. However, the effects of metallicity on our mass estimates are also tied to our choice of star formation history, since the effects of age, reddening, and metallicity are intertwined. In general, if lower-metallicity BC03 models are used, we obtain older ages, which decrease the L/M ratio and in turn increase the stellar mass estimates. Assuming higher metallicities in the BC03 models tends to decrease the L/M ratio and increase the masses. However, in the Maraston (2005) models, the L/M ratios are nearly independent of metallicity at an age of $\sim 1\,\mathrm{Gyr}$, so for a CSF history the stellar mass estimates will not change a great deal.

Yet another source of uncertainty comes from the possible contamination of the near-IR emission by an AGN. We have tried to minimize this by estimating mass from a photometric band so blue that only a very powerful AGN could heat enough dust to make a significant contribution. Most of the SEDs of our sample of SMGs show a clear stellar emission peak, suggesting that AGN are not strong contributors to the rest-frame H-band for most of

our sample. The finding of Seymour et al. (2007) from mid-IR SED modeling of powerful, high-z radio galaxies (sources which are known to contain powerful, obscured AGN) that for $\sim 70\%$ of the galaxies in their sample stellar emission strongly dominates the observed near-IR flux at rest-frame H-band, also provides support for low AGN contamination in our stellar mass estimates. However, we note that the SMGs in our sample for which we derive the largest masses are known to contain powerful AGN from their rest-frame UV/optical spectra. These sources are few in number, however, and for these sources we can take the calculated stellar mass as an upper limit.

Finally, perhaps the most important source of systematic uncertainty in our stellar mass estimates comes from the calibration of the theoretical stellar models to observable quantities. Because we use the models to obtain both the ages and L/M ratios used in the mass estimation, our stellar mass estimates are fundamentally limited by the ability of the models to predict reality. All together, a conservative estimate of the systematic uncertainties in our stellar masses is a factor of 10.

6.3.3 Stellar Mass Results for SMGs

Using the procedure described in §6.3.1, we have calculated $M_\star$ for the C05 sample of radio-detected SMGs for both the BC03 and Maraston (2005) stellar population models, including new estimates for the SMGs analyzed in Borys et al. (2005). We list in Table 6.1 the masses for individual galaxies predicted by both sets of models, along with the absolute H magnitude and A_V we obtain through the SED fitting process. In Figure 6.12 we plot the distribution of $M_\star$ for the sample for both the BC03 and the Maraston (2005) models. The histograms are similar in central value, width, and height. On average, the values of $M_\star$ derived from the BC03 models tend to be systematically larger by 10%.

We obtain a median stellar mass for the SMG sample of $M_\star = 6.9 \times 10^{10}\,M_\odot$ for the BC03 models, and a median of $M_\star = 6.3 \times 10^{10}\,M_\odot$ for the models of Maraston (2005). The inter-quartile ranges are $4.7 \times 10^{10} - 1.2 \times 10^{11}\,M_\odot$ and $4.3 \times 10^{10} - 1.0 \times 10^{11}\,M_\odot$, respectively. For the objects we have in common with Borys et al. (2005), our new masses are factor of 5-6 lower, which places them outside the given uncertainties in Borys et al. (2005). However, our median $M_\star$ for SMGs is closer to the typical SMG stellar mass estimated by Smail et al. (2004) of $3 \times 10^{10}\,M_\odot$.

Our lower masses may be a direct consequence of the different models we use to fit the

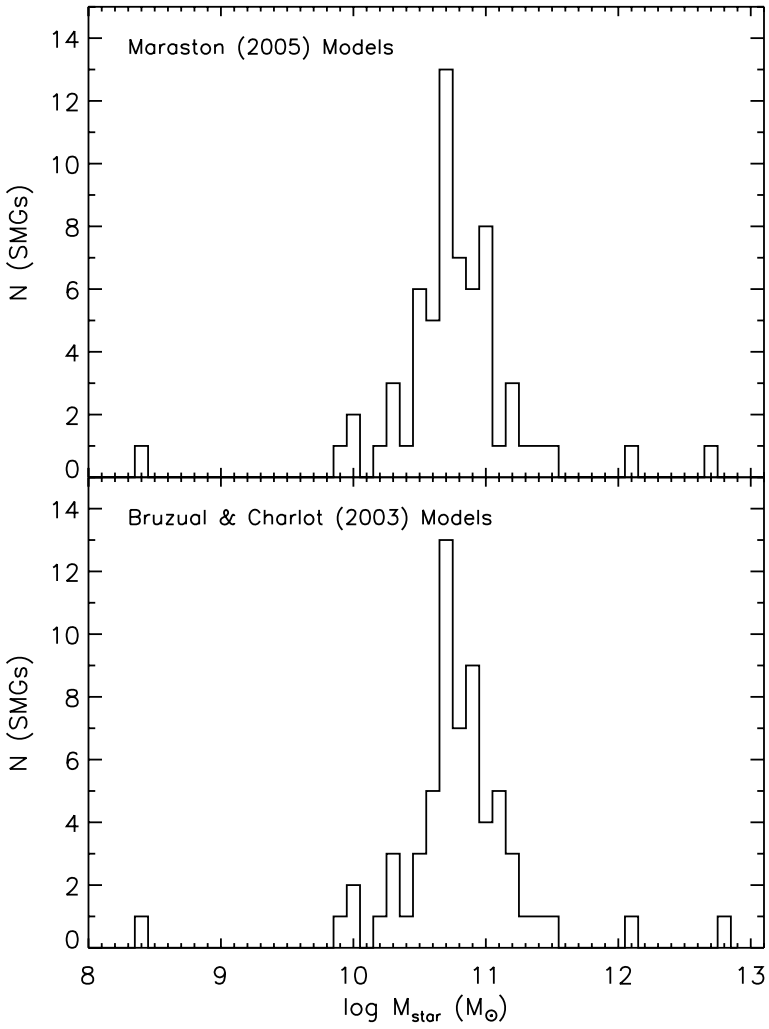

Figure 6.12 Histograms of $M_\star$ for C05 sample of SMGs using the stellar population synthesis models of Maraston (2005) (top panel) and BC03 (bottom panel).

SMG SEDs and derive the $L_H/M_\star$ ratios. Borys et al. (2005) used the stellar population models of Bruzual & Charlot (1993) to derive ages and absolute K magnitudes for the SMGs in their sample, and used the STARBURST99 stellar population models (Leitherer et al. 1999) with a Miller & Scalo (1979) IMF to obtain the M/L ratios for stellar mass calculations. The BC03 models contain updated stellar spectral libraries and improved treatment of stellar evolution, and BC03 show that the 2003 models agree better with observations in the colors and luminosities of red giant stars. The improved treatment of giant stars and improved stellar evolution prescriptions may explain why we obtain younger ages with the 2003 models than Borys et al. (2005) do with the 1993 models.

Our lower masses as compared with Borys et al. (2005) also may be a consequence of using M_H to calculate the stellar mass instead of M_K. If the X-ray detected SMGs in the sample of Borys et al. (2005) have any contribution in the K-band from their AGN, which is likely, the stellar masses may be overestimated. When we estimate $M_\star$ for our sample again, using rest-frame K-band absolute magnitudes and L/M ratios, we find a median for our sample which is approximately a factor of 2 higher, $M_{\star,K} = 1.7 \times 10^{11}\,M_\odot$, which is closer to the median of Borys et al. (2005), but still slightly less. It seems likely that some combination of model differences and AGN contribution in the K-band may be at the root of the lower masses we derive for SMGs over Borys et al. (2005), reflecting just some of the possible systematic errors associated with calculating stellar masses from fitting model stellar populations to photometric data. With these systematic errors in mind, we should re-visit the $M_{BH} - M_{\rm bulge}$ correlation for SMGs found by Borys et al. (2005) and see how the systematics affect their conclusions.

Table 6.1: Stellar Properties and Masses for Chapman et al. (2005) SMG Sample

Chapman et al. (2005) ID	M_H (mag, Vega)	A_V (mag)	$\log M_\star$, BC03 ($M_\odot$)	$\log M_\star$, M05 ($M_\odot$)
SMM J030227.73+000653.5	-26.07 ± 0.51	1.8 ± 0.3	11.14 ± 0.23	11.10 ± 0.21
SMM J030231.81+001031.3	-21.96 ± 0.38	2.1 ± 0.0	9.49 ± 0.19	9.45 ± 0.16
SMM J030236.15+000817.1	-24.95 ± 0.43	1.6 ± 0.1	10.69 ± 0.21	10.65 ± 0.18
SMM J030238.62+001106.3[a]	-19.39 ± 0.13	2.1 ± 0.3	8.47 ± 0.13	8.42 ± 0.07
SMM J030244.82+000632.3[a]	-23.22 ± 0.15	1.6 ± 0.1	10.00 ± 0.13	9.96 ± 0.08
SMM J105151.69+572636.0	-25.08 ± 0.30	2.8 ± 0.1	10.74 ± 0.17	10.70 ± 0.13
SMM J105155.47+572312.7[c]	-25.47 ± 0.36	0.9 ± 0.3	10.90 ± 0.18	10.86 ± 0.15
SMM J105158.02+571800.2	-25.87 ± 0.21	1.6 ± 0.1	11.06 ± 0.14	11.02 ± 0.10
SMM J105200.22+572420.2[b]	-23.38 ± 0.05	2.4 ± 0.6	10.06 ± 0.11	10.02 ± 0.05
SMM J105201.25+572445.7	-23.89 ± 0.16	2.4 ± 0.3	10.26 ± 0.13	10.22 ± 0.08
SMM J105207.49+571904.0	-25.40 ± 0.66	1.0 ± 0.8	10.87 ± 0.29	10.83 ± 0.27
SMM J105225.79+571906.4	-25.90 ± 0.65	0.9 ± 0.9	11.07 ± 0.28	11.03 ± 0.26
SMM J105227.58+572512.4	-25.65 ± 0.32	2.2 ± 0.2	10.97 ± 0.17	10.93 ± 0.14
SMM J105230.73+572209.5	-26.63 ± 0.22	1.4 ± 0.1	11.36 ± 0.14	11.32 ± 0.10
SMM J105238.19+571651.1	-25.32 ± 0.34	0.9 ± 0.3	10.84 ± 0.18	10.80 ± 0.14
SMM J105238.30+572435.8	-25.70 ± 0.16	2.1 ± 0.3	10.99 ± 0.13	10.95 ± 0.08
SMM J123549.44+621536.8	-26.37 ± 0.76	1.4 ± 0.1	11.26 ± 0.32	11.22 ± 0.31
SMM J123553.26+621337.7[b]	-25.16 ± 0.31	0.9 ± 0.3	10.78 ± 0.17	10.73 ± 0.13
SMM J123555.14+620901.7	-25.91 ± 0.30	1.8 ± 0.3	11.08 ± 0.17	11.03 ± 0.13
SMM J123600.15+621047.2[b,c]	-24.20 ± 0.52	2.1 ± 0.6	10.39 ± 0.23	10.35 ± 0.21
SMM J123606.72+621550.7	-26.00 ± 0.18	0.5 ± 0.2	11.11 ± 0.14	11.07 ± 0.09
SMM J123606.85+621021.4	-26.08 ± 0.47	1.5 ± 0.0	11.14 ± 0.22	11.10 ± 0.19
SMM J123616.15+621513.7	-25.36 ± 0.27	2.6 ± 0.1	10.85 ± 0.16	10.81 ± 0.11

Table 6.1 – Continued

Chapman et al. (2005) ID	M_H (mag, Vega)	A_V (mag)	$\log M_\star$, BC03 ($M_\odot$)	$\log M_\star$, M05 ($M_\odot$)
SMM J123618.33+621550.5	-24.64 ± 0.32	1.8 ± 0.3	10.57 ± 0.17	10.52 ± 0.14
SMM J123621.27+621708.4	-25.33 ± 0.32	1.5 ± 0.3	10.84 ± 0.17	10.80 ± 0.14
SMM J123622.65+621629.7	-25.51 ± 0.38	1.8 ± 0.3	10.92 ± 0.19	10.87 ± 0.16
SMM J123629.13+621045.8	-25.05 ± 0.09	3.0 ± 0.0	10.73 ± 0.12	10.69 ± 0.06
SMM J123632.61+620800.1[b,c]	-25.60 ± 0.36	1.2 ± 0.3	10.95 ± 0.18	10.91 ± 0.15
SMM J123634.51+621241.0	-25.16 ± 0.15	2.4 ± 0.3	10.77 ± 0.13	10.73 ± 0.08
SMM J123635.59+621424.1[b,c]	-26.40 ± 0.43	2.0 ± 0.5	11.27 ± 0.21	11.23 ± 0.18
SMM J123636.75+621156.1	-23.21 ± 0.08	1.6 ± 0.1	9.99 ± 0.12	9.95 ± 0.05
SMM J123707.21+621408.1	-25.26 ± 0.22	2.2 ± 0.2	10.82 ± 0.14	10.77 ± 0.10
SMM J123711.98+621325.7	-24.17 ± 0.35	1.8 ± 0.3	10.38 ± 0.18	10.33 ± 0.15
SMM J123712.05+621212.3	-24.63 ± 0.39	2.6 ± 0.1	10.56 ± 0.19	10.52 ± 0.16
SMM J123721.87+621035.3	-25.19 ± 0.25	1.8 ± 0.0	10.79 ± 0.15	10.75 ± 0.11
SMM J131201.17+424208.1	-26.39 ± 0.32	0.9 ± 0.3	11.27 ± 0.17	11.23 ± 0.14
SMM J131208.82+424129.1	-25.03 ± 0.48	2.5 ± 0.5	10.72 ± 0.23	10.68 ± 0.20
SMM J131212.69+424422.5	-24.81 ± 0.65	1.0 ± 0.8	10.64 ± 0.29	10.59 ± 0.27
SMM J131215.27+423900.9[b]	-30.24 ± 0.05	0.3 ± 0.3	12.81 ± 0.12	12.76 ± 0.05
SMM J131222.35+423814.1[b]	-28.60 ± 0.56	0.9 ± 0.3	12.15 ± 0.25	12.11 ± 0.23
SMM J131225.20+424344.5	-25.20 ± 0.15	2.0 ± 0.5	10.79 ± 0.13	10.75 ± 0.08
SMM J131225.73+423941.4	-24.72 ± 0.38	1.2 ± 0.3	10.60 ± 0.19	10.56 ± 0.16
SMM J131228.30+424454.8	-25.65 ± 0.23	1.4 ± 0.1	10.97 ± 0.15	10.93 ± 0.10
SMM J131232.31+423949.5[b]	-26.01 ± 0.44	2.1 ± 0.3	11.11 ± 0.21	11.07 ± 0.18
SMM J131239.14+424155.7	-24.43 ± 0.21	1.6 ± 0.1	10.48 ± 0.14	10.44 ± 0.10
SMM J141741.81+522823.0[b]	-27.09 ± 0.20	2.8 ± 0.1	11.55 ± 0.14	11.50 ± 0.09
SMM J141742.04+523025.7	-25.65 ± 0.11	0.9 ± 0.3	10.97 ± 0.12	10.93 ± 0.06
SMM J141802.87+523011.1	-24.74 ± 0.39	0.5 ± 0.2	10.61 ± 0.19	10.56 ± 0.16

Table 6.1 – Continued

Chapman et al. (2005) ID	M_H (mag, Vega)	A_V (mag)	$\log M_\star$, BC03 ($M_\odot$)	$\log M_\star$, M05 ($M_\odot$)
SMM J141809.00+522803.8	-26.08 ± 0.37	2.2 ± 0.2	11.14 ± 0.19	11.10 ± 0.15
SMM J163627.94+405811.2	-24.90 ± 0.22	0.8 ± 0.1	10.67 ± 0.14	10.63 ± 0.10
SMM J163631.47+405546.9	-25.22 ± 0.34	1.5 ± 0.3	10.80 ± 0.18	10.76 ± 0.14
SMM J163639.01+405635.9[b]	-24.78 ± 0.29	2.1 ± 0.3	10.62 ± 0.16	10.58 ± 0.12
SMM J163650.43+405734.5	-26.95 ± 0.52	1.0 ± 0.2	11.49 ± 0.24	11.45 ± 0.21
SMM J163658.19+410523.8	-25.11 ± 0.23	1.9 ± 0.1	10.75 ± 0.15	10.71 ± 0.10
SMM J163658.78+405728.1	-25.46 ± 0.31	2.7 ± 0.0	10.90 ± 0.17	10.85 ± 0.13
SMM J163704.34+410530.3	-23.35 ± 0.11	2.5 ± 0.5	10.05 ± 0.12	10.01 ± 0.06
SMM J163706.51+405313.8	-25.51 ± 0.20	2.5 ± 0.5	10.91 ± 0.14	10.87 ± 0.09
SMM J221725.97+001238.9	-24.16 ± 0.55	3.0 ± 0.0	10.38 ± 0.25	10.33 ± 0.22
SMM J221733.12+001120.2	-25.20 ± 0.02	2.2 ± 0.5	10.79 ± 0.11	10.75 ± 0.04
SMM J221733.91+001352.1	-25.92 ± 0.20	1.4 ± 0.1	11.08 ± 0.14	11.03 ± 0.09
SMM J221735.15+001537.2	-25.17 ± 0.74	1.7 ± 0.8	10.78 ± 0.32	10.74 ± 0.30
SMM J221735.84+001558.9	-24.98 ± 0.29	1.5 ± 0.3	10.70 ± 0.16	10.66 ± 0.12
SMM J221804.42+002154.4	-25.51 ± 0.38	1.2 ± 0.3	10.92 ± 0.19	10.87 ± 0.16
SMM J221806.77+001245.7	-25.17 ± 0.26	2.6 ± 0.1	10.78 ± 0.16	10.73 ± 0.12

[a] M_H, and thus $M_\star$, is likely underestimated by the SED fitting for this object.
[b] The SED of this object shows a red excess.
[c] The SED of this object shows a blue excess.

Our stellar mass results in this section confirm that, in general, SMGs have large stellar masses in addition to large star formation rates. The stellar masses among the SMG sample show less dispersion than their IR luminosities, and have no trend with redshift. This small range of typical stellar mass could indicate that only relatively high mass galaxies will undergo a far-IR luminous phase.

6.3.4 Implications of New $M_\star$ Estimates on the $M_{BH} - M_\star$ Relation for SMGs

Borys et al. (2005) found a tentative correlation between the rest-frame K-band luminosity and X-ray luminosity for a sample of 13 X-ray detected SMGs from the sample of C05, which the authors suggest indicates a correlation between the masses of the central black holes of SMGs and the stellar masses of their host galaxies if the X-ray emission from the galaxies arises from accretion onto a supermassive black hole. However, when they plot the black hole mass (M_{BH}), derived from the absorption-corrected X-ray luminosity assuming Eddington-limited accretion, versus stellar mass and compare to the local M_{BH}-$M_{\rm bulge}$ relation of Marconi & Hunt (2003), they found that the SMGs fell significantly below the local relation. The estimates of Borys et al. (2005) implied that the central black hole masses are ~ 50 times smaller than those of local galaxies of similar bulge mass. After examining the assumptions and uncertainties involved in their calculations of $M_\star$ and M_{BH}, they concluded that the black hole masses were the more important source of uncertainty and that, unless the lifetime of SMGs is very short ($\sim 50\,$Myr) and the accretion efficiency of the black hole is low, the central black holes of SMGs must grow significantly in order to reach the local $M_{BH} - M_{\rm bulge}$ relation.

In calculating $M_\star$ for the entire sample of SMGs from C05, we have computed new mass estimates for the SMGs analyzed in Borys et al. (2005), and here we examine the effect of our revised stellar mass estimates on the position of SMGs relative to local galaxies in the M_{BH}–$M_{\rm bulge}$ relation. In Figure 6.13 we plot the local $M_{BH} - M_{\rm bulge}$ relation found by Marconi & Hunt (2003) along with the estimates of M_{BH} of Alexander et al. (2005) and Borys et al. (2005) and our new $M_\star$ values, corrected to the same IMF as used by Borys et al. (2005). The hatched area in the diagram indicates the region in which nearly all the SMGs fell in the plot of Borys et al. (2005), and makes it immediately obvious that our new $M_\star$ estimates are lower than those of Borys et al. (2005) and bring the SMGs closer to

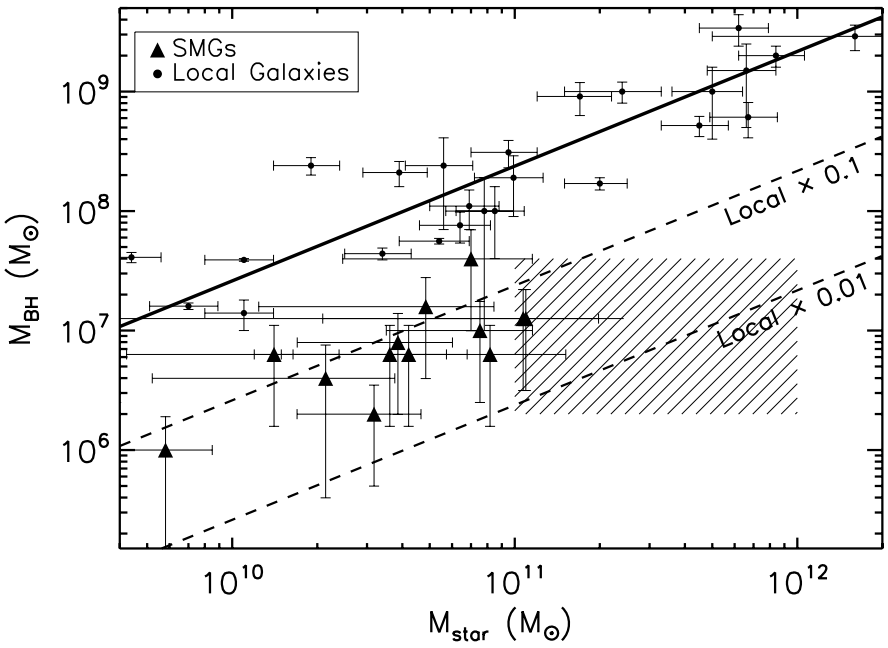

Figure 6.13 Revised M_{BH}–$M_\star$ relation for SMGs analyzed by Borys et al. (2005), using the new $M_\star$ values we have calculated in this Chapter. SMGs are represented by the filled triangles, while the small round points represent the local galaxies from the sample of Marconi & Hunt (2003) used to establish the local M_{BH}–$M_{\rm bulge}$ relation (shown as the solid line). The dotted lines represent the local relation multiplied by the indicated factors. The hatched region indicates the area in which most of the SMGs fell in the analysis of Borys et al. (2005).

the local $M_{BH} - M_{\rm bulge}$ relation. However, the SMGs still lie below the local relation by a factor of ~ 10, and thus the conclusions of Borys et al. (2005) are qualitatively unchanged.

The change in the location of SMGs in the $M_{BH} - M_\star$ relation highlights the large uncertainties associated with stellar mass estimates. In the presence of such large systematic effects it is important to consider independent checks on the derived stellar masses, for example, comparing to dynamical mass estimates or gas mass estimates where available (e.g., Erb et al. 2006). In the next section we do so, using measurements of H_2 mass from CO observations of SMGs.

6.4 Comparison to CO Results: Testing $M_\star$ and Constraints of SMG Evolution

SMGs are effectively unique among high-z galaxy populations because it is possible to constrain the gas mass and stellar mass of these objects independently: as discussed in Chapter 2, estimates of the molecular gas mass can be made from observations of CO rotational line emission at submm/mm/cm wavelengths, while stellar mass estimates can be made from analyzing the rest-frame UV through near-IR SED, as we have done in Section 6.3 above. For other high-z populations, typically it is possible to obtain either the gas mass or the stellar mass, but not both: so far only two optically-selected high-z star-forming galaxies (e.g., LBGs, BX/BM galaxies, BzK galaxies) have been detected in CO emission, both of which are highly magnified by gravitational lensing (Baker et al. 2004; Coppin et al. 2007), but many have stellar mass determinations in the literature; whereas for high-z QSOs and radio galaxies, CO emission is detectable (e.g., Hainline et al. 2004; De Breuck et al. 2005) and the gas mass can be estimated, but the stellar mass is poorly constrained because the active nucleus tends to dominate the rest-frame optical light. Thus, for the SMGs with CO observations we have powerful constraints of the baryonic mass and evolution of individual objects. The SMGs with CO detections also have dynamical mass estimates available from the CO observations, which are very important checks on the reliability of the stellar mass estimates. If the CO results currently available for SMGs are typical of the entire SMG population, then with the existing stellar mass estimates we can attempt to constrain their evolution.

For the first time, with our new stellar mass estimates for the SMG sample of C05, stellar masses are available for SMGs with CO observations; thus, we can make the first direct comparisons of gas mass to stellar mass for individual high-z SMGs. 10 of the SMGs observed in CO emission by Greve et al. (2005) overlap with our stellar mass sample, of which 5 are detected in CO. 2 additional SMGs in our stellar mass sample have been detected in CO emission by Tacconi et al. (2006). We list the CO results for these objects overlapping with our stellar mass sample in Table 6.2 and use the CO detections and upper limits of these sources, along with the dynamical masses obtained for the detections, to check our stellar mass estimates and look for evolutionary trends in the relative quantities of gas and stars in these SMGs.

Table 6.2. SMGs in C05 Sample with CO Observations

C05 ID	z_{spec}	CO Transition	$M(\mathrm{H_2})$ $\times 10^{10}\,M_\odot$	M_{dyn} $\times 10^{11}\,M_\odot$	$M_\star/M_{dyn}$ [a]	Reference
SMM J105230.73+572209.5	2.611	3→2	< 1.4	···	···	1
SMM J105238.30+572435.8	3.036	3→2	< 3.0	···	···	1
SMM J123549.44+621536.8	2.202	3→2	3.4	1.7	1.1	2
SMM J123707.21+621408.1	2.490	3→2	1.6	0.85	0.8	2
SMM J131201.17+424208.1	3.405	1→0	16	1.2	1.5	1,3
SMM J131232.31+423949.5	2.320	3→2	< 2.4	···	···	1
SMM J163631.47+405546.9	2.283	3→2	< 0.9	···	···	1
SMM J163639.01+405635.9	1.495	2→1	< 1.8	···	···	1
SMM J163650.43+405734.5	2.380	3→2	5.6	3.5	1.2	1
SMM J163658.19+410523.8	2.454	3→2	4.6	3.7	0.2	1
SMM J163706.51+405313.8	2.374	3→2	2.4	3.4	0.2	1
SMM J221735.15+001537.2	3.098	3→2	3.0	2.8	0.2	1

Note. — References: (1) Greve et al. (2005); (2) Tacconi et al. (2006); (3) Hainline et al. (2006)

[a] $M_\star/M_{dyn}$ calculated using $M_\star$ estimated from models of BC03.

6.4.1 Testing the Stellar Mass Estimates

In Figure 6.14 we compare the $M_\star$ values calculated in §6.3 to the H_2 masses of Greve et al. (2005) and Tacconi et al. (2006) for the SMGs which have both stellar mass estimates and CO observations. We plot the stellar mass estimates resulting from the stellar population models of both BC03 and Maraston (2005) to demonstrate that the choice of models has no effect on our discussion; subsequent plots in this section will use the BC03 models for simplicity. It is clear from the plot that the stellar mass tends to exceed the molecular gas mass, but by less than an order of magnitude, so it seems likely that the stellar mass estimates are not unreasonable.

In principle, a better check on the stellar masses would be to compare to the dynamical mass, M_{dyn}, so we compare the values of $M_\star$ to M_{dyn} in Table 6.2. M_{dyn} for galaxies is usually calculated as

$$M_{dyn} = A\,\frac{\sigma^2 r}{G}, \tag{6.3}$$

where σ is the velocity dispersion, and r is the radius of the galaxy. The factor A will depend on a galaxy's velocity structure, mass distribution, and whether or not the system in ellipsoidal or disk-like, and estimates of A typically range from less than 1 to more than 5. Since these types of parameters (velocity field, morphology, etc.) are typically not known for high-z galaxies, the value of A is uncertain within a factor of a few. Greve et al. (2005) warn that significant uncertainties are associated with their dynamical mass estimates, since their calculations of M_{dyn} assume the observed CO lines are a product of a merging gas-rich system. If the system is not in dynamical equilibrium, the mass distribution assumed is incorrect, or if the observed CO line is not a good tracer of the system dynamics, M_{dyn} will change because the values of A will change; thus, the dynamical masses in any case should not be considered more accurate than to within a factor of a few. Indeed, in Table 6.2, three of the SMGs have $M_\star$ larger than M_{dyn}, a clearly unphysical situation. Yet, $M_\star$ never exceeds M_{dyn} by more than a factor of 2, which is well within the systematic uncertainty in both $M_\star$ and M_{dyn}. Taking into account the systematic uncertainties and noting that the remaining 4 SMGs with CO detections have stellar masses consistent with their dynamical mass, we find the dynamical mass estimates are consistent with the stellar mass for the individual SMGs with CO observations.

Since we have such a small sample of SMGs with CO observations relative to the size of

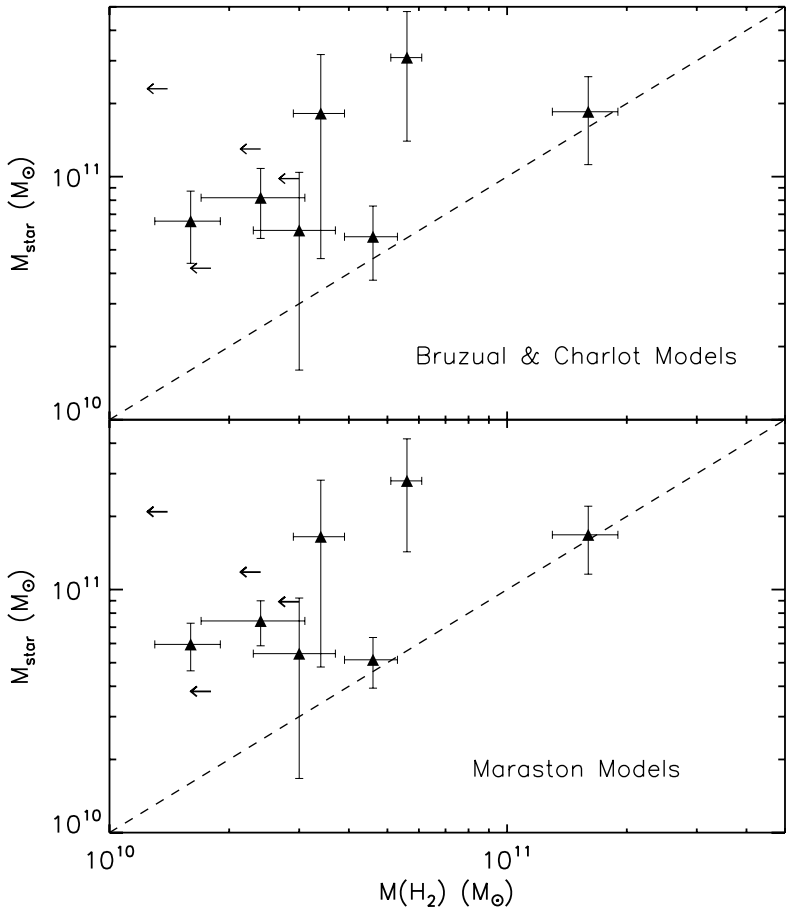

Figure 6.14 Comparison of $M(\mathrm{H_2})$ derived from CO observations to $M_\star$ estimated in Section 6.3. In the top panel, the stellar mass estimates use the models of BC03; in the bottom panel, the stellar masses are calculated using the models of Maraston (2005). The SMGs detected in CO observations are represented by filled triangles, while the SMGs observed but not detected in CO are shown as leftward-pointing arrows representing the upper limits on $M(\mathrm{H_2})$. The dotted line represents $M(\mathrm{H_2}) = M_\star$. Note that the choice of stellar population models does not impact our discussion.

the stellar mass sample, it will be more informative to check the validity of the stellar mass results with the CO results in an average sense than on a galaxy-by-galaxy basis. If we assume the properties of the CO-observed SMGs are typical of the entire C05 sample, then the typical dynamical mass is $M_{dyn} \simeq 1.2 \times 10^{11}\, M_{\odot}$, the median M_{dyn} found by Greve et al. (2005) and Tacconi et al. (2006), and the typical molecular mass is $M(\mathrm{H_2}) = 3.0 \times 10^{10}\, M_{\odot}$, the median of the combined samples of Greve et al. (2005) and Tacconi et al. (2006). The median stellar mass for the C05 sample is $M_{\star} = 6.9 \times 10^{10}\, M_{\odot}$ from §6.3.3. Thus, on average, the sum $M_{gas} + M_{\star}$ is consistent with the estimates of the dynamical mass, so we conclude that the stellar masses we have estimated are generally consistent with the the observations of the gas mass and dynamical mass of SMGs.

6.4.2 Gas Fractions, Baryonic Masses, and SMG Evolution

The relative fractions of the mass of a galaxy contributed by gas and stars give us insight into the evolutionary state of the object. For example, in local galaxies, gas fraction increases along the Hubble sequence from old, passively evolving elliptical galaxies to irregular star-forming dwarf galaxies (Roberts & Haynes 1994). Looking back at Figure 6.14, the SMGs with CO detections appear to have comparable contributions from gas and stars to the total baryonic mass. These SMGs even suggest a loose positive correlation between $M(\mathrm{H_2})$ and $M_{\star}$, similar to the the findings of Erb et al. (2006) for UV-selected galaxies at $z \sim 2$; however, the upper limits in the figure caution that generalizing on the basis of the detections may not be accurate for the SMGs, since some high-$M_{\star}$ SMGs have upper limits on the molecular gas mass that are inconsistent with them having similarly high gas masses.

Instead, we look at the relative contribution of gas and stellar mass by calculating the gas fraction $\mu = M(\mathrm{H_2})/[M_{\star} + M(\mathrm{H_2})]$, and we plot gas fraction versus $M_{\star}$ in Figure 6.15. First, we notice that the gas fractions of these SMGs are higher than is found locally for elliptical galaxies (typical $\mu \sim 10^{-4}$; Roberts & Haynes 1994), spiral galaxies ($\mu \sim 0.1$; Roberts & Haynes 1994), and ULIRGs (typical $\mu \sim 0.16$; Downes & Solomon 1998), and similar to, if not perhaps slightly lower than, the gas fractions found by Erb et al. (2006) for $z \sim 2$ UV-selected galaxies ($\mu \sim 0.1 - 0.8$) using Hα luminosities and the Kennicutt-Schmidt law (Kennicutt 1998). We also see in the plot a generally declining gas fraction as the stellar mass increases, which suggests an evolutionary trend that the SMGs with higher stellar masses have converted more of their molecular gas into stars compared with SMGs

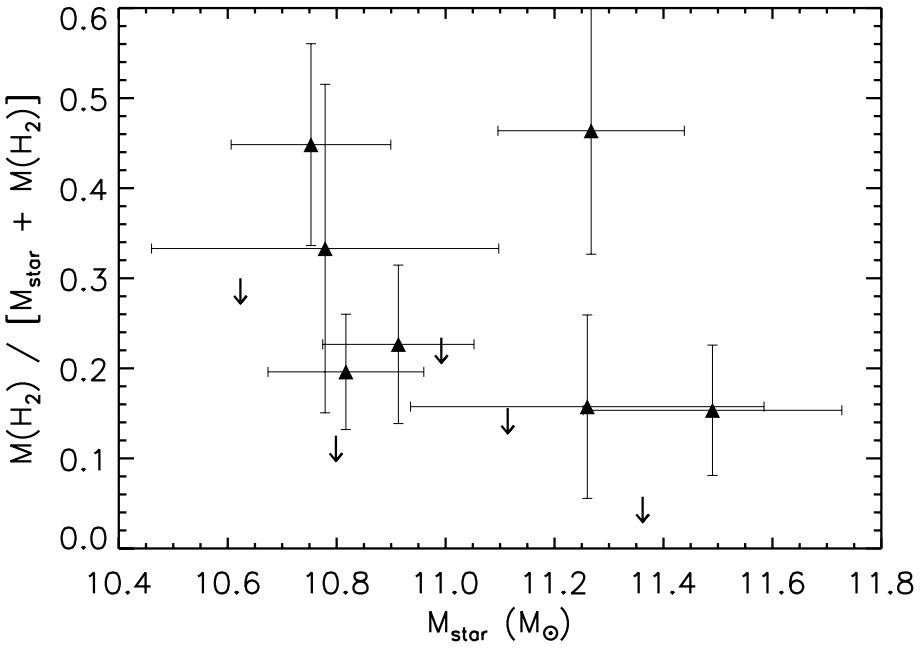

Figure 6.15 Gas fraction vs. $M_\star$ for SMGs having CO emission line observations at mm/cm wavelengths. Symbols are as in Figure 6.14.

of lower stellar mass.

However, this apparent trend may not be real: the point corresponding to the galaxy SMM J131201.17+424208.1 (SMM 13120 from Chapter 2) is an outlier with a high stellar mass and a high gas fraction. We note, though, that we have used the $M(\mathrm{H_2})$ determined from CO(1→0) observations for this galaxy since it is the most representative determination of the gas mass in this galaxy, while the other galaxies have their gas masses determined from higher-level CO transitions. It is possible that this galaxy would not appear abnormal if we used mass determinations from CO(1→0) for all of the SMGs. On the other hand, Erb et al. (2006) suggest that galaxies like SMM 13120 are young starbursts with high gas fractions. Such a scenario is possible, and we note that as SMM 13120 is the highest redshift SMG with a CO detection ($z = 3.405$), it could be in an earlier stage of evolution than $z \sim 2$ SMGs and simply a galaxy of larger total mass, but such a conclusion should not be drawn until more CO(1→0) observations are available for more SMGs.

The case of SMM J13120 brings into view an interesting question: are the SMGs at higher redshifts ($z \sim 3$) less evolved than those at lower redshifts ($z \sim 2$), meaning that

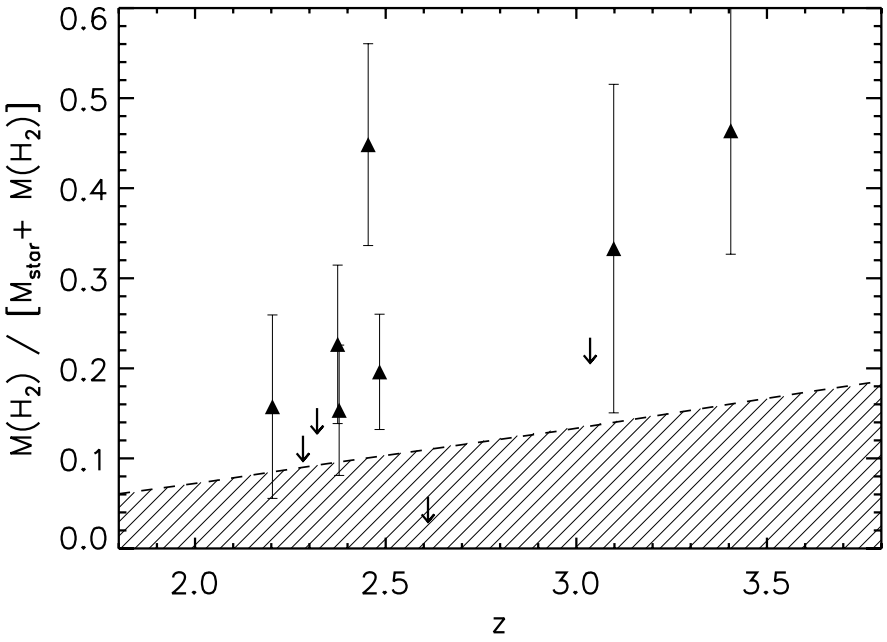

Figure 6.16 Gas fraction vs. z for SMGs with CO observations. Symbols are as in Figure 6.14. The hatched area at the bottom of the plot indicated the region rendered inaccessible by the detection limit of the CO survey, assuming the median $M_\star$ for the C05 sample.

they have converted a smaller fraction of their gas into stars? In Figure 6.16 we show the gas fraction of the SMGs with CO observations as a function of redshift. The hatched region in this figure represents the region in which selection effects from the CO observations prevent data points from falling, assuming the median $M_\star$ for the total C05 sample obtained in §6.3.3. A trend of gas fraction increasing with redshift is apparent, in spite of the large errors on the gas fraction; the trend is not entirely due to selection, as the hatched region indicates, because the stellar mass does not show a trend with redshift. It thus appears that SMGs at higher redshifts indeed have converted less of their gas mass into stars; however, substantially more CO data are required to firmly establish this trend.

We estimate the total baryonic mass for the SMGs with CO detections by summing $M_\star + M(\mathrm{H_2})$. Neglecting the systematic uncertainties in both the stellar mass and molecular gas estimates, this sum is likely a lower limit on the baryonic mass since we do not include a contribution from neutral gas. The median M_{baryon} among the 7 SMGs with CO detections in our stellar mass sample is $1.0 \times 10^{11}\,M_\odot$, similar to the stellar mass of an intermediate-

mass L^* elliptical galaxy in the local universe (Cole et al. 2001). In spite of the systematic uncertainties in $M_\star$ and $M(\mathrm{H_2})$, the stellar and gas masses together indicate that typical high-z SMGs have high baryonic masses and significant contributions to the total baryonic mass from both stars and gas.

6.5 Discussion

With our new rest-frame UV–near-IR SEDs, extinction estimates, near-IR absolute magnitudes, and stellar mass estimates for a large, representative sample of SMGs, we are able to explore several issues which have been difficult to address in the past for this class of galaxies. In this section we discuss a few of these topics: the estimation of photometric redshifts for SMGs from optical–mid-IR data, how the stellar emission of SMGs compares to local galaxies and ULIRGs, and how the stellar characteristics of SMGs compare to other populations of high-z galaxies, such as the UV, optical, and near-IR-selected galaxies.

6.5.1 Photometric Redshifts for SMGs using IRAC Data

We observed in §6.2.3 that the 1.6μm bump is clearly visible in the rest-frame UV–near-IR SEDs of most of the radio-detected SMGs in the sample of C05; if this bump could be used to determine photometric redshifts reliably for SMGs, it could be very powerful in studies of large numbers of these galaxies, since it would be possible to derive redshifts for much larger numbers of submm sources while avoiding time-intensive optical-band spectroscopy. However, the ultimate accuracy of the redshift estimate would still depend on the correct identification of the counterpart of the submm source. Sawicki (2002) demonstrated the utility of the 1.6μm bump in the SED of cool stars caused by the minimum in the opacity of the $\mathrm{H^-}$ ion as a photometric redshift indicator for high redshift galaxies. The technique was justified on the grounds that the feature is visible in the SEDs of all stellar populations except the very youngest (age $\sim 1\,\mathrm{Myr}$). Photometric redshifts for SMGs based on optical data have been shown to be fairly accurate out to $z \sim 2$; however, beyond $z \sim 2$ the photometric redshifts for SMGs have not been well-tested (Pope et al. 2005). As discussed in Chapter 4, photometric redshifts for SMGs from submm/radio data have significant uncertainties as well, related to the shape of the SED of individual SMGs.

Here, we explore the use of the IRAC data, which samples the 1.6μm bump at $z \sim 2$,

together with optical photometry in determining photometric redshifts for SMGs. Several previous studies have estimated photometric redshifts from *Spitzer* data for small numbers of SMGs: Egami et al. (2004) estimate photometric redshifts for 7 submm sources in the Lockman Hole from IRAC photometry using the 1.6μm feature, though they give no assessment of accuracy, and Pope et al. (2006) estimate photometric redshifts from IRAC and MIPS data for SMGs in the GOODS-N field by finding the linear combination of the logarithms of the *Spitzer* fluxes that minimizes the total dispersion in the photometric redshifts relative to the spectroscopic redshifts for 10 sources of known spectroscopic redshift. With our sample of ~ 70 SMGs with spectroscopic redshifts and IRAC measurements, we can best evaluate the reliability of photometric redshifts based on near-IR SED features for SMGs.

We estimate photometric redshifts for our sample of SMGs using the same photometric data used to fit the SEDs of the objects for the stellar mass estimates and once again use HYPER-Z to fit the observed SEDs to the stellar population models of BC03. We allow HYPER-Z to choose the best-fitting spectral template from a grid of models of solar metallicity, Salpeter IMF, and the simple star formation histories of instantaneous burst, constant star formation, and exponential decline with $\tau = 0.01, 0.1, 1$, and 2 Gyr. We allow the SEDs to be fit with dust extinction described by the Calzetti et al. (2000) law for starburst galaxies, as in the SED fitting for stellar mass estimates, constraining A_V to lie in the range 0–3. Finally, we constrain the redshift of each galaxy to be in the range $0 < z < 5$.

We plot the resulting best-fit photometric redshift versus spectroscopic redshift for all of the SMGs in our sample with IRAC observations in Figure 6.17. At first glace, the photometric redshift results are not encouraging: the dispersion in the redshift errors is large, $\sigma(\Delta z/[1+z]) = 0.48$. However, recalling that the different SMG fields have photometry in different numbers and ranges of photometric bands, we break down the results shown in Figure 6.17 by field in Figure 6.18, in which different SMG fields are designated by different color points. For clarity, we show the data points for the field observed in the largest number of photometric bands spanning the largest wavelength range (GOODS-N, $UBVRIz'JK$ + IRAC), the points for the field with the fewest number of photometric bands observed (Lockman Hole, usually RIK + IRAC), and two fields which are intermediate in photometric coverage (SSA 13, with $BRIz'JK$ + IRAC, and ELAIS-N2, with $BVRIK$+IRAC). The scatter of the points in different fields in Figure 6.18 clearly indicates

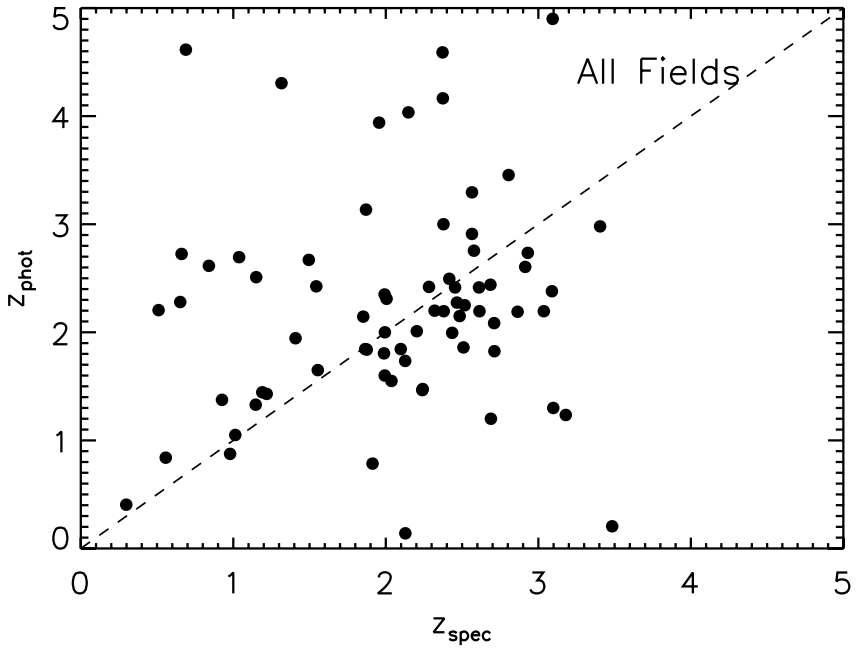

Figure 6.17 Photometric z vs. spectroscopic z for SMGs in the C05 sample with IRAC measurements. The dotted line represents $z_{phot} = z_{spec}$.

that, as might be expected, the galaxies with the most observed SED points have the best photometric redshift results, while galaxies with the fewest tend to have less reliable outcomes. The photometric redshifts for the GOODS-N field have a dispersion in redshift error of $\sigma(\Delta z/[1+z]) = 0.10$, better than than the accuracy of submm-radio photometric redshifts, and sufficient for adequate estimates of physical parameters such as luminosity. On the other hand, for sources in the Lockman Hole field the dispersion is $\sigma(\Delta z/[1+z]) = 0.74$, which is not of sufficient accuracy for most analyses. The dispersions in for the SMGs in SSA 13 and ELAIS-N2 are 0.29 and 0.43, respectively; the lower scatter in SSA 13 may reflect the presence of J photometry, which ELAIS-N2 lacks.

Our results here suggest that useful photometric redshifts can indeed be derived for SMGs when IRAC measurements are combined with sufficient photometric measurements in optical and near-IR bands to well-sample the SEDs of the galaxies across the U–K bands. It appears in this case that the 1.6μm feature in the SED can be most useful for SMGs, producing better photometric redshifts than the use of the submm-radio index. However, our results also indicate that neither IRAC data alone nor optical+near-IR data alone produce

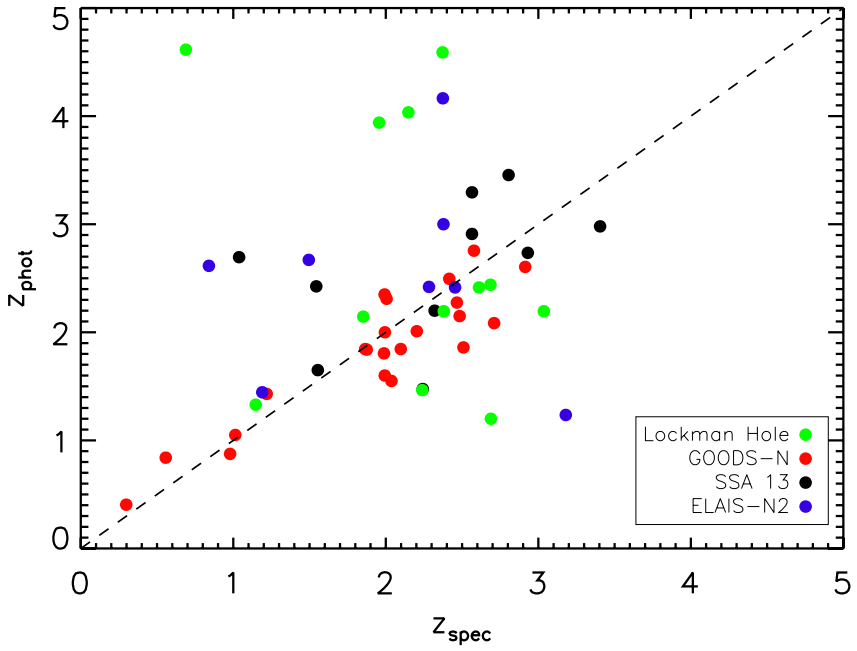

Figure 6.18 Photometric z vs. spectroscopic z for SMGs in the C05 sample with IRAC measurements, color-coded according to sky field. The dotted line represents $z_{phot} = z_{spec}$.

photometric redshifts reliable enough for science applications. Though a thorough exploration is beyond the scope of our simple test here, other methods of estimating photometric redshifts (e.g., neural networks or Bayesian techniques; see Brodwin et al. 2006; Benítez 2000) may produce better results than the χ^2-minimization of HYPER-Z for sparse SED sampling and could be tested on the C05 SMG sample.

6.5.2 Stellar Properties of SMGs and Their Relation to Local Galaxies and ULIRGs

Approximately two-thirds (46 of 67) of the C05 sample of radio-detected SMGs with IRAC observations have rest-frame UV through near-IR SEDs which are clearly consistent with dust-obscured starlight, as opposed to scattered AGN light and/or an obscured AGN. Most of these 46 SMGs also display a clear stellar bump at 1.6 μm, and less than 5 display significant contamination from optical emission lines in their photometry (consistent with the fraction of SMGs, 10%, which show strong Hα in the sample of Swinbank et al. 2004). Hence, we conclude that for the majority of the SMGs in our sample with IRAC obser-

vations, the near-IR emission is dominated by stellar light, and we can characterize the stellar populations of SMGs from the near-IR data for the majority of the galaxies. In this section, we use the results of our optical to near-IR SED fitting of the C05 SMGs to discuss stellar population characteristics of SMGs, which we compare to "normal" galaxies and ULIRGs in the local Universe. We also calculate star formation rates for the sample from our new luminosity estimates in Chapter 4 to look at star formation as a function of mass and speculate on the timescale of formation of the stars in SMGs.

Our fits with HYPER-Z produce estimates of stellar population age, extinction, and absolute magnitude, so in principle we could discuss all of these characteristics; however, as discussed in §6.2.2, our inability to constrain the star formation histories of SMGs in our SED fitting means that the ages of the stellar populations are not well constrained. The differences in different stellar population synthesis models also cause difficulties in placing constraints on the stellar population ages. As an illustrative example of the difficulty in constraining the ages, we compare the average ages we obtain for our sample from fitting instantaneous burst and constant star formation models to the rest-frame UV through near-IR SEDs to those obtained by Smail et al. (2004) in fitting different sets models of the same star formation history to the rest-frame UV through optical SEDs. One might expect that fitting models to rest-frame UV through optical data would be more sensitive to recent star formation than fitting the rest-frame UV to near-IR SEDs and thus produce younger ages; to the contrary, we find much younger average ages than Smail et al. (2004) when we fit burst models, $\sim 70 - 100\,\mathrm{Myr}$ (depending on the use of BC03 models or Maraston (2005) models) versus 310 Myr from Smail et al. (2004). We obtain much older ages from the constant star formation history models than Smail et al. (2004), 1.4 Gyr versus 530 Myr. It is very likely that the typical stellar population age lies somewhere between those predicted by the instantaneous burst and constant star formation models, thus somewhere between 100 Myr and 1 Gyr, placing the dominant populations at rather intermediate ages. However, since the particular models and star formation history used influence the ages so much, we refrain from discussing the typical ages here because it is quite unclear what the fitted ages actually represent. Thus, we restrict our discussion to those of mass, absolute magnitude, and extinction.

The visual extinction, A_V, derived from our SED fits are better constrained than the population ages, though they are still loosely dependent on star formation history. How-

ever, we have averaged the results from the different star formation histories to reduce the influence of the star formation history. We obtain a mean extinction for SMGs of $\langle A_V \rangle = 1.7 \pm 0.7$ for the models of BC03 and $\langle A_V \rangle = 1.6 \pm 0.7$ for the models of Maraston (2005) after averaging the reddenings resulting from fits of the instantaneous burst and constant star formation models. These means are similar to those found by Smail et al. (2004) and Borys et al. (2005) for SMGs and are similar to the extinction in the outer regions of relatively local ULIRGs (Scoville et al. 2000). These typical extinction levels for SMGs also suggest that our stellar mass estimates from the reddening-uncorrected absolute H-band magnitudes may be underestimates, though the fraction by which the masses are underestimated is well within the systematic uncertainties. In Figure 6.19 we plot $L_{\rm IR}$ versus A_V for the C05 sample of SMGs with IRAC observations and MIPS observations using the new estimates of $L_{\rm IR}$ we present in Chapter 4. We see that there may be a trend of decreasing IR luminosity with increasing visual extinction, and it is clear that the highest-luminosity sources have the lowest visual extinction. This trend seems counter-intuitive for SMGs, because the IR light from SMGs arises from dust emission. A possible scenario explaining the trend is that when the obscuration is lower, the dust has higher temperatures, and thus the galaxy is more luminous (for example, when an AGN has cleared away some of its surrounding obscuring material). Also, it could be that the luminosity increases as the obscuration clears, though we would expect to see the optical luminosity increase as the obscuration clears away, not the IR luminosity.

However, it is important to point out that the mean optical extinction is different for the low and high-redshift SMGs: for SMGs with $z < 1.5$, the mean is $\langle A_V \rangle = 2.1 \pm 0.4\,{\rm mag}$, while for $z > 1.5$ SMGs, the mean is $\langle A_V \rangle = 1.5 \pm 0.6$. The $z < 1.5$ SMGs also tend to have lower $L_{\rm IR}$, which might explain the trend of decreasing optical extinction with increasing luminosity. Yet, when we remove the low-z points from Figure 6.19, a trend remains, which suggests that the different nature of the low-z sources is not the only reason for the anti-correlation of A_v and $L_{\rm IR}$. If we instead remove the highest luminosity points, almost all of which are known AGN from either their optical/near-IR spectra or rest-frame UV–near-IR SEDs, the correlation disappears, indicating that the brightest SMGs could be outliers because they are dominated by an AGN with low central obscuration.

The median reddening-uncorrected absolute H-band magnitude of our sample of SMGs, leaving out the objects which were missed by the IRAC images and had poor SED fits,

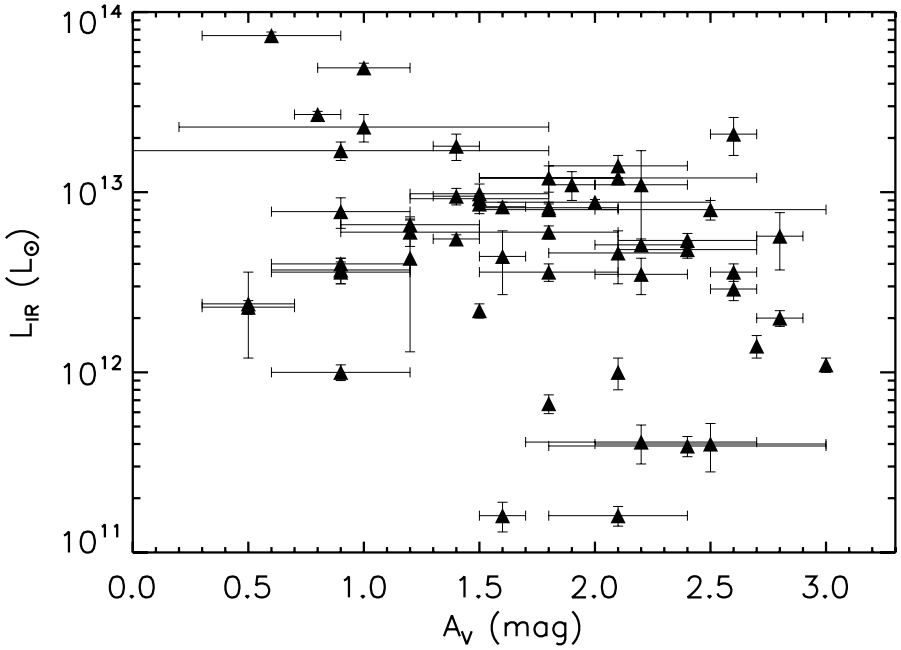

Figure 6.19 L_{IR} versus A_V for the C05 sample of radio-detected SMGs. Filled triangles represent SMGs which have both IRAC and MIPS observations with *Spitzer*.

is $M_H = -25.3$, with a standard deviation of 1.3. We also obtain a median absolute K magnitude for the same sample of $M_K = -26.6$. For normal local galaxies, $M_H^\star = -23.7$ and $M_K^\star = -23.4$ (Cole et al. 2001); thus, SMGs are brighter than local normal galaxies by factors of ~ 4 and ~ 20 in H and K, respectively. They are also intrinsically more luminous in the rest-frame near-IR than the IRAS 1-Jy sample of nearby ULIRGs, which have median absolute H and K magnitudes of $M_H \simeq -24$ (Veilleux et al. 2006) and $M_K = -25.2$ (Kim et al. 2002) and low-z radio-loud AGN, which have $\langle M_K \rangle = -25.4$ (Mauch & Sadler 2007). Assuming that majority of the near-IR luminosity arises from stars, the higher near-IR luminosity of SMGs might appear on the surface to indicate that SMGs are more massive than typical local galaxies and ULIRGs. However, the increased luminosity could instead indicate that the dominant stellar populations of SMGs are younger than in local galaxies, perhaps falling in the age range in which the contribution from TP-AGB stars is especially strong, assuming that the mass in stars has built up to a similar level as we see in local galaxies. That the dominant stellar populations are younger would make great sense, since we observe these galaxies ~ 10 Gyr ago, and would also be consistent with the recent findings

of Cirasuolo et al. (2007) that L_K^* for the near-IR luminosity function brightens by ~ 1 mag between $z = 0$ and $z = 2$. If L^* was brighter by one magnitude at $z \sim 2$, SMGs may be only a factor of ~ 10 more luminous in the near-IR than typical L^* contemporaries, and could be similarly more luminous than "normal" galaxies at their epochs as local ULIRGs are when compared to more typical local galaxies.

With our stellar mass estimates for SMGs, we can directly compare their stellar masses with local galaxies instead of relying on luminosities. As mentioned in §6.3.3, we find a median stellar mass for SMGs of $M_\star = 6.9 \times 10^{10}\,M_\odot$ from the BC03 stellar population models, and $M_\star = 6.3 \times 10^{10}\,M_\odot$ from the models of Maraston (2005). These numbers are lower than the characteristic stellar mass Cole et al. (2001) find for local galaxies using a Salpeter (1955) IMF, $M^*_{\rm stars} = 7.1 \times 10^{10} h^{-2}\,M_\odot$, and nearly an order of magnitude lower than the stellar mass of giant elliptical galaxies ($\sim 10^{12}\,M_\odot$). Consequently, typical radio-detected SMGs appear to have not yet built up the mass in stars that local massive galaxies contain, though it should be noted that the difference between the median $M_\star$ for SMGs and M^* for local massive galaxies is smaller than the systematic uncertainties in the stellar mass estimates for SMGs, and thus SMGs are not significantly less massive than local M^* galaxies. Yet, SMGs are also very gas rich relative to massive galaxies in the local universe; if the typical SMG possesses $3 \times 10^{10}\,M_\odot$ in molecular gas, as found for a smaller sample of SMGs by Greve et al. (2005), and converts all of that gas into stars over time, then the descendants of SMGs would have $M_\star \sim 10^{11}\,M_\odot$ and would be similar to M^* galaxies. The molecular gas and stellar masses typical for radio-detected SMGs also suggest that $z \sim 2$ SMGs do not possess the mass needed to transform into a giant elliptical galaxy unless they undergo further mergers. Rather, they may be progenitors of intermediate-mass elliptical galaxies, which is also the eventual fate proposed for ULIRGs by Genzel et al. (2001) and supported by Dasyra et al. (2006).

We find no trend of $M_\star$ with redshift or with $L_{\rm IR}$, which indicates that the high rates of star formation are not correlated with the mass of the host galaxy, nor does the typical mass of SMGs increase much over the cosmic time interval between $z \sim 3$ and $z \sim 1$. On the other hand, nearly all of the $z > 1$ SMGs are massive already, having masses greater than $10^{10}\,M_\odot$. Given the observed rates of star formation, can all of the stellar mass have been formed in the current IR-luminous phase? For each of the galaxies in the C05 sample with IRAC and MIPS observation, we estimate the star formation rate from the IR luminosity

estimates presented in Chapter 4 and find the amount of time necessary to form the total stellar mass we observe if the star formation rate remained constant at the level we observe. To obtain the star formation rate (SFR), we use the relation between L_{IR} and SFR of Kennicutt (1998) for a Salpeter IMF:

$$\mathrm{SFR}(M_\odot\,\mathrm{yr}^{-1}) = (1.7 \times 10^{-10}) \times L_{\mathrm{IR}}, \tag{6.4}$$

and conservatively assume that 70% of the IR emission from the SMGs can be attributed to star formation (30% to an AGN; Chapman et al. 2005; Alexander et al. 2005). We find that the average time to form the stellar mass in each SMG is 290 Myr, which is similar to or longer than the estimates of the duration of the SMG phase (50–200 Myr; Smail et al. 2004; Greve et al. 2005; Hainline et al. 2006). Unless we are observing nearly all SMGs at the end of their IR-luminous phase, which seems unlikely both statistically and from the molecular gas masses observed in SMGs, the SMGs must have formed at least some of their stellar mass prior to the burst of star formation we observe, possibly most of it. Furthermore, since the molecular gas mass is comparable to the stellar mass in SMGs, it appears that SMGs are unlikely to significantly increase their stellar mass (for example, by a factor of 10) in the future.

Putting it all together, our results confirm that the $z > 1$ radio-detected SMGs tend to be highly luminous, massive objects. They seem to simultaneously be experiencing strong, obscured starburst activity and AGN activity, as indicated by their large IR luminosities, $L_{\mathrm{IR}} > 10^{12}\,L_\odot$, both of which can be fueled by large quantities ($\sim 10^{10}\,M_\odot$) of molecular gas. From our rest-frame near-IR data it is also apparent that these SMGs are brighter in stellar emission than typical L^* galaxies and contain a significant mass ($\sim 10^{11}\,M_\odot$) in mildly obscured ($A_V \sim$ a few mag), likely intermediate-age stars (ages of a few hundred Myr to 1 Gyr), and have thus already formed much of their stellar mass prior to the activity causing the far-IR luminosity. The current star formation activity is not likely to increase the stellar mass by more than a factor of 2, based on molecular gas mass estimates for SMGs; thus, SMGs are likely already relatively mature, massive galaxies prior to the submillimeter-bright phase in which we observe them, similar to the progenitors of local ULIRGs, which are thought to be major mergers of similar-mass, gas rich galaxies (Sanders & Mirabel 1996).

6.5.3 Comparison of SMG Stellar Properties to Other High-z Galaxy Populations

The various populations of high-redshift galaxies selected at different wavelengths might seem to have little in common since at the wavelengths at which they are selected the physical mechanisms responsible for their emission are different. Also, as discussed in Chapter 1, the overlap between the galaxy populations tends to be small. Yet, all of the galaxy populations obviously have one characteristic in common, which may prove to be the key to understanding how the populations relate to one another: stars. Since stellar emission from galaxies peaks in the rest-frame near-IR, and the effects of dust are at a relative minimum in that same range of wavelength, it is likely that the most instructive way to compare the different types of high-z galaxies is by comparing their stellar properties inferred from rest-frame near-IR data. In this section we carry out such a comparison between high-z SMGs and some of the well-known high-redshift galaxy populations: LBGs, BX/BM galaxies, distant red galaxies (DRGs), BzK galaxies, and powerful high-z radio galaxies (HzRGs).

We begin by comparing stellar extinction among the galaxies. The comparison of IRAC colors between LBGs, BX/BM sources, and HzRGs in Chapter 5 suggested that the stars in SMGs are either more numerous or tend to experience more optical extinction than LBGs and BX/BM galaxies, though perhaps have similar amounts of optical extinction as HzRGs. In the previous subsection we reported that the SMGs with $z > 1.5$ had a mean and median A_V of 1.5 mag. This typical optical extinction for SMGs is larger than the mean A_V for BX/BM galaxies and LBGs found by Erb et al. (2006) and Rigopoulou et al. (2006, ~ 0.7 mag) by a factor of two, confirming that the stars in SMGs, including the older, underlying population, are typically more obscured than in UV-selected galaxies. On the other hand, the typical optical extinction of high-z SMGs is only marginally larger than that of star forming BzK galaxies ($A_V \sim 1.2$ mag; Daddi et al. 2007) and star-forming DRGs ($A_V \sim 1.2$ mag; Papovich et al. 2006). Both star-forming BzK galaxies and DRGs are thought to contain a combination of older stars and extincted young starbursts, similar to what we see for SMGs; the similar optical extinctions of the different types supports that idea. Unfortunately, we lack the data to compare optical stellar extinction in SMGs to HzRGs, since optical extinction information for the stellar populations of HzRGs is difficult

to obtain due to scattered and direct AGN light contaminating the blue portions of the rest-frame optical SED (Seymour et al. 2007).

Next, we compare the near-IR absolute magnitudes of the various high-z populations to those of SMGs, which may tell us how typical the stellar luminosity of SMGs is. In the previous section, we showed that SMGs were much brighter in the near-IR than local L^* galaxies; however, the results of Cirasuolo et al. (2007) suggest that $z \sim 2$ SMGs may not be so over-luminous when compared to other $z \sim 2$ galaxies. With space densities a factor of 100 greater than SMGs (Steidel et al. 2003, 2004), the UV-selected galaxies (LBG, BX/BM) are much more "typical" high-redshift galaxies than SMGs, so we compare here the near-IR luminosity of SMGs to the UV-selected galaxies. We have calculated M_H for the LBGs, BX/BM-selected galaxies, and DRGs from the sample of Reddy et al. (2006b) in the same way as we did for our sample of SMGs: we fit the stellar population models of BC03 and Maraston (2005) to the rest-frame UV through near-IR SEDs of the galaxies, using the data tabulated in Reddy et al. (2006b), and interpolated a rest-frame H magnitude from the best-fit SED. In this way, we obtain a median absolute H-band magnitude for the LBGs of $M_H = -24.3$, while for BX/BM galaxies and DRGs we find medians of $M_H = -24.1$ and $M_H = -24.4$, respectively. $z > 1.5$ SMGs, with median $M_H = -25.4$, are only ~ 1 mag brighter in the near-IR than UV and optically-selected galaxies at similar redshifts, which is similar to the factor by which the near-IR luminosity of local ULIRGs exceeds that of local L^* galaxies. When we compare the absolute H magnitude of SMGs to HzRGs, which are more rare than SMGs, we find that SMGs have similar, possibly slightly smaller, H-band luminosities than powerful high-z radio galaxies ($\langle M_H \rangle \sim -25.7$; Seymour et al. 2007). The difference in typical luminosity between HzRGs and SMGs is thus similar to the difference in near-IR luminosity of local ULIRGs and low-z radio-loud AGN. These results suggest a mass sequence in which UV-selected galaxies are typically less massive than SMGs, while HzRGs have similar or slightly higher stellar masses than SMGs.

We now compare the typical masses of the high-z galaxy populations directly. We first compare to galaxy samples with spectroscopic redshifts for which the stellar masses were estimated in a method consistent with what we have used in the estimates for SMGs in this Chapter. We have calculated stellar masses for the BX/BM galaxies and LBGs from the sample of Reddy et al. (2006b) using the same method we employed to obtain masses for SMGs, in order to make a consistent comparison with the SMGs. In this way, we obtain

median stellar masses of $M_\star = 1.6(1.4) \times 10^{10}\,M_\odot$ for BX/BM galaxies using the models of BC03 (Maraston 2005) and $M_\star = 1.9(1.8) \times 10^{10}\,M_\odot$ for LBGs, which are consistent with those published for the BX/BM sources in Erb et al. (2006) and for LBGs in Reddy et al. (2006b), and a factor of 3–4 lower than the median $M_\star$ we have found for $z > 1.5$ SMGs, $6.9 \times 10^{10}\,M_\odot$ (using BC03 models). Seymour et al. (2007) infer the stellar masses of their HzRG sample from rest-frame H-band in a similar way to what we have done for the SMG sample, finding a mean stellar mass of $M_\star = 2.5 \times 10^{11}\,M_\odot$, a factor of ~ 4 larger than we obtain for SMGs. Clearly, SMGs are intermediate in mass between the HzRGs and UV-selected galaxies.

In comparing to samples of optically selected galaxies, the comparisons are much more complex for several reasons: (1) most of the galaxies in the samples of optically-selected galaxies for which $M_\star$ estimates have been made do not have spectroscopic redshifts, and thus the precise overlap in redshift with other galaxy types is not well-characterized; (2) different authors have used different methods, including different star formation histories and stellar population models, to calculate stellar masses. Due to these factors, systematic errors of factors of 2–5 can exist between the samples (van der Wel et al. 2006), which must be kept in mind during the comparison. Papovich et al. (2006) and Daddi et al. (2007) obtain typical masses of $1.1 \times 10^{11}\,M_\odot$ and $\sim 2 - 3 \times 10^{10}\,M_\odot$ for their samples of star-forming DRGs and BzK galaxies, respectively, using BC03 models. Comparing all the numbers together, SMGs clearly host more stellar mass on average than LBGs and BX/BM galaxies and appear to also be more massive than star-forming BzK galaxies. On the other hand, SMGs possibly have less than or similar stellar mass to DRGs and are less massive than powerful, high-z radio galaxies. It is important to note that much of the apparent difference in average stellar mass between the populations could easily be attributed to systematic error, and thus it may be appropriate to consider at least BzK galaxies, DRGs, and SMGs to all have similar stellar masses.

The comparisons of SMGs to both local and high-z galaxy populations through near-IR observations presented here are useful to show that while the properties of the various high-z populations may be confusing at other wavelengths, in the near-IR the populations find some common ground. They all appear to be relatively massive galaxies, most of which are still forming stars at some rate on top of an existing population. The amount of dust extinction varies between the types of galaxies, however, and it is unclear why that might

be the case. It may be that the less massive galaxies have not formed as much dust as the higher mass galaxies; however, the differing extinctions could also be due to metallicity or even orientation effects. High resolution imaging and deep spectroscopy of more SMGs and more galaxies selected in the near-IR may be useful to shed some light on this matter in the future.

6.6 Summary

In this chapter we have examined the rest-frame UV through near-IR SEDs of the radio-detected SMGs from the sample of Chapman et al. (2005), and we have used these SEDs to estimate stellar masses for the individual galaxies in the sample. We found that for the majority of the SMGs the UV-through-near-IR SEDs rise steeply from the UV to the near-IR and show evidence for a stellar peak around $1.6\,\mu$m, indicating the presence of significant optical extinction of young, blue stars coupled with a massive, underlying population of older stars. A minority of our SMG sample show SEDs with upturns in the longest-wavelength IRAC bands, which suggest the presence of a powerful obscured AGN. We also showed that our photometric data spanning a broad range of wavelengths are still not sufficient to place useful constraints on the star formation history of the galaxies and, thus, the typical age of the stellar populations since our galaxies are heavily reddened and our data are not well-enough sampled near the strong age indicators of the Balmer or 4000Å breaks.

The stellar mass of the galaxies in the sample is better constrained, however, despite systematic uncertainties, and by using a constant mass-to-light ratio we find that SMGs have a median stellar mass of $6 - 7 \times 10^{10}\,M_{\odot}$, which is somewhat lower than previous estimates of stellar mass in SMGs, and thus brings SMGs closer to the locally observed $M_{BH} - M_{\star}$ correlation of Marconi & Hunt (2003). The stellar masses of SMGs appear to be larger by a factor of 3–4 than those of high-redshift UV-selected galaxies, roughly similar to optically-selected high-z galaxies, and slightly lower than the stellar masses of powerful high-z radio galaxies, though the spread in typical stellar mass of the different populations is approximately only an order of magnitude. By comparing our stellar mass estimates to molecular gas and dynamical mass estimates for 13 individual SMGs in our sample observed in CO emission lines, we find our stellar mass estimates are reasonable and that the molecular gas fraction in SMGs declines with increasing stellar mass. If the

molecular gas masses for the 13 SMGs which have estimates are typical of the entire radio-detected SMG population, then a typical lower limit to the total baryonic mass of SMGs is $\sim 10^{11}\,M_{\odot}$, and SMGs are unlikely to significantly increase their stellar mass in the current activity powering their enormous IR luminosity.

Acknowledgments We would like to thank C. Maraston for providing us with an unpublished stellar population model, as well as C. Borys, P. Capak, and K. Bundy for helpful discussions on fitting stellar population models to observed SEDs.

Chapter 7

Conclusions and Future Work

In the preceding chapters we presented new observations and analysis which contribute to the ongoing characterization of the previously mysterious population of ultraluminous submillimeter-selected galaxies (SMGs). We analyzed new CO emission observations for a small sample of SMGs, and we analyzed near, mid, and far-IR data from the *Spitzer Space Telescope* for the Chapman et al. (2005) sample of radio-detected SMGs, which is the largest sample of SMGs with spectroscopic redshifts, examining the spectral energy distributions (SEDs) of the galaxies from rest-frame UV wavelengths through radio wavelengths. From the SEDs we derived new, more accurate IR luminosities and stellar masses than was possible without *Spitzer* data, validating the results of previous studies indicating that SMGs have high stellar masses (median $M_\star \sim 6 - 7 \times 10^{10}\,M_\odot$), are highly luminous (median $L_{\rm IR} = 5.4 \times 10^{12}\,L_\odot$), and have populations of highly obscured stars at rest-frame optical wavelengths ($\langle A_V \rangle = 1.7\,{\rm mag}$) whose presence becomes very clear in the rest-frame near-IR. The rest-frame near-IR colors indicate contributions from both low-mass stars and dust emission in many $z > 2$ SMGs, though only a minority show evidence for significant contributions to $L_{\rm IR}$ from hot dust heated by active galactic nuclei (AGNs). Also, with our large sample of SMGs with spectroscopic redshifts, multi-wavelength data, and stellar mass and luminosity information (plus gas mass information for a small portion of the sample), we have been able to test several assumptions frequently used in studies of SMGs in addition to improving constraints on their fundamental properties. In this final chapter, we bring together and briefly summarize the key conclusions presented in the preceding chapters.

7.1 SMGs Are Not a Uniform Population of Galaxies

Since SMGs are, in general, highly obscured, massive galaxies in which the bolometric luminosity is dominated by strong dust emission in the far-IR bands, one may be tempted to think that the properties of SMGs can be predicted by assuming a single, representative set of characteristics. However, our findings in this thesis made clear that the SMG population consists of galaxies with varied dust and gas properties. First, as noticed by other authors (e.g., Chapman et al. 2005), we found strong differences between the SMGs at low redshift ($z < 1$) and those at higher redshifts. A significant fraction of the low redshift sources appear to be moderately-luminous ($L_{\rm IR} \sim 10^{11}\,L_{\odot}$) and very cold, having IR SEDs which peak at wavelengths longer than the *IRAS* bands; such sources were not observed among the $z > 2$ SMGs. The $z > 2$ SMGs tend to be warmer and more luminous. What was not previously known was that within the $z > 2$ sample of radio-detected SMGs there are also significant SED variations, even when the effects of luminosity are removed. SMGs of similarly high redshifts show SED variation of sometimes more than an order of magnitude at rest-frame mid and far-IR wavelengths, indicating that they have a variety of dust properties even though they are all very luminous.

Through direct comparison of the composite SEDs of samples of SMGs separated into redshift bins of $z < 1$, $z = 1 - 2$, and $z > 2$ to the SED of the nearest ULIRG, Arp 220, we found that Arp 220 is a poor SED template for both low and high-z SMGs, which stands in sharp contrast to the many studies of SMGs which have assumed that the SED of Arp 220 describes SMGs. Compared to low-z SMGs, the SED of Arp 220 peaks at a much higher frequency, and for high-z SMGs, the SED of Arp 220 is much too faint in the mid-IR due to heavy silicate absorption, which the SMGs do not have, and shows an unusual excess of emission in the submillimeter bands.

More evidence of non-uniformity in the SMG population comes from our study of CO rotational line emission in this work, in which we discussed excitation conditions in the interstellar medium of SMGs. Our small study showed that the excitation of molecular gas varies between galaxies, as does the content of cold molecular gas. For at least some SMGs, $J \rightarrow J - 1$ rotational lines of CO where $J > 3$ do not trace the total molecular gas content; thus, extrapolating gas masses from $J \geq 3$ transitions with the assumption of a brightness temperature ratio of unity between the $J \geq 3$ and the $1 \rightarrow 0$ transitions can

lead to significant underestimates of the mass of H_2. Yet, for some SMGs it seems that the higher-J transitions do adequately trace the total molecular gas mass.

7.2 The Radio Emission of SMGs Is a Good Tracer of IR Luminosity

With our *Spitzer*-MIPS data for the radio-detected SMG sample of Chapman et al. (2005), we had sufficient IR data points to constrain the IR luminosity of the galaxies without having to use radio data and assume the local far-IR–radio correlation. We first noticed that when the composite SEDs we constructed were normalized by $L_{\rm IR}$, the scatter in the radio points of the SED decreased significantly at all redshifts. Using the IR luminosity as a proxy for the far-IR luminosity, we found that the SMGs in our sample show a tight, almost linear correlation between total IR luminosity and radio luminosity over 3 orders of magnitude in luminosity, similar to the result obtained by Kovács et al. (2006) for a smaller sample of SMGs. The correlation shows no significant difference between galaxies with and without identified AGN; it thus appears that most SMGs are not radio-loud objects. The correlation we find for SMGs does not strongly differ from the $L_{\rm IR}$–radio correlation of local, lower-luminosity *IRAS*-selected galaxies; yet we cannot rule out the existence of small differences between the far-IR–radio correlation for SMGs than for local galaxies. However, estimates of $L_{\rm IR}$ for radio-detected, high-z SMGs using the local far-IR–radio correlation are not likely to be in serious error.

7.3 Molecular Gas Observations of SMGs Can Be Powerful Evolutionary Indicators

13 individual SMGs in our IRAC-observed stellar mass sample have published CO emission line observations in the literature. By comparing our stellar mass estimates to these molecular gas and dynamical mass estimates which are completely independent of the stellar mass determinations, we were not only able to verify that our stellar mass estimates were reasonable, but we found that the molecular gas fraction in the SMGs with CO observations declines with increasing stellar mass, which may be an evolutionary trend. We also found that for these galaxies, the mass in molecular gas and the mass contained in stars are com-

parable. Thus, if the molecular gas masses for the 13 SMGs which have CO observations are typical of the entire radio-detected SMG population, SMGs are unlikely to significantly increase their stellar mass (no more than by a factor of 2–5) in the current activity powering their enormous IR luminosity unless a new source of fuel appears. Also, if the median molecular gas mass of these 13 SMGs is typical of the rest of the population, a typical lower limit to the total baryonic mass of SMGs is $\sim 10^{11}\,M_{\odot}$, which suggests that they contain enough baryonic mass to transform into a massive L^{*} galaxy, but not necessarily enough mass to form a giant elliptical galaxy.

7.4 SMGs Are Among the Most Massive Galaxies of Their Epoch

We have compared the IRAC colors, near-IR absolute magnitudes, and typical stellar masses of SMGs to those of other well-known populations of high-redshift galaxies (e.g., Lyman break galaxies [LBGs], BX/BM galaxies, distant red galaxies [DRGs]) in an attempt to shed light on the relationships between these galaxies and SMGs. We found that SMGs are brighter and redder in the near-IR than UV-selected galaxies, while the IRAC colors of SMGs are quite similar to those of powerful high-z radio galaxies. The stellar masses of SMGs appear to be larger by a factor of 3–4 than those of high-redshift UV-selected galaxies and roughly similar to DRGs and BzK galaxies, but lower than the stellar masses of high-z radio galaxies. Thus, SMGs are likely not the most massive galaxies at $z \sim 2$, but they are among the more massive galaxies, providing more evidence that SMGs may not be the progenitors of the most massive galaxies in the local universe.

7.5 Future Work

Over time, we are slowly building a picture of the nature of SMGs and how they contribute to star formation in the early history of the Universe. There are still many issues that must be addressed, however, in order to fully characterize the SMG population, the physical processes responsible for their extreme luminosities, and their role in galaxy formation and mass assembly in the Universe. We describe below several areas for future study which are necessary to further characterize SMGs and their relationship to the cosmic star formation

history and other high-redshift galaxy populations. We have already begun to carry out some of this important work, though there remains a great deal more to do.

7.5.1 The Role of MicroJansky Radio Galaxies

Chapman et al. (2004) presented a sample of high-redshift, optically faint, μJy radio sources which lay at similar redshifts to the SMG population but were not detected by SCUBA. The objects showed no indication of powerful AGN in their optical spectra, suggesting that the radio emission observed comes from star formation. Both Chapman et al. (2004) and Blain et al. (2004a) propose that these optically-faint radio galaxies (OFRGs) are cousins of SMGs: highly luminous, highly obscured star forming galaxies with higher dust temperatures than SMGs, which explains why they are not detected by SCUBA at 850 μm but are detected at radio wavelengths. Blain et al. (2004a) point out that such galaxies could produce enough far-IR background radiation at wavelengths shorter than 200 μm to make up the difference between the observed far-IR background at that wavelength and the total background intensity produced by SMGs and fainter counterparts. However, *Spitzer*-MIPS measurements are required of these galaxies to confirm that they contain hot dust.

Since these OFRGs are possibly quite similar to SMGs and may provide further insight into the importance of obscured star formation in the early Universe, they are an interesting sample to which we should compare the SMGs, as done in Smail et al. (2004), for their rest-frame optical properties. However, we have left them out of the analysis in this work because we have an ongoing observational program to characterize these faint radio sources to compare them to SMGs and determine if they contribute significantly to the far-IR background from obscured star formation.

We have obtained deep *Spitzer* IRAC and MIPS imaging for a $10' \times 10'$ field in the Lockman Hole for which one of the deepest radio images ever taken ($1\sigma = 3.3\,\mu$Jy) is available from the VLA archive. The image contains over 300 faint radio sources down to $S_{1.4\mathrm{GHz}} = 16\,\mu$Jy. To determine redshifts for this sample to find the high-redshift sources, we have obtained multi-object spectroscopy with the DEIMOS instrument on the Keck II Telescope. However, from our spectra we have not yet identified any galaxies with $z > 1.3$ for comparison to the SMG sample. However, DEIMOS was designed with the goal of being sensitive to galaxies up to $z \sim 1$ (Coil et al. 2004), so our lack of detection of high-z sources may be a direct consequence of the selection function of DEIMOS. Our project to

identify high-z radio sources is ongoing since we have found 50 objects in our spectroscopic sample which show faint continuum in their DEIMOS spectra but no identifiable lines; thus, more spectroscopic follow-up is clearly required with a more blue-sensitive multi-object spectrograph (e.g., LRIS on the Keck I Telescope).

7.5.2 CO Emission in SMGs: Mass Information, Kinematics, and ISM Conditions

Observations of CO emission lines from rotational transitions will be important for constraining the mass and dynamics of SMGs and determining the excitation conditions of the star-forming gas, which will indicate the conditions under which stars are forming. However, only a small fraction of the SMG sample with available spectroscopic redshifts have CO observations. Most of these existing CO observations have spatial resolution too low to determine any dynamical information, and even fewer SMGs have been observed in multiple transitions for excitation analysis. Hence there is much to learn about the molecular gas and conditions of star formation in SMGs.

We have an ongoing observational program at the Green Bank Telescope to observe more SMGs in the CO(1→0) transition to obtain information about the mass of cold gas and set limits on the temperature and density of the gas. Unfortunately, the program has suffered delays due to instrument problems, and as the Green Bank Telescope is currently the only facility with a receiver at the frequencies required to observe CO(1→0) in $z \sim 2$ galaxies, progress in determining CO properties and excitation characteristics in SMGs has not recently been made. In only a few years, the Atacama Large Millimeter Array (ALMA) will bring about a new era in the study of molecular emission from high-redshift galaxies, broadening the range of detectable molecular transitions and providing detailed spatial and kinematic information for luminous high-redshift galaxies. CO observations of SMGs with ALMA are likely to provide tremendous detail about the dynamics, kinematics, and excitation in the ISM of SMGs.

7.5.3 The Nature of Radio-Undetected SMGs

Approximately 30% of submillimeter sources observed in deep radio surveys have not been detected in the radio, and as a result they have not been included in spectroscopic obser-

vations of SMGs because they lack precise counterpart positions. We do not know what causes these radio-undetected SMGs to be fainter in the radio than their radio-detected cousins; popular explanations for the lack of radio detection are that the lack of radio detection is due to differences in dust properties (e.g., Chapman et al. 2005; Ivison et al. 2005) or because the sources lie at higher redshift than radio detected samples (Eales et al. 2003; Younger et al. 2007). However, without knowing their redshifts, characterizations of the redshift distribution, luminosity function, and clustering of the SMG class will be not be representative of the entire population, and we may misrepresent the contributions of SMGs to the cosmic star formation history. On the other hand, positions accurate to better than $1''$ are required to carry out optical spectroscopy to obtain redshifts. By using interferometers such as the Submillimeter Array, or ALMA (in the future), we can go back and image the submillimeter sources lacking radio detections at their original wavelength of detection with much higher resolution than that achieved by SCUBA, and thus obtain more accurate source positions. However, the small fields of view of the interferometers generally restrict such observations to one high-z object at a time, and thus progress will be slow at identifying radio-undetected SMGs in such a way.

7.5.4 The More Distant Future: Far-IR and Radio Observations of Optically-Selected High-z Galaxies

The most accurate picture of the formation and evolution of galaxies and the growth of stellar mass requires comparisons of the different high-redshift galaxy populations at all wavelengths, as well as spectroscopic redshifts, so that we can make consistent comparisons of star formation rate, gas content, dynamical mass, AGN activity, and metallicity between galaxies selected at different wavelengths. Unfortunately, carrying out such investigations on large scales to build representative samples is either not possible with currently available observing facilities due to sensitivity limits (e.g., submillimeter continuum observations of most optically-selected high-z galaxies), or simply not feasible given available observing time (e.g., spectroscopy of large numbers of faint galaxies, ultradeep X-ray and radio observations of faint galaxies, molecular gas measurements for optically-selected galaxies). New observing facilities and instruments currently being built (e.g., ALMA, the Expanded Very Large Array) will provide new levels of sensitivity which will assist in detecting faint sources; however, the efficiency of observing will likely be low and still require a great deal of time to

build up representative samples of multi-wavelength data for the various galaxy types. We must look even further ahead to facilities still in the planning stages for hope of developing a complete picture of galaxy formation, e.g., to the Thirty Meter Telescope, for which spectroscopy of the different high-z populations should be comparatively quick and painless, and the Cornell-Caltech Atacama Telescope, with which wide-field surveys should be able to detect high-redshift galaxies less luminous in the far-IR than SMGs.

Appendix A

Notes on Individual Sources in the Chapman et al. (2005) SMG Sample

SMM J030238.62+001106.3: The optical–near-IR SED fit to this object in Chapter 6 is poor and M_H, and therefore the stellar mass, is likely to be underestimated.

SMM J030244.82+000632.3: The optical–near-IR SED fit to this object in Chapter 6 is poor and M_H, and therefore the stellar mass, is likely to be underestimated.

SMM J105151.69+572636.0: Also known as LE 850.7 (Ivison et al. 2002), this object is included in the study of Egami et al. (2004).

SMM J105155.47+572312.7: Egami et al. (2004) include this SMG in their sample (LE 850.18). Its optical–near-IR SED shows a blue excess.

SMM J105200.22+572420.2: Identified in Ivison et al. (2002) as LE 850.8, this SMG is known to have a companion at the same redshift (Chapman et al. 2005), and the radio source is clearly blended with its companion at 24 μm, as well as another galaxy, in such a way that our source extraction method cannot deblend the objects. Egami et al. (2004) report deblended 24 μm flux densities for the radio source, the bright companion, and the fainter companion, respectively, of $282 \pm 59\,\mu$Jy, $534 \pm 117\,\mu$Jy, and $161 \pm 47\,\mu$Jy. The optical–near-IR SED of this object shows a red excess.

SMM J105201.25+572445.7: Also known as LE 850.1, this object has a 24 μm measurement published in Egami et al. (2004).

SMM J105207.49+571904.0: This SMG has a nearby companion in IRAC 3.6 μm and 4.5 μm images with which it may be blended at 24 μm. However, the companion's flux decreases as the IRAC wavelength increases, relative to the SMG, so it is likely that the

SMG dominates the 24 μm flux listed in Table 3.6.

SMM J123553.26+621337.7: Chapman et al. (2005) find that the optical counterpart for this SMG is offset from the radio position, and at 24 μm the object is blended with 2 other sources such that it lies in between the 2 others. The SMG's radio position is not consistent with the brighter of the 2 objects, being separated by more than 3″, so it is not clear that the SMG dominates the 24 μm flux of the blended object. As a result, we list an upper limit to the flux at 24 μm. The optical–near-IR SED of this object in Chapter 6 shows a red excess.

SMM J123600.15+621047.2: The optical–near-IR SED of this SMG shows a red excess and a blue excess.

SMM J123606.85+621021.4: This SMG, which is included in the study of Pope et al. (2006) (designated there as GN22), is blended at 24 μm with an IRAC source that lies between the source apparent in the 24 μm image at the radio position of this SMG and the brighter source next to the radio position. We have chosen to list an upper limit for this source since the three sources cannot be separated by our source extraction method.

SMM J123616.15+621513.7: Referred to as GN04 by Pope et al. (2006), this SMG is blended with 2 additional IRAC sources into a single source at 24 μm, and the near neighbors may contaminate the IRAC photometry aperture. Chapman et al. (2005) states that the SCUBA source has a double radio identification, but only one of the radio sources has a spectroscopic redshift. While Pope et al. (2006) choose the 24 μm object as the correct counterpart, we regard the 24 μm flux listed in Table 3.6, which is that for the single 24 μm source, as tentative since it is unclear which of the radio sources the 24 μm object is associated with.

SMM J123621.27+621708.4: This particular source, designated GN07 by Pope et al. (2006), is known to have a double radio source identification (Chapman et al. 2005) and also has a very nearby companion in IRAC images contaminating the IRAC photometry aperture, with which it is likely to be blended at 24 μm. However, the 24 μm image appears as a point source, and thus the two sources cannot be reliably deblended. The 24 μm source center is offset from the radio-detected SMG, as well. We have tentatively identified the 24 μm object with the radio-detected SMG, but caution that in the case that the two radio/IRAC sources are at different redshifts, the radio source with the spectroscopic redshift may not be the 24 μm source.

SMM J123629.13+621045.8: While this SMG is not known to have multiple radio sources as counterparts, it appears to have a near neighbor ($\sim 1''$ away) in IRAC images contaminating the IRAC photometry aperture. This neighbor is likely to be blended with the radio source in the 24 μm image. However, the 24 μm source appears to be a point source, so it cannot be reliably de-blended into two sources. We have tentatively identified the 24 μm source with the radio-detected SMG. This source is included in the study of Pope et al. (2006), designated GN25.

SMM J123632.61+620800.1: The optical–near-IR SED of this SMG in Chapter 6 shows a red excess and a blue excess.

SMM J123635.59+621424.1: The optical–near-IR SED of this SMG shows a red excess and a blue excess.

SMM J123636.75+621156.1: No 24 μm source can be found at the radio position of this SMG; however, there is a faint source centered $\sim 4''$ away which Pope et al. (2006) associate with the submm source. As this source does not overlap the radio position and is offset by more than $2''$ from the radio position, we do not consider the SMG detected at 24 μm.

SMM J123707.21+621408.1: This particular SMG, designated GN19 by Pope et al. (2006), is listed in Chapman et al. (2005) as having 2 radio source identifications confirmed to lie at the same redshift. The two radio sources are clearly detected in IRAC images, and are probably blended at 24 μm, even though the 24 μm object appears to be a point source. It is likely that both radio sources contribute to the 24 μm flux; however, they cannot be separated at that wavelength so we cannot isolate the contributions of the two sources. However, we tentatively treat the single 24 μm source as representing the submm source.

SMM J131215.27+423900.9: The optical–near-IR SED of this SMG shows a red excess.

SMM J131222.35+423814.1: The optical–near-IR SED of this SMG shows a red excess.

SMM J131225.73+423941.4: This SMG has a near neighbor contaminating its IRAC photometry aperture.

SMM J131232.31+423949.5: The optical–near-IR SED of this SMG shows a red excess.

SMM J141741.81+522823.0: The optical–near-IR SED of this SMG shows a red excess.

SMM J141809.00+522803.8: This SMG has a near neighbor contaminating its IRAC photometry aperture.

SMM J163631.47+405546.9: This SMG has a near neighbor contaminating its IRAC photometry aperture.

SMM J163639.01+405635.9: The optical–near-IR SED of this SMG shows a red excess.

SMM J221804.42+002154.4: This SMG has a near neighbor contaminating its IRAC photometry aperture.

Bibliography

Alexander, D. M., et al. 2003, AJ, 125, 383

Alexander, D. M., Bauer, F. E., Chapman, S. C., Smail, I., Blain, A. W., Brandt, W. N., & Ivison, R. J. 2005, ApJ, 632, 736

Andreani, P., Cimatti, A., Loinard, L., & Röttgering, H. 2000, A&A, 354, L1

Antonucci, R. 1993, ARA&A, 31, 473

Appleton, P. N., et al. 2004, ApJS, 154, 147

Aretxaga, I., et al. 2007, MNRAS, 379, 1571

Armus, L., et al. 2007, ApJ, 656, 148

Ashby, M. L. N., et al. 2006, ApJ, 644, 778

Baker, A., Tacconi, L. J., Genzel, R., Lehnert, D., & Lutz, D. 2004, ApJ, 604, 125

Barger, A., et al. 1998, Nature, 394, 428

Barger, A. J., Cowie, L. L., & Wang, W. 2007, ApJ, 654, 764

Baugh, C. M., Cole, S., Frenk, C. S., & Lacey, C. G. 1998, ApJ, 498, 504

Baugh, C. M., et al. 2005, MNRAS, 356, 1191

Becker, R., White, R., & Helfand, D. 1995, ApJ, 450, 559

Benítez, N. 2000, ApJ, 536, 571

Bertin, E., & Arnouts, S. 1996, A&AS, 117, 393

Bertoldi, F., et al. 2000, A&A, 360, 92

Biggs, A. D., & Ivison, R. J. 2006, MNRAS, 371, 963

Blain, A. W. 1999a, MNRAS, 304, 669

Blain, A. W. 1999d, MNRAS, 309, 955

Blain, A. W., & Longair, M. S. 1993a, MNRAS, 264, 509

Blain, A. W., & Longair, M. S. 1993b, MNRAS, 265, L21

Blain, A. W., Jameson, A., Smail, I., Longair, M. S., Kneib, J.–P., & Ivison, R. J. 1999, MNRAS, 309, 715

Blain, A. W., Smail, I., Ivison, R. J., Kneib, J.–P., & Frayer, D. T. 2002, PhR, 369, 111

Blain, A. W. 2002, in The Cold Universe, eds. D. Pfenniger and Y. Revaz. (Berlin: Springer-Verlag), 1

Blain, A. W., Barnard, V. E., & Chapman, S. C. 2003, MNRAS, 338, 733

Blain, A. W., Chapman, S. C., Smail, I., & Ivison, R. 2004, ApJ, 611, 52

Blain, A. W., Chapman, S. C., Smail, I., & Ivison, R. 2004, ApJ, 611, 725

Bolzonella, M., Miralles, J.–M., & Pelló, R. 2000, A&A, 363, 476

Borys, C., Scott, D., Chapman, S. C., Halpern, M., Nandra, K., & Pope, A. 2004, MNRAS, 355, 485

Borys, C., Smail, I., Chapman, S. C., Blain, A. W., Alexander, D. M., & Ivison, R. J. 2005, ApJ, 635, 853

Brinchmann, J., & Ellis, R. S. 2000, ApJ, 536, L77

Brodwin, M., et al. 2006, ApJ, 651, 791

Brown, M. J., Jannuzi, B., Dey, A., & Tiede, G. P. 2005, ApJ, 621, 41

Bruzual, G., & Charlot, S. 1993, ApJ, 405, 538

Bruzual, G., & Charlot, S. 2003, MNRAS, 344, 1000

Bundy, K., Ellis, R. S., & Conselice, C. J. 2005, ApJ, 625, 621

Calzetti, D., Armus, L., Bohlin, R. C., Kinney, A. L., Koornneef, J., & Storchi-Bergmann, T. 2000, ApJ, 533, 682

Capak, P., et al. 2004, AJ, 127, 180

Caputi, K. I., et al. 2007, ApJ, 660, 97

Carilli, C. L., & Yun, M. S. 1999, ApJ, 513, L13

Carilli, C. L., et al. 2002a, AJ, 123, 1838

Carilli, C. L., et al. 2002b, ApJ, 575, 145

Chabrier, G. 2003, PASP, 115, 763

Chapman, S. C., et al. 2000, MNRAS, 319, 318

Chapman, S. C., et al. 2003a, ApJ, 585, 57

Chapman, S. C., et al. 2003c, Nature, 422, 695

Chapman, S. C., Helou, G., Lewis, G., & Dale, D. 2003b, ApJ, 588, 186

Chapman, S. C., Blain, A. W., Smail, I., & Ivison, R. J. 2005, ApJ, 622, 772

Chapman, S. C., Smail, I., Blain, A. W., & Ivison, R. J. 2004, ApJ, 614, 671

Chary, R., & Elbaz, D. 2001, ApJ, 556, 562

Cimatti, A., et al. 2002, A&A, 381, L68

Cirasuolo, M., et al. 2007, MNRAS, 380, 585

Clements, D., et al. 2004, MNRAS, 351, 447

Coil, A. L., Newman, J. A., Kaiser, N., Davis, M., Ma, C.–P., Kocevski, D., & Koo, D. 2004, ApJ, 617, 765

Cole, S., Lacey, C. G., Baugh, C. M., & Frenk, C. S. 2000, MNRAS, 319, 168

Cole, S., et al. 2001, MNRAS, 326, 255

Condon, J. J. 1992, ARA&A, 30, 575

Condon, J. J. 2003, GBT Efficiency at 43 GHz, Precision Telescope Control System Project Note 31.1, National Radio Astronomy Observatory–Green Bank

Condon, J. J., Cotton, W. D., Greisen, E. W., Yin, Q. F., Perley, R. A., Taylor, G. B., & Broderick, J. J. 1998, AJ, 115, 1693

Coppin, K., et al. 2006, MNRAS, 372, 1621

Coppin, K., et al. 2007, ApJ, 665, 936

Cowie, L. L., Barger, A. J., & Kneib, J.–P. 2002, AJ, 123, 2197

Cox, P., et al. 2002, A&A, 387, 406

Daddi, E., et al. 2000, A&A, 361, 535

Daddi, E., et al. 2004, ApJ, 600, L127

Daddi, E., et al. 2007, ApJ, in press

Dale, D. A., Helou, G., Contursi, A., Silbermann, N. A., & Kolhatkar, S. 2001, ApJ, 549, 215

Dale, D. A., & Helou, G. 2002, ApJ, 576, 159

Dale, D. A., et al. 2005, ApJ, 633, 857

Dannerbauer, H., et al. 2006, ApJ, 637, L5

Dasyra, K. M., et al. 2006, ApJ, 651, 835

De Breuck, C., Downes, D., Neri, R., van Breugel, W., Reuland, M., Omont, A., & Ivison, R. J. 2005, A&A, 430, L1

Dey, A., Graham, J. R., Ivison, R. J., Smail, I., Wright, G. S., & Liu, M. C. 1999, ApJ, 519, 610

Downes, D., Neri, R., Wiklind, T., Wilner, D. J., & Shaver, P. A. 1999, ApJ, 513, L1

Downes, D., & Solomon, P. M. 1998, ApJ, 507, 615

Drory, N., Salvato, M., Gabasch, A., Bender, R., Hopp, U., Feulner, G., & Pannella, M. 2005, ApJ, 619, L131

Dunne, L., Eales, S., Edmunds, M., Ivison, R. J., Alexander, P., & Clements, D. L. 2000, MNRAS, 315, 115

Dunne, L., & Eales, S. A. 2001, MNRAS, 327, 697

Eales, S., et al. 1999, ApJ, 515, 518

Eales, S. A., Bertoldi, F., Ivison, R., Carilli, C., Dunne, L., & Owen, F. 2003, MNRAS, 344, 169

Efstathiou, A., Rowan-Robinson, M., & Siebenmorgen, R. 2000, MNRAS, 313, 734

Egami, E., et al. 2004, ApJS, 154, 130

Elbaz, D., Cesarsky, C. J., Chanial, P., Aussel, H., Franceschini, A., Fadda, D., & Chary, R. R. 2002, A&A, 384, 848

Engelbracht, C. W., Gordon, K. D., Rieke, G. H., Werner, M. W., Dale, D. A., & Latter, W. B. 2005, ApJ, 628, L29

Engelbracht, C. W., et al. 2007, PASP, in press

Erb, D. K., Steidel, C. C., Shapley, A. E., Pettini, M., Reddy, N. A., & Adelberger, K. L. 2006, ApJ, 646, 107

Fadda, D., et al. 2006, AJ, 131, 2859

Fazio, G. G., et al. 2004, ApJS, 154, 10

Fixsen, D. J., Bennett, C. L., & Mather, J. C. 1999, ApJ, 526, 207

Fomalont, E., et al. 2006, ApJS, 167, 103

Fontana, A. 2004, A&A, 424, 23

Förster Schreiber, N. M., et al. 2004, ApJ, 616, 40

Franceschini, A., Toffolatti, L., Mazzei, P., Danese, L., & de Zotti, G. 1991, A&AS, 89, 285

Franx, M., et al. 2003, ApJ, 587, L79

Frayer, D. T., & Brown, R. L. 1997, ApJS, 113, 221

Frayer, D. T., et al. 1998, ApJ, 506, L7

Frayer, D. T., et al. 1999, ApJ, 514, L13

Frayer, D. T., et al. 2004, ApJS, 154, 137

Frayer, D. T., et al. 2006a, AJ, 131, 250

Frayer, D. T., et al. 2006b, ApJ, 647, L9

Gao, Y., & Solomon, P. M. 2004a, ApJ, 606, 271

Gao, Y., & Solomon, P. M. 2004b, ApJS, 152, 63

Garrett, M. 2002, A&A, 384, L19

Genzel, R., et al. 2001, ApJ, 563, 527

Georgakakis, A., Afonso, J., Hopkins, A. M., Sullivan, M., Mobasher, B., & Cram, L. E. 2005, ApJ, 620, 584

Giavalisco, M., et al. 2004, ApJ, 600, L93

Glazebrook, K., et al. 2004, Nature, 430, 181

Gordon, K. D., et al. 2005, PASP, 117, 503

Gordon, K. D., et al. 2007, PASP, in press

Granato, G., de Zotti, G., Silva, L., Bressan, A., & Danese, L. 2004, ApJ, 600, 580

Greve, T. R., et al. 2005, MNRAS, 359, 1165

Greve, T. R., Ivison, R. J., & Papadopoulos, P. P. 2003, ApJ, 599, 839

Greve, T. R., Ivison, R. J., & Papadopoulos, P. P. 2004a, A&A, 419, 99

Greve, T. R., Ivison, R. J., Bertoldi, F., Stevens, J. A., Dunlop, J. S., Lutz, D., & Carilli, C. L. 2004b, MNRAS, 354, 779

Hainline, L. J., Blain, A. W., Greve, T. R., Chapman, S. C., Smail, I., & Ivison, R. J. 2006, ApJ, 650, 614

Hainline, L. J., Scoville, N. Z., Yun, M. S., Hawkins, D. W., Frayer, D. T., & Isaak, K. G. 2004, ApJ, 609, 61

Helou, G., Soifer, B. T., & Rowan-Robinson, M. 1985, ApJ, 298, L7

Hildebrand, R. H. 1983, QJRAS, 24, 267

Holland, W. S., et al. 1999, MNRAS, 303, 659

Hopkins, A. M. 2004, ApJ, 615, 209

Hu, E., & Ridgeway, S. E. 1994, AJ, 107, 1303

Huang, J.–S., et al. 2005, ApJ, 634, 137

Hughes, D., et al. 1998, Nature, 394, 241

Huynh, M. T., Pope, A., Frayer, D. T., & Scott, D. 2007, ApJ, 659, 305

Ivison, R. J., et al. 2002, MNRAS, 337, 1

Ivison, R. J., et al. 2004, ApJS, 154, 124

Ivison, R. J., et al. 2005, MNRAS, 364, 1025

Kauffmann, G., & Charlot, S. 1998, MNRAS, 294, 705

Kauffmann, G., et al. 2003, MNRAS, 341, 33

Kennicutt, R. C. 1998, ApJ, 498, 541

Kim, D.–C., Veilleux, S., & Sanders, D. B. 2002, ApJS, 143, 277

Kneib, J.-P., Neri, R., Smail, I., Blain, A. W., Sheth, K., van der Werf, P., & Knudsen, K. K. 2005, A&A, 434, 819

Knudsen, K. K., et al. 2005, ApJ, 632, L9

Kong, X., et al. 2006, ApJ, 638, 72

Kovács, A., Chapman, S. C., Dowell, C. D., Blain, A. W., & Phillips, T. G. 2006, ApJ, 650, 592

Kreysa, E., et al. 1998, SPIE, 3357, 319

Kroupa, P. 2001, MNRAS, 322, 231

Lacy, M. 2004, ApJS, 154, 166

Lane, K. P., et al. 2007, MNRAS, 379, L25

Laurent, G. T., et al. 2006, ApJ, 643, 38

Ledlow, M. J., Smail, I., Owen, F. N., Keel, W. C., Ivison, R. J., & Morrison, G. E. 2002, ApJ, 577, L79

Leitherer, C., et al. 1999, ApJS, 123, 3

Lilly, S. J., Le Fevre, O., Crampton, D., Hammer, F., & Tresse, L. 1995, ApJ, 455, 50

Lutz, D., et al. 2005, ApJ, 625, L83

Makovoz, D., & Marleau, F. R. 2005, PASP, 117, 1113

Mauch, T., & Sadler, E. 2007, MNRAS, 375, 931

Mao, R. Q., et al. 2000, A&A, 358, 433

Maraston, C. 2005, MNRAS, 362, 799

Maraston, C., et al. 2006, ApJ, 652, 85

Marcillac, D., Elbaz, D., Chary, R. R., Dickinson, M., Galliano, F., & Morrison, G. 2006, A&A, 451, 57

Marconi, A., & Hunt, L. K. 2003, ApJ, 589, L21

McCarthy, P. J. 2004, ARA&A, 42, 477

Ménendez-Delmestre, K., et al. 2007, ApJ, 655, L65

Miller, G. E., & Scalo, J. M. 1979, ApJS, 41, 513

Nagamine, K., Cen, R., Hernquist, L., Ostriker, J., & Springel, V. 2004, ApJ, 610, 45

Nagamine, K., Cen, R., Hernquist, L., Ostriker, J., & Springel, V. 2005, ApJ, 627, 608

Nagamine, K., Ostriker, J. P., Fukugita, M., & Cen, R. 2006, ApJ, 653, 881

Noeske, K. G., et al. 2007, ApJ, 660, L43

Neri, R., et al. 2003, ApJ, 597, L113

Omont, A., Cox, P., Bertoldi, F., McMahon, R. G., Carilli, C., & Isaak, K. G. 2001, A&A, 374, 371

Omont, A., Petitjean, P., Guilloteau, S., McMahon, R. G., Solomon, P. M., & Pecontal, E. 1996, Nature, 382, 428

Papadopoulos, P. P, & Ivison, R. J. 2002, ApJ, 564, L9

Papadopoulos, P. P., Ivison, R. J., Carilli, C., & Lewis, G. 2001, Nature, 409, 58

Papadopoulos, P. P., Röttgering, H. J., van der Werf, P., Guilloteau, S., Omont, A., van Breugel, W. J. M., & Tilanus, R. P. J. 2000, ApJ, 528, 626

Papovich, C., Dickinson, M., & Ferguson, H. C. 2001, ApJ, 559, 620

Papovich, C., et al. 2004, ApJS, 154, 70

Papovich, C., et al. 2006, ApJ, 640, 92

Papovich, C., et al. 2007, ApJ, 668, 45

Peacock, J. A., et al. 2000, MNRAS, 318, 535

Pearson, C., & Rowan-Robinson, M. 1996, MNRAS, 283, 174

Pérez-González, P. G., et al. 2007, ApJ, in press

Pope, A., Borys, C., Scott, D., Conselice, C., Dickinson, M., & Mobasher, B. 2005, MNRAS, 358, 149

Pope, A., et al. 2006, MNRAS, 370, 1185

Pozzetti, L., et al. 2003, A&A, 402, 837

Puget, J.–L., Abergel, A., Bernard, J.–P, Boulanger, F., Burton, W. B., Désert, F.–X., & Hartmann, D. 1996, A&A, 308, L5

Reddy, N. A., Erb, D. K., Steidel, C. C., Shapley, A. E., Adelberger, K. L., & Pettini, M. 2005, ApJ, 633, 748

Reddy, N. A., et al. 2006a, ApJ, 644, 792

Reddy, N. A., Steidel, C. C., Erb, D. K., Shapley, A. E., & Pettini, M. 2006b, ApJ, 653, 1004

Richardson, K. J., White, G. J., Gee, G., Griffin, M. J., Cunningham, C. T., Ade, P. A. R., & Avery, L. W. 1985, MNRAS, 216, 713

Rieke, G. H., et al. 2004, ApJS, 154, 25

Rigopoulou, D., et al. 2006, ApJ, 648, 81

Roberts, M. S., & Haynes, M. P. 1994, ARA&A, 32, 115

Rubin, K. H. R., van Dokkum, P. G., Coppi, P., Johnson, O., Förster-Schreiber, N. M., Franx, M., & van der Werf, P. 2004, ApJ, 613, L5

Rudnick, G., et al. 2003, 599, 847

Sajina, A., Lacy, M., & Scott, D. 2005, ApJ, 621, 256

Sajina, A., Yan, L., Armus, L., Choi, P., Fadda, D., Helou, G., & Spoon, H. 2007, ApJ, 664, 713

Salpeter, E. E. 1955, ApJ, 121, 161

Sanders, D. B., & Mirabel, I. 1996, ARA&A, 34, 749

Saracco, P., et al. 2006, MNRAS, 367, 349

Sawicki, M. 2002, AJ, 124, 3050

Schlegel, D. J., Finkbeiner, D. P., & Davis, M. 1998, ApJ, 500, 525

Scoville, N. Z., et al. 2000, AJ, 119, 991

Scoville, N. Z., et al. 2007, ApJS, 172, 1

Seymour, N., et al. 2007, ApJS, 171, 353

Shapley, A. E., Steidel, C. C., Adelberger, K. L., Dickinson, M., Giavalisco, M., & Pettini, M. 2001, ApJ, 562, 95

Shapley, A. E., et al. 2005, ApJ, 626, 698

Siebenmorgen, R., & Krügel, E. 2007, A&A, 461, 445

Smail, I., Chapman, S. C., Blain, A. W., & Ivison, R. J. 2004, ApJ, 616, 71

Smail, I., Ivison, R. J., & Blain, A. W. 1997, ApJ, 490, L5

Smail, I., Ivison, R. J., Blain, A. W., & Kneib, J.-P. 2002, MNRAS, 331, 495

Solomon, P. M., Downes, D., & Radford, S. J. E. 1992b, ApJ, 398, L29

Solomon, P. M., Downes, D., Radford, S. J. E., & Barrett, J. W. 1997, ApJ, 478, 144

Somerville, R. S., Primack, J. R., & Faber, S. M. 2001, MNRAS, 320, 504

Somerville, R. S., et al. 2004, ApJ, 600, L135

Spergel, D. N., et al. 2003, ApJS, 148, 175

Spitzer Science Center. 2006, IRAC Data Handbook (Pasadena: SSC), http://ssc.spitzer.caltech.edu/irac/dh/

Spitzer Science Center. 2006, MIPS Data Handbook (Pasadena: SSC), http://ssc.spitzer.caltech.edu/mips/dh/

Stanford, S. A., Stern, D., van Breugel, W., & DeBreuck, C. 2000, ApJS, 131, 185

Steidel, C. C.,Giavalisco, M., Pettini, M., Dickinson, M., & Adelberger, K. L. 1996, ApJ, 462, L17

Steidel, C. C., Adelberger, K. L., Shapley, A. E., Pettini, M., Dickinson, M., & Giavalisco, M. 2003, ApJ, 592, 728

Steidel, C. C., Shapley, A. E., Pettini, M., Adelberger, K. L., Erb, D. K., Reddy, N. A., & Hunt, M. P. 2004, ApJ, 604, 534

Sturm, E., et al. 2000, A&A, 358, 481

Swinbank, A. M., Smail, I., Chapman, S. C., Blain, A. W., Ivison, R. J., & Keel, W. C. 2004, ApJ, 617, 64

Tacconi, L. J., et al. 2002, ApJ, 580, 73

Tacconi, L. J., et al. 2006, ApJ, 640, 228

Takata, T., et al. 2006, ApJ, 651, 713

Valiante, E., Lutz, D., Sturm, E., Genzel, R., Tacconi, L. J., Lehnert, M. D., & Baker, A. J. 2007, ApJ, 660, 1060

vanden Bout, P., Solomon, P. M., & Maddalena, R. J. 2004, ApJ, 614, L97

van der Wel, A., Franx, M., Wuyts, S., van Dokkum, P. G., Huang, J., Rix, H.–W., & Illingworth, G. D. 2006, ApJ, 652, 97

van Dokkum, P. G., et al. 2003, ApJ, 587, L83

van Dokkum, P. G., et al. 2006, ApJ, 638, L59

Veilleux, S., et al. 2006, ApJ, 643, 707

Vlahakis, C., Eales, S., & Dunne, L. 2007, MNRAS, 379, 1042

Wang, W., et al. 2004, ApJ, 613, 655

Webb, T. M. A., et al. 2003b, ApJ, 582, 6

Weedman, D., et al. 2006, ApJ, 653, 101

Weiß, A., Downes, D., Walter, F., & Henkel, C. 2005a, A&A, 440, L45

Weiß, A., Walter, F. W., & Scoville, N. Z. 2005b, A&A, 438, 533

White, S. D. M., & Rees, M. J. 1978, MNRAS, 183, 341

Williams, R. E., et al. 1996, AJ, 112, 1335

Yan, H., Dickinson, M., Giavalisco, M., Stern, D., Eisenhardt, P. R. M., & Ferguson, H. C. 2006, ApJ, 651, 24

Yan, L., et al. 2007, ApJ, 658, 778

Yao, L., Seaquist, E. R., Kuno, N., & Dunne, L. 2003, ApJ, 588, 771

Young, J. S., Schloerb, F. P., Kenney, J. D., & Lord, S. D. 1986, ApJ, 304, 443

Younger, J., et al. 2007, ApJ, in press

Yun, M. S., Reddy, N. A., & Condon, J. J. 2001, ApJ, 554, 803